

UNIVERSIDAD POLITÉCNICA DE MADRID
ESCUELA TÉCNICA SUPERIOR DE INGENIEROS AERONÁUTICOS



ADVANCES IN GLOBAL INSTABILITY
COMPUTATIONS: FROM INCOMPRESSIBLE TO
HYPERSONIC FLOW

Doctoral Thesis

By
Pedro Paredes
Aeronautical Engineer

MADRID, MARCH 2014

ESCUELA TÉCNICA SUPERIOR DE INGENIEROS AERONÁUTICOS
UNIVERSIDAD POLITÉCNICA DE MADRID

Doctoral Thesis

**Advances in Global Instability Computations:
from Incompressible to Hypersonic Flow**

by

Pedro Paredes

Aeronautical Engineer

Advisors

Vassilis Theofilis and Ardeshir Hanifi



MADRID, MARCH 2014

This page intentionally left blank



POLITÉCNICA

Tribunal nombrado por el Sr. Rector Magfco. de la Universidad Politécnica de Madrid, el día.....5.....de.....MARZO.....de 2014

Presidente: D. DANN HENNINGSON

Vocal: D. TIM COLONIUS

Vocal: D. JOSÉ MANUEL VEGA DE PRADA

Vocal: D. ALEJANDRO SEVILLA SANTIAGO

Secretario: D. FRANCISCO JOSÉ HIGUERA ANTÓN

Suplente: D. RAQUEL GÓMEZ MIGUEL

Suplente: D. JESÚS CARLOS MARTÍNEZ BAZÁN

Realizado el acto de defensa y lectura de la Tesis el día 26 de marzo de 2014 en la E.T.S.I. /Facultad.....AERONÁUTICAS.....

CalificaciónAPTO.....

EL PRESIDENTE

LOS VOCALES

EL SECRETARIO

This page intentionally left blank

Abstract

The present thesis constitutes a step forward in advancing the frontiers of knowledge of fluid flow instability from a physical point of view, as a consequence of having been successful in developing groundbreaking methodologies for the efficient and accurate computation of the leading part of the spectrum pertinent to multi-dimensional eigenvalue problems (EVP) governing instability of flows with two or three inhomogeneous spatial directions.

In the context of the numerical work presented in this thesis, the discretization of the spatial operator resulting from linearization of the Navier-Stokes equations around flows with two or three inhomogeneous spatial directions by variable-high-order stable finite-difference methods has permitted a speedup of four orders of magnitude in the solution of the corresponding two- and three-dimensional EVPs. This improvement of numerical performance has been achieved thanks to the high-sparsity level offered by the high-order finite-difference schemes employed for the discretization of the operators. This permitted use of efficient sparse linear algebra techniques without sacrificing accuracy and, consequently, solutions being obtained on typical workstations, as opposed to the previously employed supercomputers.

Besides solution of the two- and three-dimensional EVPs of global linear instability, this development paved the way for the extension of the (linear and nonlinear) Parabolized Stability Equations (PSE) to analyze instability of flows which depend in a strongly-coupled inhomogeneous manner on two spatial directions and weakly on the third. Precisely the extensibility of the novel PSE-3D algorithm developed in the framework of the present thesis to study nonlinear flow instability permits transition prediction in flows of industrial interest, thus extending the classic PSE concept which has been successfully employed in the same context to boundary-layer type of flows over the last three decades.

Typical examples of incompressible flows, the instability of which was analyzed in the present thesis without the need to resort to the restrictive assumptions used in the past, range from isolated vortices, and systems thereof, in which axial homogeneity is relaxed to consider viscous diffusion, as well as turbulent swirling jets, the instability of which is exploited in order

Abstract

to improve flame-holding properties of combustors. The instability of compressible subsonic leading-edge flows has been solved, and the wake of an isolated roughness element in a supersonic and hypersonic boundary-layer has also been analyzed with respect to its instability: excellent agreement with direct numerical simulation results has been obtained in all cases. Finally, instability analysis of Mach number 7 flow around an elliptic cone modeling the HIFiRE-5 flight test vehicle has unraveled flow instabilities near the minor-axis centerline, results comparing favorably with flight test predictions.

Resumen

Esta tesis constituye un gran avance en el conocimiento del estudio y análisis de inestabilidades hidrodinámicas desde un punto de vista físico y teórico, como consecuencia de haber desarrollado innovadoras técnicas para la resolución computacional eficiente y precisa de la parte principal del espectro correspondiente a los problemas de autovalores (EVP) multidimensionales que gobiernan la inestabilidad de flujos con dos o tres direcciones espaciales inhomogéneas, denominados problemas de estabilidad global lineal.

En el contexto del trabajo de desarrollo de herramientas computacionales presentado en la tesis, la discretización mediante métodos de diferencias finitas estables de alto orden de los EVP bidimensionales y tridimensionales que se derivan de las ecuaciones de Navier-Stokes linealizadas sobre flujos con dos o tres direcciones espaciales inhomogéneas, ha permitido una aceleración de cuatro órdenes de magnitud en su resolución. Esta mejora de eficiencia numérica se ha conseguido gracias al hecho de que usando estos esquemas de diferencias finitas, técnicas eficientes de resolución de problemas lineales son utilizables, explotando el alto nivel de dispersión o alto número de elementos nulos en las matrices involucradas en los problemas tratados. Como más notable consecuencia cabe destacar que la resolución de EVPs multidimensionales de inestabilidad global, que hasta la fecha necesitaban de superordenadores, se ha podido realizar en ordenadores de sobremesa.

Además de la solución de problemas de estabilidad global lineal, el mencionado desarrollo numérico facilitó la extensión de las ecuaciones de estabilidad parabolizadas (PSE) lineales y no lineales para analizar la inestabilidad de flujos que dependen fuertemente en dos direcciones espaciales y suavemente en la tercera con las ecuaciones de estabilidad parabolizadas tridimensionales (PSE-3D). Precisamente la capacidad de extensión del novedoso algoritmo PSE-3D para el estudio de interacciones no lineales de los modos de estabilidad, desarrollado íntegramente en esta tesis, permite la predicción de transición en flujos complejos de gran interés industrial y por lo tanto extiende el concepto clásico de PSE, el cuál ha sido empleado exitosamente durante las pasadas tres décadas en el mismo contexto para problemas de capa límite bidimensional.

Típicos ejemplos de flujos incompresibles se han analizado en este trabajo sin la necesidad de recurrir a restrictivas presuposiciones usadas en el pasado. Se han estudiado problemas vorticales como es el caso de un vórtice aislado o sistemas de vórtices simulando la estela de alas, en los que la homogeneidad axial no se impone y así se puede considerar la difusión viscosa del flujo. Además, se ha estudiado el chorro giratorio turbulento, cuya inestabilidad se utiliza para mejorar las características de funcionamiento de combustores. En la tesis se abarcan adicionalmente problemas de flujos compresibles. Se presenta el estudio de inestabilidad de flujos de borde de ataque a diferentes velocidades de vuelo. También se analiza la estela formada por un elemento rugoso aislado en capa límite supersónica e hipersónica, mostrando excelentes comparaciones con resultados obtenidos mediante simulación numérica directa. Finalmente, nuevas inestabilidades se han identificado en el flujo hipersónico a Mach 7 alrededor de un cono elíptico que modela el vehículo de pruebas en vuelo HIFiRE-5. Los resultados comparan favorablemente con experimentos en vuelo, lo que subraya aún más el potencial de las metodologías de análisis de estabilidad desarrolladas en esta tesis.

Acknowledgements

To my father and mother

In the course of this work I have been supported by many people. I want to sincerely thank all of them, without who the work would have not been so fulfilling and rewarding.

First of all, I want to thank my advisor Professor Vassilis Theofilis. He gave me the opportunity to begin learning working under his guidance during the last years of my undergraduate courses. Thanks to this, I decided to start my research career in the field of fluid mechanics, specifically in the study of flow instabilities. This thesis is the outcome of his support and advice during these years. I also want to show my gratefulness to my co-advisor Professor Ardeshir Hanifi, who hosted me in the Royal University of Technology (KTH) in Stockholm. His help and advices have been essential for the success of this work. Special acknowledgment is made to the invaluable collaboration and fruitful discussions with Dr. Daniel Rodríguez and Dr. Miguel Hermanns during my PhD. period.

During these years I had the pleasure to meet many people visiting different abroad research groups, the discussions with who are kindly appreciated. I want to thank Professors Karthik Duraisamy and Fazle Hussain for hosting me in the Stanford University in Palo Alto, Professor Rama Govindarajan for hosting me in the Jawaharlal Nehru Centre for Advanced Scientific Research in Bangalore and Professor Helen Reed for hosting me in the Texas A&M University in College Station. I would like to thank them for sharing with me their knowledge. During my stays I also had the opportunity to interact with the people from the different research groups, including the FLOW group at KTH; their warm welcomes make the time in all the destinations more than enjoyable.

It has been a pleasure to collaborate with Dr. Nicola De Tullio and Professor Neil D. Sandham. The instability analysis of the roughness element wake is a result of this collaboration, since they performed the direct numerical simulations of this problem. I also want to acknowledge the collaboration with Dr. Kilian Oberleithner and Steffen Terhaar. They conducted

Acknowledgements

the experiments and therefore made possible the instability analysis of the isothermal swirling combustor flow. Furthermore, the results on the elliptic cone flow has been possible to the collaboration with Dr. Roger Kimmel and Dr. Ryan Gosse. Fruitful discussions with Professor Peter J. Schmid, Professor Sanjiva Lele, Dr. Joseph W. Nichols, Dr. Stefan Hein, Dr. Oliver Schmidt and Iman Lashgari are also kindly appreciated.

Also, I want to show my gratitude to all the people present in the day-by-day work, that provided a great working environment. Discussions with Dr. Javier de Vicente, Dr. Leo González, Dr. Eusebio Valero and Dr. Juan Ángel Martín and with the office mates (in chronological order) Dr. Francisco Gómez, Dr. José Migel Pérez, Dr. Elmer Mateus Gennaro, Juan Ángel Tendero, Dr. Soledad Le Clainche, Mamta Jotkar, Dr. Takashi Nakazawa, Qiong Liu, Wei He and Bo An are gratefully acknowledged.

This thesis would not have been possible without the support and comprehension of my family and friends, specially I want to thank my father Pedro Paredes, my mother Juana González, my syster Elena Paredes and last, but not least, a heartfelt thanks goes out to Maria José for all her love, support and patience when I was only thinking about strange formulas.

The material is based upon work sponsored by the US Air Force Office of Scientific Research, Air Force Material Command, USAF, under Grant number FA8655-12-1-2004. The US Government is authorized to reproduce and distribute reprints for Governmental purpose notwithstanding any copyright notation thereon. The Grant is monitored by Dr. Rengasamy Ponnappan of AFOSR (originally by Dr. John Schmisser) and Dr. Gregg Abate of EOARD.

Contents

| | |
|---|------------|
| Abstract | i |
| Resumen | iii |
| Acknowledgements | v |
| Contents | vii |
| Introduction | xxi |
| 1 Hydrodynamic Instability | 1 |
| 1.1 The equations of fluid motion | 1 |
| 1.2 Instability analysis theory | 2 |
| 1.3 Modal linear stability theory | 5 |
| 1.3.1 Local instability | 8 |
| 1.3.2 Parabolized Stability Equations | 12 |
| 1.3.3 BiGlobal instability | 15 |
| 1.3.4 Three-dimensional parabolized stability equations | 17 |
| 1.3.5 TriGlobal instability | 18 |
| 2 Numerical considerations | 21 |
| 2.1 Spatial discretization | 21 |
| 2.1.1 Dispersion-Relation-Preserving schemes | 21 |

Contents

| | | |
|----------|--|-----------|
| 2.1.2 | Compact finite-difference schemes | 22 |
| 2.1.3 | Summation-by-Parts finite-difference schemes | 23 |
| 2.1.4 | Finite-difference methods with uniform error | 23 |
| 2.1.5 | Spectral collocation methods | 26 |
| 2.2 | Multidimensional differentiation matrices | 30 |
| 2.2.1 | Two-dimensional differentiation matrices | 30 |
| 2.2.2 | Three-dimensional differentiation matrices | 31 |
| 2.3 | General coordinate transformation | 32 |
| 2.3.1 | Two-dimensional transformation | 35 |
| 2.3.2 | Verification | 36 |
| 2.3.3 | One-dimensional mappings | 38 |
| 2.4 | Eigenvalue computation | 40 |
| 2.5 | Solution procedure of PSE-3D | 41 |
| 2.5.1 | Parabolic marching integration | 41 |
| 2.5.2 | Non-linear terms | 41 |
| 3 | Linear modal stability validations and numerical efficiency | 43 |
| 3.1 | Introduction | 43 |
| 3.2 | Incompressible stability analysis validations | 44 |
| 3.2.1 | Local instability analysis | 45 |
| 3.2.2 | The 2D Helmholtz EVP | 52 |
| 3.2.3 | BiGlobal instability analysis | 54 |
| 3.2.4 | The 3D Helmholtz EVP | 60 |
| 3.2.5 | The TriGlobal EVP | 61 |
| 3.3 | Compressible stability analysis validations | 65 |
| 3.3.1 | The Local EVP | 65 |
| 3.3.2 | The BiGlobal EVP | 66 |

| | | |
|----------|---|------------|
| 3.4 | The efficiency advantages of using FD-q | 72 |
| 3.4.1 | Incompressible regime operators | 73 |
| 3.4.2 | Compressible regime operators | 77 |
| 3.5 | Summary and conclusions | 81 |
| 4 | PNS solutions of incompressible and compressible base flows | 83 |
| 4.1 | Introduction | 83 |
| 4.2 | Theory | 86 |
| 4.2.1 | Parabolic Navier-Stokes equations | 86 |
| 4.3 | Numerical considerations | 87 |
| 4.3.1 | Spatial discretization | 87 |
| 4.3.2 | Non-linear marching integration | 87 |
| 4.4 | Incompressible vortex flows | 88 |
| 4.4.1 | The isolated trailing-vortex | 89 |
| 4.4.2 | The trailing counter-rotating vortex-pair | 91 |
| 4.5 | Compressible circular and elliptic cone flows | 96 |
| 4.5.1 | Circular cone | 98 |
| 4.5.2 | Elliptic cone | 98 |
| 4.6 | Summary and conclusions | 99 |
| 5 | Instability analysis of vortex flows using parabolized equations | 105 |
| 5.1 | Introduction | 105 |
| 5.2 | Results | 107 |
| 5.2.1 | The isolated trailing-vortex | 107 |
| 5.2.2 | The trailing counter-rotating vortex-pair | 111 |
| 5.3 | Summary and conclusions | 113 |

| | | |
|----------|--|------------|
| 6 | Global analysis of a turbulent swirling combustor flow | 115 |
| 6.1 | Introduction | 115 |
| 6.2 | Theory | 117 |
| 6.2.1 | Stability analysis of turbulent mean flows | 117 |
| 6.2.2 | Eddy-viscosity closure | 118 |
| 6.2.3 | Global analysis of axisymmetric flows | 119 |
| 6.3 | Experimental setup | 121 |
| 6.4 | Results | 122 |
| 6.4.1 | Experimental observations | 122 |
| 6.4.2 | Global instability analysis | 125 |
| 6.5 | Summary and conclusions | 126 |
| 7 | Roughness-induced transition in high speed boundary-layers | 127 |
| 7.1 | Introduction | 127 |
| 7.2 | Theory | 131 |
| 7.3 | Results | 132 |
| 7.3.1 | Supersonic regime | 132 |
| 7.3.2 | Hypersonic regime | 139 |
| 7.4 | Summary and conclusions | 143 |
| 8 | Instability analysis of the hypersonic flow over an elliptic cone | 145 |
| 8.1 | Introduction | 145 |
| 8.2 | Spatial BiGlobal analysis for general coordinate transformation | 147 |
| 8.3 | Numerical considerations | 149 |
| 8.3.1 | Elliptic cone transformation | 149 |
| 8.3.2 | Boundary conditions | 149 |
| 8.4 | Base flow | 150 |

| | | |
|----------|---|------------|
| 8.5 | Results | 152 |
| 8.6 | Summary and conclusions | 154 |
| 9 | Non-linear PSE-3D | 157 |
| 9.1 | Introduction | 157 |
| 9.2 | Results | 158 |
| A | Linearized Navier-Stokes equations | 161 |
| B | Temporal BiGlobal EVP operators | 165 |
| C | Spatial BiGlobal EVP operators | 169 |
| D | Non-linear PSE-3D operators | 173 |
| E | TriGlobal EVP operators | 179 |
| F | Compressible PNS operators | 183 |

Contents

List of Figures

| | | |
|-----|---|----|
| 1.1 | Schematic comparison of leading dimension of matrices discretizing local, classical PSE, BiGlobal and PSE-3D operators. | 8 |
| 2.1 | Stencils and domains of validity of individual polynomial interpolants | 24 |
| 2.2 | Comparison of non-uniform, CGL and uniform grid spacing . | 27 |
| 2.3 | Elliptic confocal grid around a 2:1 ellipse. | 37 |
| 2.4 | Solution of the 2D Helmholtz EVP in an elliptic confocal grid | 37 |
| 2.5 | Elliptic non-orthogonal grid around a 2:1 ellipse. | 38 |
| 2.6 | Solution of the 2D Helmholtz EVP in an elliptic non-orthogonal grid | 39 |
| 3.1 | Convergence history of relative error for the leading eigenmode of PPF | 47 |
| 3.2 | Eigenspectrum and psudospectrum of PPF | 49 |
| 3.3 | Eigenspectrum comparison of Blasius boundary-layer flow . . | 50 |
| 3.4 | Eigenspectrum and psudospectrum of Blasius boundary-layer flow | 51 |
| 3.5 | Convergence history of relative error for the solution of the 2D Helmholtz EVP | 52 |
| 3.6 | Convergence history of eigenmode and iso-contours of eigenfunction for the solution of the 2D Helmholtz EVP | 53 |
| 3.7 | Convergence history of the BiGlobal leading eigenmode for the rectangular duct flow | 56 |

List of Figures

| | | |
|------|--|----|
| 3.8 | Convergence history of the BiGlobal leading eigenmode for the lid-driven cavity flow | 58 |
| 3.9 | Convergence history of eigenmode and iso-surfaces of eigenfunction for the solution of the 3D Helmholtz EVP | 60 |
| 3.10 | Eigenfunctions solution of local instability analysis of compressible flat-plate boundary-layer flow | 66 |
| 3.11 | Eigenspectrum and psudospectrum of compressible flat-plate boundary-layer flow | 67 |
| 3.12 | Evolution of the norm of the propagator for compressible flat-plate boundary-layer flow at $Re = 1000$ | 67 |
| 3.13 | Evolution of the norm of the propagator for compressible flat-plate boundary-layer flow at $Re = 100$ | 68 |
| 3.14 | Velocity components of the Görtler-Hammerling mode solution of BiGlobal instability analysis of compressible attachment-line boundary-layer flow | 70 |
| 3.15 | Velocity components of the first anti-symmetric mode solution of BiGlobal instability analysis of compressible attachment-line boundary-layer flow | 71 |
| 3.16 | Sparsity pattern of incompressible BiGlobal matrices | 73 |
| 3.17 | Required memory for LU-factorization of incompressible BiGlobal EVP | 75 |
| 3.18 | Elapsed time for LU-factorization of incompressible BiGlobal EVP | 76 |
| 3.19 | Sparsity pattern of compressible BiGlobal matrices | 78 |
| 3.20 | Required memory for LU-factorization of compressible BiGlobal EVP | 79 |
| 3.21 | Elapsed time for LU-factorization of compressible BiGlobal EVP | 81 |
| 4.1 | Comparison between theoretical and PNS computed axial velocity defect and vortex radius for the non-parallel vortex | 90 |
| 4.2 | Comparisons between experimental and PNS results for the non-parallel isolated vortex | 92 |

| | | |
|------|--|-----|
| 4.3 | Sketch of the rotational transformation around the y -axis used for the computations of the counter-rotating pair of trailing vortices by PNS. | 94 |
| 4.4 | Residuals for the PNS solution of the counter-rotating vortex-pair flow | 94 |
| 4.5 | Axial vorticity of the non-parallel counter-rotating vortex pair flow computed by PNS | 95 |
| 4.6 | Evolution on streamwise direction of vortex radius for the counter-rotating vortex-pair flow computed by PNS | 96 |
| 4.7 | Evolution on streamwise direction of vortex core position for the counter-rotating vortex-pair flow computed by PNS | 97 |
| 4.8 | Comparison of PNS solutions over circular cones with theoretical predictions | 99 |
| 4.9 | Three-dimensional view of velocity flow fields on a 2:1 elliptic cone at Mach 3 and 4 | 100 |
| 4.10 | Three-dimensional view of temperature and density flow fields on a 2:1 elliptic cone at Mach 3 and 4 | 101 |
| 4.11 | Near-wall streamlines of a 7° half minor-axis angle 2:1 elliptic cone at $M = 4$ | 102 |
| 5.1 | Leading eigenmodes for the Batchelor vortex model flow computed using spatial BiGlobal instability analysis | 109 |
| 5.2 | Eigenspectrum and leading eigenmode streamwise velocity component for the Batchelor vortex model flow computed using spatial BiGlobal instability analysis | 109 |
| 5.3 | Evolution of initial eigenvalue by PSE-3D iterations | 110 |
| 5.4 | Evolution of growth rate for the non-parallel isolated vortex flow for the leading eigenmode comparing local analysis, PSE and PSE-3D results | 110 |
| 5.5 | Iso-surfaces of axial velocity amplitude functions computed by local parallel and non-parallel theories | 111 |
| 5.6 | Axial velocity of leading eigenmodes for the counter-rotating Batchelor vortex computed by spatial BiGlobal analysis | 112 |

List of Figures

| | | |
|-----|---|-----|
| 5.7 | Evolution of wavenumber and growth rate for the counter-rotating non-parallel vortex-pair flow computed by PSE-3D | 113 |
| 5.8 | Axial vorticity for counter-rotating non-parallel vortex-pair flow computed using PSE-3D | 114 |
| 6.1 | Generic burner and stereo PIV setup | 121 |
| 6.2 | Time-averaged flow field | 123 |
| 6.3 | Flow field turbulence properties | 123 |
| 6.4 | PSD of the pressure signal at the burner | 124 |
| 6.5 | Global instability analysis eigenspectrum for mean experimental swirling jet flow | 124 |
| 6.6 | Radial velocity comparisons between experimental reconstructed POD mode and eigenfunction calculated by global analysis | 125 |
| 7.1 | Streamwise velocity shear in crossflow planes of roughness-induced wake at Mach 2.5 | 134 |
| 7.2 | Comparisons between full Navier-Stokes and PSE-3D results at different streamwise positions | 135 |
| 7.3 | Spatial BiGlobal spectrum and temperature eigenfunctions of unstable modes | 136 |
| 7.4 | Mode shape comparison between Navier-Stokes and BiGlobal stability results | 137 |
| 7.5 | Comparisons between full Navier-Stokes and PSE-3D results of amplification of dominant modes | 138 |
| 7.6 | Streamwise velocity shear in crossflow planes of roughness-induced wake at Mach 6 | 140 |
| 7.7 | Contours of streamwise velocity eigenfunctions of leading roughness-induced modes at hypersonic conditions | 141 |
| 7.8 | Spatial BiGlobal spectrum and streamwise velocity eigenfunctions of unstable modes at Mach 6 | 142 |
| 7.9 | Disturbance growth rates at fixed frequency recovered by spatial BiGlobal and PSE-3D for hypersonic regime | 142 |

| | | |
|-----|--|-----|
| 8.1 | Streamwise Mach number around the HIFiRE-5 elliptic cone flow | 151 |
| 8.2 | Wavenumber and growth rate of most amplified modes for the HIFiRE-5 elliptic cone flow | 153 |
| 8.3 | Spatial BiGlobal spectrum and streamwise velocity eigenfunctions of leading centerline mode | 154 |
| 8.4 | Spatial BiGlobal spectrum and streamwise velocity eigenfunctions of leading centerline and crossflow mode | 155 |
| 9.1 | Root-mean-square evolution of streamwise velocity component for the incompressible flat-plate boundary-layer using the non-linear PSE-3D and the NOLOT/PSE codes | 158 |
| 9.2 | Amplitude evolution of streamwise velocity component for supersonic roughness-element wake flow | 160 |

List of Figures

List of Tables

| | | |
|------|---|----|
| 1.1 | Classification of modern linear stability analysis theory concepts into local (OSS), non-local (PSE) and global (BiGlobal, PSE-3D, TriGlobal) theories. | 6 |
| 2.1 | Accuracy study for different approaches of \mathcal{D}_{GL} with $N = 128$ | 29 |
| 3.1 | Examined spatial discretization methods. | 46 |
| 3.2 | BiGlobal instability analysis of the rectangular duct flow. . . | 55 |
| 3.3 | BiGlobal instability analysis of the incompressible attachment-line boundary-layer flow. | 59 |
| 3.4 | TriGlobal instability analysis of the 2D rectangular duct flow | 62 |
| 3.5 | TriGlobal instability analysis of the 2D regularized lid-driven cavity flow | 63 |
| 3.6 | TriGlobal instability analysis of the 3D regularized lid-driven cavity flow | 64 |
| 3.7 | Local modal analysis results of compressible flat-plate boundary-layer at Mach 6 | 66 |
| 3.8 | BiGlobal instability analysis of the compressible attachment-line boundary-layer flow | 69 |
| 3.9 | Required memory for LU-factorization of incompressible BiGlobal eigenvalue problem | 74 |
| 3.10 | Elapsed time for LU-factorization of incompressible BiGlobal eigenvalue problem | 76 |
| 3.11 | Required memory for LU-factorization of compressible BiGlobal eigenvalue problem | 79 |

List of Tables

| | | |
|------|---|-----|
| 3.12 | Elapsed time for LU-factorization of compressible BiGlobal eigenvalue problem | 80 |
| 5.1 | Leading eigenmodes for the Batchelor vortex model flow computed using spatial BiGlobal instability analysis | 108 |

Introduction

Linear stability theory, in part motivated by research into laminar-turbulent flow transition, has occupied a substantial part of fluid mechanics research for over a century. Numerical expediency has confined the bulk of the efforts into analyzing one-dimensional shear flows. The classic linear stability theory of Tollmien [257] is mainly concerned with individual sinusoidal waves propagating in the boundary-layer parallel to the wall. In this context, the parallel flow approximation is assumed, resulting in an ordinary differential equations (ODE)-based eigenvalue problem (EVP), which may be expressed as the Orr-Sommerfeld and Squire equations (OSE) [57, 161, 221]. The prediction of boundary-layer transition based on solutions of the OSE remains the only theoretically-founded approach in use in industry presently. However, discrepancies exist with experimental results, especially at the tip of the neutral curve of Blasius flow, as well as in boundary-layer flows in the presence of pressure gradients. The origin of the discrepancies was traced back to the existence of a small but not negligible wall-normal base flow velocity component. An instability analysis concept of the multiple-scales class, which relaxes the parallel flow approximation was introduced in the 1990s of last century [22, 100, 144], denominated Parabolized Stability Equations (PSE), owing to the change in the mathematical nature that the multiple-scales approach introduces to the linearized stability equations. A key advantage of the PSE over the OSE types of approaches is that it permits natural introduction of non-linear mode interaction and has been shown to be in excellent agreement with spatial DNS both on flat-plate boundary layer [22] and vortex flows [268]. In-depth studies of the classic PSE have appeared in the literature in the course of the past two decades [22, 37, 101, 145, 146]; see Herbert [102] for a review.

In a manner conceptually analogous to the OSE, global linear stability theory may consider base flows which are inhomogeneous in two (rather than one) spatial directions. The amplitude functions of the associated small-amplitude perturbations are now inhomogeneous in the same two spatial directions upon which the base flow depends and are periodic along the third and are obtained from numerical solution of the pertinent two-dimensional (BiGlobal) partial differential equations (PDE)-based EVP. The

three-dimensional (TriGlobal) PDE-based EVP has also been solved in a linear stability context, when no homogeneous directions existing in the base flow. Three decades of research into this type of global instability analysis has already produced a wealth of information; see Theofilis [249, 250] for a review.

The pioneering studies of inviscid instability of a vortex by Pierrehumbert [193], viscous instability analyses in the wake of the circular cylinder by Zebib [278] and the rectangular duct by Tatsumi and Yoshimura [244] fall in the category of flows with two non-periodic spatial directions; all three works employed spectral methods for the spatial discretization of the linearized operator. Almost simultaneously, finite-element methods were also used for the solution of the two-dimensional EVP by Jackson [113] and Morzyński and Thiele [178], while finite-volume methods soon followed [55]. Although finite-element or finite-volume methods are not restricted to the single-domain two-dimensional grids employed in the early spectral analyses, their low formal order of accuracy needs to be compensated in terms of grid density: should sharp gradients need to be resolved, as the case is with the amplitude functions of global eigenmodes at increasingly high Reynolds numbers, one resorts to using unstructured meshes of ever-increasing density in order to achieve convergence [e.g. 79]. In doing so, one effectively trades off the efficiency of a high-order method in favor of the flexibility offered by the unstructured mesh discretization. The case is thus set for high-order accurate, flexible and efficient numerical methods in order to solve the BiGlobal EVP. Such an approach has been introduced in the seminal work of three-dimensional instability in the wake of a circular cylinder by Barkley and Henderson [15, 98] in the form of spectral-element discretization on structured meshes. The first application of a spectral/*hp*-element method [118] to the study of a global instability problem on unstructured meshes was that of Theofilis et al. [252], who recovered instability in the wake of a NACA0012 airfoil as the leading BiGlobal eigenmode of the steady wake flow.

Regarding eigenspectrum computations, early analyses relied on full eigenspectrum computation [194, 278], which scales as $\mathcal{O}(M^2)$ and $\mathcal{O}(M^3)$ with regard to memory and CPU time requirements, respectively, if a total number of M degrees of freedom are used for the spatial discretization of the linearized operator. Both estimates present a severe limitation for full eigenspectrum computations in both two and three simultaneously discretized spatial directions. Access to the entire eigenspectrum of global EVPs is thus routinely sacrificed in present-day global instability analysis algorithms, which employ some form of subspace iteration to recover a small subset of the eigenspectrum. This practice is justified since, from a physical point of view only a relatively small part of the leading perturbations, those close to the

origin, is relevant to flow instability. On the other hand, access to the smallest eigenvalues implies inversion of the discretized linear operator; a common practice to avoid inversion, the cost of which is also $\mathcal{O}(M^2)$ and $\mathcal{O}(M^3)$ if a direct dense method is used, is to emulate the action of the inverse operator during the subspace creation, without ever forming or inverting the operator. Well-established practices in the latter context, collectively referred to as *time-stepping* methods, have been introduced by Eriksson and Rizzi [61] and Edwards et al. [59] and are in use in modern global instability analysis, such as the three-dimensional global instability analyses of Tezuka and Suzuki [246] and Bagheri et al. [11], or the modal and non-modal work of Blackburn et al. [24]. When considering non-modal linear analysis or *transient growth*, the theory pertinent to one-dimensional base flows is well developed [221] (mainly in the incompressible regime, except some works in the compressible regime as for example [91]), but little transient growth analysis of essentially multi-dimensional flows has been reported in the literature; the works of Arkevik et al. [9], Blackburn et al. [23, 25], Heaton et al. [92] and Abdessemed et al. [1] are first examples in this class of analysis, all of them in the incompressible limit, as well as the recent work of Schmidt and Rist [223] in the compressible regime. The non-modal theory use to rely in the computation of the singular value decomposition (SVD) instead of solving an EVP when considering modal theory.

Nevertheless, it may be argued that forming the matrix has certain advantages over time-stepping, the main ones being simplicity in the formation of the global EVP or SVD, and flexibility in extending the analysis into regimes that would require the availability of entirely different flow solvers, if the time-stepping approach were to be used. When the matrix is formed, it is straightforward to include in the same code compressibility effects in subsonic or supersonic flow, extend the analysis into the hypersonic regime by implementing a few additional terms in an otherwise unchanged algorithm, or include new physics, such as non-Newtonian dynamics or magnetohydrodynamics, all by appropriately modifying the linearized operator. The penalty to be paid is of course the need to store and operate large matrices which, as the resolution requirements increase, can quickly be unmanageable in all but the largest supercomputers.

For a given spatial discretization method within a matrix forming context, straightforward serial (see [249] and Supplemental Appendix 3 of [250] for an overview), as well as parallel computations (ranging from a modest number of processors [47] up to massively parallel EVP solutions [129, 208–210]) have been used for the recovery of (part of) the global eigenspectrum. A key efficiency improvement was proposed by Crouch et al. [47] who first employed sparse direct solvers for this class of problems. In order to exploit

the benefits of using sparse solvers, Merle et al. [175] compared Padé [138] and Dispersion-Relation-Preserving [240] high-order finite-difference spatial discretization schemes to the solution of the incompressible BiGlobal EVP and concluded that from a combined accuracy and efficiency perspective the DRP schemes offer the best alternative for the solution of this global EVP.

The most general case corresponds to a three-dimensional flowfield, which is inhomogeneous in all three spatial directions. A numerical solution of the PDE-based EVP resulting from the discretization of the three coupled directions, referred to as a TriGlobal stability analysis, is possible but prohibitively expensive nowadays for most applications of interest. A parabolized variation of the three-dimensional stability equations (PSE-3D) can be derived when the base flow can be assumed to experience slow variations along one of the three spatial directions. Examples of such flows are corner flows [68, 222], square or serrated-nozzle jets [128], missile-shaped bodies, i.e. circular and elliptic cones- or systems of trailing-vortices in wakes. In this manner, the three-dimensional EVP is replaced by an initial value problem that is solved using a marching integration along the slow direction. In an analogous manner to the extension of the OSS equations to the conventional PSE, the BiGlobal analysis equations are extended to the PSE-3D analysis, which appears to be the most efficient methodology for the study of wide branch of complex flows, as the examples mentioned above.

The linear PSE-3D methodology, formulated in the incompressible limit in Galionis and Hall [68] [see also 31, 32, 188] and for the first time in the compressible flow regime in [52], assumes the existence of two scales along the streamwise spatial direction: a slow one, on which the base flow varies, and a fast one, along which linear and non-linear wave-like perturbations develop. Base flow and disturbances are inhomogeneous functions of the two coordinates of the cross-sectional planes, and hence the two directions need to be resolved in a coupled manner. Therefore, the PSE-3D methodology resolves a PDE-based instability problem at each streamwise location. After initialising the PSE-3D with solutions of the spatial BiGlobal EVP at a given cross-section of the geometry analysed [188], the full three-dimensional disturbance equations are marched along the slowly varying spatial direction, solving the aforementioned PDE-based stability problem (with two-dimensional eigenfunctions) at each station. It should be noted that the term PSE-3D has been used in the literature to describe the standard PSE [102] as applied to three-dimensional boundary-layers [as in 179]. Here, the term PSE-3D is redefined in the sense of Broadhurst et al. [32] and Paredes et al. [188] to denote an instability analysis methodology in which the base flow is strongly dependent on two spatial directions.

The typical modal instability theory based on linear ordinary differential equations of OSE or the linear partial differential equations of BiGlobal analyses neglect the interaction between modes. Hence, its application is restricted to regions of small disturbance amplitude, i.e. regions where modes develop practically independent from each. Non-local non-linear methods based on PSE, as the DLR/FOI transition analysis code NOLOT/PSE [90, 94, 96] do not require linearization. Therefore, they also model the non-linear early stages of laminar-turbulent breakdown. The same methodology used for the addition of non-linear effects in the PSE is extended here for the PSE-3D, enabling the study of complex three-dimensional flows that so far were only accessible to the much more computationally expensive full Navier-Stokes spatial evolving simulations.

Besides the instability analysis theory and several applications, the computation of base flows is also treated in this thesis. It is well-known that instability analysis results are strongly dependent on the details of the base flow [250]. Small differences in the base flow can lead to remarkable differences in the predicted amplifications, due to the exponential nature of linear modal instability, while also leading to erroneous predictions of the relevant frequencies of the small amplitude perturbations. The recovery of accurate base flows using DNS in circumstances in which the flow is steady *per se* -and is thus, stable-, or along with a Newton-iteration technique [261] in those cases in which an unsteady flow would exist, though feasible, may require considerable computational resources for the three-dimensional, moderate-to-high Reynolds number flows of industrial interest. In those flows in which a predominant spatial direction exists, along which the mean properties of the flowfield vary slowly while fast variations are observed on the cross-sectional planes, simplified approaches may be available in order to circumvent the large computational cost. The geometrical particularities of this kind of flows can be exploited in order to devise *ad hoc* approaches for the computation of base flows, that result more efficient for the problem at hand than using DNS. Along the present thesis, an algorithm for the accurate and efficient computation of incompressible and compressible steady laminar base flows in which strong flow variations exist along two spatial directions, while a mild variation can be assumed along the third. This algorithm is based on the Parabolic Navier-Stokes (PNS) equations [216]. Since their appearance, these equations have been used to successfully compute supersonic and hypersonic, viscous flows; see [215, 243] for a review. The incompressible version of the PNS equations were first formulated by Rubin and Lin [214]. One of the advantages of using PNS for the computation of base flows in an instability analysis context, is the steadiness of the solutions obtained by definition. In this manner, unsteadiness in the real flow will be recovered as

instability of the base flow in a later instability analysis. It is important to notice that the same assumptions required to compute the flow field through PNS are invoked in order to perform subsequent instability analysis of these flows using PSE-3D.

The present thesis is divided into different chapters, each one addressing a differentiated objective of the present research work:

- Chapter 1: This Chapter presents a survey of the instability theory, addressing the different instability approaches depending on the dimensionality of the base flow. Besides the modal local, BiGlobal and TriGlobal analyses, attention is focused on the parabolized stability equations for two- and three-dimensional flows, namely the classical PSE and the PSE-3D respectively.
- Chapter 2: In this Chapter different numerical methods for matrix formation approach are briefly described. Special attention is firstly devoted to the spatial discretization. Then, the equations used for analytical grid transformation, the eigenvalue computation algorithm and the solution procedure for PSE-3D are explained.
- Chapter 3: A unified solution framework is presented for one-, two- or three-dimensional complex non-symmetric EVPs, respectively governing linear modal instability of fluid flows in rectangular domains having two, one or no homogeneous spatial directions. The solution algorithm is based on subspace iteration in which the spatial discretization matrix is formed, stored and inverted serially. Results delivered by spectral collocation based on the Chebyshev-Gauss-Lobatto (CGL) points and a suite of high-order finite-difference methods comprising the previously employed for this type of work Dispersion-Relation-Preserving (DRP) and Padé finite-difference schemes, as well as the Summation-by-parts (SBP) and the new high-order finite-difference scheme of order q (FD- q) have been compared from the point of view of accuracy and efficiency in standard validation cases of temporal local and BiGlobal linear instability. The FD- q method is found to significantly outperform all other finite difference schemes in solving classic linear local, BiGlobal, and TriGlobal EVPs, as regards both memory and CPU time requirements. Results shown in the present study disproves the paradigm that spectral methods are superior to finite difference methods in terms of computational cost, at equal accuracy, FD- q spatial discretization delivering a speedup of $\mathcal{O}(10^4)$.
- Chapter 4: Flows of practical significance exist, like systems of trailing vortices or the flow around the nose of an aerospace vehicle and the

associated circular- and elliptic-base cone models, which are inhomogeneous in two and weakly dependent along the third spatial direction. Exploiting these characteristics, an integration of the Navier-Stokes equations using the PNS concept is proposed for the recovery of steady solutions, that might be used subsequently in the scope of primary instability analyses. The PNS equations are first formulated in the incompressible regime in a cylindrical coordinate frame, and used to calculate the solution of an isolated, axisymmetric non-parallel (axially developing) vortex. Then, the fully three-dimensional flow corresponding to a counter-rotating pair of non-parallel vortices is obtained by PNS. Furthermore, the PNS equations are formulated in compressible regime using an arbitrary coordinate transformation. For verification purposes, the boundary-layer solution around a circular cone at zero angle of attack is compared in the incompressible limit with theoretical profiles. At supersonic speed, at which an oblique shock appears, the recovered shock wave angle is compared with theoretical predictions in the same circular cone geometry. Finally, the entire flow field around a 2:1 elliptic cone, including the imbedded shock and the three-dimensional boundary-layer, is recovered at Mach numbers 3 and 4.

- Chapter 5: In the literature, the flows addressed in the previous Chapter, which are inhomogeneous in two and weakly dependent on the third spatial direction, have been analyzed by simplified methodologies those do not take in account the three-dimensionality or by the very expensive, in terms of computational requirements, spatially evolving DNS. Exploiting the properties of these problems, the PSE-3D arise to be the best candidates for their instability analysis. Focusing on the incompressible vortex flows, the standard PSE in cylindrical coordinates is used along with the non-parallel vortex base flow computed by PNS, as a validation test for the PSE-3D algorithm presented herein. The fully three-dimensional counter-rotating vortex-pair flow is analyzed through PSE-3D.
- Chapter 6: In this Chapter, the global mode in a strongly swirling turbulent combustor flow undergoing vortex breakdown is experimentally and analytically investigated. The experiment shows a self-excited global flow oscillation at a well-defined frequency. Based on the mean flow field, a global hydrodynamic stability analysis is carried out. The dampening effect of the Reynolds stresses are accounted for by an estimated eddy viscosity. The global analysis successfully predicts the frequency of the global mode and yields the global shape of the instability.
- Chapter 7: The linear instability induced by an isolated roughness ele-

ment in a boundary-layer at Mach 2.5 and 6 is analyzed in this Chapter through direct numerical simulations, aided by spatial BiGlobal and PSE-3D stability analyses. It is important to understand transition in this flow regime since the process can be slower than in incompressible flow and is critical to prediction of local heat loads on next-generation flight vehicles. The results show that the roughness element, with a height of the order of the boundary-layer displacement thickness, generates a convectively unstable wake, which is composed of a low velocity streak surrounded by a three-dimensional high-shear layer and is able to sustain the rapid growth of a number of instability modes. The most unstable of these modes are associated with varicose or sinuous deformations of the low-velocity streak; they are a consequence of the instability developing in the three-dimensional shear layer as a whole (the varicose mode) or in the lateral shear layers (the sinuous mode). At the hypersonic regime, the Mach 6 case, boundary-layer modes develop at high frequencies and are also covered here. The independently performed Navier-Stokes, spatial BiGlobal and PSE-3D stability results are in excellent agreement with each other, validating the use of simplified theories for roughness-induced transition involving wake instabilities.

- Chapter 8: In this Chapter, the linear instability of the three-dimensional boundary-layer over the HIFiRE-5 flight test geometry, i.e. a rounded-tip 2:1 elliptic cone, is analyzed through spatial BiGlobal analysis, in a effort to understand transition and accurately predict local heat loads on this configuration. The base flow is computed at flight conditions of Mach 7 flow at altitude of 33.0 *km* and unit Reynolds number 1.89×10^6 /*m* using the US3D non-equilibrium solver by Gosse et al. [81]. The stability analysis results reveal that the leading unstable modes peak on the mushroom-like structure formed near the minor-axis meridian. On account of the three-dimensionality of the elliptic cone boundary-layer, this produces spanwise pressure gradients, inducing crossflow from the leading edge (major-axis meridian) to the centerline (minor-axis meridian), resulting in a lift-up of low momentum boundary-layer fluid at the centerline. An unstable fluid structure, which is composed of a low velocity streak surrounded by a three-dimensional high-shear layer, is thus generated and is found to sustain the rapid growth of instability modes.
- Chapter 9: In this Chapter, in an analogous manner to the addition of non-linear effects into the conventional PSE, the linear PSE-3D are extended to predict the non-linear development of perturbations on this kind of complex three-dimensional flows. This new in-house developed

code is used firstly on the flat-plate boundary-layer, showing excellent agreement with PSE results, and secondly on the wake of an isolated roughness-element imbedded in a supersonic boundary-layer.

Most of the material in the present thesis, along with additional specific details, has been compiled in the following list of publications:

- Journal articles

- Gómez, F., Le Clainche, S., Paredes, P., Hermanns, M., Theofilis, V. (2012) “Four decades of studying global linear instability: progress and challenges”, *AIAA Journal*, 50, 2731-2743.
- Paredes, P., Hermanns, M., Le Clainche, S., Theofilis, V. (2013) “Order 10^4 speedup in global linear instability analysis using matrix formation”, *Computer Methods in Applied Mechanics and Engineering*, 253, 287-304
- De Tullio, N., Paredes, P., Sandham, N.D., Theofilis, V. (2013) “Laminar-turbulent transition induced by a discrete roughness element in a supersonic boundary layer”, *Journal of Fluid Mechanics*, 735, 613-646
- Paredes, P., Rodríguez, D., Theofilis, V. (2013) “Three-dimensional solutions of trailing-vortex flows using parabolized equations”, *AIAA Journal*, 51(12), 2763-2770.
- Paredes, P., Theofilis, V. (in review) “The centerline global mode in Mach 7 flow on the HIFiRE-5 elliptic cone”, *Journal of Fluids and Structures*
- Paredes, P., Terhaar, S., Oberleithner, K. and Theofilis, V. (in preparation) “On the global instability of an isothermal swirling combustor flow”, *Journal of Fluid Mechanics*
- Paredes, P., Theofilis, V., Kimmel, R. and Gosse, R. (in preparation) “Global instability mechanisms on the HIFiRE-5 elliptic cone model flow”, *Journal of Fluid Mechanics*

- Conference papers

- De Vicente, J., Paredes, P., Valero, E. and Theofilis, V. (2011) “Wave-like disturbances on the downstream wall of an open cavity”, 6th AIAA Theoretical Fluid Mechanics Conference, Honolulu, Hawaii, USA, 27-30 June 2011, AIAA 2011-3754

- Paredes, P., Theofilis, V., Rodríguez, D. and Tendero, J.A. (2011) “The PSE-3D instability analysis methodology for flows depending strongly on two and weakly on the third spatial dimension”, 6th AIAA Theoretical Fluid Mechanics Conference, Honolulu, Hawaii, USA, 27 - 30 June 2011, AIAA 2011-3752
- Paredes, P., Theofilis, V. and Rodríguez, D. (2012) “Parabolic Navier-Stokes solutions of trailing vortex”, 42nd AIAA Fluid Dynamics Conference, New Orleans, Louisiana, USA, 25 - 28 June 2012, AIAA 2012-3348
- Gómez, F., Theofilis, V., Paredes, P., Liu, Q. and He, W. (2012) “On the role of global flow instability analysis in closed loop flow control”, 6th AIAA Flow Control Conference, New Orleans, Louisiana, USA, 25 - 28 June 2012, AIAA 2011-3754
- Gómez, F., Paredes, P., Gómez, R., Theofilis, V. (2012) “Global stability of cubic and large aspect ratio three-dimensional lid-driven cavities”, 42nd AIAA Fluid Dynamics Conference, New Orleans, Louisiana, USA, 25 - 28 June 2012, AIAA 2012-3274
- Paredes, P. and Theofilis, V. (2013) “Accurate Parabolic Navier-Stokes solutions of the supersonic flow around and elliptic cone”, 51st AIAA Aerospace Sciences Meeting, Grapevine, Texas, USA, 7 - 10 January 2013, AIAA 2013-0670
- Tendero, J.A., Paredes, P., Roura, M., Govindarajan, R. and Theofilis, V. (2013) “BiGlobal and point vortex methods for the instability analysis of wakes”, 43rd AIAA Fluid Dynamics Conference, San Diego, California, USA, 24 - 27 June 2013, AIAA 2013-2820
- Paredes, P., Gennaro, E., Hermanns, M. and Theofilis, V. (2013) “On global linear instability analysis of hypersonic flow around a model re-entry vehicle”, 43rd AIAA Fluid Dynamics Conference, San Diego, California, USA, 24 - 27 June 2013, AIAA 2013-2820
- Paredes, P. and Theofilis, V. (2013) “Spatial linear global instability analysis of the HIFiRE-5 elliptic cone model flow”, 43rd AIAA Fluid Dynamics Conference, San Diego, California, USA, 24 - 27 June 2013, AIAA 2013-2880
- Paredes, P. and Theofilis, V. (2014) “Traveling global instabilities on the HIFiRE-5 elliptic cone model flow”, 52nd AIAA Aerospace Science Meeting, National Harbor, Maryland, USA, 13 - 17 January 2014, AIAA 2014-0075
- Paredes, P., Gennaro, E. and Theofilis, V. (2014) “Toward reliable and efficient laminar-turbulent flow transition predictions in su-

personic and hypersonic flows over complex geometries”, 54th Israel Annual Conference on Aerospace Sciences, Tel-Aviv & Haifa, Israel, 19 - 20 February 2014

- Paredes, P., De Tullio, N., Sandham, N.D. and Theofilis, V. (2014) “Instability study of the wake behind a discrete roughness element in a hypersonic boundary-layer”, Instability and Control of Massively Separated Flows, Prato, Italy, 4 -6 September 2013
- Tendero, J.A., Paredes, P., Roura, M., Govindarajan, R. and Theofilis, V. (2014) “Filament vortex and global instability analysis of the Crow mode”, Instability and Control of Massively Separated Flows, Prato, Italy, 4 - 6 September 2013

Chapter 1

Hydrodynamic Instability

Hydrodynamic instability mostly studies the behavior of a laminar flow field upon the introduction of small-amplitude perturbations, in order to improve the understanding of the processes involved in the onset of unsteadiness and the transition of laminar flow to a turbulent regime.

1.1 The equations of fluid motion

The equations governing the motion of a viscous Newtonian fluid are obtained by imposing conservation of mass, momentum and energy. The result is a system of nonlinear partial differential equations (PDEs), so called the Navier-Stokes equations, which can be written as

$$\frac{\partial \rho^*}{\partial t^*} + \nabla \cdot (\rho^* \mathbf{u}^*) = 0, \quad (1.1)$$

$$\rho^* \left[\frac{\partial \mathbf{u}^*}{\partial t^*} + (\mathbf{u}^* \cdot \nabla) \mathbf{u}^* \right] = -\nabla p^* + \nabla [\lambda^* (\nabla \cdot \mathbf{u}^*)] + \nabla \cdot [\mu^* ((\nabla \mathbf{u}^*) + (\nabla \mathbf{u}^*)^T)], \quad (1.2)$$

$$\rho^* c_p^* \left[\frac{\partial T^*}{\partial t^*} + (\mathbf{u}^* \cdot \nabla) T^* \right] = \nabla \cdot (\kappa^* \nabla T^*) + \frac{\partial p^*}{\partial t^*} + (\mathbf{u}^* \cdot \nabla) p^* + \lambda^* (\nabla \cdot \mathbf{u}^*)^2 + \frac{\mu^*}{2} [(\nabla \mathbf{u}^*) + (\nabla \mathbf{u}^*)^T]^2 \quad (1.3)$$

where t^* is the time, \mathbf{u}^* is the velocity vector, ρ^* the density, p^* the pressure, T^* the temperature, c_p^* the specific heat, κ^* the thermal conductivity, μ^* the first coefficient of viscosity, and λ^* the second coefficient of viscosity. The equation of state is given by the perfect gas relation $p^* = \rho^* \mathcal{R} T^*$. Note that using the Stoke's law $\lambda^* = -2/3\mu^*$ and the asterisk denotes dimensional quantities.

The fluid variables are non-dimensionalized as follows. Lengths are scaled by a reference length l_r^* , velocities by u_r^* and temperature by T_r^* . The reference pressure is $p_r^* = \rho_r^* (u_r^*)^2$, the free-stream sound speed is denoted

1. Hydrodynamic Instability

by s_r^* , and $\gamma = c_{p,r}^*/c_{v,r}^*$. The resulting dimensionless parameters are the Reynolds number, $Re = \rho_r^* u_r^* l_r^* / \mu_r^*$, the Prandtl number to $Pr = c_{p,r}^* \mu_r^* / \kappa_r^*$, the Mach number $M = u_r^* / s_r^*$ and the Eckert number $Ec = (u_r^*)^2 / (c_{p,r}^* T_r^*) = (\gamma - 1)M^2$. The equation of state in dimensionless form becomes

$$p = \frac{1}{\gamma M^2} \rho T \quad (1.4)$$

where the constant of perfect gases is fixed to $\gamma = 1.4$ and the Prandtl number $Pr = 0.72$. Sutherland's law is used for the viscosity coefficient

$$\mu = (T)^{3/2} \frac{1 + S}{T + S} \quad (1.5)$$

with $\mu_s^* = 1.716 \times 10^{-5} \text{ N s/m}^2$, $T_s^* = 273.15 \text{ K}$ and $S = 110.4 \text{ K/T}_s^*$ for air in standard conditions. The thermal conductivity of the medium is taken equal to the viscosity coefficient $\bar{\kappa} = \bar{\mu}$.

A simplification of the resulting flow equations (1.1-1.3) is obtained when considering an incompressible flow of a Newtonian fluid. The assumption of incompressibility rules out the possibility of sound or shock waves to occur; so this simplification is not useful if these phenomena are of interest. The incompressible flow assumption typically holds well even when dealing with a compressible fluid, such as air at standard sea level temperature, at low Mach numbers (even when flowing up to about $M = 0.3$). Taking the incompressible flow assumption into account and assuming constant viscosity, the Navier-Stokes equations written in dimensionless form become

$$\nabla \cdot \mathbf{u} = 0, \quad (1.6)$$

$$\frac{\partial \mathbf{u}}{\partial t} + \mathbf{u} \cdot \nabla \mathbf{u} = -\nabla p + \frac{1}{Re} \nabla^2 \mathbf{u}, \quad (1.7)$$

where equations (1.6) and (1.7) are called the continuity and momentum equations respectively. Along the present Chapter, the stability analysis theories will be presented in Cartesian coordinates at the incompressible flow regime for simplicity of notation. Their compressible versions are written in the subsequent Appendices.

1.2 Instability analysis theory

The analysis of flow stability is based on the equations of motion (1.1-1.3) and monitors the development in time and space of linear modal small-amplitude perturbations upon a given flow through the solution of the lin-

earized Navier-Stokes equations (LNSE). In order to proceed, the fluid variables $\mathbf{q} = (\rho, u, v, w, T)^T$ are decomposed into a steady *base flow* $\bar{\mathbf{q}} = (\bar{\rho}, \bar{u}, \bar{v}, \bar{w}, \bar{T})^T$ and unsteady *small-amplitude perturbations* $\tilde{\mathbf{q}} = (\tilde{\rho}, \tilde{u}, \tilde{v}, \tilde{w}, \tilde{T})^T$:

$$\mathbf{q}(\mathbf{x}, t) = \bar{\mathbf{q}}(\mathbf{x}) + \epsilon \tilde{\mathbf{q}}(\mathbf{x}, t), \quad \epsilon \ll 1. \quad (1.8)$$

By introducing the previous decomposition of variables (1.8) into the governing equations (1.1-1.3) and neglecting the non-linear terms of $\mathcal{O}(\epsilon^2)$ and $\mathcal{O}(\epsilon^3)$, the LNSE are recovered (see Appendix A). In the incompressible limit, the LNSE are written as

$$\nabla \cdot \tilde{\mathbf{u}} = 0 \quad (1.9)$$

$$\frac{\partial \tilde{\mathbf{u}}}{\partial t} + \bar{\mathbf{u}} \cdot \nabla \tilde{\mathbf{u}} + \tilde{\mathbf{u}} \cdot \nabla \bar{\mathbf{u}} = -\nabla p + \frac{1}{Re} \nabla^2 \tilde{\mathbf{u}} \quad (1.10)$$

The aforementioned LNSE can be written as initial-value-problem in the form

$$\mathcal{B}(Re, M, \bar{\mathbf{q}}) \frac{d\tilde{\mathbf{q}}}{dt} = \mathcal{A}(Re, M, \bar{\mathbf{q}}) \tilde{\mathbf{q}}, \quad (1.11)$$

and solutions to this system of PDEs are considered.

The operators \mathcal{A} and \mathcal{B} are associated with the spatial discretization of the LNSE and comprise the basic state, $\bar{\mathbf{q}}(\mathbf{x})$ and its spatial derivatives. In case of steady basic flows, the separability between time and space coordinates in (1.11) permits introducing a Fourier decomposition in time through the expression $\tilde{\mathbf{q}} = \hat{\mathbf{q}} \exp(-i\omega t)$, leading to the generalized matrix eigenvalue problem (EVP)

$$\mathbf{A}\hat{\mathbf{q}} = \omega \mathbf{B}\hat{\mathbf{q}}, \quad (1.12)$$

in which matrices \mathbf{A} and \mathbf{B} discretize the operators \mathcal{A} and \mathcal{B} , respectively, and incorporate the boundary conditions. Details on the eigenvector $\hat{\mathbf{q}}$ will be provided in what follows. Re-writing (1.11) in matrix form as

$$\frac{d\hat{\mathbf{q}}}{dt} = \mathbf{C}\hat{\mathbf{q}}, \quad (1.13)$$

where $\mathbf{C} = \mathbf{B}^{-1}\mathbf{A}$, in which the inversion \mathbf{B} is permissible due to its non-singular nature in the compressible regime, this autonomous system has the explicit solution

$$\hat{\mathbf{q}}(t) = \exp(\mathbf{C}t) \hat{\mathbf{q}}(0) \equiv \Phi(t)\hat{\mathbf{q}}(0). \quad (1.14)$$

Here, $\hat{\mathbf{q}}(0) \equiv \hat{\mathbf{q}}(t=0)$ and the matrix exponential, $\Phi(t) \equiv \exp(\mathbf{C}t)$, is known as the propagator operator. In the case that the base flow has a time-periodic dependence, the propagator operator is denoted as the monodromy matrix [118] and Floquet theory is applicable [15, 99].

The linearization of the equations of motion is correct while the disturbance amplitude remains small enough for the non-linear terms to be negligible. This statement should be kept in mind as the true non-linear system can become unstable under finite-amplitude disturbances, under conditions in which the linearized system will stay stable. One physical example of this is the laminar-turbulent transition originated by the transient or non-modal growth of initially small disturbances, that can be stable in a linear approach (see Butler and Farrell [33] for a review). Both modal- and non-modal growth may be studied by equation (1.15), although the modal approach is addressed in computationally more efficient manner by numerical solution of equation (1.12).

A solution of the initial value problem (1.13), which is valid for the non-normal matrices discretizing the LNSE, distinguishes between the limits $t \rightarrow 0$ and $t \rightarrow \infty$; while the latter limit may be described by the EVP (1.12), growth, σ , of an initial linear perturbation, $\hat{\mathbf{q}}(0)$, may be computed at all times via

$$\sigma^2 = \frac{\langle \exp(\mathbf{C}^*t) \exp(\mathbf{C}t) \hat{\mathbf{q}}(0), \hat{\mathbf{q}}(0) \rangle}{\langle \hat{\mathbf{q}}(0), \hat{\mathbf{q}}(0) \rangle} = \frac{\langle \Phi^*(t) \Phi(t) \hat{\mathbf{q}}(0), \hat{\mathbf{q}}(0) \rangle}{\langle \hat{\mathbf{q}}(0), \hat{\mathbf{q}}(0) \rangle}, \quad (1.15)$$

which permits the study of both modal and non-modal perturbation growth, the latter also called transient growth, in a unified framework.

Implicit here is the definition of an inner product, (\cdot, \cdot) , and the associated adjoint \mathbf{C}^* of the matrix \mathbf{C} , which discretizes the operator \mathcal{C} .

The discussion is completed by introducing the singular value decomposition (SVD) of the propagator operator

$$e^{\mathbf{C}t} = \mathbf{U} \Sigma \mathbf{V}^T. \quad (1.16)$$

Here the unitary matrices \mathbf{V} and \mathbf{U} respectively comprise (as their column vectors) initial and final states, as transformed by the action of the propagator operator, while Σ is diagonal and contains the associated growth σ as the corresponding singular value. The SVD may be utilized to compute optimal perturbations, whose are recovered as the first column of matrix \mathbf{U} in equation (1.16).

The relationship between transient growth and the non-orthogonal properties of the linear operators describing local linear flow instability in the incompressible limit for one-dimensional problems, the so-called Orr-Sommerfeld equation (OSE), have been investigated by Trefethen et al. [259] and Reddy et al. [198] using the concept of pseudospectrum. In addition to investigating the development of disturbances based on eigenmodes, the pseudospectrum

analysis is adapted to the present context in order to explore the potential for transient growth due to non-orthogonality.

Analysis proceeds by computing the pseudospectrum of the matrix discretizing the linearized equations, $\mathbf{C} = \mathbf{B}^{-1}\mathbf{A}$, via computation of the eigen-spectrum ω of this matrix \mathbf{C} , perturbed by a small amount, according to

$$(\mathbf{C} + \mathbf{E})\hat{\mathbf{q}} = \omega\hat{\mathbf{q}}. \quad (1.17)$$

Here \mathbf{E} is of the same dimension as \mathbf{A} and contains homogeneously distributed random elements between 0 and ϵ . The literature uses the definition of the norm $\|\mathbf{E}\|$ in order to quantify the perturbation of \mathbf{A} ; see Schmid and Henningson [221] for a complete description. The sensitivity of eigenvalues can also be represented using the resolvent $(\omega\mathbf{I} - \mathbf{A})^{-1}$, leading to a similar definition of the ϵ -pseudo eigenvalue ω . In that context a large norm of the resolvent implies strong sensitivity to forcing, which in turn may be related to transient growth.

Non-modal BiGlobal instability analysis is an emerging field of research, while the bulk of global instability analyses performed in the quarter-century of history of the subject concern the numerical solution of the EVP, mainly in two spatial dimensions.

1.3 Modal linear stability theory

The above generic discussion is applicable to any linearization of the governing equations following the decomposition of flow quantities (1.8). Furthermore, in modal linear stability theory, the perturbation term is usually written as the product of an amplitude function and a phase function, $\tilde{\mathbf{q}} = \hat{\mathbf{q}}\Theta$. Table 1.1 summarizes the different instability approaches arranged by increasing constraints to the basic flow. However, depending on the dimensionality of the base flow analyzed, the resulting theoretical frameworks involve numerical solutions that require orders-of-magnitude different levels of computational work for their solution. In this Section the different frameworks in use in the context of modern linear stability theory are detailed, and the associated terminology is introduced. Table 1.1 presents the assumptions underlying the analysis, classified by the number of *resolved* inhomogeneous spatial directions in the basic flow $\bar{\mathbf{q}}$.

Table 1.1: Classification of modern linear stability analysis theory concepts into local (OSS), non-local (PSE) and global (BiGlobal, PSE-3D, TriGlobal) theories.

| Denomination | Assumptions | Base Flow | Amplitude Functions | Phase Function Θ |
|---------------------|--|-------------------------------|-------------------------------|---|
| TriGlobal | - | $\bar{\mathbf{q}}(x, y, z)$ | $\hat{\mathbf{q}}(x, y, z)$ | $\exp\{-\omega t\}$ |
| PSE-3D [†] | $\partial_x \bar{\mathbf{q}} \ll \partial_y \bar{\mathbf{q}}, \partial_z \bar{\mathbf{q}}$ | $\bar{\mathbf{q}}(x^*, y, z)$ | $\hat{\mathbf{q}}(x^*, y, z)$ | $\exp\left\{\int \alpha(x') dx' - \omega t\right\}$ |
| BiGlobal | $\partial_x \bar{\mathbf{q}} = 0$ | $\bar{\mathbf{q}}(y, z)$ | $\hat{\mathbf{q}}(y, z)$ | $\exp\{\alpha x - \omega t\}$ |
| PSE [†] | $\partial_x \bar{\mathbf{q}} \ll \partial_y \bar{\mathbf{q}}, \partial_z \bar{\mathbf{q}} = 0$ | $\bar{\mathbf{q}}(x^*, y)$ | $\hat{\mathbf{q}}(x^*, y)$ | $\exp\left\{\int \alpha(x') dx' + \beta z - \omega t\right\}$ |
| OSE | $\partial_x \bar{\mathbf{q}} = \partial_z \bar{\mathbf{q}} = 0$ | $\bar{\mathbf{q}}(y)$ | $\hat{\mathbf{q}}(y)$ | $\exp\{\alpha x + \beta z - \omega t\}$ |

[†] denotes potential extension to include nonlinear mode interaction.

* denotes a slowly-varying spatial direction.

The best known context of *classic* or *local* linear stability theory assumes a single inhomogeneous spatial direction in both the basic flow and the amplitude functions, indicated by y in the last line of Table 1.1. Examples of flows to which classic local linear theory may be applied are parallel shear flows [221], in which the velocity vector comprises a streamwise and a spanwise component, $\bar{\mathbf{q}} = (\bar{u}_1(y), 0, \bar{u}_3(y))^T$, both of which are functions of the transverse spatial coordinate, y , as well as for example isolated vortices or circular ducts, the base flow velocity of which depends on the radial coordinate alone [123]. Separation of variables in the operator describing the linear perturbations permits the introduction of Fourier decompositions along the homogeneous streamwise, x , and spanwise, z , spatial directions and the linearized equations of motion may be re-written to arrive at variants of the OSE. Numerical solution of this class of EVP is straightforward and practically all present-day laminar-turbulent transition analysis employs variants of this equation, also appropriately extended in the supersonic [164] and hypersonic regimes [162, 165, 235]. On the other hand, the linear (and non-linear) stability of boundary-layer flows, in which a small but non-zero wall-normal velocity component exists in the base flow and the dependence of the latter on the streamwise coordinate, x , is much weaker than that along the wall-normal, y , can be studied by the Parabolized Stability Equations (PSE), shown in Table 1.1. Unlike an EVP-based solution, PSE solve a marching integration of the LNSE along the streamwise spatial direction, and is known as a *non-local* instability analysis; Herbert [102] provides an introduction to the PSE.

The remaining three entries in Table 1.1 are collectively known as *global* linear theory. The key difference with classic linear theory or the PSE lies in the number of inhomogeneous spatial directions on which the base flow depends and the related number of periodic directions assumed. Because of this, OSE and PSE result in a system of ordinary differential equations (ODE). BiGlobal theory assumes the existence of a single homogeneous spatial direction and fully resolves in a coupled manner the other two, while TriGlobal analysis does not make any assumptions on homogeneity; respectively a two-dimensional and a three-dimensional PDE-based EVP results. Between the two concepts, PSE-3D assumes the existence of a base state which depends strongly on two and weakly on the third spatial dimension. The amplitude functions in both BiGlobal linear analysis and PSE-3D are two-dimensional functions of the resolved spatial coordinates, while those pertinent to TriGlobal analysis are three-dimensional functions of three simultaneously resolved spatial coordinates.

The leading dimension of the matrices discretizing the system of two-dimensional PDE describing the PSE-3D and spatial BiGlobal analysis EVP

1. Hydrodynamic Instability

is several orders of magnitude (depending in the number of discretization nodes) larger than the equivalent when solving the system of one-dimensional ODE corresponding to the classical PSE and local stability equations. Figure 1.1 shows a schematic comparison of their leading dimension for compressible flow regime.

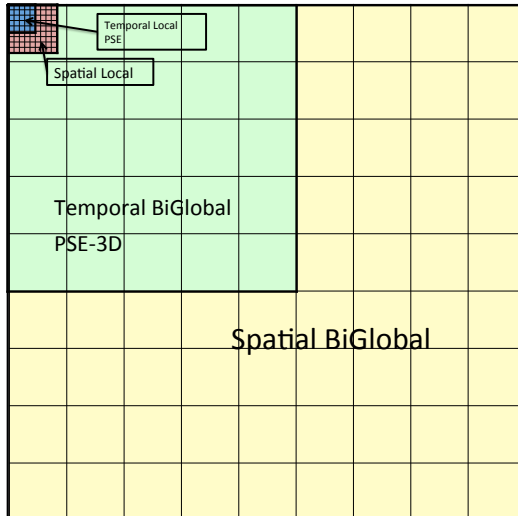


Figure 1.1: Schematic comparison of leading dimension of matrices discretizing local, classical PSE, BiGlobal and PSE-3D operators.

1.3.1 Local instability

The basic flow is assumed to be homogeneous in two of the three spatial directions, here x and z . Assuming that the basic flow is only dependent on one, y , out of the three spatial directions, the coefficients of the resulting EVP are (x, z) -independent, and without loss of generality modal perturbations get the form

$$\mathbf{q}(x, y, z, t) = \hat{\mathbf{q}}(y) \exp[i(\alpha x + \beta z - \omega t)] \quad (1.18)$$

where the new periodicity lengths $L_x = 2\pi/\alpha$ and $L_z = 2\pi/\beta$ have been imposed to the disturbances shape in the x - and z - direction respectively. Upon substitution of the ansatz (1.18) in the incompressible LNSE (1.9-1.10), results the system of equations

$$\mathcal{L}\hat{u} + \bar{u}_y \hat{v} + i\alpha \hat{p} = 0 \quad (1.19)$$

$$\mathcal{L}\hat{v} + \mathcal{D}_y\hat{p} = 0 \quad (1.20)$$

$$\mathcal{L}\hat{w} + \bar{w}_y\hat{v} - i\beta\hat{p} = 0 \quad (1.21)$$

$$i\alpha\hat{u} + \mathcal{D}_y\hat{v} + \hat{w}_z = 0 \quad (1.22)$$

where $\mathcal{L} = i\alpha\bar{u} + i\beta\bar{w} - \frac{1}{Re}(\mathcal{D}_{yy}^2 - \beta^2 - \alpha^2) - i\omega$, \mathcal{D}_y being the first derivative matrix and \mathcal{D}_{yy}^2 the second derivative matrix respect to y direction. The compressible version of equations (1.19-1.22) can be found in the work of Malik [164].

The system of ODEs described by equations (1.19-1.22) can be reduced to a system of two coupled equations when $\bar{w} = 0$, by eliminating the pressure variable in v -equation and introducing the normal vorticity $\hat{\eta} = \partial\hat{u}/\partial z - \partial\hat{w}/\partial x$. The resulting set of equations is

$$\begin{aligned} \left[(-i\omega + i\alpha\bar{u})(\mathcal{D}_{yy}^2 - k^2) - i\alpha\bar{u}_{yy} - \frac{1}{Re}(\mathcal{D}_{yy}^2 - k^2)^2 \right] \hat{v} &= 0 \quad (1.23) \\ \left[(-i\omega + i\alpha U) - \frac{1}{Re}(\mathcal{D}_{yy}^2 - k^2) \right] \hat{\eta} &= -i\beta U_y \hat{v} \end{aligned}$$

where the wavenumber $k^2 = \alpha^2 + \beta^2$ has been introduced. This problem is usually complemented with the boundary conditions $\hat{v} = d\hat{v}/dy = \hat{\eta} = 0$ at solid walls or in the far field. However, this choice of boundary conditions for the far field is not justified when a continuous spectrum exists.

Equation (1.23) is called the Orr-Sommerfeld equation, and has been widely used since its introduction in the beginning of the XX century [57, 152]. This equation is a one-dimensional EVP for the evolution of viscous wave-like disturbances, superposed to a basic flow given by a velocity profile $\bar{u}(y)$. Despite its apparent simplicity, it provides the exact eigenmodes of strictly parallel flows like plane-Poiseuille and Couette flows, and good approximations for quasi-parallel, slowly diverging flows like the Blasius boundary-layer. It is worth mentioning the inviscid equivalent of the OSE, that was derived by Lord Rayleigh, and yields exact solutions for parallel inviscid shear flows, and good approximations for slowly diverging flows like the unbounded mixing layer. Equation (1.24) is known as the Squire equation. For disturbances with $\hat{v} = 0$, it becomes an EVP for pure normal vorticity disturbances. For $\hat{v} \neq 0$, i.e. for eigenmodes solution of the OSE, equation (1.24) is a linear problem for the normal disturbance vorticity.

The instability problem as presented from the beginning considers the growth in time of disturbances. However, many of the instability phenomena relevant to laminar-to-turbulent transition evolves in space rather than in time, as the classic picture of transition in boundary-layer flows. The

1. Hydrodynamic Instability

local instability problem, based on the parallel flow assumption, can even consider evolutions in space or time.

The distinction of spatial and temporal instability problems is due to historical reasons. The temporal problem was the first to be employed because its simplicity, predicting reasonably well the dominant frequencies in shear-flows. The spatial problem attained higher importance later in the study of instability waves originated by periodic forcing, e.g. vibrating ribbons in boundary-layers, closely modeling the initial stages of the transition to turbulence. However, both spatial and temporal problems are particular cases in which the wave-like perturbations grow only in space or in time. The instability waves can grow simultaneously in space and in time, and both α and ω can be complex quantities in general. The relation between the wavenumbers α and β , the frequency ω , and other parameters involved is referred to as the dispersion relation:

$$\mathcal{D}(\alpha, \omega; \beta, Re, M) = 0. \quad (1.25)$$

The wave-like disturbances characterized by complex α and ω values can grow in space and simultaneously decay in time, or viceversa. The dispersion relation (1.25) maps points in the complex ω -plane to points in the complex α -plane, thus determining the behavior of the wave. A wave-like disturbance is said to be convectively unstable if after its introduction it experiences growth while it moves downstream, but in the initial location it decays and finally vanishes. On the other hand, a disturbance is absolutely unstable if it grows in the location where it is introduced, being also possible a growth downstream and upstream of the initial location. Absolute instability [106, 107] would appear if there exist waves with group velocity $c_g = 0$ and positive temporal growth rate $\omega_i > 0$. Those disturbances would determine the border between parametric regions of absolute instability and convective instability.

Mathematically, the (linear) *temporal EVP*, can be written as a generalized EVP:

$$\mathcal{A} \cdot \hat{\mathbf{q}} = \omega \mathcal{B} \cdot \hat{\mathbf{q}} \quad (1.26)$$

where $\hat{\mathbf{q}} = [\hat{\rho}, \hat{u}, \hat{v}, \hat{w}, \hat{T}]^T$ and the (nonlinear) *spatial EVP*,

$$\mathcal{A} \cdot \hat{\mathbf{q}} = \sum_{k=1}^2 \alpha^k \mathcal{B}_k \cdot \hat{\mathbf{q}}. \quad (1.27)$$

In order to solve numerically the quadratic EVP, it must be previously reduced to a linear EVP. The latter problem can be converted into a (larger by a factor equal to the degree of non-linearity) linear EVP, as shown by

Theofilis [247], using the companion matrix method [30, 93], in which an auxiliary vector $\hat{\mathbf{q}}^* = [\hat{\rho}, \hat{u}, \hat{v}, \hat{w}, \hat{T}, \alpha\hat{u}, \alpha\hat{v}, \alpha\hat{w}, \alpha\hat{T}]^T$ is defined, resulting in

$$\mathcal{A} \cdot \hat{\mathbf{q}}^* = \alpha \mathcal{B} \cdot \hat{\mathbf{q}}^*. \quad (1.28)$$

The numerical procedure for the numerical solution of EVPs (1.26) and (1.28) is discussed in the Chapter 2 devoted to numerical methods.

Temporal Local instability formulation

The operators \mathcal{A} and \mathcal{B} defining (1.26) in the incompressible limit written using matrix notation become

$$\mathcal{A} = \begin{pmatrix} \mathcal{L}_T & \bar{u}_y & 0 & i\alpha \\ 0 & \mathcal{L}_T & 0 & \mathcal{D}_y \\ 0 & \bar{w}_y & \mathcal{L}_T & i\beta \\ i\alpha & \mathcal{D}_y & i\beta & 0 \end{pmatrix} \quad (1.29)$$

$$\mathcal{B} = \begin{pmatrix} i & 0 & 0 & 0 \\ 0 & i & 0 & 0 \\ 0 & 0 & i & 0 \\ 0 & 0 & 0 & 0 \end{pmatrix} \quad (1.30)$$

where $\mathcal{L}_T = i\alpha i + \bar{w}_y i\beta - \frac{1}{Re}(\mathcal{D}_{yy}^2 - \beta^2 - \alpha^2)$. Here $\alpha, \beta \in \mathbb{R}$ are a wavenumber parameter, related with the periodicity length along the homogeneous spatial directions, x and z , through $\alpha = 2\pi/L_x$ and $\beta = 2\pi/L_z$. The sought complex eigenvalue is $\omega = \omega_r + i\omega_i$, the real part being a circular frequency, while the imaginary part is the temporal amplification/damping rate.

Spatial Local instability formulation

The operators \mathcal{A} and \mathcal{B} defining (1.28) in the incompressible limit written using matrix notation become

$$\mathcal{A} = \begin{pmatrix} \mathcal{L}_S & \bar{u}_y & 0 & 0 & 0 & 0 & 0 \\ 0 & \mathcal{L}_S & 0 & \mathcal{D}_y & 0 & 0 & 0 \\ 0 & \bar{w}_y & \mathcal{L}_S & i\beta & 0 & 0 & 0 \\ 0 & \mathcal{D}_y & i\beta & 0 & 0 & 0 & 0 \\ 0 & 0 & 0 & 0 & \mathcal{I} & 0 & 0 \\ 0 & 0 & 0 & 0 & 0 & \mathcal{I} & 0 \\ 0 & 0 & 0 & 0 & 0 & 0 & \mathcal{I} \end{pmatrix} \quad (1.31)$$

$$\mathcal{B} = \begin{pmatrix} -i\bar{u} & 0 & 0 & -i & -\frac{1}{Re} & 0 & 0 \\ 0 & -i\bar{u} & 0 & 0 & 0 & -\frac{1}{Re} & 0 \\ 0 & 0 & -i\bar{u} & 0 & 0 & 0 & -\frac{1}{Re} \\ -i & 0 & 0 & 0 & 0 & 0 & 0 \\ \mathcal{I} & 0 & 0 & 0 & 0 & 0 & 0 \\ 0 & \mathcal{I} & 0 & 0 & 0 & 0 & 0 \\ 0 & 0 & \mathcal{I} & 0 & 0 & 0 & 0 \end{pmatrix} \quad (1.32)$$

where $\mathcal{L}_S = -i\omega - \frac{1}{Re}(\mathcal{D}_{yy}^2 - \beta^2)$. Here $\omega \in \mathbb{R}$ is a real frequency parameter and $\beta \in \mathbb{R}$ is a real wavenumber, $\beta = 2\pi/L_z$, while $\alpha \in \mathbb{C}$ is the sought eigenvalue, the real part of which is related with the periodicity length along the homogeneous spatial direction, x , through $\alpha_r = 2\pi/L_x$ and the imaginary part, α_i is the spatial amplification/damping rate.

1.3.2 Parabolized Stability Equations

Parabolized Stability Equations (PSE) have opened new avenues to the analysis of the streamwise growth of linear and nonlinear disturbances in slowly varying shear flows such as boundary-layers, jets, and far wakes. Growth mechanisms include both algebraic transient growth and exponential growth through primary and higher instabilities. In contrast to the eigensolutions of traditional linear stability equations, PSE solutions incorporate inhomogeneous initial and boundary conditions as do numerical solutions of the Navier-Stokes equations. The PSE are valid for convectively unstable flows in which the root-mean-square of the variables profiles vary slowly in the streamwise direction, i.e. $\frac{\partial}{\partial x} = \mathcal{O}(\varepsilon)$, with $\varepsilon \ll 1$, for example being $\varepsilon = \mathcal{O}(Re^{-1})$ in boundary-layer flows.

The velocity components \bar{u} and \bar{w} exhibit small variations in the streamwise and spanwise direction, and the component \bar{v} normal to the surface is non-zero to provide the mass parameter as the displacement thickness changes.

The disturbance quantities are expanded in terms of their truncated Fourier components assuming that are periodic in time

$$\tilde{\mathbf{q}}(x, y, z, t) = \sum_{m=-M}^M \sum_{n=-N}^N \check{\mathbf{q}}_{m,n}(x, y) \exp[i(m\beta z - n\omega t)]. \quad (1.33)$$

Furthermore, $\check{\mathbf{q}} = (\check{\rho}, \check{u}, \check{v}, \check{w}, \check{T})$ is defined as a fast varying wavy function

with a slowly varying amplitude

$$\check{\mathbf{q}}(x, y) = \hat{\mathbf{q}}(x, y) \exp \left[i \int_x \alpha(x') dx' \right], \quad (1.34)$$

where $\hat{\mathbf{q}}(x, y)$ varies slowly with x . Note that $\check{\mathbf{q}}_{-m, -n}$ is equal to the complex conjugate of $\check{\mathbf{q}}_{m, n}$. The sub-index m, n is suppressed for simplicity when appropriate.

Within the PSE approximation, the streamwise derivatives of $\hat{\mathbf{q}}$ take the form

$$\frac{\partial^k \check{\mathbf{q}}}{\partial x^k} = i^k \left[\alpha^k \hat{\mathbf{q}} - ik\alpha^{k-1} \frac{\partial \hat{\mathbf{q}}}{\partial x} - i \frac{k(k-1)}{2} \alpha^{k-2} \frac{d\alpha}{dx} \hat{\mathbf{q}} \right] \exp \left[i \int_x \alpha(x') dx' \right], \quad (1.35)$$

and for the first and second derivative, the above expression becomes

$$\frac{\partial \check{\mathbf{q}}}{\partial x} = \left(i\alpha \hat{\mathbf{q}} + \frac{\partial \hat{\mathbf{q}}}{\partial x} \right) \exp \left[i \int_x \alpha(x') dx' \right], \quad (1.36)$$

$$\frac{\partial^2 \check{\mathbf{q}}}{\partial x^2} = \left(-\alpha^2 \hat{\mathbf{q}} + 2i\alpha \frac{\partial \hat{\mathbf{q}}}{\partial x} + i \frac{d\alpha}{dx} \hat{\mathbf{q}} \right) \exp \left[i \int_x \alpha(x') dx' \right]. \quad (1.37)$$

Substituting (1.34) and the first and second streamwise derivatives (1.36-1.37) into the LNSE (A.1-A.5), and neglecting terms of $\mathcal{O}(\varepsilon^2)$ as $\alpha_x \hat{\mathbf{q}}_x$, $\hat{\mathbf{q}}_{xx}$, α_{xx} and higher derivatives with respect to x or streamwise derivatives in the viscous part of the equations, the non-linear PSE are written in a compact form as

$$(\mathcal{L}_{m,n} + \mathcal{M}_{m,n} \mathcal{D}_x) \hat{\mathbf{q}}(x, y) = \mathcal{F}_{m,n}(x, y) \exp \left[-i \int_x \alpha_{m,n}(x') dx' \right], \quad (1.38)$$

where \mathcal{D}_x is the being the first derivative operator respect to x direction and $\mathcal{F}_{m,n}$ is the Fourier component of the total forcing, \mathcal{F} , which comprises the non-linear terms on disturbance variables

$$\mathcal{F} = \sum_{n=-M}^M \sum_{n=-N}^N \mathcal{F}_{m,n}(x, y) \exp [i(m\beta z - n\omega t)]. \quad (1.39)$$

The entries of the coefficient matrices for $\mathcal{L}_{m,n}$ and $\mathcal{M}_{m,n}$ and vector components of \mathcal{F} can be found in [90, 94, 96] for the compressible regime and are expressed as follow in the incompressible limit

$$\mathcal{L}_{m,n} = \begin{pmatrix} \mathcal{L}_0 + \bar{u}_x & \bar{u}_y & 0 & i\alpha \\ \bar{v}_x & \mathcal{L}_0 + \bar{v}_y & 0 & \mathcal{D}_y \\ \bar{w}_x & \bar{w}_y & \mathcal{L}_0 & i\beta \\ i\alpha & \mathcal{D}_y & i\beta & 0 \end{pmatrix}_{m,n}, \quad (1.40)$$

$$\mathcal{M}_{m,n} = \begin{pmatrix} \bar{u} & 0 & 0 & 1 \\ 0 & \bar{u} & 0 & 0 \\ 0 & 0 & \bar{u} & 0 \\ 1 & 0 & 0 & 0 \end{pmatrix}, \quad (1.41)$$

$$\mathcal{F} = \begin{pmatrix} \tilde{u}\tilde{u}_x + \tilde{v}\tilde{u}_y \\ \tilde{u}\tilde{v}_x + \tilde{v}\tilde{v}_y \\ \tilde{u}\tilde{w}_x + \tilde{v}\tilde{w}_y \\ 0 \end{pmatrix}, \quad (1.42)$$

where $\mathcal{L}_0 = \bar{u}i\alpha + \bar{v}D_y + \bar{w}i\beta - \frac{1}{Re}(D_{yy}^2 - \beta^2 - \alpha^2) - i\omega$. The linear PSE equations are recovered by setting zero forcing term, what is equivalent to neglect terms of $\mathcal{O}(\epsilon^2)$. Here, $\omega \in \mathbb{R}$ is a real frequency parameter and $\beta \in \mathbb{R}$ is a real wavenumber, $\beta = 2\pi/L_z$, while $\alpha \in \mathbb{C}$ is sought.

The normalization condition

An ambiguity exists in the PSE formulation, in which the changes in amplitude along the slow spatial direction can be contained both in the amplitude function $\hat{\mathbf{q}}$ or in the phase function of equation (1.34). A normalization condition is required in order to close the formulation of the problem (see Herbert [101, 102] for a review). In this work, the following normalization condition is used:

$$\int_{\Omega} \bar{\rho}^{1/2} \hat{\mathbf{u}}^\dagger \frac{\partial(\bar{\rho}^{1/2} \hat{\mathbf{u}})}{\partial x} d\Omega = \int_{\Omega} \frac{1}{2} \frac{\partial}{\partial x} \bar{\rho} |\hat{\mathbf{u}}|^2 d\Omega = 0 \quad (1.43)$$

where $\hat{\mathbf{u}} = (\hat{u}, \hat{v}, \hat{w})^T$. This normalization imposes that the kinetic energy of the shape functions remains independent of x . Thus, the amplitude growth is absorbed into the phase function.

The effective growth rate computed by PSE is formulated as

$$\sigma_K = -\alpha_i + \frac{1}{2} \frac{d \ln[K(x)]}{dx}, \quad \text{with} \quad K(x) = \int_{\Omega} \bar{\rho} (\hat{u}\hat{u}^\dagger + \hat{v}\hat{v}^\dagger + \hat{w}\hat{w}^\dagger) d\Omega, \quad (1.44)$$

in order to take into account the residual slow variation of disturbance kinetic energy, K , with x .

Numerical stability

Inspection of this system suggests a parabolic set of equations that can be solved by treating the x direction as a pseudo-time, marching in this direction. The studies of Li and Malik [144, 146], found that these equations

are mathematically elliptic, and are numerically ill-posed. Choosing a sufficiently large marching step, however, negates the upstream influence and was found to give accurate results. Li and Malik [144] found that, for a backward difference scheme in x , a limit of

$$\Delta x > \frac{1}{|\alpha|} \quad (1.45)$$

needs to be placed on the marching step size.

1.3.3 BiGlobal instability

Assuming that the basic flow is now dependent on two out of the three spatial coordinates, the two-dimensional parallel flow is assumed and the BiGlobal instability theory is applicable (see Theofilis [249], [250] for a review).

The disturbances are three-dimensional, but a sinusoidal dependence with the homogeneous x -direction is assumed, with the periodicity length $L_x = 2\pi/\alpha$ as follows

$$\bar{\mathbf{q}}(x, y, z, t) = \hat{\mathbf{q}}(y, z) \exp[i(\alpha x - \omega t)]. \quad (1.46)$$

Upon substitution of the ansatz (1.46) in the incompressible LNSE (1.9-1.10), results the system of equations

$$\mathcal{L}\hat{u} + \bar{u}_y\hat{v} + \bar{u}_z\hat{w} + i\alpha\hat{p} = 0 \quad (1.47)$$

$$(\mathcal{L} + \bar{v}_y)\hat{v} + \bar{v}_z\hat{w} + \hat{p}_y = 0 \quad (1.48)$$

$$(\mathcal{L} + \bar{w}_z)\hat{w} + \bar{w}_y\hat{v} + \hat{p}_z = 0 \quad (1.49)$$

$$i\alpha\hat{u} + \hat{v}_y + \hat{w}_z = 0 \quad (1.50)$$

where $\mathcal{L} = i\alpha\bar{u} + \bar{v}\mathcal{D}_y + \bar{w}\mathcal{D}_z - \frac{1}{Re}(\mathcal{D}_{yy}^2 + \mathcal{D}_{zz}^2 - \alpha^2) - i\omega$, \mathcal{D}_z being the first derivative matrix and \mathcal{D}_{zz}^2 the second derivative matrix respect to z direction.

Temporal BiGlobal instability formulation

Written using matrix notation, the operators \mathcal{A} and \mathcal{B} defining (1.26) become:

$$\mathcal{A} = \begin{pmatrix} \mathcal{L}_T & \bar{u}_y & \bar{u}_z & i\alpha \\ 0 & \mathcal{L}_T + \bar{v}_y & \bar{v}_z & \mathcal{D}_y \\ 0 & \bar{w}_y & \mathcal{L}_T + \bar{w}_z & \mathcal{D}_z \\ i\alpha & \mathcal{D}_y & \mathcal{D}_z & 0 \end{pmatrix} \quad (1.51)$$

$$\mathcal{B} = \begin{pmatrix} i & 0 & 0 & 0 \\ 0 & i & 0 & 0 \\ 0 & 0 & i & 0 \\ 0 & 0 & 0 & 0 \end{pmatrix} \quad (1.52)$$

where $\mathcal{L}_T = i\alpha\bar{u} + \bar{v}\mathcal{D}_y + \bar{w}\mathcal{D}_z - \frac{1}{Re}(\mathcal{D}_{yy}^2 + \mathcal{D}_{zz}^2 - \alpha^2)$. Following the same reasoning made in the temporal local instability formulation, here $\alpha \in \mathbb{R}$ is a wavenumber parameter, related with the periodicity length along the homogeneous spatial direction, x , through $\alpha = 2\pi/L_x$, while the sought complex eigenvalue is ω .

The entries of the matrices discretizing the operators \mathcal{A} and \mathcal{B} defining (1.26) in the compressible regime are found in Appendix B for the choice of variables used in this work $\mathbf{q} = (\rho, u, v, w, T)$, while Theofilis and Colonius [251] and Robinet [207] show the equations for $\mathbf{q} = (u, v, w, T, p)$.

Spatial BiGlobal instability formulation

Written using matrix notation, the operators \mathcal{A} and \mathcal{B} defining (1.28) become:

$$\mathcal{A} = \begin{pmatrix} \mathcal{L}_S & \bar{u}_y & \bar{u}_z & 0 & 0 & 0 & 0 \\ 0 & \mathcal{L}_S + \bar{v}_y & \bar{v}_z & \mathcal{D}_y & 0 & 0 & 0 \\ 0 & \bar{w}_y & \mathcal{L}_S + \bar{w}_z & \mathcal{D}_z & 0 & 0 & 0 \\ 0 & \mathcal{D}_y & \mathcal{D}_z & 0 & 0 & 0 & 0 \\ 0 & 0 & 0 & 0 & \mathcal{I} & 0 & 0 \\ 0 & 0 & 0 & 0 & 0 & \mathcal{I} & 0 \\ 0 & 0 & 0 & 0 & 0 & 0 & \mathcal{I} \end{pmatrix} \quad (1.53)$$

$$\mathcal{B} = \begin{pmatrix} -i\bar{u} & 0 & 0 & -i & -\frac{1}{Re} & 0 & 0 \\ 0 & -i\bar{u} & 0 & 0 & 0 & -\frac{1}{Re} & 0 \\ 0 & 0 & -i\bar{u} & 0 & 0 & 0 & -\frac{1}{Re} \\ -i & 0 & 0 & 0 & 0 & 0 & 0 \\ \mathcal{I} & 0 & 0 & 0 & 0 & 0 & 0 \\ 0 & \mathcal{I} & 0 & 0 & 0 & 0 & 0 \\ 0 & 0 & \mathcal{I} & 0 & 0 & 0 & 0 \end{pmatrix} \quad (1.54)$$

where $\mathcal{L}_T = -i\omega + \bar{v}\mathcal{D}_y + \bar{w}\mathcal{D}_z - \frac{1}{Re}(\mathcal{D}_{yy}^2 + \mathcal{D}_{zz}^2)$. Following the same reasoning made in the spatial local instability formulation, here $\omega \in \mathbb{R}$ is a real frequency parameter, while $\alpha \in \mathbb{C}$ is the sought eigenvalue.

1.3.4 Three-dimensional parabolized stability equations

The most general case corresponds to a three-dimensional flowfield, which is inhomogeneous in all three spatial directions. A numerical solution of the PDE-based EVP resulting from the discretization of the three coupled direction, referred to a TriGlobal stability analysis, is possible but prohibitively expensive nowadays for most applications of interest. A parabolized variation of the three-dimensional stability equations (PSE-3D) can be derived when the basic flow can be assumed to experience slow variations along one of the three spatial directions (see Table 1.1). In this manner, the three-dimensional EVP is replaced by an initial value problem that is solved using a marching integration along the slow spatial direction.

Following the same reasoning made on the classical PSE, the PSE-3D are valid for convectively unstable flows in which the root-mean-square of the variables profiles vary slowly in the streamwise direction. The disturbance quantities are expanded in terms of their truncated Fourier components assuming that are periodic in time

$$\tilde{\mathbf{q}}(x, y, z, t) = \sum_{n=-N}^N \check{\mathbf{q}}_n(x, y, z) \exp[-in\omega t]. \quad (1.55)$$

Furthermore, we write the $\check{\mathbf{q}}$ as a fast varying wavy function with a slowly varying amplitude

$$\check{\mathbf{q}}(x, y, z) = \hat{\mathbf{q}}(x, y, z) \exp \left[i \int_x \alpha(x') dx' \right], \quad (1.56)$$

where $\hat{\mathbf{q}}(x, y, z)$ varies slowly with x . The subindex n will be suppressed for simplicity when appropriate.

Substituting (1.56) and the first and second streamwise derivatives (1.36-1.37) into the LNSE (A.1-A.5), and neglecting terms of $\mathcal{O}(\varepsilon^2)$ as $\alpha_x \hat{\mathbf{q}}_x$, $\hat{\mathbf{q}}_{xx}$, α_{xx} and higher derivatives with respect to x or streamwise derivatives in the viscous part of the equations, the compressible linear non-linear PSE-3D equations are written in a compact form as

$$(\mathcal{L}_n + \mathcal{M}_n \mathcal{D}_x) \hat{\mathbf{q}}(x, y, z)_n = \mathcal{F}_n(x, y, z) \exp \left[-i \int_x \alpha_n(x') dx' \right], \quad (1.57)$$

where \mathcal{F}_n is the Fourier component of the total forcing,

$$\mathcal{F} = \sum_{n=-N}^N \mathcal{F}_n(x, y, z) \exp[-in\omega t]. \quad (1.58)$$

1. Hydrodynamic Instability

The entries of the coefficient matrices for \mathcal{L}_n and \mathcal{M}_n and vector components of \mathcal{F} can be found in Appendix D for compressible flows and are expressed in the incompressible limit as follows

$$\mathcal{L}_{m,n} = \begin{pmatrix} \mathcal{L}_0 + \bar{u}_x & \bar{u}_y & \bar{u}_z & i\alpha \\ \bar{v}_x & \mathcal{L}_0 + \bar{v}_y & \bar{v}_z & \mathcal{D}_y \\ \bar{w}_x & \bar{w}_y & \mathcal{L}_0 + \bar{w}_z & \mathcal{D}_z \\ i\alpha & \mathcal{D}_y & \mathcal{D}_z & 0 \end{pmatrix}_{m,n}, \quad (1.59)$$

$$\mathcal{M}_{m,n} = \begin{pmatrix} \bar{u} & 0 & 0 & 1 \\ 0 & \bar{u} & 0 & 0 \\ 0 & 0 & \bar{u} & 0 \\ 1 & 0 & 0 & 0 \end{pmatrix}, \quad (1.60)$$

$$\mathcal{F} = \begin{pmatrix} \tilde{u}\tilde{u}_x + \tilde{v}\tilde{u}_y + \tilde{w}\tilde{u}_z \\ \tilde{u}\tilde{v}_x + \tilde{v}\tilde{v}_y + \tilde{w}\tilde{v}_z \\ \tilde{u}\tilde{w}_x + \tilde{v}\tilde{w}_y + \tilde{w}\tilde{w}_z \\ 0 \end{pmatrix}, \quad (1.61)$$

where $\mathcal{L}_0 = \bar{u}i\alpha + \bar{v}\mathcal{D}_y + \bar{w}\mathcal{D}_z - \frac{1}{Re}(\mathcal{D}_{yy}^2 - \mathcal{D}_{zz}^2 - \alpha^2) - i\omega$. The linear PSE equations are recovered by setting zero forcing term, what is equivalent to neglect terms of $\mathcal{O}(\epsilon^2)$. As in the PSE theory, $\omega \in \mathbb{R}$ is a real frequency parameter and $\alpha \in \mathbb{C}$ is sought.

The normalization condition

Following the same explanation of the classical PSE, the used normalization condition is equation (1.43), but here the integral is two-dimensional over the plane normal to the marching direction.

Numerical stability

Following the same reasoning made on the classical PSE, the PSE-3D contain also some residual ellipticity, as was shown by Broadhurst and Sherwin [31]. The marching integration is performed using an implicit scheme along with a sufficiently large streamwise step satisfying equation (1.45).

1.3.5 TriGlobal instability

The TriGlobal analysis is the most general case with the perturbations being non-homogeneous in the three spatial directions and modal perturbations get

the form

$$\tilde{\mathbf{q}}(x, y, z, t) = \hat{\mathbf{q}}(x, y, z) \exp[-\omega t] \quad (1.62)$$

where the definition $\omega \rightarrow i\omega$ is used to have a real arithmetic EVP. In this case, ω_i is the circular frequency and ω_r is the damping/growth rate.

Upon substitution of equation (1.62) into the incompressible LNSE (1.9-1.10), the operators \mathcal{A} and \mathcal{B} of equation (1.26) define a PDE-based problem with real arithmetic as follows

$$\mathcal{A} = \begin{pmatrix} \mathcal{L} + U_x & U_y & U_z & \mathcal{D}_x \\ V_x & \mathcal{L} + V_y & V_z & \mathcal{D}_y \\ W_x & W_y & \mathcal{L} + W_z & \mathcal{D}_z \\ \mathcal{D}_x & \mathcal{D}_y & \mathcal{D}_z & 0 \end{pmatrix}, \quad \mathcal{B} = \begin{pmatrix} 1 & 0 & 0 & 0 \\ 0 & 1 & 0 & 0 \\ 0 & 0 & 1 & 0 \\ 0 & 0 & 0 & 0 \end{pmatrix}, \quad (1.63)$$

where $\mathcal{L} = \bar{u}\mathcal{D}_x + \bar{v}\mathcal{D}_y + \bar{w}\mathcal{D}_z - \frac{1}{Re}(\mathcal{D}_{xx}^2 + \mathcal{D}_{yy}^2 + \mathcal{D}_{zz}^2)$ and \mathcal{D}_{xx}^2 being the second derivative matrix respect to x direction. The entries of the coefficient matrices for \mathcal{A} and \mathcal{B} can be found in Appendix E for compressible flows. Although TriGlobal instability results for compressible flows are not shown in this work, the equations will be referenced when solving complex geometries using spatial BiGlobal and PSE-3D by using a generalized coordinate system transformation.

1. Hydrodynamic Instability

Chapter 2

Numerical considerations

2.1 Spatial discretization

The spatial discretization plays a very important role in matrix storing and forming approach for solving EVPs. Special attention is devoted to the high order finite-difference methods developed by Hermanns and Hernández [103], since it is employed here for the first time in the global instability field.

2.1.1 Dispersion-Relation-Preserving schemes

The main objective of Dispersion Relation Preserving (DRP) finite-difference schemes is to present an optimized high order finite-difference scheme which minimizes dispersion wave errors. Therefore, this scheme supports not only consistency, stability and convergence but also wave solutions with the same characteristics as the linearized Euler equations in the case of small amplitude waves. The methodology of this method is briefly introduced in this paper and is explained more in detail by Tam and Webb [240].

Considering the model wave equation

$$\frac{\partial u}{\partial t} = c \frac{\partial u}{\partial x}, \quad (2.1)$$

and using the spatial discretization on a uniform grid spacing Δx , the next expression gives the first order spatial derivative at the nodal point l :

$$\left(\frac{\partial u}{\partial x} \right)_l \simeq \frac{1}{\Delta x} \sum_{j=-N}^M a_j u_{l+j}, \quad (2.2)$$

where the finite-difference coefficients a_j need to be determined. Additionally to the fulfillment of the classical finite-difference relations among the coefficients a_j to ensure a certain order of convergence, the DRP methods

2. Numerical considerations

impose additional conditions based on the minimization of the integrated error E , defined by the Euclidean norm,

$$E = \int_{-\pi/2}^{\pi/2} |\alpha\Delta x - \hat{\alpha}\Delta x|^2 d(\alpha\Delta x), \quad (2.3)$$

where α is the physical wavenumber and $\hat{\alpha}$ is the effective wavenumber of the finite-difference approximation obtained from applying a spatial Fourier transformation to equation (2.2). This additional condition seeks to improve the spectral resolution capabilities of the explicit finite-difference method [240].

The procedure to calculate second derivatives is similar to the one explained before. These coefficients are presented in the work of Paredes et al. [189] for a finite-difference scheme of order 8. Following the methodology employed by Merle et al. [174], the boundary formulations for the first and second order derivatives correspond to standard finite-difference schemes of lower accuracy order. However, in the present procedure, the order of the boundary formulations are kept of the same order than the inner finite-difference scheme. Such difference is necessary in order to get the proper slope of the relative error curves that proves the order of the method.

2.1.2 Compact finite-difference schemes

The implicit scheme or compact finite-difference scheme described in Lele [138] is briefly presented next. These schemes are generalizations of the Padé schemes. The considered mesh is again a regular one with a constant grid spacing Δx . The generalizations for the first and second derivatives have the following form:

$$\begin{aligned} & \beta f'_{j-2} + \alpha f'_{j-1} + f'_j + \alpha f'_{j+1} + \beta f'_{j+2} \\ = & c \frac{f_{j+3} - f_{j-3}}{6\Delta x} + b \frac{f_{j+2} - f_{j-2}}{4\Delta x} + a \frac{f_{j+1} - f_{j-1}}{2\Delta x}, \quad (2.4) \\ & \beta f''_{j-2} + \alpha f''_{j-1} + f''_j + \alpha f''_{j+1} + \beta f''_{j+2} \\ = & c \frac{f_{j+3} - 2f_j + f_{j-3}}{9\Delta x^2} + b \frac{f_{j+2} - 2f_j + f_{j-2}}{4\Delta x^2} + a \frac{f_{j+1} - 2f_j + f_{j-1}}{\Delta x^2} \end{aligned} \quad (2.5)$$

Following the methodology employed by Colonius [43], the boundary formulation employed for the first and second derivatives is a finite-difference compact scheme with smaller order than the inner scheme. However, the present formulation keeps the same order used in the inner finite-difference scheme for the boundary formulations. Thanks to this, the proper slope of the relative error curves that proves the order of the method is recovered.

2.1.3 Summation-by-Parts finite-difference schemes

Summation-by-Parts (SBP) operators can be used to construct time-stable high-order accurate finite-difference schemes as a discretization of the integration by parts formula. In this paper the basic idea of the method construction is briefly presented, which is explained more in detail in [36, 170, 234].

Considering the hyperbolic scalar equation $u_t + u_x = 0$, integration by parts can be expressed as

$$\frac{d}{dt} \|u\|^2 = -(u, u_x) - (u_x, u) = -u^2 \Big|_b^a, \quad (2.6)$$

where (u, v) is the standard L^2 inner product on $[a, b]$ and $\|u\|^2 = (u, u)$ is the associated L^2 norm. Considering the approximation of the equation $v_t + \mathcal{D}_x v = 0$, being v the discrete counter part of u , a difference operator $\mathcal{D}_x = H^{-1}Q$ is an SBP operator if $Q + Q^T = B$, where $B = \text{diag}(-1, 0, \dots, 0, 1)$. The procedure to calculate second derivatives is following as well a discretization of the integration by parts formula similar to the one previously explained. The coefficients used to perform first and second derivatives for a finite-difference scheme of order 8 can be found in [170].

2.1.4 Finite-difference methods with uniform error

The here called FD-q method developed by Hermanns and Hernández [103] is a new high order finite-difference method employed to solve global instability problems for the first time [189]. Therefore, more attention is paid in the description of this numerical method. The idea behind FD-q is to construct a non-uniform finite-difference scheme based on the philosophy behind Chebyshev Gauss-Lobatto collocation points which minimize interpolation errors.

The approach followed for the derivation of the finite-difference approximation is briefly presented in this Subsection. See the work by Hermanns and Hernández [103] for in-depth details of the presented method as well as its application to time evolution problems.

Piecewise polynomial interpolation

In order to derive the finite-difference approximations to the spatial derivatives of a general function $u(x, t)$, a piecewise polynomial interpolant is con-

2. Numerical considerations

structured that matches the discrete values $u_i(t)$ of the function $u(x, t)$ at the grid nodes x_i , and whose derivatives are then computed to obtain the sought finite-difference formulas. Figure 2.1 represents such a piecewise polynomial interpolant formed out of individual polynomial interpolants $I_i(x)$ which are only valid in their respective domains of validity Ω_i . Each of these domains Ω_i includes the corresponding grid node x_i and their union is equal to the whole domain $[-1, +1]$ of the problem.

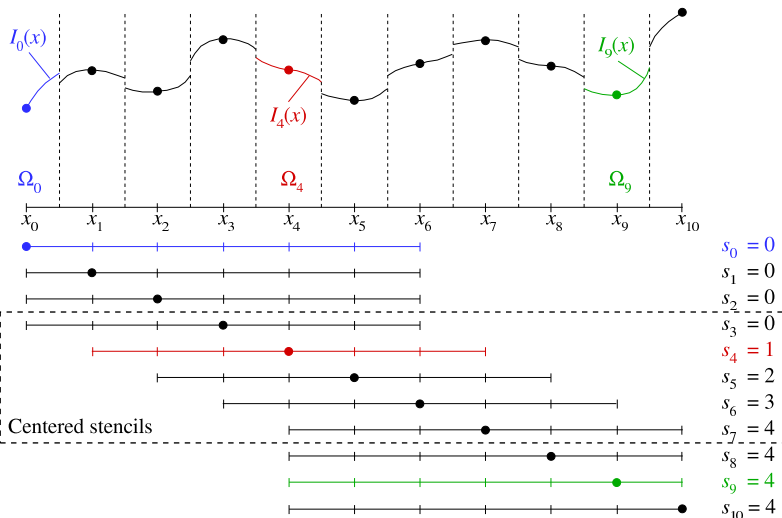


Figure 2.1: Stencils, seeds s_i , and domains of validity Ω_i of the individual polynomial interpolants $I_i(x)$ of a piecewise polynomial interpolation of degree $q = 6$ on 11 nodes ($N = 10$). The dashed box separates the centered stencils from those affected by the presence of the boundaries.

Given a set of grid nodes, the expressions for $I_i(x)$ can readily be obtained through the Lagrange interpolation formula [66, 104]:

$$I_i(x) = \sum_{j=s_i}^{s_i+q} \ell_{ij}(x) u_j, \quad \ell_{ij}(x) = \prod_{\substack{m=0 \\ s_i+m \neq j}}^q \frac{x - x_{s_i+m}}{x_j - x_{s_i+m}}. \quad (2.7)$$

where q is the polynomial degree and the seed s_i is the index of the left most node x_i involved in the construction of the interpolant $I_i(x)$. For the case of even polynomial degrees, which is the choice from now on, the following selection of values for s_i is made:

$$\{s_i\} = \underbrace{\{0, \dots, 0\}}_{q/2 \text{ times}}, \underbrace{\{0, 1, \dots, N - q\}}_{\text{centered FD}}, \underbrace{\{N - q, \dots, N - q\}}_{q/2 \text{ times}}. \quad (2.8)$$

The piecewise polynomial interpolant represented in figure 2.1 corresponds to the case of $q = 6$ and $N = 10$. As can be seen from the represented stencils of the individual interpolants, sufficiently far away from the boundaries, the above selection of seeds leads to centered finite-difference formulas, whereas close to the boundaries the stencils are biased towards the center of the domain in order to only make use of existing grid nodes.

It should be noted, that in virtue of the uniqueness of the interpolating polynomials, the finite-difference formulas obtained from the differentiation of the piecewise polynomial interpolant introduced above coincide with the ones obtained by classical means. Thus, no differences compared to conventional finite-difference methods on arbitrary grids exist, only the way in which they are formulated and derived, but not in the end result.

Uniform interpolation errors

In the above definition of the piecewise polynomial interpolant the choice of grid nodes x_i has been left open so far. However, by their proper selection it is possible to make the interpolation error of the piecewise polynomial interpolant to be uniform across the interval $[-1, +1]$. The result is a non-uniform grid that is unique for each pair of values of q and N . This same idea underlies the Chebyshev interpolation, where the condition that the interpolation error is uniform across the interval $[-1, +1]$ is also imposed, but this time on a single polynomial interpolant instead [28, 111]. The result is also a non-uniform grid, known as the Chebyshev roots or Chebyshev-Gauss quadrature points, that is unique for each value of N . Both approaches achieve the same result, namely the suppression of the Runge phenomenon that spoils the accuracy of high order polynomial interpolations close to the ends of the interpolation interval.

In figure 2.2 the resulting grid spacings $\Delta x_i = x_{i+1} - x_i$ for the piecewise polynomial interpolant and for the Chebyshev interpolant are shown for different cases, both of them normalized with the uniform grid spacing $\Delta x_{i,\text{Eq}} = 2/N$. The details of the algorithm for the derivation of the former one can be found in [103], while the derivation of the Chebyshev grids can be found in any classical textbook on spectral collocation methods or interpolation theory [28, 104, 111]. The case $q = 6$ and $N = 10$ from figure 2.1 is shown in figure 2.2(a), where it can be seen that the proposed non-uniform grid for the piecewise polynomial interpolant lies in between the uniform grid and the Chebyshev grid.

Very enlightening are the following limiting cases: (i) $q \ll N$ and (ii)

$q = N$. In the first case, only a few points $\mathcal{O}(q)$ close to the boundaries need to be clustered in order to control the interpolation error, while far from the boundaries the grid points are equally spaced, as seen in figure 2.2(b), where the case of a piecewise polynomial interpolant for $q = 6$ and $N = 30$ is shown. In the second case, when $q = N$, only one interpolating polynomial can be constructed out of the $N + 1$ grid nodes, thus $I_0(x) = I_1(x) = \dots = I_N(x)$. Due to the uniqueness of the interpolating polynomials and the fact that the same error uniformization strategy is used for the piecewise polynomial interpolant than for the Chebyshev interpolant, both approaches are identical. Thus, in the limit $q = N$, the proposed piecewise polynomial interpolant with the proposed non-uniform grid presents all the properties of spectral collocation methods, especially their spectral accuracy [28, 34, 65].

When $q < N$, most of the nodes are affected by the presence of the boundaries and the resulting grid point distributions are in between the two limiting cases. This can be seen in figure 2.2(c), where the grid spacing of the proposed non-uniform grids for different values of q and $N = 50$ are shown. As the degree of the interpolation increases, the node distribution approaches the Chebyshev grid, while for small values of q it is more close to the uniform grid. Figure 2.2(d) shows that the minimum grid spacing Δx_{\min} present in the proposed non-uniform grids is always greater than the minimum grid spacing $\Delta x_{\min, \text{Ch}}$ of the Chebyshev grid. Moreover, from the figure it can be inferred that $\Delta x_{\min} = \mathcal{O}(\Delta x_{\min, \text{Ch}} N/q) = \mathcal{O}((qN)^{-1})$.

2.1.5 Spectral collocation methods

The limit of $q = N$ in the FD- q methodology is the Chebyshev-Gauss-Lobatto spectral collocation method. These methods offer an optimal compromise between the highest accuracy possible and the necessity of reducing the amount of information to be stored. The reason of the high accuracy of (collocation) spectral methods lies on the use of high-order interpolating polynomials, comprising all the points in the discretization domain. Spectral methods use all the points and the error is $\varepsilon = \mathcal{O}((1/N)^N) \rightarrow \mathcal{O}(e^{-N})$ [28, 34].

Non-periodic boundary conditions

Chebyshev-Gauss-Lobatto (CGL) points, indicated for the non-periodic configurations of interest, are used here.

The Chebyshev polynomial of degree n , $T_n(x)$, is given explicitly in terms

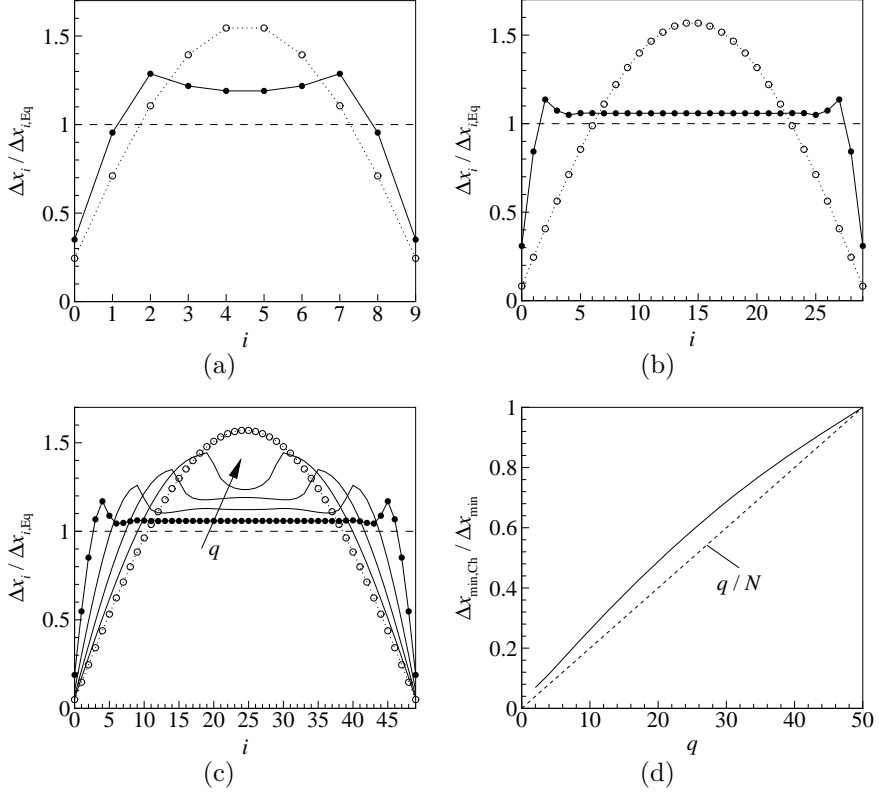


Figure 2.2: Grid spacing $\Delta x_i = x_{i+1} - x_i$ of the non-uniform grid for the piecewise polynomial interpolation (solid line), for the Chebyshev interpolation (dotted line), and for the uniform grid (dashed line) normalized with the uniform grid spacing $\Delta x_{i,Eq} = 2/N$ for (a) $q = 6$ and $N = 10$, (b) $q = 6$ and $N = 30$, and (c) $q = 10, 20, 30, 40$ and $N = 50$. (d) Variation of $\Delta x_{\min,Ch} / \Delta x_{\min}$ with q of the non-uniform grid for the piecewise polynomial interpolation with $N = 50$.

2. Numerical considerations

of trigonometric functions by

$$T_n(x) = \cos(n\theta), \quad x = \cos(\theta). \quad (2.9)$$

From the trigonometric representation of this expression it is clear that the extrema of $T_N(x)$ are ± 1 . The collocation derivative matrix for the Gauss-Lobatto grid is defined by the set of zeros of T_{N+1} and is evaluated in the interval $[-1,1]$. The Chebyshev-Gauss-Lobatto (CGL) points are

$$x_j = \cos(j\pi/N), \quad j = 0, 1, \dots, N. \quad (2.10)$$

Any function $f(x)$ can be expressed via the expansion:

$$f_N(x_j) = \sum_{k=0}^N a_k T_k(x_j), \quad (2.11)$$

where a_k are the series coefficient and k is the order of Chebyshev polynomial.

The elements of D depend solely on the set of discretization points [82]

$$\mathcal{D}_{i,j} = \begin{cases} \frac{2N^2+1}{6}, & i = j = 0 \\ -\frac{y_j}{2(1-y_j^2)}, & i = j \neq 0, N \\ \frac{\bar{c}_i}{\bar{c}_j} \frac{(-1)^{i+j}}{y_i - y_j}, & i \neq j \\ -\frac{2N^2+1}{6}, & i = j = N \end{cases} \quad (2.12)$$

where

$$\bar{c}_j = \begin{cases} 2, & j = 0, N \\ 1, & 1 \leq j \leq N-1 \end{cases} \quad (2.13)$$

An expression for the second derivative matrix can be found in [60]

$$\mathcal{D}_{i,j}^2 = \begin{cases} \frac{(-1)^{(i+j)} y_i^2 + y_i y_j - 2}{\bar{c}_j (1-y_j^2)(y_i - y_j)^2}, & 1 \leq i \leq N-1, 0 \leq j \leq N, i \neq j \\ -\frac{(N^2-1)(1-y_i^2)+3}{3(1-y_i^2)^2}, & 1 \leq j = i \leq N-1 \\ \frac{2}{3} \frac{(-1)^j (2N^2+1)(1-y_j)-6}{\bar{c}_j (1-y_j)^2}, & i = 0, 1 \leq j \leq N \\ \frac{2}{3} \frac{(-1)^{j+N} (2N^2+1)(1+y_j)-6}{\bar{c}_j (1+y_j)^2}, & i = N, 0 \leq j \leq N-1 \\ \frac{N^4-1}{15}, & i = j = 0, i = j = N \end{cases} \quad (2.14)$$

However, alternative expressions that reduce the impact of the round-off errors resulting from subtraction of nearly equal quantities are preferred. With this aim, the most obvious approach to reducing the impact of subtracting nearly equal numbers for the Chebyshev derivative matrices is to

Table 2.1: Accuracy study for different approaches of \mathcal{D}_{GL} with $N = 128$

| Case | x | $f(x) = e^x$ | $\mathcal{D}f(x)$ | $\mathcal{D}^2f(x)$ | $\mathcal{D}^4f(x)$ |
|------|-----|---------------|-------------------|---------------------|---------------------|
| 1 | 1 | 2.71828182845 | 2.71828182679 | 2.71827011478 | -89.670055389 |
| | 0 | 1.00000000000 | 1.00000000000 | 1.00000000128 | 0.99997886179 |
| | -1 | 0.36787944117 | 0.36787944146 | 0.36787697207 | -23.832031250 |
| 2 | 1 | | 2.71828182679 | 2.71828711319 | 95.2748298645 |
| | 0 | | 1.00000000000 | 1.00000000005 | 0.99999436007 |
| | -1 | | 0.36787944146 | 0.36787962165 | 13.4882812500 |
| 3 | 1 | | 2.71828182845 | 2.71828175174 | 1.90732192993 |
| | 0 | | 0.99999999999 | 0.99999999996 | 1.00000016850 |
| | -1 | | 0.36787944115 | 0.36787954252 | 1.19531250000 |

Case 1: \mathcal{D} calculated using equation (2.12) and $\mathcal{D}^2 = \mathcal{D} \cdot \mathcal{D}$

Case 2: \mathcal{D} and \mathcal{D}^2 calculated using equations (2.12) and (2.14) respectively

Case 3: \mathcal{D} calculated using equation (2.15) and $\mathcal{D}^2 = \mathcal{D} \cdot \mathcal{D}$

use trigonometric identities, giving the next derivative matrix [34]:

$$\mathcal{D}_{i,j} = \begin{cases} \frac{2N^2+1}{6}, & i = j = 0 \\ -\frac{y_j}{2\sin^2(j\pi/N)}, & i = j \neq 0, N \\ \frac{\bar{c}_i}{2\bar{c}_j} \frac{(-1)^{i+j}}{\sin[(i+j)\pi/2N]\sin[(i-j)\pi/2N]}, & i \neq j \\ -\frac{2N^2+1}{6}, & i = j = N \end{cases} \quad (2.15)$$

Table 2.1 shows a study of the recovered results using different approaches for \mathcal{D} . The minimum error is achieved in the Case 3: \mathcal{D} calculated using equation (2.15) and $\mathcal{D}^2 = \mathcal{D} \cdot \mathcal{D}$.

Periodic boundary conditions

Some problems allow the use of periodic boundary conditions in some spatial directions. The method used to discretize these spatial coordinates is the Fourier spectral collocation method.

The definition of derivative matrix coefficients on a periodic grid depends on the choice of grid points, N , either being even or odd. Here, the N is chosen always even for this discretization. The mesh spacing, $h = 2\pi/N$, implies that wavenumbers differing by an integer multiple of $2\pi/h$ are indistinguishable on the grid, and thus it will be enough to confine our attention to wavenumbers in the range $k \in [-\pi/h, \pi/h]$. The waves in physical space

2. Numerical considerations

must be periodic over the interval $[0, 2\pi]$, and only waves $\exp(ikx)$ with integer wavenumbers have the required period 2π .

The elements of D and D^2 can be written as

$$\mathcal{D}_{i,j} = \begin{cases} 0, & i = j \\ \frac{1}{2}(-1)^{i+j} \cot[(i-j)\pi/(N+1)], & i \neq j \end{cases} \quad (2.16)$$

$$\mathcal{D}_{i,j}^2 = \begin{cases} -\frac{(N+1)^2}{12} - \frac{1}{6}, & i = j \\ -\frac{1}{2}(-1)^{i+j} \csc^2[(i-j)\pi/(N+1)], & i \neq j \end{cases} \quad (2.17)$$

where $i, j = 0, 1, \dots, N$. See [28, 34, 82] for more details.

2.2 Multidimensional differentiation matrices

The differentiation matrices can be formed from the one-dimensional differential operator placing every coefficient in its respective row and column or easily if Kronecker tensor product (\otimes) is considered [258]. The Kronecker product of two matrices A and B of dimension $p \times q$ and $r \times s$ respectively is denoted by $A \otimes B$ of dimension $pr \times qs$. For instance

$$\begin{pmatrix} 1 & 2 \\ 3 & 4 \end{pmatrix} \otimes \begin{pmatrix} a & b \\ c & d \end{pmatrix} = \left(\begin{array}{cc|cc} a & b & 2a & 2b \\ c & d & 2c & 2d \\ \hline 3a & 3b & 4a & 4b \\ 3c & 3d & 4c & 4d \end{array} \right). \quad (2.18)$$

Using this tensor product, the two-dimensional derivatives matrices are computed. In what follows, let $[a, b] \times [c, d]$ be the computational domain discretized using the same number of points in each direction (N).

2.2.1 Two-dimensional differentiation matrices

The differentiation matrices in a two-dimensional problem are

$$\mathcal{D}_x = \mathcal{D} \otimes I =$$

$$= \left(\begin{array}{ccc|ccc} d_{0,0} & & & & & & d_{0,N} & & & & & \\ & d_{0,0} & & & & & & d_{0,N} & & & & \\ & & \ddots & & & & & & \ddots & & & \\ & & & d_{0,0} & & & & & & d_{0,N} & & \\ \hline & & & & \ddots & & & & & & & \\ \hline d_{N,0} & & & & & & d_{N,N} & & & & & \\ & d_{N,0} & & & & & & d_{N,N} & & & & \\ & & \ddots & & & & & & \ddots & & & \\ & & & d_{N,0} & & & & & & d_{N,N} & & \end{array} \right) \quad (2.19)$$

$$\mathcal{D}_y = I \otimes \mathcal{D} = \left(\begin{array}{cccc|ccc} d_{0,0} & d_{0,1} & \cdots & d_{0,N} & & & & & & & & \\ d_{1,0} & d_{1,1} & \cdots & d_{1,N} & & & & & & & & \\ & & \ddots & & & & & & & & & \\ d_{N,0} & d_{N,1} & \cdots & d_{N,N} & & & & & & & & \\ \hline & & & & \ddots & & & & & & & \\ \hline & & & & & & d_{0,0} & d_{0,1} & \cdots & d_{0,N} & & \\ & & & & & & d_{1,0} & d_{1,1} & \cdots & d_{1,N} & & \\ & & & & & & & & \ddots & & & \\ & & & & & & d_{N,0} & d_{N,1} & \cdots & d_{N,N} & & \end{array} \right) \quad (2.20)$$

where I is the $N \times N$ identity matrix.

Second order derivative matrices are built using the same technique $\mathcal{D}_{xx} = \mathcal{D}^2 \otimes I$, $\mathcal{D}_{yy} = I \otimes \mathcal{D}^2$, and $\mathcal{D}_{xy} = (I \otimes \mathcal{D}) \times (\mathcal{D} \otimes I)$.

2.2.2 Three-dimensional differentiation matrices

The differentiation matrices in a three-dimensional problem are

$$\mathcal{D}_x = \mathcal{D} \otimes I \otimes I \quad (2.21)$$

$$\mathcal{D}_y = I \otimes \mathcal{D} \otimes I \quad (2.22)$$

$$\mathcal{D}_z = I \otimes I \otimes \mathcal{D} \quad (2.23)$$

where I is the $N \times N$ identity matrix. Second order derivative matrices are built using the same technique.

2.3 General coordinate transformation

Let the position vector in the Cartesian coordinate system be defined as

$$\mathbf{x} = x(\xi, \eta, \zeta)\mathbf{j}_1 + y(\xi, \eta, \zeta)\mathbf{j}_2 + z(\xi, \eta, \zeta)\mathbf{j}_3, \quad (2.24)$$

where ξ , η and ζ are three independent curvilinear coordinates and \mathbf{j}_1 , \mathbf{j}_2 and \mathbf{j}_3 orthogonal unit vectors in the physical domain.

A general transformation follows

$$\xi = \xi(x, y, z), \quad (2.25)$$

$$\eta = \eta(x, y, z), \quad (2.26)$$

$$\zeta = \zeta(x, y, z), \quad (2.27)$$

which can be used to transform the governing equations from the physical domain (x, y, z) to the computational domain (ξ, η, ζ) . Using the chain rule of partial differentiation, the partial derivatives become

$$\frac{\partial}{\partial x} = \xi_x \frac{\partial}{\partial \xi} + \eta_x \frac{\partial}{\partial \eta} + \zeta_x \frac{\partial}{\partial \zeta}, \quad (2.28)$$

$$\frac{\partial}{\partial y} = \xi_y \frac{\partial}{\partial \xi} + \eta_y \frac{\partial}{\partial \eta} + \zeta_y \frac{\partial}{\partial \zeta}, \quad (2.29)$$

$$\frac{\partial}{\partial z} = \xi_z \frac{\partial}{\partial \xi} + \eta_z \frac{\partial}{\partial \eta} + \zeta_z \frac{\partial}{\partial \zeta}. \quad (2.30)$$

The metrics $(\xi_x, \xi_y, \xi_z, \eta_x, \eta_y, \eta_z, \zeta_x, \zeta_y, \zeta_z)$ appearing in these equations can be determined in the following manner. Firstly, they are written in matrix form as

$$\begin{pmatrix} d\xi \\ d\eta \\ d\zeta \end{pmatrix} = \begin{pmatrix} \xi_x & \xi_y & \xi_z \\ \eta_x & \eta_y & \eta_z \\ \zeta_x & \zeta_y & \zeta_z \end{pmatrix} \begin{pmatrix} dx \\ dy \\ dz \end{pmatrix}. \quad (2.31)$$

In a like manner, the next expression is written as

$$\begin{pmatrix} dx \\ dy \\ dz \end{pmatrix} = \begin{pmatrix} x_\xi & x_\eta & x_\zeta \\ y_\xi & y_\eta & y_\zeta \\ z_\xi & z_\eta & z_\zeta \end{pmatrix} \begin{pmatrix} d\xi \\ d\eta \\ d\zeta \end{pmatrix}. \quad (2.32)$$

Therefore

$$\begin{aligned} & \begin{pmatrix} \xi_x & \xi_y & \xi_z \\ \eta_x & \eta_y & \eta_z \\ \zeta_x & \zeta_y & \zeta_z \end{pmatrix} = \begin{pmatrix} x_\xi & x_\eta & x_\zeta \\ y_\xi & y_\eta & y_\zeta \\ z_\xi & z_\eta & z_\zeta \end{pmatrix}^{-1} \\ & = J \begin{pmatrix} y_\eta z_\zeta - y_\zeta z_\eta & -(x_\eta z_\zeta - x_\zeta z_\eta) & x_\eta y_\zeta - x_\zeta y_\eta \\ -(y_\xi z_\zeta - y_\zeta z_\xi) & x_\xi z_\zeta - x_\zeta z_\xi & -(x_\xi y_\zeta - x_\zeta y_\xi) \\ y_\xi z_\eta - y_\eta z_\xi & -(x_\xi z_\eta - x_\eta z_\xi) & x_\xi y_\eta - x_\eta y_\xi \end{pmatrix} \end{aligned} \quad (2.33)$$

where J is the Jacobian of the transformation,

$$J = \frac{\partial(\xi, \eta, \zeta)}{\partial(x, y, z)} = \begin{vmatrix} \xi_x & \xi_y & \xi_z \\ \eta_x & \eta_y & \eta_z \\ \zeta_x & \zeta_y & \zeta_z \end{vmatrix} \quad (2.34)$$

which can be evaluated in the following manner

$$\begin{aligned} J &= 1/J^{-1} = 1 / \frac{\partial(x, y, z)}{\partial(\xi, \eta, \zeta)} = 1 / \begin{vmatrix} x_\xi & x_\eta & x_\zeta \\ y_\xi & y_\eta & y_\zeta \\ z_\xi & z_\eta & z_\zeta \end{vmatrix} \\ &= 1 / [x_\xi(y_\eta z_\zeta - y_\zeta z_\eta) - x_\eta(y_\xi z_\zeta - y_\zeta z_\xi) + x_\zeta(y_\xi z_\eta - y_\eta z_\xi)] \end{aligned} \quad (2.35)$$

The metrics can be readily determined if analytical expressions are available for the inverse of the transformation:

$$x = x(\xi, \eta, \zeta), \quad (2.36)$$

$$y = y(\xi, \eta, \zeta), \quad (2.37)$$

$$z = z(\xi, \eta, \zeta). \quad (2.38)$$

For cases where the transformation is the direct result of a grid generation scheme, the metrics can be computed numerically.

In order to express second order derivatives in terms of computational coordinate derivatives, the next equivalence, written using Einstein notation, is used:

$$\frac{\partial f}{\partial x_i} = \xi_{x_i}^j \frac{\partial f}{\partial \xi^j} = J \frac{\partial}{\partial \xi^j} \left(\frac{\xi_{x_i}^j f}{J} \right) - J f \left[\frac{\partial}{\partial \xi^j} \left(\frac{\xi_{x_i}^j}{J} \right) \right], \quad (2.39)$$

where $f = f(x, y, z)$ is an arbitrary scalar function, $i = 1, 2, 3$, $j = 1, 2, 3$, $(x_1, x_2, x_3) = (x, y, z)$ and $(\xi^1, \xi^2, \xi^3) = (\xi, \eta, \zeta)$. The term in square brackets is equal to zero. This can be verified by substituting the metrics given by equation (2.33) into this term. Then, using the above expression (2.39), the

2. Numerical considerations

second order derivative with respect to the physical coordinates x_i and x_j of an arbitrary scalar function f is expressed as follows

$$\begin{aligned}\frac{\partial^2 f}{\partial x_i \partial x_j} &= \xi_{x_i}^k \frac{\partial}{\partial \xi^k} \left(\xi_{x_j}^l \frac{\partial f}{\partial \xi^l} \right) = J \frac{\partial}{\partial \xi^k} \left(\frac{\xi_{x_i}^k \xi_{x_j}^l \frac{\partial f}{\partial \xi^l}}{J} \right) \\ &= \xi_{x_i}^k \xi_{x_j}^l \frac{\partial^2 f}{\partial \xi^k \partial \xi^l} + J \frac{\partial}{\partial \xi^k} \left(\frac{\xi_{x_i}^k \xi_{x_j}^l}{J} \right) \frac{\partial f}{\partial \xi^l}.\end{aligned}\quad (2.40)$$

Particularly, the second order derivatives $\frac{\partial^2}{\partial y^2}$, $\frac{\partial^2}{\partial z^2}$ and $\frac{\partial^2}{\partial y \partial z}$ are

$$\begin{aligned}\frac{\partial^2}{\partial y^2} &= \xi_y^2 \frac{\partial^2}{\partial \xi^2} + \eta_y^2 \frac{\partial^2}{\partial \eta^2} + \zeta_y^2 \frac{\partial^2}{\partial \zeta^2} \\ &+ 2\xi_y \eta_y \frac{\partial^2}{\partial \xi \partial \eta} + 2\xi_y \zeta_y \frac{\partial^2}{\partial \xi \partial \zeta} + 2\eta_y \zeta_y \frac{\partial^2}{\partial \eta \partial \zeta} \\ &+ J \left[\frac{\partial}{\partial \xi} \left(\frac{\xi_y^2}{J} \right) + \frac{\partial}{\partial \eta} \left(\frac{\xi_y \eta_y}{J} \right) + \frac{\partial}{\partial \zeta} \left(\frac{\xi_y \zeta_y}{J} \right) \right] \frac{\partial}{\partial \xi} \\ &+ J \left[\frac{\partial}{\partial \xi} \left(\frac{\xi_y \eta_y}{J} \right) + \frac{\partial}{\partial \eta} \left(\frac{\eta_y^2}{J} \right) + \frac{\partial}{\partial \zeta} \left(\frac{\eta_y \zeta_y}{J} \right) \right] \frac{\partial}{\partial \eta} \\ &+ J \left[\frac{\partial}{\partial \xi} \left(\frac{\xi_y \zeta_y}{J} \right) + \frac{\partial}{\partial \eta} \left(\frac{\eta_y \zeta_y}{J} \right) + \frac{\partial}{\partial \zeta} \left(\frac{\zeta_y^2}{J} \right) \right] \frac{\partial}{\partial \zeta}\end{aligned}\quad (2.41)$$

$$\begin{aligned}\frac{\partial^2}{\partial z^2} &= \xi_z^2 \frac{\partial^2}{\partial \xi^2} + \eta_z^2 \frac{\partial^2}{\partial \eta^2} + \zeta_z^2 \frac{\partial^2}{\partial \zeta^2} \\ &+ 2\xi_z \eta_z \frac{\partial^2}{\partial \xi \partial \eta} + 2\xi_z \zeta_z \frac{\partial^2}{\partial \xi \partial \zeta} + 2\eta_z \zeta_z \frac{\partial^2}{\partial \eta \partial \zeta} \\ &+ J \left[\frac{\partial}{\partial \xi} \left(\frac{\xi_z^2}{J} \right) + \frac{\partial}{\partial \eta} \left(\frac{\xi_z \eta_z}{J} \right) + \frac{\partial}{\partial \zeta} \left(\frac{\xi_z \zeta_z}{J} \right) \right] \frac{\partial}{\partial \xi} \\ &+ J \left[\frac{\partial}{\partial \xi} \left(\frac{\xi_z \eta_z}{J} \right) + \frac{\partial}{\partial \eta} \left(\frac{\eta_z^2}{J} \right) + \frac{\partial}{\partial \zeta} \left(\frac{\eta_z \zeta_z}{J} \right) \right] \frac{\partial}{\partial \eta} \\ &+ J \left[\frac{\partial}{\partial \xi} \left(\frac{\xi_z \zeta_z}{J} \right) + \frac{\partial}{\partial \eta} \left(\frac{\eta_z \zeta_z}{J} \right) + \frac{\partial}{\partial \zeta} \left(\frac{\zeta_z^2}{J} \right) \right] \frac{\partial}{\partial \zeta}\end{aligned}\quad (2.42)$$

$$\begin{aligned}\frac{\partial^2}{\partial z \partial y} &= \frac{\partial^2}{\partial z \partial y} = \xi_y \xi_z \frac{\partial^2}{\partial \xi^2} + \eta_y \eta_z \frac{\partial^2}{\partial \eta^2} + \zeta_y \zeta_z \frac{\partial^2}{\partial \zeta^2} \\ &+ (\xi_y \eta_z + \xi_z \eta_y) \frac{\partial^2}{\partial \xi \partial \eta} + (\xi_y \zeta_z + \xi_z \zeta_y) \frac{\partial^2}{\partial \xi \partial \zeta} + (\eta_y \zeta_z + \eta_z \zeta_y) \frac{\partial^2}{\partial \eta \partial \zeta} \\ &+ J \left[\frac{\partial}{\partial \xi} \left(\frac{\xi_y \xi_z}{J} \right) + \frac{\partial}{\partial \eta} \left(\frac{\xi_y \eta_z}{J} \right) + \frac{\partial}{\partial \zeta} \left(\frac{\xi_y \zeta_z}{J} \right) \right] \frac{\partial}{\partial \xi}\end{aligned}$$

$$\begin{aligned}
 & + J \left[\frac{\partial}{\partial \xi} \left(\frac{\xi_z \eta_y}{J} \right) + \frac{\partial}{\partial \eta} \left(\frac{\eta_y \eta_z}{J} \right) + \frac{\partial}{\partial \zeta} \left(\frac{\eta_y \zeta_z}{J} \right) \right] \frac{\partial}{\partial \eta} \\
 & + J \left[\frac{\partial}{\partial \xi} \left(\frac{\xi_z \zeta_y}{J} \right) + \frac{\partial}{\partial \eta} \left(\frac{\eta_z \zeta_y}{J} \right) + \frac{\partial}{\partial \zeta} \left(\frac{\zeta_y \zeta_z}{J} \right) \right] \frac{\partial}{\partial \zeta}
 \end{aligned} \tag{2.43}$$

2.3.1 Two-dimensional transformation

In the case of a two-dimensional transformation of the form

$$\xi = \xi(x, y), \tag{2.44}$$

$$\eta = \eta(x, y), \tag{2.45}$$

the partial derivatives become

$$\frac{\partial}{\partial x} = \xi_x \frac{\partial}{\partial \xi} + \eta_x \frac{\partial}{\partial \eta}, \tag{2.46}$$

$$\frac{\partial}{\partial y} = \xi_y \frac{\partial}{\partial \xi} + \eta_y \frac{\partial}{\partial \eta}. \tag{2.47}$$

The metrics $(\xi_x, \xi_y, \eta_x, \eta_y)$ appearing in these equations can be determined as

$$\begin{pmatrix} \xi_x & \xi_y \\ \eta_x & \eta_y \end{pmatrix} = \begin{pmatrix} x_\xi & x_\eta \\ y_\xi & y_\eta \end{pmatrix}^{-1} = J \begin{pmatrix} y_\eta & -x_\eta \\ -y_\xi & x_\xi \end{pmatrix},$$

where J is the Jacobian of the transformation,

$$J = \frac{\partial(\xi, \eta)}{\partial(x, y)} = \begin{vmatrix} \xi_x & \xi_y \\ \eta_x & \eta_y \end{vmatrix} = 1 \left/ \begin{vmatrix} x_\xi & x_\eta \\ y_\xi & y_\eta \end{vmatrix} \right. = 1/[x_\xi y_\eta - x_\eta y_\xi]. \tag{2.48}$$

Using the same methodology of the general three-dimensional case, the second order derivatives are written as

$$\begin{aligned}
 \frac{\partial^2}{\partial x^2} & = \xi_x^2 \frac{\partial^2}{\partial \xi^2} + \eta_x^2 \frac{\partial^2}{\partial \eta^2} + 2\xi_x \eta_x \frac{\partial^2}{\partial \xi \partial \eta} \\
 & + J \left[\frac{\partial}{\partial \xi} \left(\frac{\xi_x^2}{J} \right) + \frac{\partial}{\partial \eta} \left(\frac{\xi_x \eta_x}{J} \right) \right] \frac{\partial}{\partial \xi} \\
 & + J \left[\frac{\partial}{\partial \xi} \left(\frac{\xi_x \eta_x}{J} \right) + \frac{\partial}{\partial \eta} \left(\frac{\eta_x^2}{J} \right) \right] \frac{\partial}{\partial \eta} \\
 \frac{\partial^2}{\partial y^2} & = \xi_y^2 \frac{\partial^2}{\partial \xi^2} + \eta_y^2 \frac{\partial^2}{\partial \eta^2} + 2\xi_y \eta_y \frac{\partial^2}{\partial \xi \partial \eta} \\
 & + J \left[\frac{\partial}{\partial \xi} \left(\frac{\xi_y^2}{J} \right) + \frac{\partial}{\partial \eta} \left(\frac{\xi_y \eta_y}{J} \right) \right] \frac{\partial}{\partial \xi}
 \end{aligned} \tag{2.49}$$

$$+ J \left[\frac{\partial}{\partial \xi} \left(\frac{\xi_y \eta_y}{J} \right) + \frac{\partial}{\partial \eta} \left(\frac{\eta_y^2}{J} \right) \right] \frac{\partial}{\partial \eta} \quad (2.50)$$

$$\begin{aligned} \frac{\partial^2}{\partial x \partial y} &= \xi_x \xi_y \frac{\partial^2}{\partial \xi^2} + \eta_x \eta_y \frac{\partial^2}{\partial \eta^2} + (\xi_x \eta_y + \xi_y \eta_x) \frac{\partial^2}{\partial \xi \partial \eta} \\ &+ J \left[\frac{\partial}{\partial \xi} \left(\frac{\xi_x \xi_y}{J} \right) + \frac{\partial}{\partial \eta} \left(\frac{\xi_x \eta_y}{J} \right) \right] \frac{\partial}{\partial \xi} \\ &+ J \left[\frac{\partial}{\partial \xi} \left(\frac{\xi_y \eta_x}{J} \right) + \frac{\partial}{\partial \eta} \left(\frac{\eta_y \eta_x}{J} \right) \right] \frac{\partial}{\partial \eta} \end{aligned} \quad (2.51)$$

2.3.2 Verification

The above expressions are verified solving the two-dimensional Helmholtz eigenvalue problem,

$$\left(\frac{\partial^2}{\partial x^2} + \frac{\partial^2}{\partial y^2} \right) \phi = -\lambda^2 \phi, \quad (2.52)$$

for orthogonal and non-orthogonal transformations. The two-dimensional differentiation matrices are computed using the definitions (2.49-2.50) and the results are checked against those recovered using differentiation matrices computed by simply multiplying first order derivative matrices, $\mathcal{D}_{xx} = \mathcal{D}_x \cdot \mathcal{D}_x$, $\mathcal{D}_{yy} = \mathcal{D}_y \cdot \mathcal{D}_y$.

Firstly, the next orthogonal elliptic confocal transformation is used

$$x = c \cosh \eta \cos \xi, \quad y = c \sinh \eta \sin \xi. \quad (2.53)$$

The domain is discretized using $N_\xi = 60$ Fourier collocation points for $\xi \in [0, 2\pi]$ and $N_\eta = 61$ Chebyshev-Gauss-Lobatto collocation points for $\eta \in [\eta_0, \eta_R]$. The parameters of the transformation (2.53) are selected for an ellipse of aspect ratio $AR = 2$, $\eta_0 = \operatorname{atanh}(1/AR)$, $c = AR/\sinh(\eta_0)$ and $\eta_R = \operatorname{acosh}(10/c)$. Figure 2.3 shows the grid corresponding to the selection of parameters and discretization points.

Figure 2.4(a) shows the first eigenvalues corresponding to the Helmholtz problem (2.52) discretized in the geometry defined by equation (2.53), using different definitions for the differentiation matrices. The second order derivative matrices are defined using (2.49-2.50) (referenced as D^2) and by simply multiplying the first order derivative matrices $\mathcal{D}_{xx} = \mathcal{D}_x \cdot \mathcal{D}_x$, $\mathcal{D}_{yy} = \mathcal{D}_y \cdot \mathcal{D}_y$ (referenced as DD). This fact verify the procedure used here and makes possible to compute second order derivatives using finite-difference schemes without lost of accuracy. Another advantage has been observed when using

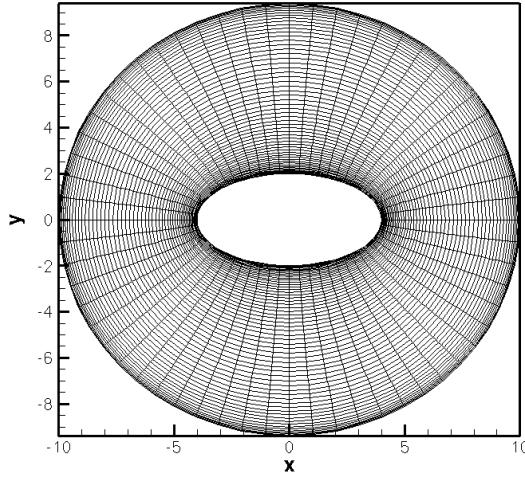


Figure 2.3: Elliptic confocal grid around a 2:1 ellipse.

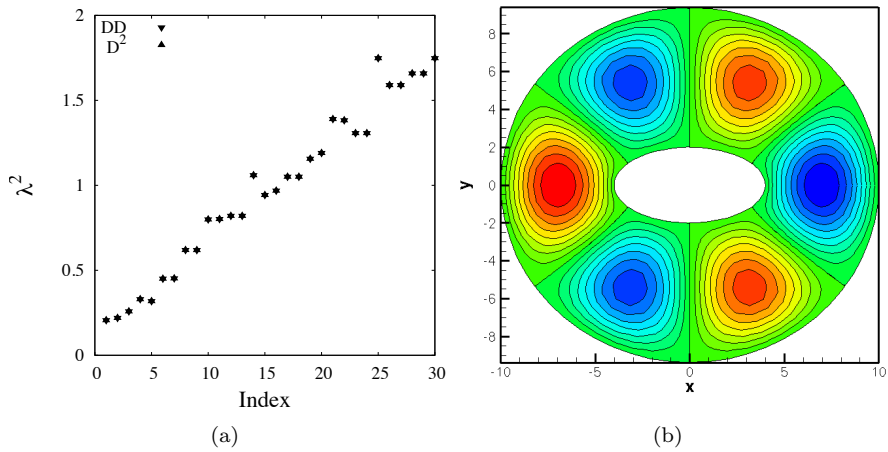


Figure 2.4: Eigenspectrum of Helmholtz problem (2.52) discretized in the orthogonal grid shown in figure 2.3 and iso-contours of normalized eigenfunction with index 7.

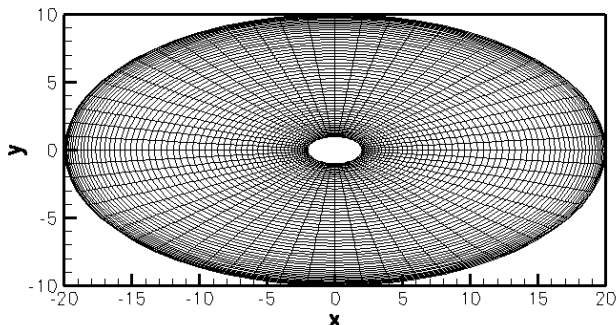


Figure 2.5: Elliptic non-orthogonal grid around a 2:1 ellipse.

the definitions (2.49-2.50), resulting in a considerable computational requirement reduction.

A more stringent test is a non-orthogonal transformation, since the cross-derivatives appearing in equations (2.49-2.50) are non-zero. The elliptic transformation

$$x = AR\eta \cos \xi, \quad y = \eta \sin \xi. \quad (2.54)$$

is used here with similar parameters to the previous case, $AR = 2$, $\eta_0 = 1$ and $\eta_R = 10$, and same number of discretization points. The resulting grid is plotted in figure 2.5.

Figure 2.6(a) shows again perfect agreement for results recovered using definitions (2.49-2.50) (referenced as D^2) and by simply multiplying the first order derivative matrices $\mathcal{D}_{xx} = \mathcal{D}_x \cdot \mathcal{D}_x$, $\mathcal{D}_{yy} = \mathcal{D}_y \cdot \mathcal{D}_y$ (referenced as DD).

2.3.3 One-dimensional mappings

In some flows, the calculation domain has to be mapped onto the standard domain of the employed spatial discretization through the one-dimensional mapping $\eta = \eta(\xi)$, ξ being the standard collocation points. The derivative matrices $D_{i,j}^{(m)}$ for each spatial direction has to be independently redefined to incorporate the stretching transformation as

$$\hat{D}_{k,j}^1(\eta) = \frac{d\xi}{d\eta} D_{k,j}^1(\xi) \quad (2.55)$$

$$\hat{D}_{k,j}^2(\eta) = \left(\frac{d\xi}{d\eta} \right)^2 D_{k,j}^2(\xi) + \frac{d^2\xi}{d\eta^2} D_{k,j}^1(\xi) \quad (2.56)$$

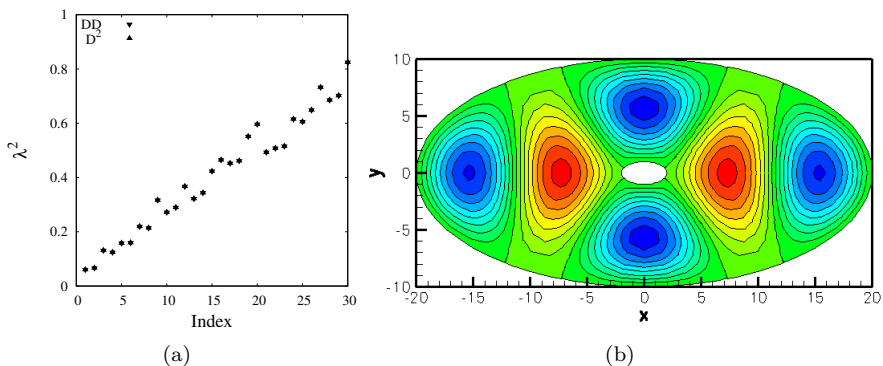


Figure 2.6: Eigenspectrum of Helmholtz problem (2.52) discretized in the non-orthogonal grid shown in figure 2.5 and iso-contours of normalized eigenfunction with index 7.

$$\hat{D}_{k,j}^3(\eta) = \left(\frac{d\xi}{d\eta}\right)^3 D_{k,j}^3(\xi) + 3\frac{d^2\xi}{d\eta^2}\frac{d\xi}{d\eta}D_{k,j}^2(\xi) + \frac{d^3\xi}{d\eta^3}D_{k,j}^1(\xi) \quad (2.57)$$

$$\begin{aligned} \hat{D}_{k,j}^4(\eta) &= \left(\frac{d\xi}{d\eta}\right)^4 D_{k,j}^{(4)}(\xi) + 6\frac{d^2\xi}{d\eta^2}\left(\frac{d\xi}{d\eta}\right)^2 D_{k,j}^3(\xi) \\ &+ 3\left(\frac{d^2\xi}{d\eta^2}\right)^2 D_{k,j}^2(\xi) + 4\frac{d^3\xi}{d\eta^3}\frac{d\xi}{d\eta}D_{k,j}^2(\xi) + \frac{d^4\xi}{d\eta^4}D_{k,j}^1(\xi) \end{aligned} \quad (2.58)$$

Derivatives of the interpolating polynomials are then calculated in the standard manner with $D_{i,j}^m$ replace by $\hat{D}_{i,j}^m$.

Two mappings are used in this work between CGL or FD-q grids ($\xi \in [-1, 1]$) and the actual physical domain. The next transformation obtains a domain in the entire real axis [95],

$$\eta = \eta_0 + \eta_\infty \frac{\tan\left(\frac{c\pi}{2}\xi\right)}{\tan\left(\frac{c\pi}{2}\right)}, \quad (2.59)$$

where η is the discretized spatial direction, and η_0 and η_∞ are the respective center-point and far-field truncation locations. Another transformation is used here in order to map the calculation domain grid $\eta \in [0, \eta_\infty]$ into the grid $\xi \in [-1, 1]$ [164],

$$\eta_j = l \frac{1 - x_j}{1 + s + \xi_j}, \quad s = 2l/\eta_\infty, \quad l = \frac{\eta_\infty \eta_h}{\eta_\infty - 2\eta_h}, \quad (2.60)$$

being η_∞ the location where the calculation domain is truncated and η_h the domain location that splits in two halves the number of discretization points.

2.4 Eigenvalue computation

The generalized EVP (1.26) must be constructed and solved employing adequate algorithms, taking into account the memory and CPU-time requirements when the matrices are formed and stored. Although the newly developed code allows the use of dense or sparse linear algebra, the sparse version is much more efficient and it is the one used here. The complex matrices \mathbf{A} and \mathbf{B} discretizing the operators of equation (1.26) are built using an in-house modified version of the SPARSKIT2 library [219] to work with complex arithmetic. To solve the eigenvalue problem, the Arnoldi algorithm [218] is employed, combined with the MUMPS library [5, 6] (MULTifrontal Massively Parallel Solver) to perform the LU-decomposition and solve the linear algebraic systems with the possibility of making serial and parallel computations.

The Arnoldi algorithm delivers a number of eigenvalues on the vicinity of a specific estimate value. Such value is set in the vicinity of the unstable/least-stable eigenvalue. Computational cost is notoriously reduced employing Arnoldi algorithm instead of the classical QZ method. More details can be found in the literature [218, 249].

The number of eigenvalues delivered is determined by the freely chosen Krylov subspace dimension, whose limit is the leading dimension of matrices \mathbf{A} and \mathbf{B} . A so-called shift-and-invert strategy is also implemented in this eigenvalue problem solver. The problem solved is the following

$$\mathcal{C}\mathbf{X} = \mu\mathbf{X}, \quad \mathcal{C} = (\mathcal{A} - \sigma\mathcal{B})^{-1}\mathcal{B}, \quad \mu = \frac{1}{\omega - \sigma}. \quad (2.61)$$

where the Krylov subspace is constructed by

$$\mathcal{K}_m = \text{span}(\mathbf{v}, \mathcal{C} \cdot \mathbf{v}, \mathcal{C}^2 \cdot \mathbf{v}, \dots, \mathcal{C}^{m-1} \cdot \mathbf{v}) \quad (2.62)$$

where m is the dimension of the subspace.

The vectors forming the basis are ordered by columns into the matrix \mathbf{V}_m . The projection of the linear operator on the basis \mathbf{V}_m yields the relation

$$\mathbf{V}_m^H \mathcal{C} \mathbf{V}_m = \mathbf{H}_m, \quad (2.63)$$

where \mathbf{H}_m is an upper triangular Hessenberg matrix. The restriction of the eigenvalue problem to the Krylov subspace \mathcal{K}_m is

$$\mathbf{H}_m \mathbf{V}_m^H \cdot \hat{\mathbf{q}} = \mu \mathbf{V}_m^H \cdot \hat{\mathbf{q}}. \quad (2.64)$$

The eigenvalues of the Hessenberg matrix \mathbf{H}_m are approximations to the m largest eigenvalues of the original problem. If $y_i^{(m)}$ is the eigenvector

corresponding to the i -th eigenvalue of \mathbf{H}_m the corresponding approximation to the eigenvector of the original problem, known as Ritz vector, is

$$\hat{\mathbf{q}}_i = \mathbf{V}_m \cdot \mathbf{y}^{(m)}. \quad (2.65)$$

2.5 Solution procedure of PSE-3D

2.5.1 Parabolic marching integration

The next solution procedure is equivalent for classical PSE, with the exception of having $\hat{\mathbf{q}}_j(y, z)$ instead of $\hat{\mathbf{q}}_j(y)$. Therefore, the involved integrals are two-dimensional instead of one-dimensional. The parabolic PDE system of equations (1.57) is solved by marching along the streamwise direction. The derivative in the marching direction is approximated by the implicit backward Euler scheme:

$$(\hat{\mathbf{q}}_x)_{j+1} \approx \frac{1}{\Delta x_j} (\hat{\mathbf{q}}_{j+1} - \hat{\mathbf{q}}_j), \quad (2.66)$$

where $j \geq 0$ is the step index and $\hat{\mathbf{q}}_j = \hat{\mathbf{q}}_j(y, z) = \hat{\mathbf{q}}(x_j, y, z)$. In addition to this first order scheme, the newly-developed code incorporates the option to use a second order scheme. Equation (1.57) becomes

$$[\Delta x_j \mathcal{L}_{j+1}^k + \mathcal{M}_{j+1}^k]_n \hat{\mathbf{q}}_{n,j+1}^k = [\Delta x_j \mathcal{F}_{j+1}^k + \mathcal{M}_{j+1}^k]_n \hat{\mathbf{q}}_{n,j}, \quad (2.67)$$

where k is the iteration index. Starting with an initial guess $\alpha_{j+1}^0 = \alpha_j$, according to the first approximation $\alpha_x = 0$, $\hat{\mathbf{q}}_{j+1}^0$ is obtained from equation (1.57). Then, the normalization condition (1.43) is used to estimate a new α_{j+1} :

$$\alpha_{j+1}^{k+1} = \alpha_{j+1}^k - \frac{i}{\Delta x_j} \frac{\int_{\Omega} (\rho_b)_{j+1}^{1/2} \hat{\mathbf{u}}_{j+1}^{\dagger k} [(\rho_b)_{j+1}^{1/2} \hat{\mathbf{u}}_{j+1}^k - (\rho_b)_j^{1/2} \hat{\mathbf{u}}_j] d\Omega}{\int_{\Omega} (\rho_b)_{j+1} |\hat{\mathbf{u}}_{j+1}^k|^2 d\Omega}. \quad (2.68)$$

Once the wavenumber is updated, equation (2.67) is solved for the new shape functions, and the value of α is recalculated. The iteration continues until the normalization condition is satisfied to within some specified residual r (i.e. $|\alpha^{k+1} - \alpha^k| < r = 10^{-8}$ in the present computations).

2.5.2 Non-linear terms

Computationally, the Fourier component of the forcing term, \mathcal{F}_n , can be computed using different algorithms. When solving classical non-linear PSE

2. Numerical considerations

and the number of modes in consideration is large enough, the Fast Fourier Transform (FFT) is used. In order to proceed, firstly, $\tilde{\mathbf{q}}$ is calculated from equation (1.56). Then, \mathcal{F} is calculated in the physical space using the equations of Appendix D and finally \mathcal{F}_n is computed by performing the FFT of \mathcal{F} . However, for the PSE-3D results shown here, the Fourier modes of the non-linear terms, \mathcal{F}_n , are computed directly in the Fourier space using the convolution operation.

The computation of the non-linear terms requires some previous operations to calculate the streamwise derivatives of perturbation variables. Since the second derivatives of the disturbances with respect to x appear only in the viscous terms, the following formula

$$\frac{\partial^2 \tilde{\mathbf{q}}}{\partial x^2} = \sum_{n=-N}^N -\alpha_n^2 \tilde{\mathbf{q}} \exp[-in\omega t], \quad (2.69)$$

is consistent with the order of magnitude analysis made for the derivation of the linear terms. First derivatives of the disturbances with respect to x can be written as

$$\frac{\partial \tilde{\mathbf{q}}}{\partial x} = \sum_{n=-N}^N \left(\frac{\partial \hat{\mathbf{q}}}{\partial x} + i\alpha_n \hat{\mathbf{q}} \right) \exp \left[i \int_x \alpha(x') dx' \right] \exp[-in\omega t]. \quad (2.70)$$

This may cause that some terms smaller than $\mathcal{O}(\varepsilon)$ appear in the forcing terms.

Chapter 3

Linear modal stability validations and numerical efficiency

3.1 Introduction

The present contribution revisits the numerical solution of the EVP arising in global linear stability theory using matrix formation and spatial discretization of the spatial operator by means of the previously employed Padé compact [138] and Dispersion-Relation-Preserving [240] schemes, as well as standard high-order finite-differences, Summation-By-Parts operators [170, 234], and the less-known very high order finite-difference schemes of Hermanns and Hernández [103]. All results are compared against those delivered by the spectral collocation method based on (standard and coordinate-transformed) Chebyshev Gauss-Lobatto grids.

Although the main focus of the present work is global instability analysis in two or three inhomogeneous spatial directions, the one-dimensional EVP governing local flow stability is also solved, since its well-known highly accurate results assist quantification of the error associated with each spatial discretization method. The potential of the most accurate finite-difference method identified to permit transient growth analyses [221] is demonstrated also in this local linear stability limit. For the sake of quantifying errors in the numerical solution of the two- and three-dimensional global linear stability EVP, solution of the Helmholtz equation in two and three spatial dimensions is also presented using the spatial discretization methods discussed earlier since, on the one hand analytically-known solutions exist for the Helmholtz EVP and on the other hand the Laplacian operator in two and three spatial dimensions is a key element in the construction of the respective BiGlobal and TriGlobal EVPs.

3.2 Incompressible stability analysis validations

In the incompressible limit, validations commence with the well-known OSE, to which the global EVP reduces in case of parallel one-dimensional flows. Results are presented for the plane Poiseuille flow (PPF) [127, 185] and for the Blasius boundary-layer [160].

EVPs whose spatial dependence is described by the Poisson operator are subsequently solved by the present methodology, in both two and three spatial dimensions. The attractiveness of this spatial operator resides in the existence of analytically-known results in regular two- and three-dimensional geometries and also in the fact that this spatial operator is at the heart of the global EVP in both two and three spatial dimensions. Attention will be paid to the accurate recovery of analytically known results of the Poisson operator, the Helmholtz EVP, which is at the elliptic part of the linearized Navier-Stokes equations governing instability in both two and three spatial dimensions:

$$\Delta\phi + \lambda^2\phi = 0, \quad (3.1)$$

where λ^2 is the sought real eigenvalue and can be determined analytically for simple geometries [177]. This problem is also recovered by simplification from the linearized Euler equations, neglecting flow altogether and keeping only the pressure.

Global modal instability analysis results are obtained in five fluid flow applications, three in a BiGlobal and two in a TriGlobal EVP context. The BiGlobal EVPs to solve differ in the number of base flow components: in the rectangular duct [244] only one such component exists, and the EVP is complex; in the 2D lid-driven cavity [248], two base flow velocity components exist, while the wavenumber vector is normal to the base flow plane, and the stability EVP is real; in the swept attachment-line boundary-layer [153] all three base flow components exist and the EVP is again complex. Finally, TriGlobal linear instability EVPs are solved, treating all three inhomogeneous spatial dimensions in a coupled manner. This is the most stringent test to which the proposed spatial discretization is performed. The same rectangular duct and 2D lid-driven cavity problems studied by BiGlobal analysis are solved by TriGlobal analysis. The solution is obtained at length-to-depth ratio of unity and a spanwise domain extent defined by the maximally amplified BiGlobal eigenmode, with which the TriGlobal analysis results are compared. Furthermore, the 3D lid-driven cavity flow instability problem is solved using TriGlobal matrix-formation analysis. It is worth noting that the very first TriGlobal instability analysis to appear in the literature was performed relatively recently in a time-stepping context [246], while presently

four more such analyses are available [11, 63, 74, 178]. Of these, one [178] is performed in a matrix-forming context, while two in a time-stepping technique, all concerning the cubic lid-driven cavity with singular lid motion [63, 74].

The elliptic EVP (1.26) must be complemented with adequate boundary conditions for the disturbance variables. In the presence of solid walls, no-slip condition is implemented, and far from the wall all disturbances decay to zero. Boundary conditions for the disturbance pressure do not exist physically; instead on the boundaries, compatibility conditions are used derived from the Navier-Stokes equations at the boundary of the domain (see Theofilis et al. [254]).

3.2.1 Local instability analysis

The one-dimensional LNSE is the limit to which the global eigenvalue problem reduces in case of parallel flows. Results are presented for the PPF (PPF) [127, 185], the bounded nature of which implies the existence of a discrete eigenspectrum only, and for the Blasius boundary-layer [160], where both discrete and continuous branches of the spectrum exist.

In order to assess the ability of the proposed spatial discretization to perform transient growth studies, the well-known pseudospectra of the OSE [198] are also obtained.

Eigenspectrum of PPF

The temporal stability analysis of the PPF is considered first. The stability EVP [185] is solved at $Re = 10000, \alpha = 1$ and spanwise wavenumber $\beta = 0$, for which the converged leading eigenvalue in double precision arithmetic has been provided by Kirchner [127] as being $\omega_{r,c} + i\omega_{i,c} = 0.2375264888204682 + i0.0037396706229799$. Owing to the relatively small leading matrix dimension, the dense linear algebra subroutine ZGGEV of LAPACK, based on the QZ algorithm [76], is used for the solution of the EVP. The examined spatial discretizations are summarized in Table 3.1. All these finite-difference methods are implemented at order 8 and on uniform grids, except for the last one, FD-q, which employs its particular grid. In addition, FD-q method is implemented not only at order 8, but also at order 16, in order to prove the capability of this method of reaching very high order schemes and its good behavior. In figure 3.1, relative error of the leading eigenvalue as function of the leading matrix dimension $N + 1$ is presented in

3. Linear modal stability validations and numerical efficiency

Table 3.1: Examined spatial discretization methods.

| Spatial discretization method | Acronym | Refereces |
|---|---------|------------|
| Spectral collocation | CGL | [28, 34] |
| Standard centered finite-differences | STD | - |
| Compact finite-differences | Padé | [138] |
| Dispersion-Relation-Preserving finite-differences | DRP | [240] |
| Summation-by-parts operators | SPB | [170, 234] |
| Finite difference methods with uniform error | FD-q | [103] |

order to compare accuracy between the different numerical methods. The relative error is defined in the following way:

$$\varepsilon_\omega = \left| \frac{\omega_i - \omega_{i,c}}{\omega_{i,c}} \right|, \quad (3.2)$$

where ω_i is the computed imaginary part of the eigenvalue using $N + 1$ nodes and $\omega_{i,c}$ the corresponding converged value quoted above.

Several observations are worthy of discussion on the basis of these results and the analogous ones of the mode frequency, as well as all qualitatively identical results obtained for FD-q at different combinations of discretization nodes, $N + 1$, and orders, q , not presented here. First, it is seen that, compared with any finite-difference method, the spectral collocation method needs less grid points to obtain a converged result, a fact which is well-known from classic linear stability studies [e.g. 164]. Second, when monitoring finite-difference discretizations of the same order (here methods of order 8 are shown), the standard and the compact finite-differences, the DRP and the SBP methods all require practically the same resolutions in order to deliver amplification rate results converged to the same degree. However, fastest convergence, compared with any of the examined finite-difference methods of the same order, is offered by the FD-q8 method. In the example presented, in order to achieve a relative error of $\mathcal{O}(10^{-6})$ in the amplification rate, $N \approx 200$ points are needed by FD-q8 and $N \approx 500$ by all

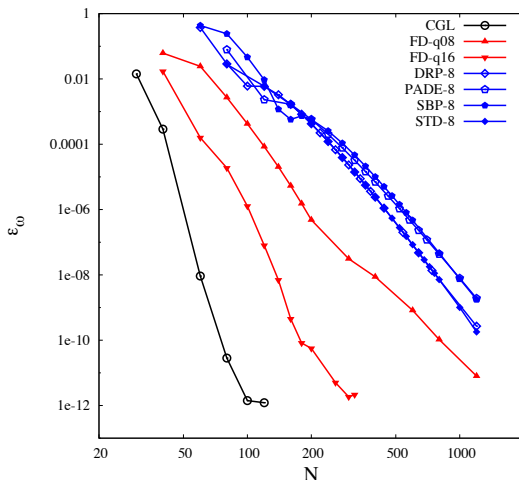


Figure 3.1: Convergence history of relative error for the amplification rate of the leading eigenmode of PPF at $Re = 10000$, $\alpha = 1$, obtained by (black) spectral collocation using CGL and (blue) high-order finite-difference methods of order 8: STD, Padé, DRP, SBP, as well as (red) FD- q with $q = 8$ and $q = 16$. $N + 1$ is the total number of discretization points.

other finite-difference methods despite having all of them the same formal order of accuracy/convergence. Conversely, and much more important from the point of view of the subsequent use of the FD- q methods as the basis for spatial discretization in the multi-dimensional EVPs, at a given affordable level of discretization, say $N = 200$ points, STD, Padé, SBP and DRP methods of order 8 have a relative error of $\mathcal{O}(10^{-3})$ in the recovery of the leading eigenmode, while the error of the FD- $q8$ method is $\mathcal{O}(10^{-6})$. Third, as the order of the FD- q method is increased, its results approach those of the spectral collocation method, with which the method becomes identical when $q = N$ as discussed in Subsection 2.1.4; the FD- $q16$ results shown in figure 3.1 are typical for the convergence history shown by FD- q methods of order $8 < q < N$, requiring only $N \approx 100$ points to achieve the specified relative error level of $\mathcal{O}(10^{-6})$, or attaining an accuracy of $\mathcal{O}(10^{-10})$ for $N = 200$ points.

In summary, at all orders examined, the FD- q method performs better than all of the well-known high-order finite-difference methods. This is attributed to the fact that the FD- q method minimizes the interpolation error both at the interior and boundary (and near-boundary) points in a self-consistent uniform manner. In order for the standard high-order, Padé,

DRP or SBP schemes to become competitive with FD- q , higher formal orders need to be used compared with that employed in the FD- q method. However, that increase in the order may not be straightforward for some schemes at $q \geq 8$ [234] or the resulting finite-difference method may be unstable.

On the other hand, for those methods for which using $q > 8$ is possible, the increase in bandwidth resulting from a comparatively high value of q is not an issue from the point of view of efficiency, when the one-dimensional EVP is solved using full eigenspectrum computations and the QZ algorithm. However, FD- q has a competitive advantage in performing global instability analyses, where exploitation of the matrix sparsity is essential; there one seeks to use the method having optimal convergence and accuracy properties between all available having the same sparsity pattern, as will be discussed in subsequent sections.

Pseudospectrum of PPF

The non-modal scenario for laminar-turbulent flow transition is now well-understood [221], the concept of pseudospectrum [259] being central to its theoretical description. Here, the pseudospectrum of PPF (PPF) is shown comparing, for brevity, Chebyshev-Gauss-Lobatto collocation (CGL) and FD- $q16$.

As shown above, results obtained are representative of all combinations of number of discretization points, N , and finite-difference method order, q for FD- q ; $N = 128$ and $q = 16$ are used presently, and the pseudospectrum has been computed using *EigTool* [275].

Figure 3.2 shows the eigenspectrum and pseudospectrum obtained by the spectral collocation and FD- q methods. Eigenspectrum results are graphically indistinguishable from each other while the pseudospectrum, plotted here at different levels of matrix perturbations, corresponding to 10^{-7} for the innermost to 10^{-2} in the outermost curve in figure 3.2, only shows discrepancies at large matrix perturbation levels. However, given that $q \ll N$, the overall agreement is quite satisfactory. If an improved agreement is sought, the order q or the number of points N may be increased in order for the FD- q method to deliver results approaching those obtained by the spectral collocation method. As mentioned, though, it is not perfect agreement of the FD- q with the spectral collocation method that is sought, but rather the ability of the former method to deliver accurate description of the pseudospectrum, as shown in the results of figure 3.2, at a smaller cost thanks to the fact that $q \ll N$, thus improving the sparsity pattern.

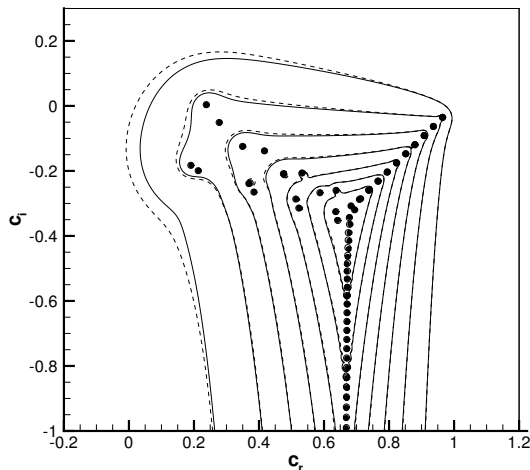


Figure 3.2: Eigenspectrum and pseudospectrum of PPF at $Re = 10^4, \alpha = 1$, obtained by spectral collocation using CGL and high-order finite-difference method FD-q. Solid lines and empty circles correspond to CGL and dashed lines and solid circles to FD-q16, both of them with $N + 1 = 129$ discretization points. Levels from inner to outer isoline, $10^{-7}, 10^{-6}, 10^{-5}, 10^{-4}, 10^{-3}$ and 10^{-2} . Note that $c = \omega/\alpha$ refers to phase velocity.

Eigenspectrum of the Blasius boundary-layer

The accuracy properties of the FD-q method are preserved in open flows, where a mapping transformation is needed to transfer data from the standard domain $x \in [-1, 1]$ of both the CGL and the FD-q methods onto a semi-infinite domain $y \in [0, y_\infty]$ with transformation (2.60), setting $y_\infty = 150$ and $y_h = 5$.

Figure 3.3 shows the leading unstable eigenmode and the least stable part of the Blasius eigenspectrum at $Re_{\delta^*} = 580$ and $\alpha = 0.179$ [160], as recovered by the CGL spectral collocation method on $N + 1 = 101$ points, as well as FD-q12 and FD-q24 on the same number of nodes. Even at a value of q which is an order of magnitude smaller than N , the entire discrete eigenspectrum is seen to be recovered by the FD-q method as reliable as by the CGL spatial discretization. None of the three methods is capable of capturing the continuous spectrum correctly; as is known analytically, the latter is a vertical line at $c_r = \omega_r/\alpha = 1$ (c refers to phase velocity). Interestingly, even at $q = 12$ the discrete approximation of the continuous spectrum is more vertical than the one delivered by the spectral collocation method, although as q increases the FD-q and spectral results come closer,

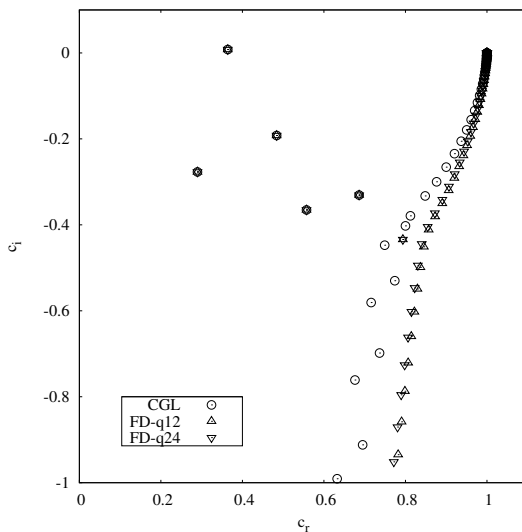


Figure 3.3: Eigenspectrum of Blasius boundary-layer flow at $Re_{\delta^*} = 580$ and $\alpha = 0.179$, obtained with spectral collocation based on mapped CGL and two high-order finite-difference methods FD-q of order 12 and 24 with $N + 1 = 101$ discretization points. Note that $c = \omega/\alpha$ refers to phase velocity.

and collapse onto each other at $q = N$, pointing towards the existence of an optimum value of q which for the moment is unknown *a priori*. Finally, an additional discrete mode is recovered at $c_r = 0.8$ using the FD-q12 and FD-q24 methods due to the displacement of the continuous part of the spectrum.

Pseudospectrum of the Blasius boundary-layer

This Subsection of validation of results of the FD-q method against known solutions of the one-dimensional EVP closes with the presentation of the pseudospectrum of Blasius flow at the same parameters as those at which the eigenspectrum has been obtained. Figure 3.4 presents the eigenspectrum obtained by the spectral collocation method, already shown in figure 3.3, alongside the one delivered by FD-q16, which exhibits the properties discussed in the previous Subsection. In addition, the pseudospectrum obtained at perturbation levels of 10^{-7} to 10^{-2} (inner-to-outer curves) is shown. As in the case of the PPF, close qualitative agreement is seen between the two sets of results, although the poor recovery of the continuous spectrum by both,

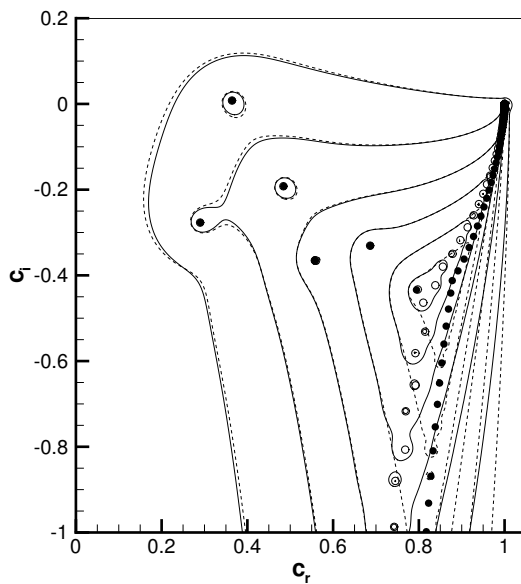


Figure 3.4: Eigenspectrum and pseudospectrum of the Blasius boundary-layer flow at $Re_{\delta^*} = 580$ and $\alpha = 0.179$, obtained by spectral collocation using CGL and FD-q. Solid lines and empty circles correspond to CGL and dashed lines and solid circles to FD-q16, both of them with $N + 1 = 129$ discretization points. Levels from inner to outer isoline, 10^{-7} , 10^{-6} , 10^{-5} , 10^{-4} , 10^{-3} and 10^{-2} .

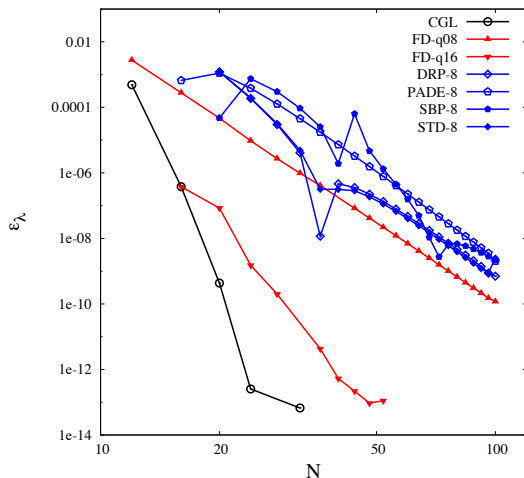


Figure 3.5: Convergence history of the solution of the 2D Helmholtz EVP for the eigenvalue $\lambda^2/(\pi^2/4) = 34$, obtained by (black) spectral collocation using CGL and (blue) high-order finite-difference methods of order 8: STD, Padé, DRP, SBP, as well as (red) FD- q with $q = 8$ and $q = 16$. The number of discretization nodes used is the same in both spatial directions and is denoted by $N + 1$.

the spectral and the finite-difference methods, results in larger discrepancies in the pseudospectrum in that region. By contrast, the pseudospectrum associated with the discrete eigenvalues is reproduced in close agreement by both methods, despite the fact that $q = 16$ is an order of magnitude smaller than $N + 1 = 129$, the discretization nodes used in both methods.

3.2.2 The 2D Helmholtz EVP

In two spatial dimensions the Helmholtz EVP (3.1) is

$$\left(\frac{\partial^2}{\partial x^2} + \frac{\partial^2}{\partial y^2} \right) \phi + \lambda^2 \phi = 0. \quad (3.3)$$

Such problem is useful in assessing the accuracy of the proposed spatial discretization method comparing the recovered eigenvalues with the analytical solution of this problem in the rectangular membrane domain $\Omega = \{x \in [-1, 1]\} \times \{y \in [-1, 1]\}$ [e.g. 177]. Such solution is the following:

$$\lambda_{n_x, n_y}^2 = \frac{\pi^2}{4} (n_x^2 + n_y^2); \quad n_x, n_y = 1, 2, 3, \dots \quad (3.4)$$

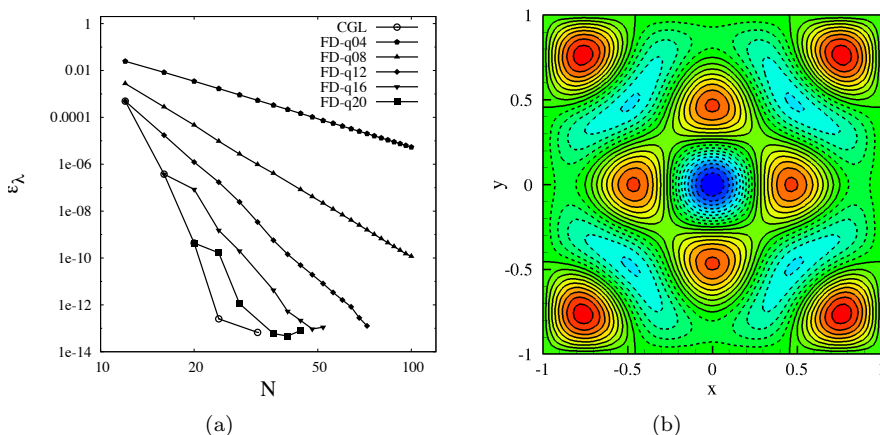


Figure 3.6: (a) Convergence history of the solution of the 2D Helmholtz EVP for the eigenvalue $\lambda^2/(\pi^2/4) = 34$, obtained using CGL and a suite of FD-q methods of orders 4, 8, 12, 16 and 20. The number of discretization nodes used is the same in both spatial directions and is denoted by $N+1$. (b) Corresponding eigenfunction using FD-q12 with $N_x \times N_y = 80^2$. Shown are contours (-0.9:0.1:0.8) with isolines of positives (solid line) and negatives (dashed line) values.

Higher eigenvalues/eigenfunctions ($n_x, n_y \gg 1$) are of special interest due to the need of using a relatively high number of nodes for an accurate description. This is in contrast with the first few eigenvalues, which are already recovered using $N \approx 10$.

Figure 3.5 shows the convergence history of the numerical solution of the 2D Helmholtz problem for a high eigenvalue ($\lambda^2/(\pi^2/4) = 34$) comparing the same finite-difference methods used to obtain the OSE results in figure 3.1. Similar conclusions to the one reached in the OSE solved in the previous applications are also drawn here: maintaining the order of the scheme (order 8) FD-q presents higher accuracy than the other finite-difference methods, and with a higher order (order 16), FD-q reaches double-precision employing a number of nodes only two times larger than employing the spectral collocation method.

Figure 3.6(a) shows the convergence history of the numerical solution of the 2D Helmholtz problem for the same eigenvalue. Different orders of FD-q methods are implemented and compared with CGL spectral collocation method. Special interest is focused on intermediate values of the order of the method, e.g. $q = 12$. In such case single-precision convergence is achieved using approximately two times more discretization points than with

the spectral collocation method. In addition, double-precision convergence is achieved with less than four times more nodes than the ones required by the spectral collocation method. For completeness, figure 3.6(b) displays the eigenfunction corresponding to the eigenvalue $\lambda^2/(\pi^2/4) = 34$, obtained numerically using FD-q12 with $N_x \times N_y = 80^2$.

3.2.3 BiGlobal instability analysis

Attention is now turned to the main subject of this paper, namely modal global linear instability, discussing BiGlobal instability first. Three applications are selected for validation purposes: the rectangular duct [244], the lid-driven cavity [3, 248] and the swept leading-edge boundary-layer [153, 253]. As mentioned at the beginning of this Section, these problems are selected because they are governed by one, two and three base flow velocity components, respectively, and also permit validating both the real and the complex form of the EVP.

The rectangular duct flow

In two coupled spatial directions, the rectangular duct [244] of cross-sectional aspect ratio A , driven by a constant pressure gradient along the axial (unbounded) direction, is the two-dimensional extension of the PPF. Its base flow is known analytically [211] and has a single component along the (homogeneous) wavenumber vector direction. Considering the rectangular duct defined in the domain $\Omega = \{z \in [-A, A]\} \times \{y \in [-1, 1]\}$, a constant pressure gradient in the unbounded x direction drives a steady laminar flow which is independent of x and possesses a velocity vector $\bar{\mathbf{u}} = [\bar{u}(z, y), 0, 0]^T$ with a single velocity component $\bar{u}(z, y)$ along the x spatial direction. The latter satisfies the Poisson equation that may be solved in series form [211]. Global flow instability in this application is governed by a complex EVP.

Table 3.2 presents convergence history results for the numerical solution of the 2D EVP presented in equation (1.26) using the matrices (1.51) with base flow velocity $\bar{\mathbf{u}} = [\bar{u}(z, y), 0, 0]^T$, using CGL and FD-q16 at a subcritical Reynolds number, $Re = 1000$, and wavenumber parameter $\alpha = \pi$. In addition, Richardson-extrapolation results are also shown. Considering the Richardson extrapolation value of CGL spectral collocation method as converged eigenvalue, 8 decimal digits are converged in ω_r and 9 in ω_i when using CGL methods with $N^2 \geq 60^2$. On the other hand, the same order of convergence is reached when using FD-q16 with $N^2 \geq 90^2$. Figure 3.7 shows the convergence history for the different spatial discretization schemes, using

3.2. Incompressible stability analysis validations

Table 3.2: Convergence history of BiGlobal instability analysis of rectangular duct flow at $A = 1$, $Re = 1000$ and $\alpha = \pi$ comparing the leading eigenmode results using CGL and FD-q16 and the corresponding Richardson extrapolations.

| | N^2 | ω_r | ω_i |
|-----------------|---------|--------------|----------------|
| CGL | 30^2 | 2.9027647730 | -0.10353535398 |
| | 40^2 | 2.9027654432 | -0.10352492808 |
| | 50^2 | 2.9027654495 | -0.10352492616 |
| | 60^2 | 2.9027654518 | -0.10352492608 |
| | 70^2 | 2.9027654528 | -0.10352492609 |
| Richardson Ext. | | 2.9027654541 | -0.10352492635 |
| FD-q16 | 30^2 | 2.9027679758 | -0.10352715467 |
| | 50^2 | 2.9027654409 | -0.10352492446 |
| | 70^2 | 2.9027654496 | -0.10352492422 |
| | 90^2 | 2.9027654520 | -0.10352492512 |
| | 110^2 | 2.9027654529 | -0.10352492555 |
| Richardson Ext. | | 2.9027654541 | -0.10352492637 |

the converged result of Table 3.2, $\omega = 2.9027654541 - i0.10352492635$, as correct value. Different slopes arise due to the discontinuities of the derivatives in the corners of the domain [34]. As expected, the convergence rate for FD-q16 and CGL are better than for the order 8 schemes. However, the higher degree of sparsity in the 8th-order scheme makes FD-q8 the more efficient one in terms of the numerical solution of this problem.

The regularized lid-driven cavity

The two-dimensional lid-driven cavity, three-dimensional (non-zero spanwise wavenumber) BiGlobal instability analysis of which was first performed using singular boundary conditions [3, 248], is solved next, after regularizing

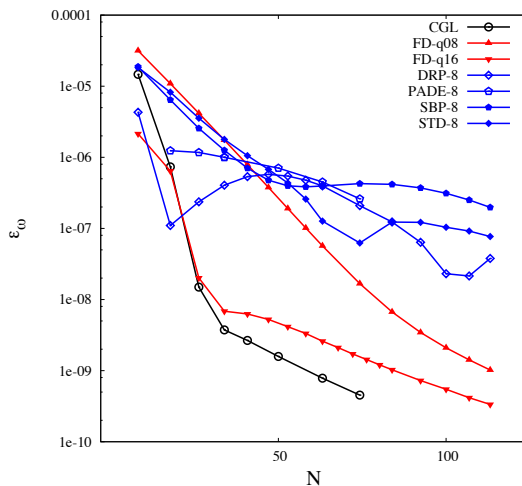


Figure 3.7: Convergence history of the BiGlobal EVP applied to the rectangular duct flow at $Re = 1000$ and $\alpha = \pi$, with $A = 1$ for the eigenvalue $\omega = 2.9027654541 - i0.10352492635$, obtained by (black) spectral collocation using CGL and (blue) high-order finite-difference methods of order 8: STD, Padé, DRP, SBP, as well as (red) FD- q with $q = 8$ and $q = 16$. The number of discretization nodes used is the same in both spatial directions and is denoted by $N + 1$.

the lid motion. Regularization eliminates the corner singularities at the two ends of the moving lid and permits obtaining highly-accurate base flow solutions. Regarding global instability in this problem, the wavenumber vector is normal to the plane on which the base flow develops, and a simple transformation of the linearized Navier-Stokes equations reduces the two-dimensional EVP into one governed by real coefficients [249].

The direction z is taken to be in the direction of the motion of the lid and y to be along the normal to this direction. The base flow is considered independent of the third (spanwise) direction x . Thus, the domain is defined as $\Omega = \{z \in [0, A]\} \times \{y \in [0, 1]\}$, where A is the aspect ratio. The steady base flow vector under these assumptions has two velocity components, $\bar{\mathbf{u}} = [0, \bar{v}(z, y), \bar{w}(z, y)]^T$, and it is obtained by solving the vorticity-transport equation (see [249] for more details). The boundary conditions are $\bar{v} = 0$ on all four walls and $\bar{w} = 0$ in all the walls but the corresponding to the lid where

$$\bar{w} = [1 - (2z - 1)^{16}]^2, \quad z \in [0, 1]. \quad (3.5)$$

In this manner, the discontinuity in the boundary condition at $\bar{w}(z = 0, y = 1)$ and $\bar{w}(z = 1, y = 1)$ of the lid-driven cavity flow [73, 227] is avoided, since

it is a potential source of suboptimal convergence.

Figure 3.8 presents convergence history results using the same suite of 8th-order finite-difference methods used so far, in addition to FD-q16 and CGL. At the conditions at which the EVP in equation (1.26) with the matrices (1.51) is solved, the leading eigenmode is stationary, so comparisons are performed using only the imaginary part of the leading eigenvalue. The converged value used for this result is the average obtained with the Richardson extrapolations of the CGL and FD-q16 results. The same qualitative conclusions reached by application of these discretization methods in the previous problems are reached here too, namely that the FD-q methods are superior in terms of accuracy to all other finite-difference approaches.

It is worth noting in this context that the only previous known work in the literature which compares finite-difference and spectral collocation methods for global instability analysis is the work by Merle et al. [175] who also used the lid-driven cavity as test. The conclusion reached in that work was that the DRP scheme is the best alternative in terms of computational cost to CGL from a combined accuracy and efficiency perspective. This conclusion is superseded by the results of figure 3.8: while the DRP method has the same formal resolution capacity as standard, Padé or SBP finite-differences, and may indeed be more efficient than some of the other methods examined (comparisons in [175] were confined to Padé and DRP), the 8th-order member of the FD-q methods family significantly outperforms all its peers; using $N = 100$ it delivers a relative error of the most unstable eigenmode of $\mathcal{O}(10^{-4})$, as opposed to $\mathcal{O}(10^{-2})$ that all other finite-difference methods deliver. In addition, due to the nature of the method, the sparsity of DRP is smaller than the one of FD-q when the order of the method is the same in both numerical schemes. As in the previously studied problems, increasing the order of the FD-q method utilized delivers results approximating those obtained by the spectral collocation method.

The swept attachment-line boundary-layer flow

Still within a BiGlobal context, the EVP governing instability of the incompressible swept Hiemenz flow is also solved using the proposed spatial discretization methods. Unlike the two previous two-dimensional base flows, here all three base flow velocity components are present and no reductions of the LNSE are possible. Here again a complex EVP needs to be solved. One advantage of this application is that the base flow is obtained by the solution of systems of coupled ordinary differential equations at arbitrarily high precision. In addition, accurate global instability results of this flow are available

3. Linear modal stability validations and numerical efficiency

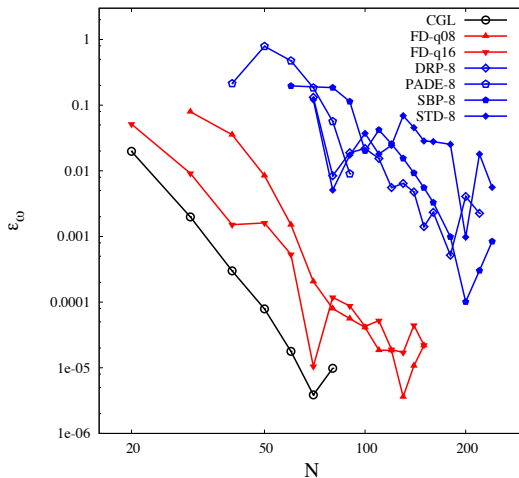


Figure 3.8: Convergence history of the BiGlobal EVP applied to the regularized lid-driven cavity flow at $Re = 1000$ and $\alpha = 15$, with $A = 1$ for the most unstable eigenvalue $\omega = i0.108337$, obtained by (black) spectral collocation using CGL grid and (blue) high-order finite-difference methods of order 8: STD, Padé, DRP, SBP, as well as (red) FD- q with $q = 8$ and $q = 16$. The number of discretization nodes used is the same in both spatial directions and is denoted by $N + 1$.

[153] and have been modeled by simple one-dimensional EVPs in both the orthogonal [253], and the non-orthogonal [191] leading-edge boundary-layer flow, providing highly accurate data to compare against.

The base flow is provided by the swept Hiemenz boundary-layer, which models steady stagnation line flow. The velocity components are independent of the homogeneous direction along the attachment line, x , which is assumed to be infinite, while all three base flow velocity components are taken to depend on the wall-normal direction y . Moreover, the chordwise velocity component $\bar{w}(y, z)$ is taken to be linearly dependent on the chordwise coordinate z , while the wall-normal velocity component $\bar{v}(y)$ and the velocity component $\bar{u}(y)$ along the attachment line are taken to be independent of z [211].

The EVP in equation (1.26) with the matrices (1.51) is solved with this attachment-line boundary-layer base flow using the same set of parameters of Lin and Malik [153]: $Re = 800$ and $\alpha = 0.255$. The transformation used for the wall-normal direction y is the same as the one used for the Blasius boundary-layer problem (2.60) but with $y_\infty = 150$ and $y_h = 4$. In the chordwise coordinate, a linear transformation is used to map the standard

3.2. Incompressible stability analysis validations

Table 3.3: BiGlobal instability analysis of the incompressible attachment-line boundary-layer flow with at $Re = 800$ and $\alpha = 0.255$. The first two most unstable modes, GH and A1 are shown. Comparison with the results presented by Lin and Malik [153]. Note that $c = \omega/\alpha$ refers to phase velocity.

| | N^2 | $c_r(GH)$ | $c_i(GH)(\times 10^2)$ | $c_r(A1)$ | $c_i(A1)(\times 10^2)$ |
|-----------|--------|------------|------------------------|------------|------------------------|
| CGL | 30^2 | 0.35840506 | 0.58473709 | 0.35791126 | 0.41108252 |
| | 40^2 | 0.35841015 | 0.58531622 | 0.35792172 | 0.41104656 |
| | 50^2 | 0.35840978 | 0.58532857 | 0.35792622 | 0.41027206 |
| | 60^2 | 0.35840997 | 0.58531393 | 0.35792318 | 0.40962663 |
| FD-q16 | 30^2 | 0.35842026 | 0.58484758 | 0.35792767 | 0.40974017 |
| | 50^2 | 0.35840951 | 0.58533098 | 0.35791855 | 0.40989817 |
| | 70^2 | 0.35840947 | 0.58529166 | 0.35791927 | 0.40986547 |
| | 90^2 | 0.35840990 | 0.58532679 | 0.35791979 | 0.40988838 |
| FD-q8 | 30^2 | 0.35840088 | 0.58685134 | 0.35790972 | 0.41179370 |
| | 50^2 | 0.35841011 | 0.58540140 | 0.35797511 | 0.40990771 |
| | 70^2 | 0.35840976 | 0.58530175 | 0.35791916 | 0.40989455 |
| | 90^2 | 0.35840991 | 0.58532658 | 0.35791980 | 0.40988576 |
| L&M [153] | | 0.35840982 | 0.58532472 | 0.35791970 | 0.40988667 |

3. Linear modal stability validations and numerical efficiency

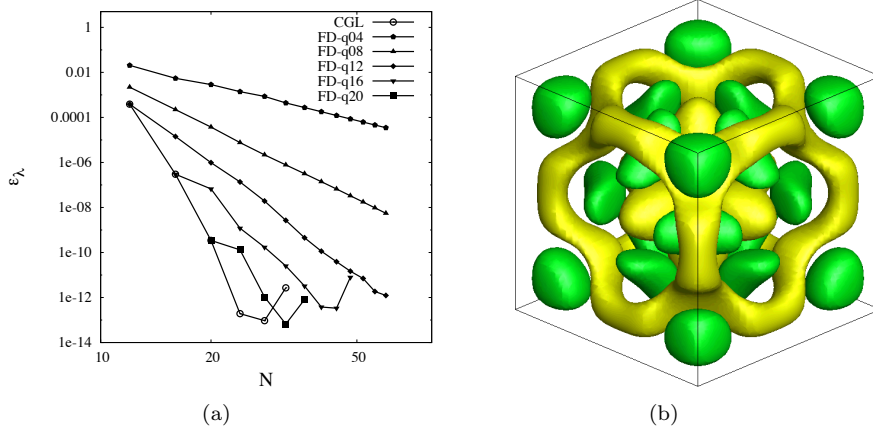


Figure 3.9: (a) Convergence history of the solution of the 3D Helmholtz EVP for the eigenvalue $\lambda^2/(\pi^2/4) = 43$, obtained using CGL and a suite of FD-q methods of orders 4, 8, 12, 16 and 20. The number of discretization nodes used is the same in the three spatial directions and is denoted by $N + 1$. (b) Iso-surfaces of the corresponding eigenfunction obtained using FD-q12 with $N_x \times N_y \times N_z = 60^3$.

CGL or FD-q domain into $z \in [-200, 200]$. Table 3.3 shows comparisons with the converged results of Lin and Malik [153] using CGL, FD-q8 and FD-q16 for the first two most unstable modes. FD-q8 and FD-q16 results show very good agreement with the literature result and even outperform the CGL results of the second eigenvalue using low resolution (e.g. $N_x \times N_y = 50^2$), which is more difficult to be calculated numerically, due to the closeness between both modes.

3.2.4 The 3D Helmholtz EVP

In three spatial dimensions the Helmholtz EVP (3.1) is defined by the following equation:

$$\left(\frac{\partial^2}{\partial x^2} + \frac{\partial^2}{\partial y^2} + \frac{\partial^2}{\partial z^2} \right) \phi + \lambda^2 \phi = 0, \quad (3.6)$$

Such problem is useful in assessing the accuracy of the proposed spatial discretization method, especially in the recovery of the higher eigenvalues/eigenfunctions, $n_x, n_y, n_z \gg 1$. The recovered eigenvalues are compared with the analytical solution of this problem in the domain $\Omega = \{x \in$

$[-1, 1] \times \{y \in [-1, 1]\} \times \{z \in [-1, 1]\}$ [177]. Such solution is the following:

$$\lambda_{n_x, n_y, n_z}^2 = \frac{\pi^2}{4} [n_x^2 + n_y^2 + n_z^2]; \quad n_x, n_y, n_z = 1, 2, 3, \dots \quad (3.7)$$

Figure 3.9(a) shows the convergence history of the eigenvalue $\lambda^2/(\pi^2/4) = 43$. Conclusions analogous to those reached in the two-dimensional Helmholtz EVP and in the previously addressed applications are also drawn here. Special interest is focused on intermediate values of the order of the method, e.g. $q = 12, q = 14$. Single-precision convergence is achieved using approximately two times more discretization points than with spectral collocation methods, and double-precision convergence is achieved with less than four times more nodes than with spectral collocation methods.

For completeness, figure 3.9(b) displays the eigenfunction corresponding to the eigenvalue ($\lambda^2/(\pi^2/4) = 43$), obtained numerically using FD-q12, showing that a non-trivial structure in terms of gradients is obtained. As with its two-dimensional analogous, reliable spatial discretization of the three-dimensional Poisson operator sets the scene for the solution of the TriGlobal EVP.

3.2.5 The TriGlobal EVP

Finally, the TriGlobal linear instability EVP in equation (1.26) formed by the matrices (1.63) is solved, treating all three inhomogeneous spatial dimensions in a coupled manner.

Using the two-dimensional rectangular duct and regularized lid-driven cavity base flows previously calculated, a three-dimensional, spanwise homogeneous base flow is constructed and analyzed by solving the three-dimensional EVP without exploitation of the spanwise periodicity. Furthermore, the instability analysis of the three-dimensional lid-driven cavity flow in absence of homogeneous spatial directions is solved. This is the most stringent test to which the proposed spatial discretization is exposed. In view of the results, only the FD-q method is used for the solution of equation (1.26) formed by the matrices (1.63).

The rectangular duct flow

The rectangular duct flow is analyzed also with TriGlobal analysis at $Re = 1000$, employing FD-q10 in both z and y directions. For the TriGlobal

3. Linear modal stability validations and numerical efficiency

Table 3.4: TriGlobal instability analysis of the rectangular duct flow in the domain $\Omega = \{x \in [-1, 1]\} \times \{y \in [-1, 1]\} \times \{z \in [-1, 1]\}$ at $Re = 1000$ using FD-q10 for z and y direction with $N + 1$ points and Fourier collocation with N_F points in x .

| $N^2 \times N_F$ | ω_r | ω_i | Mem. (MB) | T_{LU} (s) | T_{AR} (s) |
|------------------|------------|--------------|-------------------|------------------|------------------|
| $32^2 \times 12$ | 2.90275822 | -0.103516753 | 4862 [†] | 353 [†] | 0.8 [†] |
| $40^2 \times 12$ | 2.90276481 | -0.103523881 | 2980 | 1006 | 8.8 |
| $48^2 \times 12$ | 2.90276539 | -0.103524652 | 4611 | 1735 | 16.4 |
| $42^2 \times 16$ | 2.90276510 | -0.103524201 | 6253 | 3345 | 19.0 |
| $56^2 \times 12$ | 2.90276545 | -0.103524809 | 6539 | 5247 | 20.6 |

T_{LU} and T_{AR} respectively refer to time spent in the LU decomposition of the matrix and the Arnoldi iteration.

[†] refers to Out-of-Core while rest are In-Core calculations.

analysis, N_F Fourier collocation points are used along the spanwise direction, in order to discretize a spanwise length $L_x = 2\pi/\alpha_{BG}$. The parameter $\alpha_{BG} = \pi$ is chosen to enable direct comparisons of the present TriGlobal with the results obtained by the solution of the BiGlobal analysis in which only (z, y) are discretized in a coupled manner, $\omega = 2.902765454 - i0.1035249264$. Results are presented in Table 3.4, where a very good agreement between BiGlobal and TriGlobal analysis results is observed: the damping rate obtained by BiGlobal analysis using the highest attainable resolution on the used desktop computer, $N_z \times N_y = 70^2$ CGL points and that delivered by the TriGlobal analysis with $N_z \times N_y = 56^2$ FD-q10 points and $N_F = 12$ Fourier collocation points, have a relative difference of $\mathcal{O}(10^{-7})$.

The two-dimensional regularized lid-driven cavity

Here, the two-dimensional regularized lid-driven cavity flow is analyzed with TriGlobal analysis. For the solution of equation (1.26) formed by the matrices (1.63), N_F Fourier collocation points are used along the spanwise direction, in order to discretize a spanwise length $L_x = 2\pi/\alpha_{BG}$, and FD-q10 in both of the z and y directions. The parameters $Re = 1000$ and $\alpha_{BG} = 15$ are chosen in order to directly compare the present TriGlobal results with the converged BiGlobal result shown in figure 3.8, $\omega = i0.108337$. The re-

3.2. Incompressible stability analysis validations

Table 3.5: TriGlobal instability analysis of the regularized lid-driven cavity flow in the domain $\Omega = \{z \in [0, 1]\} \times \{y \in [0, 1]\} \times \{x \in [0, 2\pi/15]\}$ at $Re = 1000$ using FD-q10 for z and y direction with $N + 1$ points and Fourier collocation with N_F points in x .

| $N^2 \times N_F$ | ω_i | Memory (MB) | T_{LU} (s) | T_{AR} (s) |
|------------------|------------|-------------------|------------------|------------------|
| $32^2 \times 12$ | 0.102726 | 4920 [†] | 377 [†] | 0.9 [†] |
| $40^2 \times 12$ | 0.106135 | 3226 | 1447 | 8.8 |
| $48^2 \times 12$ | 0.106903 | 4578 | 1819 | 15.8 |
| $42^2 \times 16$ | 0.106538 | 6061 | 3097 | 16.5 |
| $56^2 \times 12$ | 0.106804 | 6704 | 3947 | 25.4 |

T_{LU} and T_{AR} respectively refer to time spent in the LU decomposition of the matrix and the Arnoldi iteration.

[†] refers to Out-of-Core while rest are In-Core calculations.

sults are presented in Table 3.5, where an acceptable agreement between BiGlobal and TriGlobal analysis results is observed: the damping rate obtained by BiGlobal analysis using $N_z \times N_y = 70^2$ CGL points and the one delivered by TriGlobal analysis with $N_z \times N_y = 56^2$ FD-q10 points and $N_F = 12$ Fourier collocation points show a relative difference of $\mathcal{O}(10^{-3})$. This discrepancy is expected to improve by increasing resolutions.

The three-dimensional regularized lid-driven cavity

The last test to which FD-q methods are subject is the three-dimensional regularized lid-driven cavity flow. The base flow is computed with an in-house developed steady-state high order spectral collocation DNS solver [78]. The already showed substantial efficiency improvement over spectral collocation offered by the FD-q finite-difference discretization method in combination with sparse matrix storage and inversion permits solving the canonical TriGlobal linear modal instability problem in the cubic lid-driven cavity [63, 74] serially, on a workstation having 8GB of memory. While details of the physics of this problem are discussed in the work of Gómez et al. [78], Table 3.6 shows the computing requirements for the reliable solution of this problem, using the matrix-forming approach.

Table 3.6: TriGlobal instability analysis of the regularized cubic lid-driven cavity flow in the domain $\Omega = \{x \in [0, 1]\} \times \{y \in [0, 1]\} \times \{z \in [0, 1]\}$ at $Re = 200$ using matrix formation. FD-q finite-differences of orders q and N number of points in each of the three spatial directions are used. The leading eigenvalue is shown in terms of damping rate ω_r and frequency ω_i .

| N^3 | q | ω_r | ω_i | Memory (MB) | T_{LU} (s) | T_{AR} (s) |
|--------|-----|------------|------------|-------------------|-------------------|-------------------|
| 20^3 | 4 | 0.41796 | 0.15894 | 665 | 17 | 0.1 |
| 26^3 | 4 | 0.41475 | 0.13689 | 2172 | 84 | 0.4 |
| 32^3 | 4 | 0.41601 | 0.13405 | 5904 | 332 | 1.1 |
| 38^3 | 4 | 0.41585 | 0.13278 | 3742 [†] | 1126 [†] | 12.4 [†] |
| 20^3 | 6 | 0.41262 | 0.13152 | 1224 | 67 | 0.2 |
| 26^3 | 6 | 0.41606 | 0.13191 | 4296 | 265 | 0.7 |
| 32^3 | 6 | 0.41601 | 0.13191 | 4217 [†] | 1214 [†] | 10.7 [†] |
| 20^3 | 8 | 0.41711 | 0.13223 | 1926 | 142 | 0.3 |
| 26^3 | 8 | 0.41650 | 0.13187 | 6666 | 677 | 1.1 |

T_{LU} and T_{AR} respectively refer to time spent in the LU decomposition of the matrix and the Arnoldi iteration.

[†] refers to Out-of-Core while rest are In-Core calculations.

3.3 Compressible stability analysis validations

3.3.1 The Local EVP

The stability analysis of the zero-pressure-gradient boundary-layer flow at hypersonic regime ($M = 6$) is solved under the parallel flow assumption using local theory. The parameters selected in this computation are $Re = 1000$, $\alpha = 0.8$ and $\psi = \tan^{-1}(\beta/\alpha) = 45$ deg.

The solution of the generalized EVP (1.26) applied to this problem is observed in figure 3.11, where the eigenvalues are plotted using $N = 129$ discretization points using FD-q16 (right triangles) and FD-q24 (left triangles). The mapping applied to the spatial scheme (2.60) uses the same parameters for both discretizations, $\eta_h = 20$ and $\eta_\infty = 150$. The boundary conditions are Dirichlet for the three components of velocity and temperature at the wall and far field. The pressure/density component does not need boundary conditions. The purpose of setting two spatial discretization is the identification of spurious and converged modes. Two modes are identified in figure 3.11, being A the leading mode, which corresponds to the first Mack mode [161], and B an arbitrary acoustic mode. The eigenvalues of this modes are exposed in Table 3.7. Well agreement is observed against the literature predictions for the leading mode. The eigenvectors of both modes are showed in figure 3.10 versus the wall normal direction. The nature of the compressible modes become clear by inspection of the first Mack mode eigenfunction (figures 3.10(a), 3.10(b), 3.10(c) and 3.10(d)). As the Mach number increases, sharp gradients develop both in the near-wall region and the neighborhood of the critical layer, the latter moving well into the free-stream. The acoustic modes (figures 3.10(e), 3.10(f), 3.10(g) and 3.10(h)) develops wave-like behavior at high wall-normal coordinate values, i.e. at the free-stream region.

After the modal analysis, attention is paid to the non-modal lineal results. For that, the matrix discretizing the operator \mathcal{C} of equation (1.13), $\mathbf{C} = \mathbf{B}^{-1}\mathbf{A}$, is formed in a straightforward manner thanks to the non-singularity of matrix \mathbf{B} , unlike in the incompressible case. The pseudospectrum of this matrix is showed in figure 3.11. Also, the results for two spatial discretization, FD-q16 (dashed lines) and FD-q24 (solid lines), are showed. The pseudospectrum isoline $\epsilon = 10^{-4}$ cross the unstable border on closely to the leading mode. Figure 3.12 shows the evolution of the norm of the discretization of the propagator operator, $\|\mathbf{e}^{\mathbf{C}t}\|$. After a transient growth at short times (3.12(b)), reaching a value around $\|\mathbf{e}^{\mathbf{C}t}\| \approx 150$ at $t = 10$, an exponential behavior is exhibited for larger times. The exponential slope of

3. Linear modal stability validations and numerical efficiency

Table 3.7: Local modal analysis results of compressible flat-plate boundary-layer at $M = 6$, $Re = 1000$, $\alpha = 0.8$ and $\beta = 0.8$ using FDq-24 with $N + 1 = 129$ discretization points. The two modes shown are identified with A and B in Figure 3.11. The leading mode (mode A) is compared with the result of Theofilis and Colonius [251].

| Mode | ω_r | ω_i |
|-----------|-------------|-------------|
| A | 0.072489745 | 0.001054002 |
| T&C [251] | 0.072487839 | 0.001052149 |
| B | 0.050920988 | 0.000023752 |

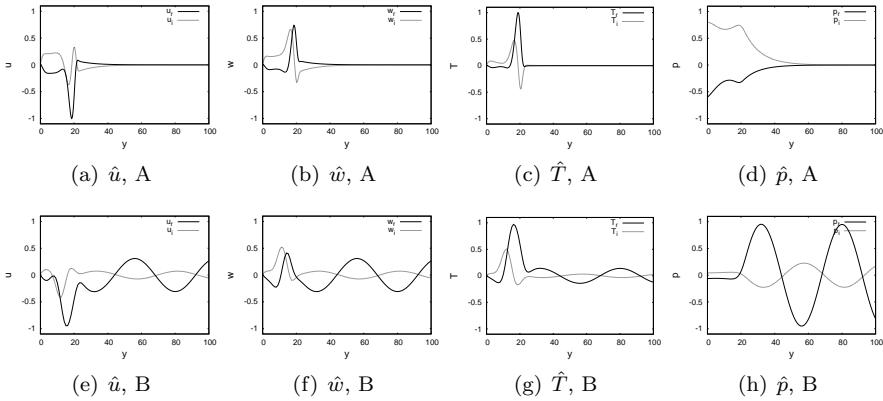


Figure 3.10: Components of the first Mack mode (A) and an arbitrary acoustic mode (B) eigenvectors of compressible flat-plate boundary-layer flow at $M = 6$, $Re = 1000$, $\alpha = 0.8$ and $\beta = 0.8$.

this region, 0.00105035, matches the leading mode growth rate.

Same calculation is showed in figure 3.13 at same parameters but decreasing the Reynolds number up to $Re = 100$, for which all the modes are stable. In this case, the maximum transient growth $\|e^{Ct}\| \approx 150$ is reached at $t \approx 750$, and following this time, an oscillatory decreasing of the norm is observed.

3.3.2 The BiGlobal EVP

The stability analysis of the compressible orthogonal swept leading-edge flow at $M = 0.9$ and $Re = 800$ is solved using temporal BiGlobal analysis theory.

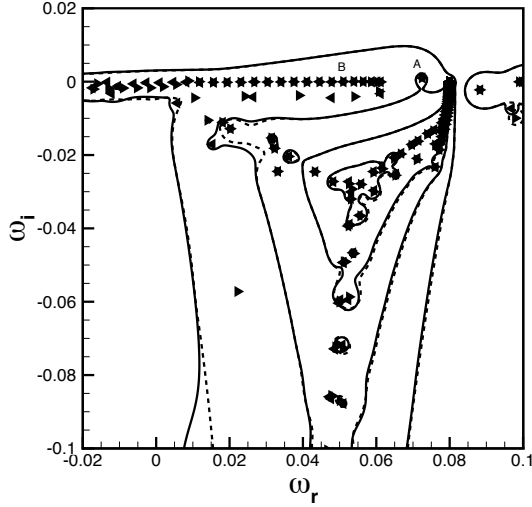


Figure 3.11: Spectrum and pseudospectrum of matrix \mathbf{C} for flat-plate boundary-layer flow at $Ma = 6$, $Re = 1000$, $\alpha = 0.8$ and $\beta = 0.8$. Two different discretizations, FD-q16 (right triangles and dashed lines) and FDq-24 (left triangles and solid lines), both with $N = 129$ discretization points, are used for identifying non-spurious modes. The mode identified with A is the leading mode and the mode B is an acoustic mode. Levels from inner to outer isoline, 10^{-7} , 10^{-6} , 10^{-5} , 10^{-4} .

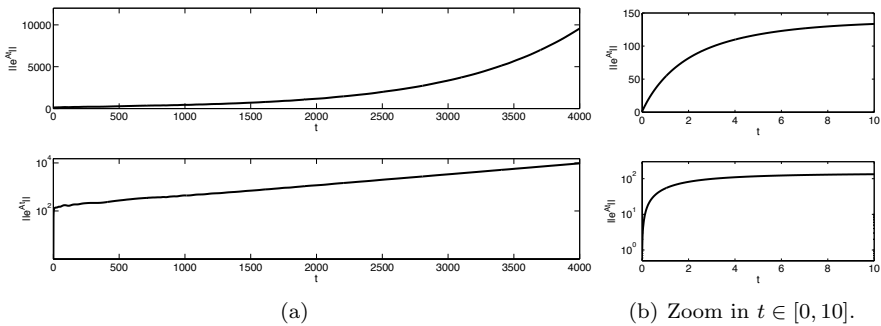


Figure 3.12: Evolution of the norm of the propagator operator, $\|e^{\mathbf{C}t}\|$ for flat-plate boundary-layer flow at $Ma = 6$, $Re = 1000$, $\alpha = 0.8$ and $\beta = 0.8$ using FD-q24 with $N = 129$ discretization points.

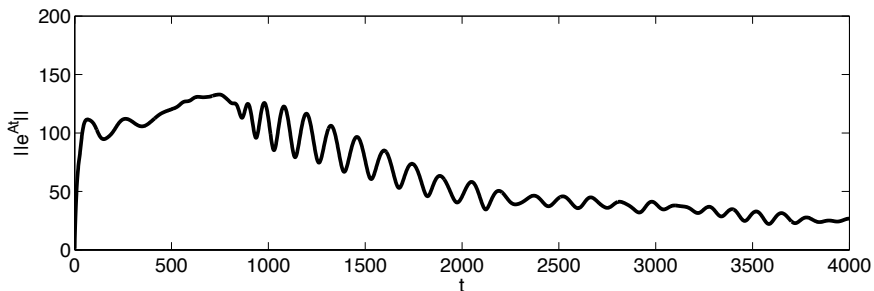


Figure 3.13: Evolution of the norm of the propagator operator, $\|e^{Ct}\|$ for flat-plate boundary-layer flow at $Ma = 6$, $Re = 100$, $\alpha = 0.8$ and $\beta = 0.8$ using FD-q24 with $N = 129$ discretization points.

The base flow analyzed here is the same used in [72, 255].

The boundary conditions used for the temporal BiGlobal EVP (1.26) are no-slip on the perturbation velocities at the wall, alongside with homogeneous Dirichlet condition for temperature and at the far-field, a fast decay in the wall-normal direction is assumed for all disturbances, permitting the imposition of homogeneous Dirichlet conditions at large distance from the wall, $y_\infty = 100$. At a large distance from the attachment-line, along the z -direction, $z = \pm L_z$ (setting $L_z = 100$ as in [72]), the homogeneous condition $\mathcal{D}_{zz}^2(\hat{u}, \hat{v}, \hat{w}, \hat{T}) = 0$ is used, which is equivalent to a linear extrapolation from the interior of the computational domain.

Table 3.8 shows the convergence history of the two most amplified modes, the GH (Görtler-Hammerling or first symmetric mode) and the A1 (first antisymmetric mode), compared with the results of Gennaro et al. [72]. The non-uniform high-order finite-difference scheme FD-q8 of eighth order [103] is used for discretization of both spatial direction. The wavenumber, taken from [72] for comparison purpose, is $\alpha = 0.19$. It is very surprising that a similar level of accuracy is recovered by CGL, FD-q16 and even for FD-q8 with the same number of discretization points $N_y = N_z = 60$. The absolute error achieved for the leading mode, i.e. the GH mode, is $\mathcal{O}(10^{-8})$. The A1 mode also is recovered by FD-q16 and FD-q8 with the same absolute error for approximately same number of discretization points. Figures 3.14 and 3.15 show the real and imaginary part of the eigenvectors \hat{u} and \hat{w} for the GH and A1 modes respectively.

3.3. Compressible stability analysis validations

Table 3.8: BiGlobal instability analysis of the compressible attachment-line boundary layer flow with at $Re = 800$, $M = 0.9$ and $\alpha = 0.19$. The first two most unstable modes, GH and A1 are shown. Comparison with the results presented by Gennaro et al. [72], where the authors used $N_z = 140$ STD nodes of sixth order and $N_y = 140$ CGL nodes. Note that $N = N_y = N_z$.

| | N^2 | $\omega_r(GH)$ | $\omega_i(GH)$ | $\omega_r(A1)$ | $\omega_i(A1)$ |
|--------|--------|----------------|----------------|----------------|----------------|
| CGL | 30^2 | 0.076470803 | 0.001189096 | 0.076325574 | 0.000576254 |
| | 40^2 | 0.076472284 | 0.001187837 | 0.076329702 | 0.000575014 |
| | 50^2 | 0.076472281 | 0.001187836 | 0.076329243 | 0.000574900 |
| | 60^2 | 0.076472275 | 0.001187834 | 0.076329278 | 0.000574939 |
| FD-q16 | 50^2 | 0.076472269 | 0.001187838 | 0.076329292 | 0.000574931 |
| | 60^2 | 0.076472275 | 0.001187831 | 0.076329285 | 0.000574934 |
| | 70^2 | 0.076472274 | 0.001187833 | 0.076329282 | 0.000574932 |
| | 80^2 | 0.076472274 | 0.001187837 | 0.076329282 | 0.000574936 |
| FD-q8 | 50^2 | 0.076472282 | 0.001187879 | 0.076329313 | 0.000574981 |
| | 60^2 | 0.076472276 | 0.001187858 | 0.076329293 | 0.000574943 |
| | 70^2 | 0.076472272 | 0.001187841 | 0.076329285 | 0.000574938 |
| | 80^2 | 0.076472275 | 0.001187839 | 0.076329287 | 0.000574936 |
| G [72] | | 0.07647184 | 0.00118942 | 0.07632667 | 0.00057823 |

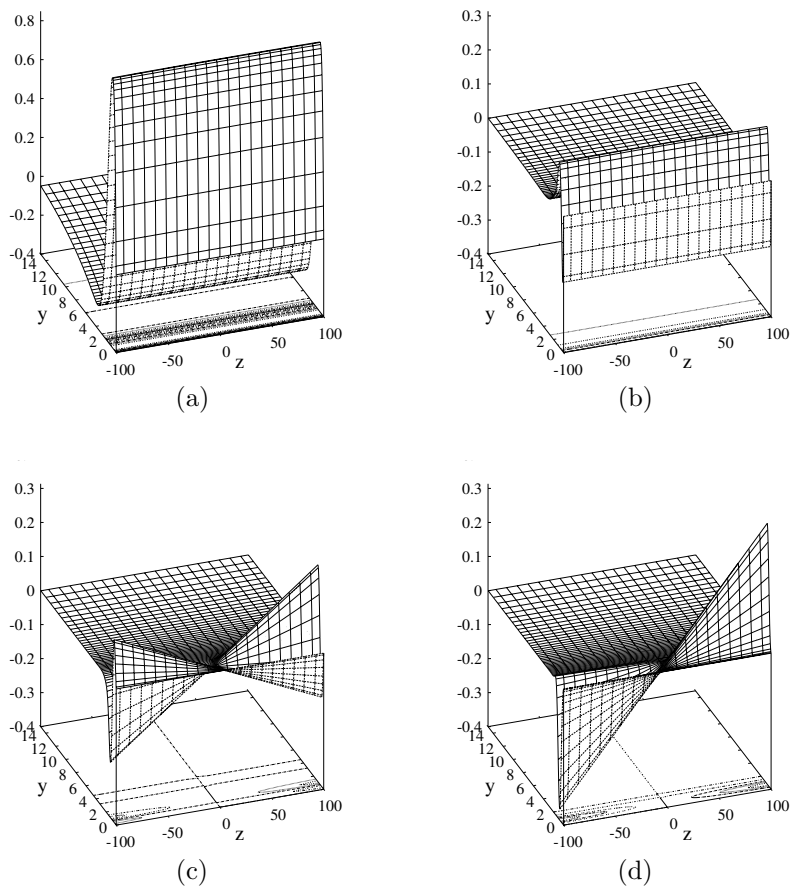


Figure 3.14: Eigenfunctions at $M = 0.9$, $Re = 800$ and $\alpha = 0.19$ corresponding to the mode GH ((a) $Re(\hat{u})$, (b) $Im(\hat{u})$, (c) $Re(\hat{w})$ and (d) $Im(\hat{w})$).

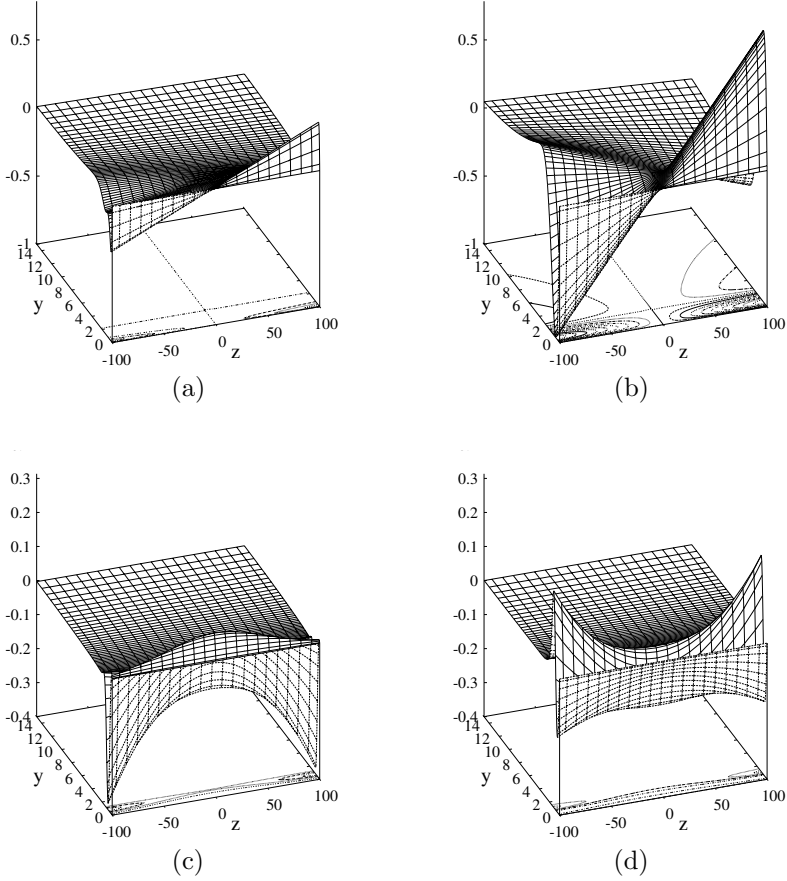


Figure 3.15: Eigenfunctions at $M = 0.9$, $Re = 800$ and $\alpha = 0.19$ corresponding to the mode A1 ((a) $Re(\hat{u})$, (b) $Im(\hat{u})$, (c) $Re(\hat{w})$ and (d) $Im(\hat{w})$).

3.4 The efficiency advantages of using FD-q

Once the accuracy of FD-q method has been established, attention may be turned to the efficiency advantage that they offer over spectral collocation methods. The solution algorithm is based on subspace iteration in which the spatial discretization matrix is formed, stored and LU-decomposed using sparse linear algebra routines and, therefore, the sparsity pattern is the key parameter for the success of the overall algorithm. Only the FD-q spatial discretization has been monitored in terms of the memory and CPU time requirements for the serial solution of the incompressible BiGlobal EVP, on account of the superior accuracy properties of this over other finite-difference methods of the same formal order (and sparsity pattern). A visual indication of the savings expected by using a given FD-q method over the CGL spatial discretization is offered by the sparsity patterns resulting from spatial discretization of the left-hand-side BiGlobal matrix \mathcal{A} of equation (1.26) for incompressible flows, respectively shown in figure 3.16(a) for CGL and figure 3.16(b) for FD-q4, both plotted using $N = 20$. The key parameter when a sparse solver is used is the number of non-zero elements (NNZ). In most of the differential operators, this parameter is reduced by a factor of $\mathcal{O}(q + 1/N + 1)$, with q the order of the used finite-difference scheme (i.e. $q + 1$ is the stencil of the scheme) and $N + 1$, the number of points used to discretize the problem in each spatial direction for all the differentiation matrices. For the more stringent case of compressible BiGlobal instability analyses, or when non-orthogonal curvilinear mappings are used to discretize the problem, cross-derivatives are present in the differential operators. In this case, NNZ is reduced by a factor of $\mathcal{O}((q + 1/N + 1)^2)$.

The computational requirements of the overall numerical solution of the EVP are imposed by those of the LU-decomposition of the sparse matrix. The required memory and elapsed time for this factorization cannot be predicted *a priori* and the ratio $(q + 1/N + 1)$, elevated to a power to be determined later, is used next to relate the required memory and elapsed time of the LU-decomposition of FD-q with those of CGL spatial discretization. The flow instability problem chosen to study computational requirements is one in which all velocity components and their derivatives need to be discretized: the attachment-line boundary-layer flow problem. Spatial discretization methods used are the CGL discretization working in dense (results taken from [72]) and comparing them with the respective results corresponding to sparse CGL, FD-q8, FD-q16 and FD-q24 spatial discretizations.

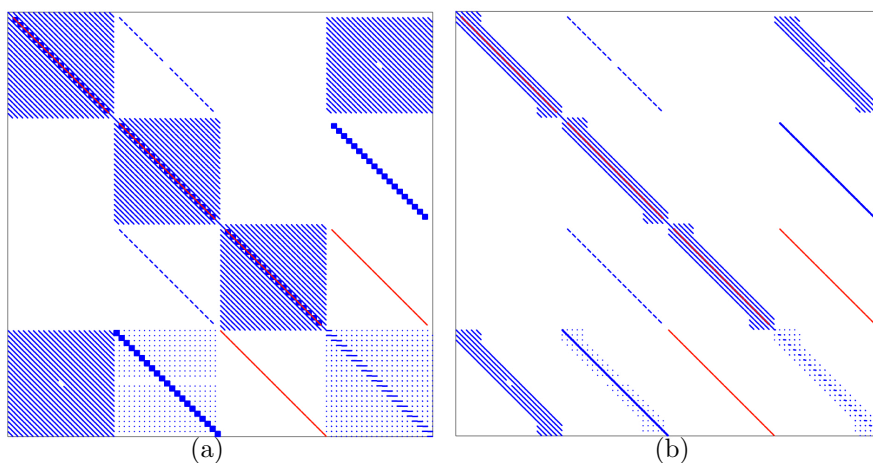


Figure 3.16: Sparsity pattern of the left-hand-side BiGlobal operator matrix with $N + 1 = 21$ discretization points per spatial direction using (a) CGL and (b) FD- $q4$ in the attachment line boundary-layer problem. (blue) Real part and (red) imaginary part of the non-zero elements.

3.4.1 Incompressible regime operators

Focusing firstly on the incompressible regime and setting $N = N_z = N_y$, the leading dimension of the matrix operator is $M = 4(N + 1)^2$.

Table 3.9 shows the required memory for the LU decomposition of the BiGlobal EVP matrix using dense and sparse routines in conjunction with CGL discretization, as well as three members of the FD- q family and sparse linear algebra. The quantity of required memory when working in sparse is significantly reduced respect to the quantity of required memory working in dense, which is theoretically $\text{Mem} \approx \mathcal{O}(M^2) \approx \mathcal{O}(N^4)$. The memory requirements of the FD- $q8$ method are found to be smaller by one order of magnitude compared with those of the CGL method. In order to obtain a relation between the respective quantities the formula

$$\text{Mem}_{\text{FD-}q} = \left(\frac{q + 1}{N + 1} \right)^a \times \text{Mem}_{\text{CGL}}, \quad (3.8)$$

is assumed and used to identify (fit) the constant exponent a using the results of Table 3.9, plotted in figure 3.17(a). Independently both the CGL and the FD- q results are taken to follow a curve $\text{Mem} \propto (N + 1)^\alpha$. This exponent is $\alpha_{\text{CGL}} = 4.1$ for the sparse CGL method, which is very close to the theoretical exponent of 4 for dense computations, while the values 2.7,

3. Linear modal stability validations and numerical efficiency

Table 3.9: Memory requirements for the LU decomposition (MB) in the attachment line boundary layer problem, using different resolutions and working with dense algebra for CGL and sparse algebra for CGL, FD-q24, FD-q16 and FD-q8. Note that $N = N_x = N_y$.

| N | CGL _{dense} | CGL _{sparse} | FD-q24 | FD-q16 | FD-q8 |
|----|----------------------|-----------------------|--------|--------|-------|
| 40 | 760 | 584 | 444 | 246 | 107 |
| 50 | 1747 | 1350 | 705 | 457 | 179 |
| 60 | 3494 | 3078 | 1217 | 775 | 284 |
| 70 | 6230 | 5544 | 1889 | 1174 | 436 |

2.8 and 2.6 have been identified for FD-q24, FD-q16 and FD-q8, respectively. Using the average between the three FD-q cases, $\alpha_{\text{FD-q}} = 2.7$, the constant exponent of equation (3.8) is approximated by $a = \alpha_{\text{CGL}} - \alpha_{\text{FD-q}} = 1.4$. Figure 3.17(b) shows the collapse of all FD-q curves using equation (3.8) and these constant values. The required memory for FD-q scales as $\text{Mem}_{\text{FD-q}} \approx \mathcal{O}(N^{2.7}) \approx \mathcal{O}(M^{1.3})$, which outperforms computations using CGL, the latter scaling as $\text{Mem}_{\text{CGL}} \approx \mathcal{O}(M^2)$.

Turning to the elapsed time for serial LU factorization of the matrix pertinent to the same global stability EVP, results in Table 3.10 are presented for the same methods. The theoretical prediction of $\mathcal{O}(M^3) \approx \mathcal{O}(N^6)$ is verified by the CGL either sparse or dense results. The most striking result of this table is the order(s) of magnitude decrease of CPU time that the FD-q method offers, when compared with either of the CGL sparse or dense solution.

In order to quantify the relation between the elapsed times required by the CGL and the FD-q methods, the formula

$$\text{Time}_{\text{FD-q}} = \left(\frac{q+1}{N+1} \right)^b \times \text{Time}_{\text{CGL}}, \quad (3.9)$$

is assumed and used to fit the constant exponent b . Figure 3.18(a) shows the results of Table 3.10. As in the case of memory requirements, either method is taken to follow a curve $\text{Time} \propto (N+1)^\beta$. For the CGL method the exponent extracted from the results is $\beta_{\text{CGL}} = 6.0$, which is exactly the theoretical exponent for dense calculations, while the exponent values of 3.8, 3.7 and

3.4. The efficiency advantages of using FD-q

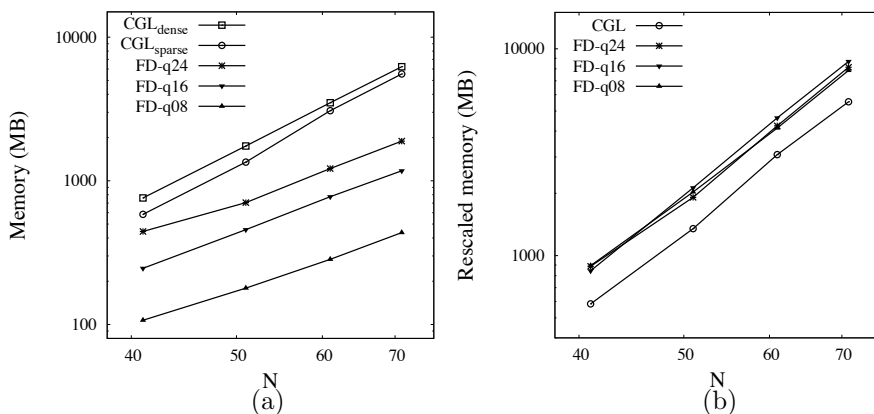


Figure 3.17: (a) Required memory and (b) rescaled memory for LU-factorization of incompressible BiGlobal EVP using the equation (3.8) versus number of discretization points per direction, $N + 1$.

3.1 have been obtained for FD-q24, FD-q16 and FD-q8, respectively. Again, using the average value of the three FD-q cases, $\beta_{\text{FD-q}} = 3.5$, the constant exponent of equation (3.9) is approximated by $b = \beta_{\text{CGL}} - \beta_{\text{FD-q}} = 2.5$. Figure 3.18(b) shows the collapse of the FD-q CPU-time curves onto a single FD-q curve, which has the same slope as that obtained using CGL discretization, when equation (3.9) is used with this parameter value. Therefore, the CPU time for FD-q scales as $\text{Time}_{\text{FD-q}} \approx \mathcal{O}(N^{3.5}) \approx \mathcal{O}(M^{1.7})$, instead of $\text{Time}_{\text{CGL}} \approx \mathcal{O}(M^3)$ for CGL.

The reductions in computational effort by the sparse solution of the BiGlobal EVP in which the matrix is formed using the FD-q methods are made palpable by recalling the largest such solution to-date, namely the massively parallel computations of Kitsios et al. [129], Rodríguez and Theofilis [209]. The latter work was performed on the JUGENE supercomputing facility¹, on which 2048 processors were used in order to distribute the 1 TB large matrix resulting from the CGL spectral collocation discretization of the incompressible operator on a $N_z \times N_y = 250^2$ grid, employing the parallel dense linear algebra library ScaLAPACK [26], with an elapsed time of ≈ 10.5 hours of wall-clock time (≈ 22000 total hours of CPU time). Using the BiGlobal results of figure 3.8 as a guidance, and employing the relation $N_{\text{CGL}} \approx 2 N_{\text{FD-q8}}$ at which the CGL and the FD-q8 spatial discretizations both reach a relative error of $\varepsilon_\omega \approx 10^{-5}$ in the leading eigenmode, the results of Kitsios et al. [129], Rodríguez and Theofilis [209] could be obtained by

¹http://www.fz-juelich.de/ias/jsc/EN/Home/home_node.html

3. Linear modal stability validations and numerical efficiency

Table 3.10: Elapsed time for the LU decomposition (s) in the attachment line boundary layer flow problem, using different resolutions and working with dense algebra for CGL and sparse algebra for CGL, FD-q24, FD-q16 and FD-q8.

| N | CGL _{dense} | CGL _{sparse} | FD-q24 | FD-q16 | FD-q8 |
|----|----------------------|-----------------------|--------|--------|-------|
| 40 | 152.7 | 34.7 | 18.0 | 7.6 | 2.0 |
| 50 | 553.9 | 97.0 | 33.1 | 16.8 | 3.6 |
| 60 | 1603.4 | 292.0 | 80.2 | 35.2 | 6.3 |
| 70 | 4665.8 | 516.3 | 136.8 | 57.3 | 10.8 |

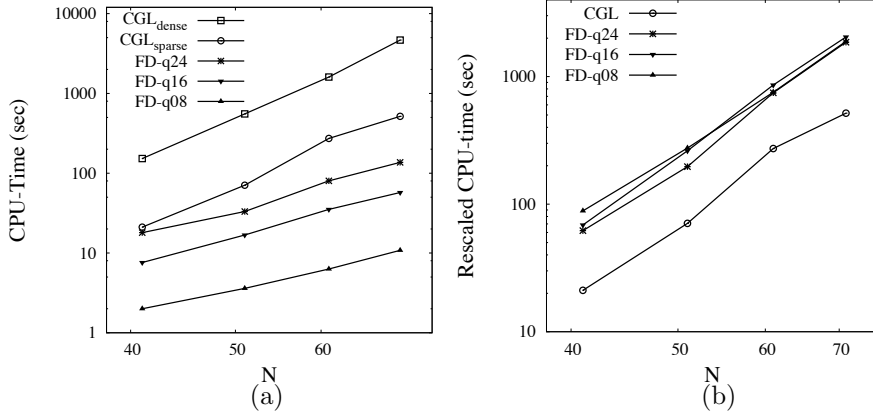


Figure 3.18: (a) Elapsed time and (b) rescaled CPU-time for LU-factorization of incompressible BiGlobal EVP using the equation (3.9) versus number of discretization points per direction, $N + 1$.

employing $N_z \times N_y = 500^2$ FD- $q8$ points. The memory estimation provided by the sparse direct solver MUMPS on a serial desktop is 28 GB for *in-core* and 3.2 GB for *out-of-core* calculations. The estimation of the respective elapsed time is calculated by extrapolating the results of Table 3.10 for CGL sparse results to $N = 500$ with the previously calculated slope $\beta_{\text{CGL}} = 6.0$, resulting $\text{Time}_{\text{CGL}} \approx 18000$ CPU hours, and then using equation (3.9) to obtain the estimation of $\text{Time}_{\text{FD-}q8} \approx 46$ CPU minutes.

In order to complete the cost estimations, the relation $N_{\text{CGL}} \approx 4 N_{\text{FD-}q8}$, observed in the results of figure 3.6(a) at which the CGL and the FD- $q8$ spatial discretizations both reach a relative error of $\varepsilon_\lambda \approx 10^{-9}$ in the leading eigenmode, is adopted. Now, using $N_{\text{FD-}q8} = 1000$, the memory estimation provided by MUMPS is 137 GB for *in-core* and 13.3 GB for *out-of-core* calculations. For the time estimation, following the same procedure, the result of $\text{Time}_{\text{FD-}q8} \approx 9$ CPU hours is obtained. While these estimates are one order of magnitude larger than those corresponding to $N_z \times N_y = 500^2$ FD- $q8$ collocation nodes, the FD- q methods still offer an interesting alternative to the commonly employed spectral collocation methods for this class of stability problems.

3.4.2 Compressible regime operators

Secondly, the same efficiency test is performed in the compressible regime. Setting $N = N_z = N_y$, the resulting leading dimension of the matrix operators is $M = 4(N + 1)^2$.

A visual indication of the savings expected by using a given FD- q method over the CGL spatial discretization is offered by the sparsity patterns resulting from spatial discretization of the left-hand-side BiGlobal matrix \mathbf{A} of equation (1.26), respectively shown in figure 3.19(a) for CGL and figure 3.19(b) for FD- $q4$, both plotted using $N = 20$. Within the compressible BiGlobal instability analyses, or when non-orthogonal curvilinear mappings are used to discretize the problem, cross-derivatives are present in the differential operators. In this case, NNZ is reduced by a factor of $\mathcal{O}((q + 1)/(N + 1))^2$.

Table 3.11 shows the required memory for the LU decomposition of the BiGlobal EVP matrix using dense and sparse routines in conjunction with CGL discretization, as well as three members of the FD- q family and sparse linear algebra. The quantity of required memory when working in sparse is significantly reduced respect to the quantity of required memory working in dense, which is theoretically $\text{Mem} \approx \mathcal{O}(M^2) \approx \mathcal{O}(N^4)$. The memory

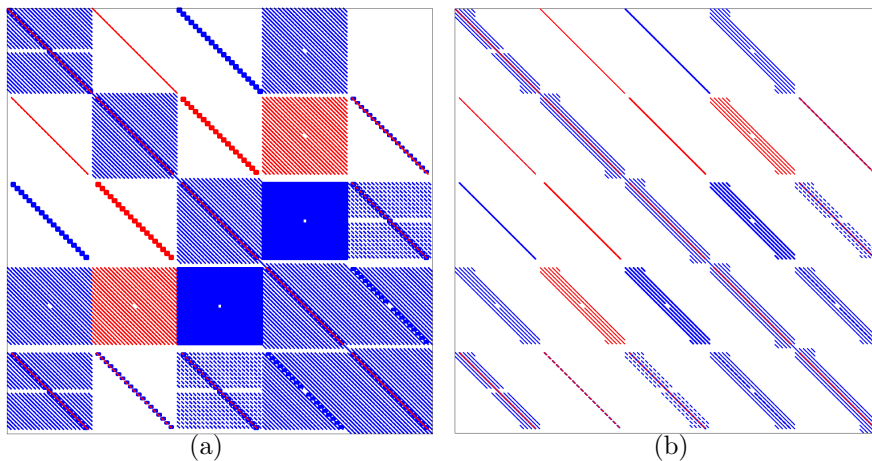


Figure 3.19: Sparsity pattern of the left-hand-side compressible BiGlobal operator matrix with $N + 1 = 21$ discretization points per spatial direction using (a) CGL and (b) FD-q4 in the attachment line boundary-layer problem. (blue) Real part and (red) imaginary part of the non-zero elements.

requirements of the FD-q8 method are found to be smaller by one order of magnitude compared with those of the CGL method. In order to obtain a relation between the respective quantities, the formula (3.8) is used again to identify (fit) the constant exponent a using the results of Table 3.9, plotted in figure 3.20(a). Independently both the CGL and the FD-q results are taken to follow a curve $\text{Mem} \propto (N + 1)^\alpha$. This exponent is $\alpha_{\text{CGL}} = 3.83$ for the sparse CGL method, which is very close to the theoretical exponent of 4 for dense computations, while the values 2.74 and 2.63 have been identified for FD-q16 and FD-q8, respectively. Using the average between the three FD-q cases, $\alpha_{\text{FD-q}} = 2.69$, the constant exponent of equation (3.8) is approximated by $a = \alpha_{\text{CGL}} - \alpha_{\text{FD-q}} = 1.15$. Figure 3.20(b) shows the collapse of all FD-q curves using equation (3.8) and these constant values. The required memory for FD-q scales as $\text{Mem}_{\text{FD-q}} \approx \mathcal{O}(N^{2.7}) \approx \mathcal{O}(M^{1.3})$, which outperforms computations using CGL, the latter scaling as $\text{Mem}_{\text{CGL}} \approx \mathcal{O}(M^{1.9})$.

Turning to the elapsed time for serial LU factorization of the matrix pertinent to the same global stability EVP, results in Table 3.12 are presented for the same methods. The most striking result of this table is the order(s) of magnitude decrease of CPU time that the FD-q method offers, when compared with either of the CGL sparse or dense solution.

In order to quantify the relation between the elapsed times required by

Table 3.11: Memory requirements for the LU decomposition (MB) in the compressible attachment line boundary layer problem, using different resolutions for CGL, $FD-q16$ and $FD-q8$. Note that $N = N_y = N_z$ and * refers to extrapolated values.

| N | CGL | $FD-q16$ | $FD-q8$ |
|----|--------|----------|---------|
| 40 | 1561 | 462 | 202 |
| 50 | 3686 | 887 | 354 |
| 60 | 7141 | 1432 | 578 |
| 70 | 12888* | 2125 | 864 |
| 80 | 21351* | 3010 | 1195 |

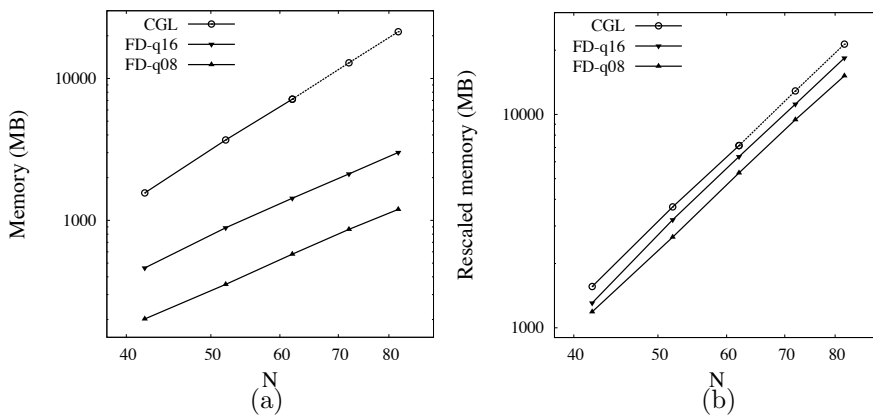


Figure 3.20: (a) Required memory and (b) rescaled memory for LU-factorization of incompressible BiGlobal EVP using the equation (3.8) versus number of discretization points per direction, $N + 1$.

3. Linear modal stability validations and numerical efficiency

Table 3.12: Elapsed time for the LU decomposition (s) in the attachment line boundary layer flow problem, using different resolutions for CGL, FD-q24, FD-q16 and FD-q8. Note that $N = N_y = N_z$ and * refers to extrapolated values.

| N | CGL | FD-q16 | FD-q8 |
|----|-------|--------|-------|
| 40 | 84 | 22 | 5.6 |
| 50 | 285 | 40 | 10 |
| 60 | 840 | 95 | 18 |
| 70 | 1990* | 162 | 30 |
| 80 | 4267* | 250 | 47 |

the CGL and the FD-q methods, the formula (3.9) is used again to fit the constant exponent b . Figure 3.21(a) shows the results of Table 3.12. As in the case of memory requirements, either method is taken to follow a curve $\text{Time} \propto (N + 1)^\beta$. For the CGL method the exponent extracted from the results is $\beta_{\text{CGL}} = 5.79$, which is nearly the theoretical exponent for dense calculations, $\text{Time} \approx \mathcal{O}(M^3) = \mathcal{O}(N^6)$, while the exponent values of 3.69 and 3.29 have been obtained for FD-q16 and FD-q8, respectively. Again, using the average value of the three FD-q cases, $\beta_{\text{FD-q}} = 3.49$, the constant exponent of equation (3.9) is approximated by $b = \beta_{\text{CGL}} - \beta_{\text{FD-q}} = 2.30$. Figure 3.21(b) shows the collapse of the FD-q CPU-time curves onto a single FD-q curve, which has the same slope as that obtained using CGL discretization, when equation (3.9) is used with this parameter value. Therefore, the CPU time for FD-q scales as $\text{Time}_{\text{FD-q}} \approx \mathcal{O}(N^{3.5}) \approx \mathcal{O}(M^{1.7})$, instead of $\text{Time}_{\text{CGL}} \approx \mathcal{O}(M^{2.9})$ for CGL.

Regarding the accuracy conclusions of Table 3.8, using FD-q8 at similar accuracy for $N^2 = 60$ one order of memory reduction (see Table 3.11) and a speed up factor of $\text{Time}_{\text{CGL}}/\text{Time}_{\text{FD-q8}} \approx 50$ (see Table 3.12) result. In more complex problems, where the number of discretization points is much larger, several orders of magnitude of CPU requirement savings would be expected as shown in the incompressible limit.

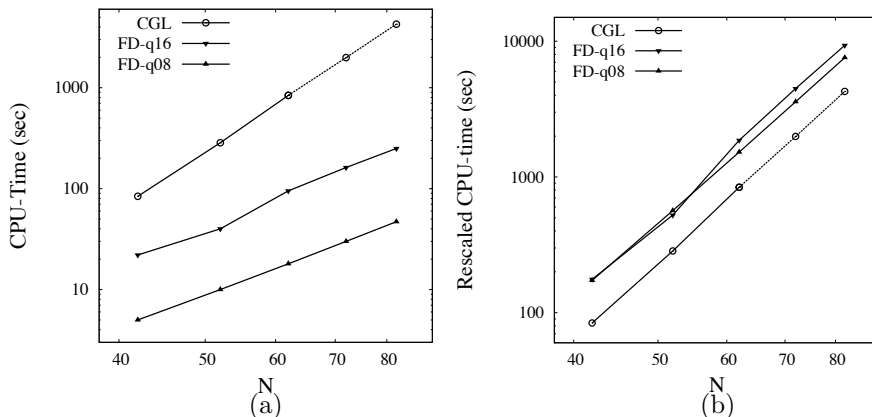


Figure 3.21: (a) Elapsed time and (b) rescaled CPU-time for LU-factorization of incompressible BiGlobal EVP using the equation (3.9) versus number of discretization points per direction, $N + 1$.

3.5 Summary and conclusions

The prime consideration in performing numerical solutions of the linear flow instability EVPs is accuracy. Following the influential work of Orszag [185], spectral spatial discretization has historically been the method of choice for spatial discretization of the linear local stability analysis operator, a tendency which to a large extent continues presently in the context of global linear flow instability analysis. The present contribution has presented a comparison of a suite of high-order finite-difference spatial discretizations of the linear stability operator in regular Cartesian two- and three-dimensional domains and compared the respective results against those delivered by standard multi-dimensional spectral collocation discretization of the same spatial operators. The FD- q method [103] has been found to outperform all its peers at any given formal order of accuracy, and tend toward the spectral results in the limit of the bandwidth of the differentiation matrix being equal with the leading matrix dimension, $q \rightarrow N$. Exploiting the sparsity at $q \ll N$, accurate results have been delivered at orders of magnitude less storage and serial CPU time requirements, compared with the standard spectral collocation approach based on the (unmapped or mapped) Chebyshev Gauss-Lobatto grid. This permits a drastic reduction of the computing hardware on which state-of-the-art global linear instability analyses are performed when the spatial discretization matrix is stored and LU-decomposed. Results obtained demonstrate a memory reduction from $\mathcal{O}(M^2)$ to $\mathcal{O}(M^{1.3})$,

3. Linear modal stability validations and numerical efficiency

being M the leading dimension of the matrix operator, as well as a reduction of CPU time from $\mathcal{O}(M^3)$ to $\mathcal{O}(M^{1.7})$. Subsequently, the usage of FD-q delivers a speedup of $\mathcal{O}(10^4)$ and a memory reduction of $\mathcal{O}(10^3)$ in the most challenging global linear stability calculation made so far using matrix formation [129, 209], which used spectral collocation methods for the spatial discretization. Both improvements permit performing TriGlobal linear instability analyses on a modern desktop computer with modest computational effort.

Chapter 4

Parabolic Navier-Stokes solutions of incompressible and compressible base flows

4.1 Introduction

The present Chapter presents an algorithm for the accurate and efficient computation of incompressible and compressible steady laminar base flows in which strong flow variations exist along two spatial directions, while a mild variation can be assumed along the third. The algorithm is based on the Parabolic Navier-Stokes (PNS) equations [216]. Since their appearance, these equations have been used to successfully compute supersonic and hypersonic, viscous flows; see [215, 243] for a review. The incompressible version of the PNS equations were first formulated by Rubin and Lin [214]. One of the advantages of using PNS for the computation of base flows in an instability analysis context, is the steadiness of the solutions obtained by definition. In this manner, unsteadiness in the real flow will be recovered as instability of the base state in a later instability analysis.

An example of this concept is the recent work of Duck [58], where inviscid instability is studied upon the solution of systems of trailing vortices which are computed by a formulation of the three-dimensional boundary-layer equations. The application of the PNS equations to recover the solution of an isolated vortex in cylindrical coordinates is related to the quasi-cylindrical boundary-layer approximation used by Hall [89] and Trigub [260]. Both the latter and the formulation used by Duck [58] can be regarded as further approximations of the PNS. In the quasi-cylindrical boundary-layer approximation, the radial velocity and axial derivatives are dropped from most of the equations. In the three-dimensional boundary-layer approximation used by Duck [58], the transversal velocities to the axial direction are assumed of order \bar{u}/Re , being \bar{u} the axial velocity. The main objective of these works is the analysis of the vortex breakdown phenomenon. The

axisymmetric vortex breakdown study was followed in the 90's by Beran and Culick [19] and Wang and Rusak [265], who constructed the bifurcation diagram for swirling flows in a pipe. Later, Wang and Rusak [266, 267] presented a novel theory based on a rigorous mathematical analysis, recovering the flow behavior of previous computations and providing a solid theoretical understanding of the dynamics of axisymmetric swirling flows in a pipe. These works were extended for a diverging pipe by Rusak and Judd [217].

Turning the attention now to high speed flows, the circular and elliptic cones are frequently used models to understand transition over components of next-generation aerospace vehicles. Flows around both geometries give rise to a three-dimensional boundary-layer. The process of transition in these kind of flows is highly complex, since besides the second mode disturbances that often dominated in two-dimensional/axisymmetric hypersonic flows, also first mode and crossflow instabilities all become relevant mechanisms in the transition process. These scenarios have been reported in numerous experimental research efforts in both configurations, the circular cone at non-zero angle of attack (AoA) [126, 231, 233, 237] and the elliptic cone at zero AoA [109, 195, 224, 225]. Furthermore, recently large-scale computations [13, 16, 85, 86] and stability calculations [39, 131, 147, 148, 190] have appeared in the literature, reporting the co-existence of all these scenarios and mostly focusing on the crossflow instability.

The first PNS calculations of three-dimensional viscous flows over cone-based shaped bodies at non-zero AoA was presented by Lin and Rubin [154, 155], where the authors computed the boundary-layer over a slender cone at moderate incidence (ratio between AoA and half-cone vertex angle is lower or equal than 2). The same authors also published the PNS calculations on spinning cones at nonzero AoA [156]. Almost contemporary, Helliwell and Lubard [97, 157] developed their PNS code and showed calculations over a circular cone at high AoA. In the next decade, Tannehill et al. [242] developed a general PNS code to compute the steady supersonic viscous flow around arbitrary body shapes at high AoA and used it to calculate the laminar flow over a slab delta wing with 70° sweep at AoA up to 41.5° and Mach numbers equal to 6.8 and 9.6. Some years later, Lawrence et al. [135] showed PNS calculations for two body shapes: a circular cone of 10° half-angle at AoA = 12°, 20° and 24° and an elliptic cone-based all-body hypersonic vehicle at AoA = 0° and 10°, which can be considered as the first PNS calculation of the viscous flow over an elliptic cone. Motivated by the NASP effort in the early 90s, Stuckert and Reed [236] presented PNS base flow computations and local modal stability analysis of hypersonic, chemically reacting, viscous flow over a circular cone at zero AoA. The supersonic and hypersonic PNS calculations research of the three-dimensional boundary-layer over elliptic

cross-section cones was undertaken by Lyttle and Reed [158], who presented solutions for adiabatic wall elliptic cones of eccentricities of 2:1, 3:1 and 4:1 at $M = 4$, applying Reynolds number correlations based on the parameter R (see Reed and Haynes [201]) for stability analysis. The parameter R for these configurations peaked near the top centerline, outside the region of validity of the above correlation. Boundary-layer velocity profiles near the top centerline were inflectional and unstable. Kimmel et al. [125] used an extended version of the the UPS PNS code [134, 232], enabling the study of cool-wall cases, for computing the base flow around cones with eccentricities of 1.5:1, 2:1 and 4:1 at $M = 7.95$.

The PNS equations are derived from the Navier-Stokes equations by assuming steadiness and, based on the relative smallness of the streamwise flow variations, neglecting the viscous streamwise derivative terms. Then, the equations change their mathematical nature from elliptic to parabolic, and a parabolic integration along the streamwise direction is possible. The numerical solution of the problem for flows of practical application is challenging, as it involves the inversion of the large matrices that result from the discretization of a system of two-dimensional PDE. The challenge is met in the present work using stable high-order finite-difference schemes, developed recently by Hermanns and Hernández [103], together with the parallelizable sparse matrix linear algebra package MUMPS [5, 6]. This combination exploits the high level of sparsity offered by the finite-difference spatial differentiation, improving substantially the numerical efficiency while keeping accuracy. In the previous Chapter 3, a systematic study on global stability problems using the same combination shows that the solution of PDE-based problems of the same kind of those treated here is feasible for typical desktop computers.

The PNS equations are formulated and the numerical solution procedure are presented in what follows. Solution of a non-parallel isolated vortex and comparisons with theoretical predictions [17] and experiments [53] are presented in Section 4.4. Then, the fully three-dimensional flowfield corresponding to two counter-rotating vortices is computed by PDE-based PNS equations. The effect of the distance between the vortices on their axial development is studied. Furthermore, verifications and validations of the newly-developed code are carried out solving the flow around a circular cone at zero AoA. Solutions of the supersonic flow around a 7° half minor-axis angle 2:1 elliptic cone at Mach numbers 3 and 4 are also presented.

4.2 Theory

4.2.1 Parabolic Navier-Stokes equations

The derivation of the PNS equations from the three-dimensional steady Navier-Stokes equations (1.1-1.3) is valid in the limit of large Reynolds number when the flow configuration is predominant along the streamwise direction and exhibits a slow spatial dependence in the same direction, ξ . Therefore, the streamwise viscous derivative terms are negligible compared to the normal and transverse viscous derivative terms:

$$L_\xi \gg L_\eta, L_\zeta, \quad \partial(\cdot)/\partial\xi \ll \partial(\cdot)/\partial\eta, \partial(\cdot)/\partial\zeta, \quad \partial(\cdot)^2/\partial^2\xi \ll \partial(\cdot)^2/\partial^2\eta, \partial(\cdot)^2/\partial^2\zeta, \quad (4.1)$$

where L_ξ , L_η and L_ζ are the characteristic lengths on the streamwise and normal to it spatial directions respectively. Hence, the PNS equations are derived here by simply dropping second order partial derivatives with respect to the streamwise direction from the steady Navier-Stokes equations (1.1-1.3) [243]. When there is no flow, or reversed flow along the slow direction, the downstream integration of the Navier-Stokes equations is not correct, and numerical instabilities will prevent the recovery of converged solutions.

The parabolization of equations is not totally correct due to the term \bar{p}_ξ , which is associated with the left-running characteristic (for subsonic flows only) allowing upstream influence. The technique for handling the pressure gradient term was proposed by Vigneron et al. [264]. In this approach, the upstream propagation is suppressed by splitting the pressure gradient term into an explicit and an implicit parts. This is made by multiplying the streamwise pressure gradient \bar{p}_ξ by a parameter Ω given by

$$\Omega = \begin{cases} \frac{\gamma M_\xi^2}{1+(\gamma-1)M_\xi^2} & M_\xi < 1, \\ 1 & M_\xi \geq 1, \end{cases} \quad (4.2)$$

where $M_\xi = M\bar{u}_\xi/\sqrt{\bar{T}}$ is the streamwise Mach number and \bar{u}_ξ the velocity component in the streamwise direction, ξ . The remainder streamwise pressure gradient part is evaluated explicitly from previous marching steps.

The vector of fluid variables is defined as $\bar{\mathbf{q}} = (\bar{\rho}, \bar{u}, \bar{v}, \bar{w}, \bar{T})^T$. The resulting PNS equations are a system of nonlinear partial differential equations. In order to solve the system, a marching integration in ξ is used together with Newton iteration for solving the implicit scheme. The linear system solved to update the solution in each ξ -station is

$$\mathcal{J}(\bar{\mathbf{q}}^{n-1})\Delta\bar{\mathbf{q}} = \mathcal{F}_{\bar{\mathbf{q}}}(\bar{\mathbf{q}}^{n-1})\Delta\bar{\mathbf{q}} = -\mathcal{F}(\bar{\mathbf{q}}^{n-1}), \quad (4.3)$$

where $\mathcal{J} = \mathcal{F}_{\bar{\mathbf{q}}}$ is the Jacobian of the operator \mathcal{F} , $\Delta\bar{\mathbf{q}} = (\Delta\bar{\rho}, \Delta\bar{u}, \Delta\bar{v}, \Delta\bar{w}, \Delta\bar{T})^T$ and $\bar{\mathbf{q}}^n = \bar{\mathbf{q}}^{n-1} + \Delta\bar{\mathbf{q}}$. The equation (4.3) is written using matrix formation in Appendix F. The PNS equations have to be complemented with appropriate boundary condition depending on the particular problem.

4.3 Numerical considerations

4.3.1 Spatial discretization

The spatial discretization in the streamwise direction, ξ , is performed using Backward Differentiation Formulas (BDF). The BDF have the following general form for a k -step method

$$\frac{\partial\bar{\mathbf{q}}_m}{\partial\xi} = \Delta\xi \sum_{i=0}^k a_i \bar{\mathbf{q}}_{m-i}, \quad (4.4)$$

where $\bar{\mathbf{q}}_m = \bar{\mathbf{q}}(\xi_m)$ and a_i are the scheme's coefficients. A two-step BDF ($a_0 = 1$, $a_1 = -4/3$, $a_2 = 1/3$) with constant step-size $\Delta\xi$ is convergent for index 2 DAEs and gives second order accuracy in $\Delta\xi$. No higher order scheme is used in $\Delta\xi$ since, as has been mention before, the flow fields studied here exhibit a mild variation in this direction. This scheme needs two previous steps to evaluate the ξ -derivative. The one-step BDF, which is equivalent to the backward Euler method, $a_0 = 1$ and $a_1 = -1$, is used for the first step, started with an initial flow field.

The two directions of the normal plane to the streamwise marching direction, (η, ζ) , are discretized using the stable high-order finite-differences numerical schemes of order q (FD-q) recently developed by Hermanns and Hernández [103] and reviewed in Subsection 2.1.4. An exception is the non-parallel isolated vortex problem, which is assumed to be axisymmetric in the absence of instabilities and in consequence the azimuthal direction is homogeneous. Owing to this, the PNS equations are reduced to a system of ODE depending solely on the radial coordinate, which is discretized using the Chebyshev-Gauss-Lobatto (CGL) spectral collocation method [28, 34].

4.3.2 Non-linear marching integration

As has been mentioned above, the derivation of the PNS equations implies a change in the mathematical nature of the steady Navier-Stokes equations, from elliptic to parabolic, and a marching integration on the streamwise

direction is permissible. The resulting discretized PNS equations are a system of nonlinear PDE. In order to solve the system, a marching integration along ξ is used together with the Newton iteration method for solving the non-linear implicit scheme. The linear system of equation (4.3) is solved for update the solution in each ξ -station. The inversion of the matrix discretizing the Jacobian operator \mathcal{J} , which leading dimension is $\mathcal{O}(10^4 - 10^5)$, is performed using the parallelizable sparse matrix linear algebra package MUMPS [5, 6] and the SPARSKIT2 library [219]. When the PNS equations are reduced to a system of ODEs, a parabolic integration is affordable using dense algebra.

4.4 Incompressible vortex flows

Two different flow configurations are considered here in the incompressible limit. First, an isolated axisymmetric trailing-vortex is computed. The homogeneity on the azimuthal direction permits reducing the problem to a ODE-based PNS in cylindrical coordinates. The solution recovered is compared with theoretical predictions [17] and stereo-PIV experiments [53]. The second configuration is a pair of counter-rotating vortices, a problem in which the number of inhomogeneous directions cannot be reduced on account of symmetries and PDE-based PNS must be solved.

In this Section, the Cartesian coordinate system, $(\xi, \eta, \zeta) = (x, y, z)$ is considered, with the exception of the isolated trailing-vortex case. The resulting set of equations is modified here to reduce the derivative order of \bar{v} with respect to y and of \bar{w} with respect to z from second order to first order using the total pressure $\bar{q} = \bar{p} + (\bar{v}^2 + \bar{w}^2)/2 + 1/Re \bar{u}_x$ and the stream-wise vorticity $\bar{\zeta} = \bar{v}_z - \bar{w}_y$ [168]. This reduces also the number of boundary conditions to be imposed. The resulting set of equations for a Cartesian coordinate system is given by:

$$\bar{u} \bar{u}_x + \bar{v} \bar{u}_y + \bar{w} \bar{u}_z = -\bar{p}_{\infty,x} + \frac{1}{Re}(\bar{u}_{yy} + \bar{u}_{zz}), \quad (4.5)$$

$$\bar{u} \bar{v}_x + \bar{w} \bar{\zeta} = -\bar{q}_y + \frac{1}{Re} \bar{\zeta}_z, \quad (4.6)$$

$$\bar{u} \bar{w}_x - \bar{v} \bar{\zeta} = -\bar{q}_z - \frac{1}{Re} \bar{\zeta}_y, \quad (4.7)$$

$$\bar{u}_x + \bar{v}_y + \bar{w}_z = 0, \quad (4.8)$$

being $\bar{p}_{\infty,x}$ the streamwise derivative of the free-stream pressure, which enter into the equations as a known function. The streamwise pressure gradient,

\bar{p}_x is dropped for parabolization of equations. The flows considered in this work are not subjected to a free-stream pressure gradient, so $\bar{p}_{\infty,x} = 0$.

4.4.1 The isolated trailing-vortex

For initialization of the PNS marching integration, the asymptotic parallel Batchelor vortex [17] is used here. The Batchelor model vortex is a self-similar solution assuming that the vortex core radius r behaves as $r \propto \sqrt{x}$ when the axial (or streamwise) is $x \gg 1$.

If $(\bar{u}_x, \bar{u}_r, \bar{u}_\theta)$ denote the non-dimensional velocity components in the axial x , radial r (i.e. $r^2 = (y - y_c)^2 + (z - z_c)^2$ with (y_c, z_c) the coordinates of the vortex axis) and azimuthal θ directions respectively, the non-dimensional parallel-flow version of Batchelor's equations can be written as

$$\bar{u}_x = 1 - \gamma_0 \exp(-r/\delta_0)^2, \quad (4.9)$$

$$\bar{u}_r = 0, \quad (4.10)$$

$$\bar{u}_\theta = \frac{\kappa_0}{r} \{1 - \exp(-r/\delta_0)^2\}, \quad (4.11)$$

where $\gamma_0 = \bar{u}_c^*/\bar{u}_\infty^*$ is the axial velocity defect, \bar{u}_c^* is the core vortex velocity and \bar{u}_∞^* is the free-stream velocity (stars denote dimensional quantities), δ_0 is the initial core vortex radius and $\kappa_0 = \Gamma^*/(2\pi\bar{u}_\infty^*\delta_0^*)$ is the swirl strength parameter, which is related to the q -Vortex swirl parameter q , commonly used in the literature [123, 171], as

$$q = \frac{\kappa_0}{\gamma_0\delta_0}. \quad (4.12)$$

The Reynolds number is defined using the free-stream velocity \bar{u}_∞^* , the kinematic viscosity coefficient ν^* and initial core vortex radius, δ_0^* , as

$$Re = \frac{\bar{u}_\infty^*\delta_0^*}{\nu^*}. \quad (4.13)$$

Since the core vortex radius is the selected length scale, $\delta_0 = 1$.

The incompressible PNS equations (4.5-4.8) are used here in cylindrical coordinates, particularized for axisymmetric flow,

$$\bar{u}_x \frac{\partial \bar{u}_x}{\partial x} + \bar{u}_r \frac{\partial \bar{u}_x}{\partial r} = \frac{1}{Re} \left(\frac{\partial^2 \bar{u}_x}{\partial r^2} + \frac{1}{r} \frac{\partial \bar{u}_x}{\partial r} \right), \quad (4.14)$$

$$\bar{u}_x \frac{\partial \bar{u}_r}{\partial x} + \bar{u}_r \frac{\partial \bar{u}_r}{\partial r} - \frac{\bar{u}_\theta^2}{r} = -\frac{\partial \bar{p}}{\partial r} + \frac{1}{Re} \left(\frac{\partial^2 \bar{u}_r}{\partial r^2} + \frac{1}{r} \frac{\partial \bar{u}_r}{\partial r} - \frac{\bar{u}_r}{r^2} \right) \quad (4.15)$$

4. PNS solutions of incompressible and compressible base flows

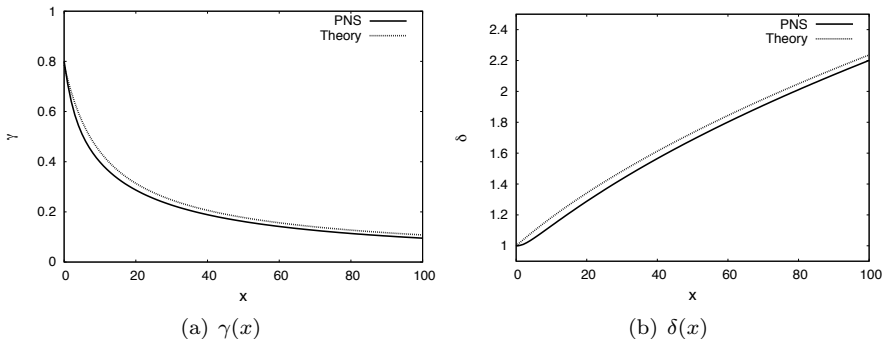


Figure 4.1: Axial velocity defect $\gamma(x)$ and vortex radius $\delta(x)$ computed by PNS (solid line) at $Re = 100$ for the non-parallel vortex with initial parameters $\kappa_0 = 0.8$ and $\gamma_0 = 0.8$, compared to the theoretical curves [17] (dotted line).

$$\bar{u}_x \frac{\partial \bar{u}_\theta}{\partial x} + \bar{u}_r \frac{\partial \bar{u}_\theta}{\partial r} + \frac{\bar{u}_\theta \bar{u}_r}{r} = \frac{1}{Re} \left(\frac{\partial^2 \bar{u}_\theta}{\partial r^2} + \frac{1}{r} \frac{\partial \bar{u}_\theta}{\partial r} - \frac{\bar{u}_\theta}{r^2} \right), \quad (4.16)$$

$$\frac{\partial \bar{u}_x}{\partial x} + \frac{1}{r} \frac{\partial (r \bar{u}_r)}{\partial r} = 0. \quad (4.17)$$

The axis conditions for axisymmetric flow are $(\partial \bar{u}_x / \partial r, \bar{u}_r, \bar{u}_\theta) = (0, 0, 0)$ [17]. The pressure level is arbitrarily set to $\bar{p} = 0$ at the axis. At the upper edge of the domain, asymptotic boundary conditions for the streamwise velocity, $\bar{u}_x = 1$, and azimuthal velocity, $\bar{u}_\theta = 0$, are imposed.

The selected computational domain is discretized using $N_r = 101$ CGL points ($r \in [-1, 1]$) mapped to $r \in [0, r_\infty]$ with the transformation of equation (2.60), setting $r_\infty = 200$ and $r_h = 4$, and $\Delta x = 0.5$ for the marching direction.

Figure 4.1 shows the evolution of the axial velocity defect at $r = 0$, $\gamma(x)$, and the vortex radius, $\delta(x)$, along the axial direction for $Re = 100$, $\kappa_0 = 0.8$ and $\gamma_0 = 0.8$. Both magnitudes are compared with the theoretical predictions of Batchelor [17]. Figure 4.1(a) shows the comparison with the axial velocity defect at the axis of the vortex,

$$\gamma(x)_{TH} = K^2 \frac{\log(x/Re)}{8x/Re} + \frac{L}{8x/Re}, \quad (4.18)$$

where K and L are free constant fitted for best comparison. The agreement between the theoretical and PNS computed curves improves as γ decreases, consistently with the assumption used by Batchelor [17], $\gamma \ll 1$. Figure 4.1(b) reflects close agreement of the vortex radius, $\delta(x)$, computed by PNS

using the definition based on the vorticity polar moment,

$$\delta(x) = \left[\frac{2\pi}{\Gamma} \int_r (\bar{\zeta} r^3) dr \right]^{1/2}, \quad \bar{\zeta} = \frac{1}{r} \frac{\partial(r \bar{u}_\theta)}{\partial r}, \quad (4.19)$$

and the one predicted by the theoretical curve [17]:

$$\delta(x)_{TH} = \delta_0 \left(1 + \frac{4x}{\delta_0^2 Re} \right)^{1/2}. \quad (4.20)$$

The initial transient observed in the PNS solution is attributed to the adjustment of the initial condition to the PNS equations, since the Batchelor's solution (4.9-4.11) does not take into account the radial velocity component. This component is essential in enforcing a divergence-free velocity field when the solution is axially divergent.

In order to check the reliability of these computations, results are compared with the experiments of Del Pino et al. [53]. These authors compared stereo Particle Image Velocimetry (PIV) measurements of the trailing vortex behind a wing in a water tunnel with the theoretical models of Batchelor [17] and Moore and Saffman [176]. Figure 4.2 shows comparisons between the numerical results delivered by the PNS equations (4.14-4.17), initialized with the parallel Batchelor vortex (4.9-4.11), for $\kappa_0 = 0.75$ and $\gamma_0 = 0.95$, and the experimental curves [53] at two downstream positions, $x/Re = 0.41$ and $x/Re = 0.65$, chosen in order to match the experimental profiles. The axial coordinate is expressed as x/Re since the isolated vortex is theoretically self-similar as shown by equations (4.18) and (4.20). Axial and azimuthal velocities match very well the experimental profiles. The small differences present at large r values may be due to the Batchelor vortex model used at the initial position of the marching integration, the assumptions done using PNS or the errors associated with measuring devices of the experiments. Comparisons for larger radial coordinate are not performed since experimental results are not available.

4.4.2 The trailing counter-rotating vortex-pair

By contrast to the isolated vortex considered before, the solution of the non-parallel vortex-pair is not axisymmetric, and cannot be reduced to an ODE with the use of cylindrical coordinates, thus requiring the PDE-based PNS equations (4.5-4.8). The flowfield corresponding to a counter-rotating vortex pair, used as initial condition for the parabolic integration of the PNS, is constructed as the linear sum of two Batchelor parallel vortices, defined

4. PNS solutions of incompressible and compressible base flows

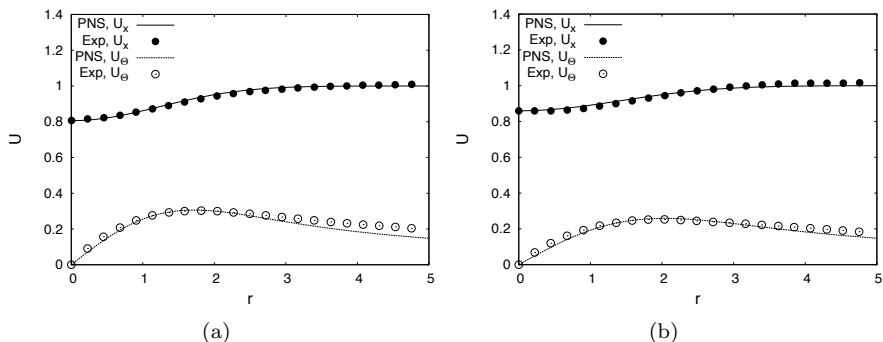


Figure 4.2: Comparisons between the experimental results of Del Pino et al. [53] and numerical results delivered by PNS for the non-parallel vortex with initial parameters $\kappa_0 = 0.95$ and $\gamma_0 = 0.75$ at positions (a) $x/Re = 0.41$ and (b) $x/Re = 0.65$ for the azimuthal velocity, \bar{u}_θ , and axial velocity, \bar{u}_x .

by equations (4.9-4.11), as follows

$$\bar{u} = 1 - \sum_{n=1}^2 \gamma_n \exp(-r_n/\delta_n)^2, \quad (4.21)$$

$$\bar{v} = - \sum_{n=1}^2 \left\{ \frac{\kappa_n}{r_n^2} (z - z_n) \left(1 - \exp(-r_n/\delta_n)^2 \right) \right\}, \quad (4.22)$$

$$\bar{w} = \sum_{n=1}^2 \left\{ \frac{\kappa_n}{r_n^2} (y - y_n) \left(1 - \exp(-r_n/\delta_n)^2 \right) \right\}, \quad (4.23)$$

where $r_n^2 = (y - y_n)^2 + (z - z_n)^2$ and (y_n, z_n) denotes the center of the n ($= 1, 2$) vortex. Defining d as the initial distance between the vortex cores, the vortices are located at $(y_1, z_1) = (d/2, 0)$ and $(y_2, z_2) = (-d/2, 0)$. The two vortices are counter-rotating, $\kappa_1 = -\kappa_2 = \kappa_0$, and have the same axial velocity defect, $\gamma_1 = \gamma_2 = \gamma_0$.

In order to reduce the computational requirements, the symmetries existing in the problem, \bar{u} and \bar{w} symmetric and \bar{v} antisymmetric with respect to the plane $y = 0$, have been exploited. Therefore, the computational domain is reduced to $\Omega = \{x \in [0, x_\infty]\} \times \{y \in [0, y_\infty]\} \times \{z \in [-z_\infty, z_\infty]\}$.

For counter-rotating vortex-pairs, a downward induced velocity exists because of the interaction between the vortices on the (y, z) -plane, causing the downwash displacement of the vortices. A rotation of the computational domain is used to keep the vortex cores approximately at the center

of the domain during the marching integration, significantly reducing the discretization area and therefore the number of discretization points required in the z -direction. Using the magnitude of the velocity induced between the vortices for the initial profile, $\bar{v}_d = \kappa_0/d$, the computational domain is rotated an angle

$$\theta_d = \text{atan}(\bar{v}_d) = \text{atan}(\kappa_0/d), \quad (4.24)$$

along the y -axis as can be observed in the sketch of figure 4.3. An axes translation can also be used, introducing some additional terms into the equations. In this case, the PNS equations (4.5-4.8) are expressed in the new coordinate axes

$$x' = x, \quad y' = y, \quad z' = z + \bar{v}_d x, \quad (4.25)$$

resulting

$$\bar{u} \bar{u}_{x'} + \bar{v} \bar{u}_{y'} + (\bar{w} + \bar{v}_d \bar{u}) \bar{u}_{z'} = -\bar{p}_{\infty, x'} + \frac{1}{Re} (\bar{u}_{y'y'} + (1 + \bar{v}_d^2) \bar{u}_{z'}) \quad (4.26)$$

$$\bar{u} \bar{v}_{x'} + (\bar{w} + \bar{v}_d \bar{u}) \bar{v}_{z'} - \bar{w} \bar{w}_{y'} = -\bar{q}_{y'} + \frac{1}{Re} (-\bar{w}_{y'z'} + (1 + \bar{v}_d^2) \bar{v}_{z'}) \quad (4.27)$$

$$\bar{u} \bar{w}_{x'} + \bar{v} \bar{w}_{y'} + \bar{v}_d \bar{u} \bar{w}_{z'} - \bar{v} \bar{v}_{z'} = -\bar{q}_{z'} - \frac{1}{Re} (-\bar{v}_{y'z'} + \bar{w}_{y'y'} + \bar{v}_d^2 \bar{w}_{z'}) \quad (4.28)$$

$$\bar{u}_{x'} + \bar{v}_d \bar{u}_{z'} + \bar{v}_{y'} + \bar{w}_{z'} = 0, \quad (4.29)$$

where the total pressure is here defined as $\bar{q} = \bar{p} + (\bar{v}^2 + \bar{w}^2)/2 + 1/Re (\bar{u}_{x'} + \bar{v}_d \bar{u}_{z'})$. The results delivered by the two approaches, axes rotation and translation, are nearly indistinguishable, as show in figure 4.7. As a second validation test, the computed flowfields were introduced into the full Navier-Stokes equations. The computed residuals are shown in figure 4.4, and consistently with the approximations taken (see Section 4.2) are of order ϵ (being ϵ the level of accuracy set in the Newton iteration procedure) in the continuity, y - and z -momentum equations, while in the x -momentum equation the residual is of order $\bar{p}_x \approx \mathcal{O}(1/Re)$, since the term \bar{p}_x is dropped in order to parabolize the equations. These residuals are related to the leading eigenmodes of a linear stability problem; see the structure of the modes found by González et al. [79] and the discussion about the relation between residuals and flow instabilities of Theofilis [250].

The domain is discretized using $N_z = 160$ points for the z -direction, mapped using Equation (2.59) setting $z_\infty = 40$ and $c_z = 0.90$ to concentrate points in the vortex cores, and $N_y = 181$ points, mapped using equation (2.60), $y_\infty = 40$ and $y_h = 8$. A constant marching step $\Delta x = 0.5$ is selected. Tenth-order stable high-order finite differences (FD-q10) are used for the differentiation along the two spatial directions. The boundary conditions

4. PNS solutions of incompressible and compressible base flows

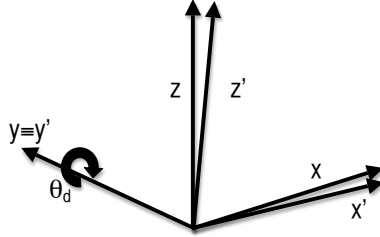


Figure 4.3: Sketch of the rotational transformation around the y -axis used for the computations of the counter-rotating pair of trailing vortices by PNS.

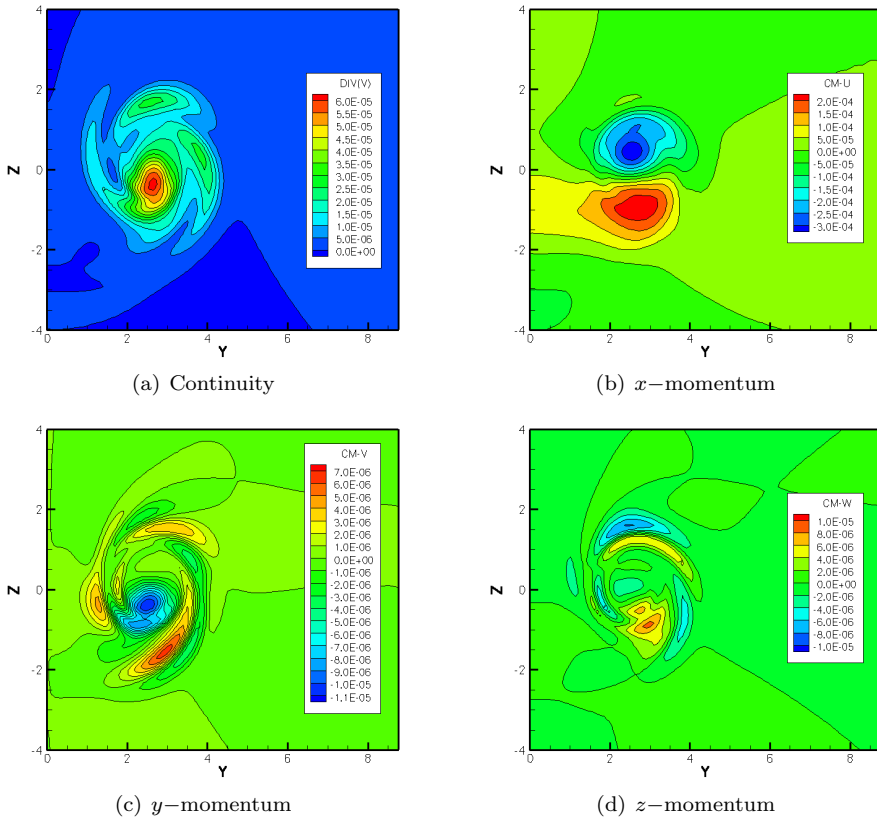


Figure 4.4: Residuals of the full Navier-Stokes equations for the PNS computed solution of the counter-rotating vortex-pair flow at $x = 20$ with an initial distance between vortex cores $d = 5$, setting $Re = 3000$, $\kappa_0 = 0.4$ and $\gamma_0 = 0.8$.

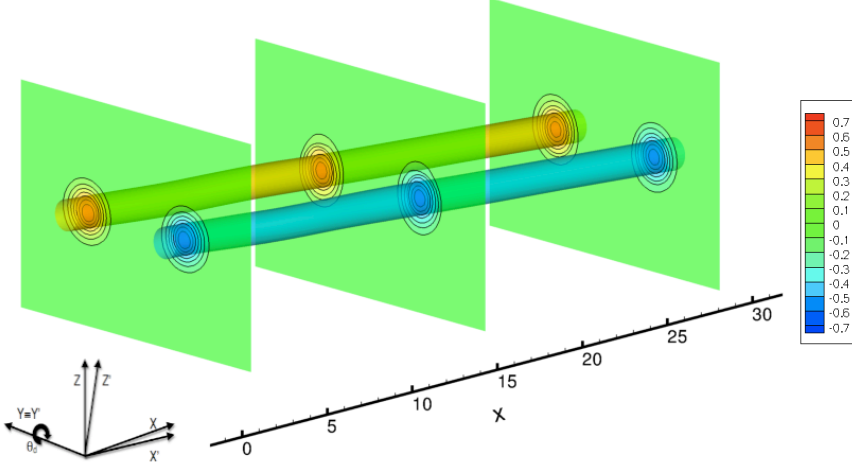


Figure 4.5: Iso-contours and iso-surfaces of axial vorticity of the non-parallel counter-rotating vortex-pair at $Re = 3000$ for the initial parameters $\kappa_0 = 0.4$ and $\gamma_0 = 0.8$, computed by PNS methodology.

imposed by the symmetries are $(\bar{u}_y, \bar{v}, \bar{w}_y) = (0, 0, 0)$ at $y = 0$ and asymptotic boundary condition for the streamwise velocity, $\bar{u} = 1$, and normal velocity $\bar{w} = 0$ are imposed at y_∞ , where it is also set the total pressure level, $\bar{q} = 0$. Periodic boundary conditions are imposed at z_∞ .

Figure 4.5 shows a three-dimensional visualization of the counter-rotating vortex-pair flowfield by iso-surfaces and iso-contours of axial vorticity at $Re = 3000$. The vortices are defined by the initial parameters $\gamma_0 = 0.8$, $\kappa_0 = 0.4$ and the distance between the cores $d = 6$. The downwash displacement of the vortices, caused by the induced velocity, \bar{v}_d , is clearly visible.

Figure 4.6 shows the evolution of the vortex radius $\delta = (\delta_y^2 + \delta_z^2)^{1/2}$ based on the vorticity polar momentum on the half-plane [229], defined as

$$\delta_y^2 = \frac{1}{\Gamma} \int \int_{z>0} \bar{\zeta} (y - y_c)^2 dy dz, \quad \delta_z^2 = \frac{1}{\Gamma} \int \int_{z>0} \bar{\zeta} (z - z_c)^2 dy dz, \quad (4.30)$$

where (y_c, z_c) denotes the position of the vorticity centroids,

$$y_c = \frac{1}{\Gamma} \int \int_{z>0} y \bar{\zeta} dy dz, \quad z_c = \frac{1}{\Gamma} \int \int_{z>0} z \bar{\zeta} dy dz. \quad (4.31)$$

The interaction between the vortices is illustrated by the differences with the theoretical curve for one isolated vortex (4.20): as the distance between

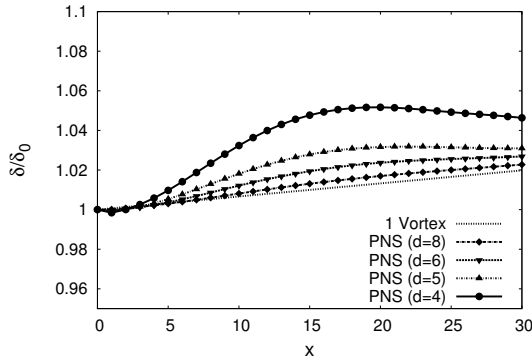


Figure 4.6: Evolution on streamwise direction of vortex radius $\delta(x)$ computed by PNS equations (4.5-4.8) with four different initial distances between the vortex cores ($d = 4, 5, 6$ and 8) and the theoretical value for one isolated vortex with the same parameters of figure 4.5 ($\kappa_0 = 0.4, \gamma_0 = 0.8$).

vortices, d , increases, the vortex radius curve, $\delta(x)$, tends to the theoretical value for one isolated vortex. For the smaller initial distances between vortices, cases $d = 4$ and 5 , the vortex radius stops growing about $x \approx 20$ and then decays slowly downstream. This behavior is attributed to the inviscid interaction between the core vortices as the ratio δ_0/d becomes significant. It is important to note that the swirl strength parameter also affects this phenomenon.

Figure 4.7 shows the evolution along the axial direction of the vortex core locations (4.31). As shown in figure 4.7(a), the y_c coordinate experiments an initial shift due to the adjustment of the initial condition, which is not a solution of the PNS equations. Downstream, a mild displacement increases the distance between the vortices. This phenomenon impacts on the z_c coordinate, by decreasing the downward induced velocity, as shown in figure 4.7(b). Stronger effects are observed for smaller initial distances. Figure 4.7 also reflects the very good agreement between the results recovered by translation and rotation of axes.

4.5 Compressible circular and elliptic cone flows

This Section firstly presents validations of the compressible PNS code solving the boundary-layer around a circular cone at zero AoA in the incompressible and compressible regimes. Secondly, the supersonic flow solutions around a

4.5. Compressible circular and elliptic cone flows

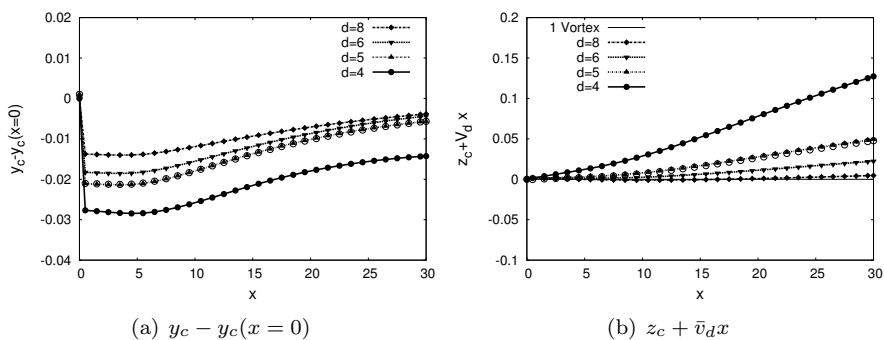


Figure 4.7: Evolution on the streamwise direction of the vortex core position (a) y_c and (b) $z_c + \bar{v}_d x$ for $d = 4, 5, 6$ and 8 setting the same parameters of figure 4.5 ($\kappa_0 = 0.4, \gamma_0 = 0.8$). The open circles correspond to the equations (4.26-4.29) with axes translation for $d = 5$

2:1 elliptic cone at Mach numbers 3 and 4 are presented, also at zero AoA.

The marching integration needs to be feed by an initial condition. Free-stream conditions, $\bar{\mathbf{q}}_\infty = (\bar{\rho}_\infty, \bar{u}_\infty, \bar{v}_\infty, \bar{w}_\infty, \bar{T}_\infty)^T$, i.e. $\bar{\mathbf{q}}_\infty = (1, 1, 0, 0, 1)^T$ for AoA=0°, are imposed at the vertex of the cone and the solution at an initial station ξ_0 is converged after some Newton iterations.

A three-dimensional coordinate transformation of the form

$$\xi = \xi(x), \quad \eta = \eta(x, y, z), \quad \zeta = \zeta(x, y, z), \quad (4.32)$$

are used to transform the governing equations into the (ξ, η, ζ) system. This transformation restricts the (η, ζ) solution surfaces to be in a plane normal to the x axis, resulting $\xi_y = \xi_z = 0$. Using the chain rule, the derivatives with respect to physical coordinates system are related to those with respect to the computational coordinates system through the metrics $(\xi_x, \eta_x, \eta_y, \eta_z, \zeta_x, \zeta_y, \zeta_z)$. More details are found in Subsection 2.3.

The PNS marching scheme (4.3) has to be complemented with appropriate boundary conditions. For the cases studied here, the flow around a circular cone and around an elliptic cone, the symmetries of the problem are exploited for reducing computational requirements and the corresponding boundary conditions are imposed for the azimuthal direction, ζ . No-slip conditions are imposed at the wall, $\eta = 0$, together with Neumann conditions for temperature and density, which implies having adiabatic wall. Results showed here are recovered using free-stream conditions at the top boundary $\eta = 1$ and therefore the shock wave is immersed in the domain.

4.5.1 Circular cone

The mesh surrounding a circular cone is calculated using a modification of the cylindrical transformation, written as

$$x = \xi, \quad y = (\xi \tan \alpha + \eta \eta_\infty) \sin \zeta, \quad z = (\xi \tan \alpha + \eta \eta_\infty) \cos \zeta, \quad (4.33)$$

where $\eta \in [0, 1]$ and η_∞ controls the far-field boundary.

The flow around a circular cone is well understood thanks to the axisymmetric condition, in which the streamlines remain in meridian planes. The boundary-layer equations under rotational symmetry were first given by Mangler [167] in the incompressible limit, introducing the Mangler transformation, which converts the well-known Falker-Skan boundary-layer solutions into the ones around circular cones. Figure 4.8(a) shows the streamwise velocity profiles for a circular cone with half angle $\alpha = 15^\circ$ setting $M = 10^{-3}$ and $Re = 100$ comparing with Mangler theory [167] at three different streamwise positions, $x = 100, 200$ and 300 . Excellent agreement is observed, having an overlapping of the profiles.

The theory of inviscid supersonic flow past a circular-based cone at zero incidence (see Shapiro [228] for more details) indicates that, for $M > 1.2$ and a half cone angle less than 55° , the resulting shock wave is attached to the cone vertex, and the flow at the cone surface is at constant velocity, pressure, and temperature. These properties base the analysis of Taylor and Maccoll [245], in which the shock angle β is predicted versus the Mach number and half cone angle α . Figure 4.8(b) shows the comparisons between the PNS results and the inviscid theory predictions for Mach numbers 2 and 3. Excellent agreement is again observed.

4.5.2 Elliptic cone

For the elliptic cone problem, a modified confocal elliptic transformation is used,

$$x = \xi, \quad y = c\xi \sinh(\eta_0 + \eta \eta_\infty) \sin \zeta, \quad z = c\xi \cosh(\eta_0 + \eta \eta_\infty) \cos \zeta, \quad (4.34)$$

where c sets the half angle of the cone minor-axis, $c = \text{atan}\alpha / \sinh \eta_0$, and η_0 is a parameter controlling the Aspect Ratio (AR) of the cone, $\eta_0 = \text{atanh}(1/AR)$.

In the elliptic cone problem, the three-dimensionality of the flow makes it unaffordable from an analytical point of view and more complex numerical

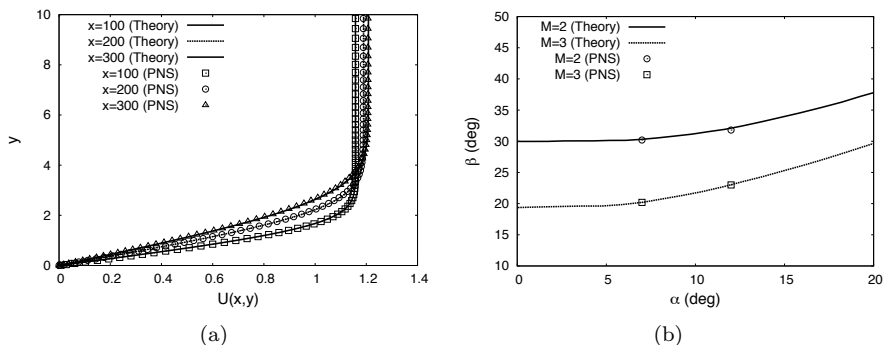


Figure 4.8: Comparisons of theoretical predictions and results delivered by the newly-developed PNS code. Figure 4.8(a) shows the streamwise velocity profiles in a circular cone with half angle $\alpha = 15^\circ$ setting $M = 10^{-3}$ comparing with Mangler theory [167] at different streamwise positions. Figure 4.8(b) shows the shock angle β versus the half cone angle α for Mach numbers 2 and 3 comparing with the Taylor and Maccoll theoretical predictions [245].

tools are needed to recover the flow field. The three-dimensionality of the flow inevitable produces spanwise pressure gradients, which induce crossflow, at locations where the flow direction of the interior of the boundary-layer is no longer co-planar with the edge velocity vector. This phenomenon causes the appearance of two main regions in the elliptic cone flow, the attachment-line on the leading edge, i.e. the major-axis, and the top centerline, i.e. the minor-axis, where a lift-up process is observed.

The supersonic flow around a 7° half minor-axis angle angle 2:1 elliptic cone is solved at Mach numbers 3 and 4. Figures 4.9 and 4.10 show the iso-contours of the flow field variables from $Re_x = 10^4$ to $Re_x = 3 \times 10^4$. The shock wave layer is clearly visible in the density plots 4.10(c) and 4.10(d). The crossflow region is observed in figures 4.9(c) and 4.9(f), near the wall of the cone, where $\bar{w} < 0$. Figure 4.11 shows some near-wall streamlines for the $M = 4$ case, differentiating the two mentioned main regions of the flow, the attachment-line at the leading edge and the lift-up over the top centerline.

4.6 Summary and conclusions

A PNS algorithm has been developed and validated in a systematic manner and solutions of two different flows are obtained. Using this methodology, steady incompressible three-dimensional flows with one slowly-varying spa-

4. PNS solutions of incompressible and compressible base flows

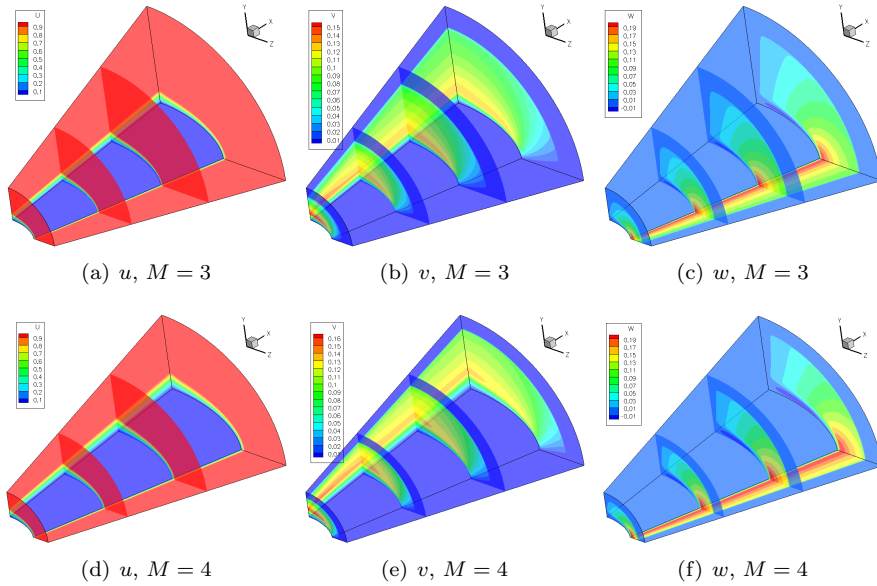


Figure 4.9: Three velocity components of the flow field from $Re_x = 10^4$ to $Re_x = 3 \times 10^4$ for a 7° half minor-axis cone angle elliptic cone of aspect ratio 2 at Mach numbers 3 and 4.

tial direction can be solved without resorting to a fully three-dimensional spatially evolving DNS and thus saving several orders-of-magnitude of computational effort in the computation of steady solutions to serve as base flow in subsequent stability analysis. The algorithm has been formulated and results have been obtained for the incompressible and compressible flow regimes.

Focusing firstly on the incompressible limit, two different vortical flows have been computed, a non-parallel trailing vortex and a system of two counter-rotating vortices which are allowed to interact. The non-parallel trailing vortex is computed by PNS equations in cylindrical coordinates initialized with the Batchelor vortex [17]. The solution differs from Batchelor's model in the existence of a radial velocity component, arising from the inhomogeneity on the axial direction. Results are compared with theoretical predictions and stereo-PIV experiments [53], validating the present algorithm. In the case of a pair of counter-rotating vortices, a downward induced velocity exists and the domain is transformed using two approaches, an axes rotation and a translation. Both domain transformations delivered nearly indistinguishable solutions. The PNS computed results converge to those of

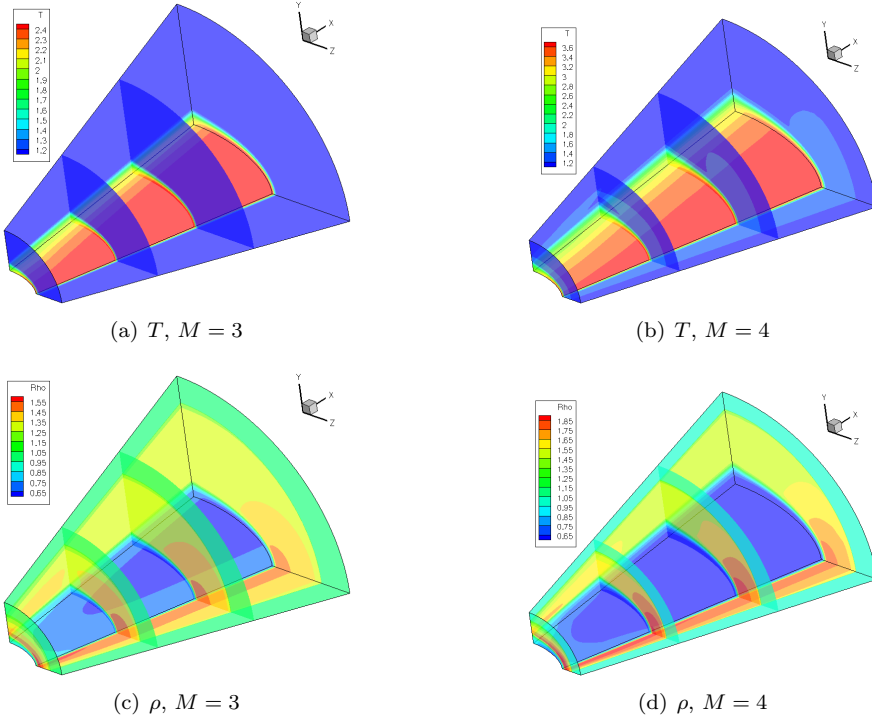


Figure 4.10: Temperature and density components of the flow field from $Re_x = 10^4$ to $Re_x = 3 \times 10^4$ for a 7° half minor-axis cone angle elliptic cone of aspect ratio 2 at Mach numbers 3 and 4.

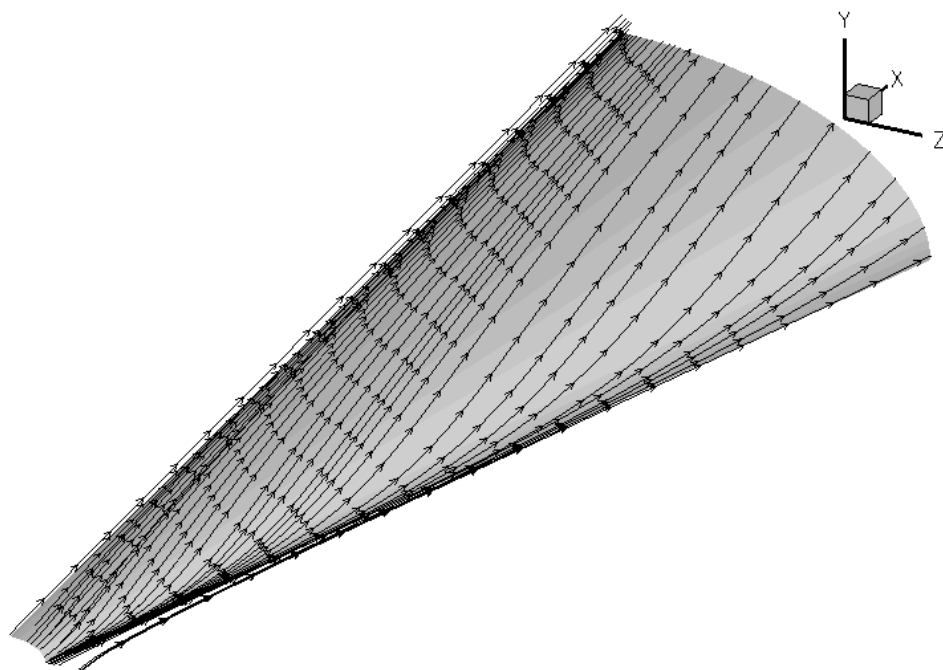


Figure 4.11: Near-wall streamlines of a 7° half minor-axis angle 2:1 elliptic cone at $M = 4$.

the isolated vortex as distance between vortices increases. It is found that, as vortices become closer, the mutual interaction results in an increase of the vortex radii, accompanied by a decrease in the downward induced velocity. It should be noted that the steady nature of the PNS equations prevents the recovery of elliptic instability induced by one vortex on the other. Subsequent stability analysis of the computed incompressible vortex base flows using three-dimensional Parabolized Stability Equations (PSE-3D) is shown in next Chapter 5.

On the other hand, solutions of the supersonic flows around the circular and elliptic cones computed using a newly-developed compressible PNS code are presented. The boundary-layer solution around a circular cone at zero angle of attack is compared in the incompressible limit with theoretical profiles. Also, the recovered shock wave angle at supersonic conditions is compared with theoretical predictions in the same circular-base cone geometry. Both results show excellent agreement with theoretical predictions. The fully three-dimensional flow field surrounding a 7° half minor-axis cone angle elliptic cone of aspect ratio 2 at supersonic regime is presented. The domain is chosen such as that the shock position and the compressible boundary-layer are captured. The two main features of this flow are identified, the attachment line at the leading edge and the lift-up over the top centerline. The crossflow region is also clearly visible in the three-dimensional plots, showing potential crossflow mechanisms of transition.

4. PNS solutions of incompressible and compressible base flows

Chapter 5

Instability analysis of trailing vortex flows using parabolized equations

5.1 Introduction

The stability analysis of the incompressible vortex steady base flows computed in the previous Section 4.4 using the PNS equations is performed here. The model typically analyzed when considering trailing vortices flows is the Batchelor [17] vortex, initially investigated by Lessen and Paillet [139], Lessen et al. [140] and more recently by Khorrami et al. [123]. Several spiral modes of instability were identified but their relation with the abrupt change in structure and subsequent vortex breakdown is not fully understood yet; where vortex breakdown is defined following Leibovich [136, 137] as, "*a disturbance characterized by the formation of an internal stagnation point on the vortex axis*". It has been suggested that one reason why local stability theory proves inadequate in predicting breakdown consistently is because, similar to the parallel boundary layer assumption, it neglects axial velocity and pressure gradients, such as axial deceleration, that may influence the vortex. This was confirmed by the DNS results of Abid and Brachet [2], who related the spiral instability eigenmode with a lateral expansion of the vortex cross section. As a direct consequence of the assumption of streamwise periodicity, these results fail to identify a significant axial loss in velocity. However, it is recently becoming clear that the assumption of homogeneity in one spatial direction may be overtly restrictive even in as simple a flow as a single spatially-developing viscous vortex as seen in the results of Broadhurst et al. [32], who analyzed a temporally and a spatially-developing Batchelor vortex both by DNS. In the first case, the temporal-evolving vortex in which the axial direction was artificially kept homogeneous, these authors predicted linear instability by local analysis, observed also in the DNS results, in whose it is followed by nonlinear saturation. By contrast, the nonlinear development of instability in the Batchelor vortex is qualitatively different when the vortex is allowed to evolve spatially. Then, a streamwise

loss in energy (initiated by the linear mode of instability), will lead to the formation of an internal stagnation point and ultimate vortex breakdown. The assumption of axial homogeneity of a base flow vortex employed in all previous global analyses was relaxed by Heaton et al. [92], who studied the more realistic spatially developing Batchelor vortex model. These authors documented the modifications that the classic Batchelor eigenspectrum experiences and the ensuing potential for transient growth exhibited by the spatially developing flow, computing the base flow and studying its stability using an axisymmetric DNS.

Modeling the trailing-vortex system behind an aircraft as an isolated vortex is quite restrictive as it assumes an axisymmetric base flow, thus it neglects in principle the influence of any neighboring vortices. Crow [49], Widnall [272], Jiménez [115], Crouch [46] and Fabre and Jacquin [62], amongst others, have used vortex filament methods to analyze the instabilities triggered by interaction between neighboring vortices. However, vortex core instabilities [171] or absolute instability [54] are beyond the scope of a vortex filament approach. In addition, the vortex filament method has limitations (besides that of strictly being applicable to inviscid flow) in the permissible distributions of vorticity in the wake, in terms of both strength and placement of the constitutive vortices.

As mentioned in Chapter 1, the instability analysis technique that may consider base flows inhomogeneous in two or three (rather than one) spatial directions is called global linear stability theory, referenced as BiGlobal or TriGlobal analysis for two and three inhomogeneous directions, respectively. Hein and Theofilis [95] presented some numerical results for the flow developing downstream from two counter-rotating Batchelor vortices, with the axial velocity component neglected, computed with a two-dimensional DNS. The instability analysis was performed by BiGlobal analysis, which considers the quasi-steady and the axially-homogeneous approximations in the base flow; recovering both classic long- (Crow) and short-wavelength instabilities. The work of González et al. [79] shows a similar study, but considering axial flow, finding only short-wavelength instabilities. Another related study of non-axisymmetric/system of vortices is that of Lacaze et al. [132], in which the stability of flows with no/little axial flow was studied. The authors focused on the short-wavelength instabilities, specifically on the elliptic instability, observed on an isolated vortex subject to a stationary strain field. The elliptical instability is believed to take place in various contexts ranging from three-dimensional transition in shear flows [18] to vortex interactions [142]; see Kerswell [121] for a review.

In a first approximation, the system of counter-rotating vortex-pair flow

may be analyzed by BiGlobal instability analysis, neglecting the the existence of a small, but not negligible, dependence of the fluid variables on the axial direction. Therefore, a three-dimensional analysis is needed, but treating the three spatial directions as inhomogeneous, the TriGlobal analysis requires the numerical solution of the PDE-based EVP resulting from the discretization of the three coupled directions, which is possible but prohibitively expensive nowadays for most applications of interest. To study the instability of this flow, the PSE-3D analysis results to be the most efficient methodology.

In what follows, these approaches are used along with the non-parallel isolated vortex, comparing PSE-3D against conventional PSE in cylindrical coordinates and spatial BiGlobal stability. The PSE-3D methodology is used to study the instability properties of the fully three-dimensional counter-rotating vortex-pair flow field, computed by PNS equations in Section 4.4.

5.2 Results

5.2.1 The isolated trailing-vortex

The stability analysis is performed upon the previously showed trailing line vortex base flow computed by PNS of figure 4.1, with $Re = 3000$, $\kappa_0 = 0.8$ and $\gamma_0 = 0.8$. The conventional PSE in cylindrical coordinates (see [188] for more details) and the PSE-3D are used along with this base flow for cross-validation purposes. The PSE in cylindrical coordinates uses the same spatial discretization of PNS, $N_r = 101$ CGL points mapped with equation (2.60) setting $r_\infty = 200$ and $r_h = 4$, and PSE-3D uses $(N + 1)^2 = 121^2$ FD-q10 points for both y and z directions, mapping the square domain with equation (2.59) setting $c_y = c_z = 0.96$ and $y_\infty = z_\infty = 40$. The marching step of both the PSE and PSE-3D is $\Delta x = 1$.

Figure 5.1 shows the leading spatial eigenmodes computed by Spatial BiGlobal instability analysis of the Batchelor vortex model of equations (4.9-4.11) with $\kappa_0 = 0.8$ and $\gamma_0 = 0.8$ at $Re = 3000$. The different modes appearing in figure 5.1 correspond to discrete modes and present a periodic structure in the azimuthal direction, with the wavenumber assigned by m . In the range of frequencies analyzed, the most unstable mode occurs for $m = 2$, frequency $\omega = 1.75$, wavenumber $\alpha_r = 1.212$ and growth rate $-\alpha_i = 0.725$. From this maximum at $m = 2$, a linear trend defines the maximum growth rate, $-\alpha_i$, for increasing m . These maxima are specified in Table 5.1. Figure 5.2(a) shows the eigenspectrum at $\omega = 4.6$. A branch of eigenvalues appears

5. Instability analysis of vortex flows using parabolized equations

Table 5.1: Spatial BiGlobal leading eigenmodes of each family represented by the number of lobes, m , for the Batchelor vortex model flow (4.9-4.11) with $\kappa_0 = 0.8$, $\gamma_0 = 0.8$, $\delta_0 = 1$ at $Re = 3000$.

| m | 1 | 2 | 3 | 4 | 5 | 6 |
|-------------|-------|-------|-------|-------|-------|-------|
| ω | 0.86 | 1.75 | 2.70 | 3.65 | 4.56 | 5.49 |
| α_r | 0.543 | 1.212 | 1.792 | 2.399 | 2.897 | 3.466 |
| $-\alpha_i$ | 0.185 | 0.725 | 0.690 | 0.663 | 0.636 | 0.605 |

for $\alpha_r = 0$ and $\alpha_i < 0$, which corresponds to a discretized spectrum of upstream moving pressure waves. This branch is suppressed in the PSE approximation in order to permit a stable numerical integration along the axial direction, as discussed by Li and Malik [145]. In addition, a branch of discrete eigenvalues is found, describing a near-vertical line. The modes inside this branch have the same wavenumber m . Note that when a one-dimensional stability analysis such as the OSE in cylindrical coordinates is used, the wavenumber m is a parameter of the problem. The BiGlobal analysis recovers the results of several local analysis at the same time. Figure 5.2(b) shows the real part of the initial axial velocity amplitude eigenfunction of the most unstable mode, which corresponds to a five lobes ($m = 5$) spiral-eigenmode.

Initial conditions need to be specified for the PSE marching integration. The most common method used in conventional PSE is to draw on the local analysis of weakly non-parallel flow, $\bar{\mathbf{q}}_0$, in order to obtain a complex wavenumber, α_0 , and shape function, $\hat{\mathbf{q}}_0$, at initial axial location for an specific Re and ω [101]. In this work, the parallel-flow approximation along the axial direction is considered, so the spatial BiGlobal problem obtains a first approximation to the complex wavenumber and shape functions. Afterwards, this result is refined by PSE-3D iterations introducing the non-parallel effects to α_0 and $\hat{\mathbf{q}}_0$. In the case that an arbitrary eigenmode is given at the initial position, by marching integration upon the base flow $\bar{\mathbf{q}}_0$, the leading eigenmode is recovered by PSE-3D as can be observed in figure 5.3. This fact gives more advantages to the PSE-3D methodology, because the leading eigenmode is an attractor of the system.

Figure 5.4 shows the evolution of the spatial growth rate, $-\alpha_i$, along the

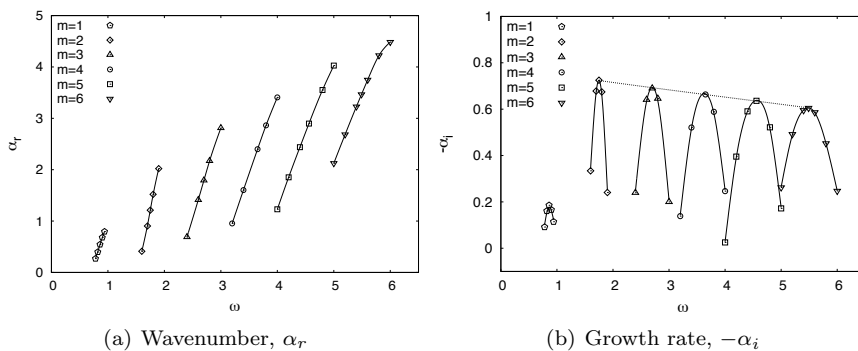


Figure 5.1: Unstable spatial eigenmodes, represented by their (a) wavenumber, α_r , and (b) growth rate, $-\alpha_i$, of the Batchelor vortex model of equations (4.9-4.11) with $\kappa_0 = 0.8$, $\gamma_0 = 0.8$ at $Re = 3000$, obtained by spatial BiGlobal analysis. Symbols indicate different azimuthal wavenumbers or number of lobes, m .

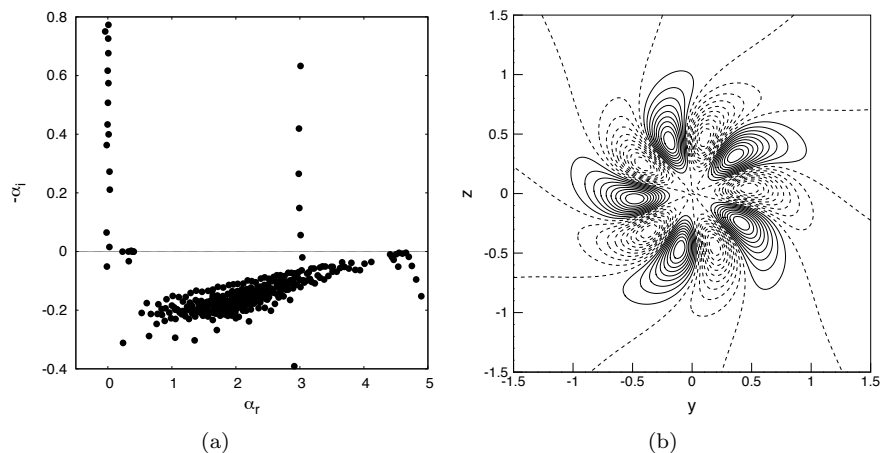


Figure 5.2: Eigenspectrum of the parallel Batchelor vortex model (4.9-4.11) defined with the parameters $\gamma_0 = 0.8$ and $\kappa_0 = 0.8$ at $Re = 3000$ and $\omega = 4.6$. The most unstable eigenmode is plotted in Fig. 5.2(b) with iso-contours $\hat{u}_r/|u| = (-0.9 : 0.1 : 0.9)$ of normalized real part of axial velocity amplitude function (dashed lines correspond to negative values).

5. Instability analysis of vortex flows using parabolized equations

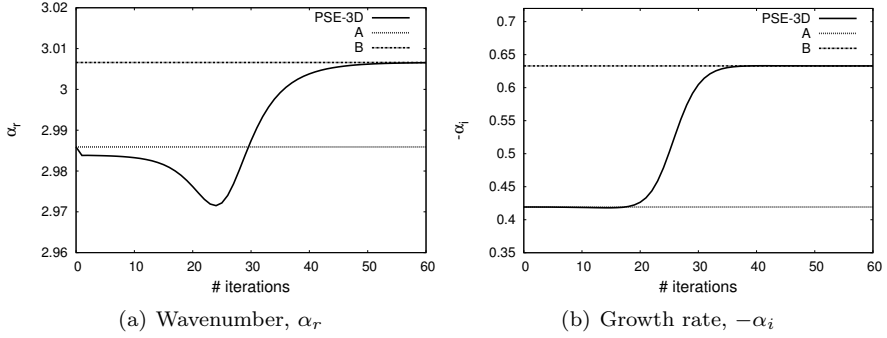


Figure 5.3: Evolution of initial complex wavenumber by PSE-3D iterations on the initial station from the second most unstable eigenmode (A) shown in the spectrum of figure 5.2(a) to the leading eigenmode (B) for the vortex model of equations (4.9-4.11) defined with the parameters $\gamma_0 = 0.8$ and $\kappa_0 = 0.8$ at $Re = 3000$ and $\omega = 4.6$.

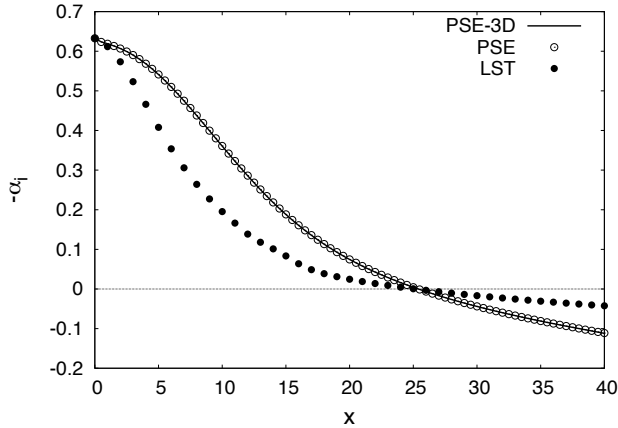


Figure 5.4: Evolution of growth rate for the non-parallel vortex flow ($\kappa_0 = 0.8$, $\gamma_0 = 0.8$) for the most unstable eigenmode at the selected parameters ($Re = 3000$, $\omega = 4.6$), comparing conventional PSE with cylindrical coordinates and PSE-3D results for a cross-validation test. Also, the leading eigenmode at each station is computed by local analysis (LST).

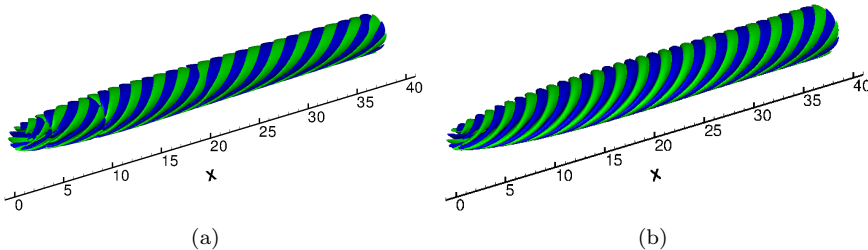


Figure 5.5: Iso-surfaces ($\tilde{u}/|\tilde{u}_0| = 10$ and $\tilde{u}/|\tilde{u}_0| = -10$) of axial velocity amplitude functions of figure 5.4 by local theory, in this case by spatial BiGlobal analysis, and PSE-3D.

axial direction computed using PSE-3D and conventional PSE with cylindrical coordinates [188]. Excellent agreement exists between the results delivered by both methodologies. The main target of this work is to prove the profit of using non-parallel or non-local analysis instead of using local stability analysis. For example at $x = 10$, a gap larger than the 50 % of relative error between both local and non-local analyses is observed. It is important to note that, although large discrepancies exist in terms of relative error between both curves, they cross the neutral stability threshold, $\alpha_i = 0$, at same axial position $x \approx 25.4$. Figure 5.5 compares the reconstruction of the three-dimensional solutions, showing again notable differences between the results delivered by both approaches.

5.2.2 The trailing counter-rotating vortex-pair

The non-parallel counter-rotating vortex-pair base flow computed by PNS in Section 4.4 is now analyzed by PSE-3D, since it is the only analysis methodology capable to it, regardless the prohibitively expensive TriGlobal instability analysis. The next results are corresponding to fixed $Re = 3000$ and $\omega = 2.55$. The computational domain in the $y - z$ plane is truncated at $(y_\infty, z_\infty) = (35, 35)$. It is discretized using $N_y \times N_z = 181 \times 121$ FD-q10 nodes mapped by equation (2.59) setting $c_z = 0.85$ and $c_y = 0.93$, but the case with $d = 8$, in which $N_y = 201$.

Firstly, the spatial BiGlobal analysis is used to obtain the most spatial amplified eigenmode for the initial integration station. Two eigenmodes are found with equal growth rate, one symmetric and another antisymmetric. Figure 5.6 shows the shape functions of the most spatially amplified modes, corresponding to the $d = 6$ case. The spatial structure is similar to the

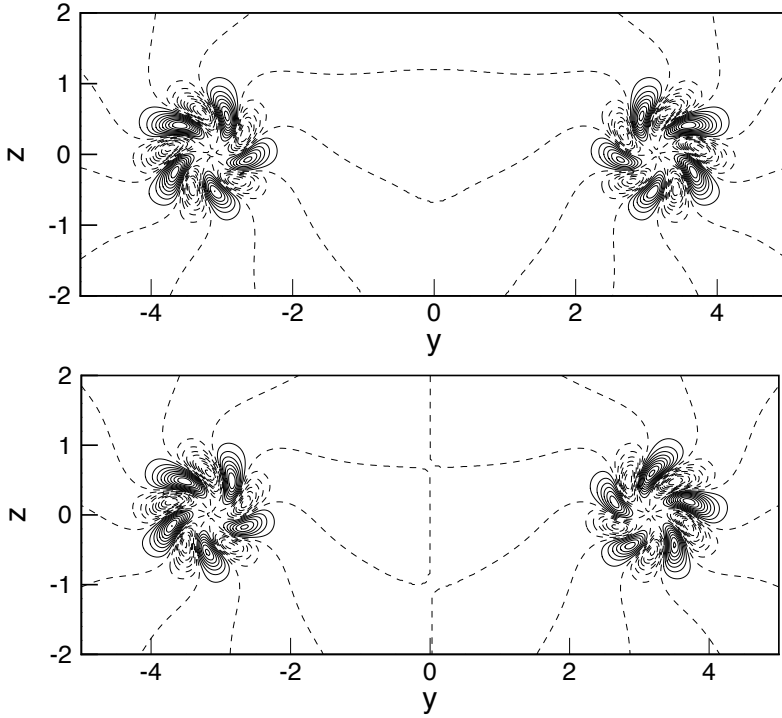


Figure 5.6: The most unstable eigenmodes of the counter-rotating Batchelor vortex (4.21-4.23) with $d = 6$, $\gamma_0 = 0.8$ and $\kappa_0 = 0.4$ at $Re = 3000$ and $\omega = 2.55$, (*upper*) symmetric and (*lower*) antisymmetric eigenmodes plotted with iso-contours $\hat{u}/|u| = (-0.9 : 0.1 : 0.9)$ of normalized real part of axial velocity amplitude function (dashed lines correspond to negative values).

eigenfunction recovered for the isolated vortex flow analysis, with five lobes per vortex, $m = 5$. Same shape functions is observed for $d = 4$ and $d = 8$ with same parameters.

Figure 5.7 shows the axial evolution of the wavenumber $\alpha_r(x)$ and the amplification rate $-\alpha_i(x)$, these curve are identical for both symmetric and antisymmetric eigenmodes. As the vortices are initially located farther, more similarities are found with the isolated vortex analysis results. The trend of the curve changes when the vortices are initially located closer, $d = 4$. Surprisingly, the stabilization of the flow is inverted from $x \approx 10$ to $x \approx 25$.

Figure 5.8 shows the iso-surfaces of axial vorticity flowfield for the initial most unstable perturbations (plotting the symmetric eigenmode). The inho-

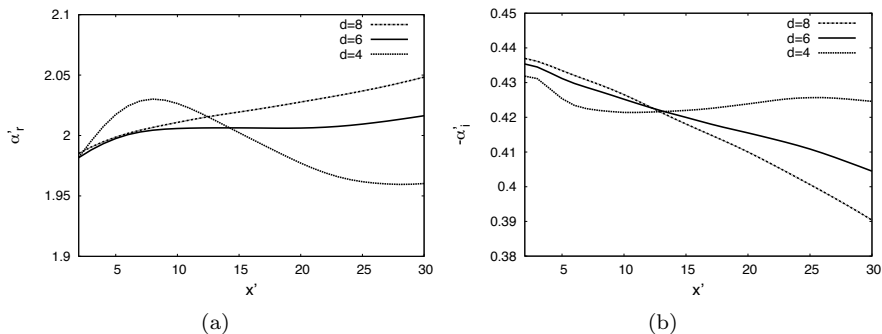


Figure 5.7: Evolution of (a) wavenumber and (b) growth rate for the counter-rotating non-parallel vortex-pair flow with $\gamma_0 = 0.8$ and $\kappa_0 = 0.4$ initial parameters, at $Re = 3000$ and frequency $\omega = 2.55$, corresponding the leading spatial eigenmode for three different initial distances between vortices $d = 4, 6$ and 8 .

mogeneous nature of the underlying flow is evident in the non-axisymmetric shape of the amplitude functions of perturbations.

5.3 Summary and conclusions

The combination of parabolized equations, PNS equations for the computation of steady base flows and PSE-3D methodology for their latter stability analysis, is found to be the best candidate for the analysis of spatial developing vortical flows and extensively to a wide range of complex three-dimensional flows with a slow-varying spatial direction, instead of using a fully three-dimensional spatially evolving DNS and thus saving several orders-of-magnitude of computational effort. Two different flows have been analyzed, the realistic non-parallel trailing line vortex and a system of two counter-rotating vortices, whose are allowed to interact. Spatial BiGlobal EVP and PSE-3D analysis have been developed and validated with results of local analysis and PSE upon the previously mentioned base flows. Comparisons of local and non-local stability analyses of an isolated vortex, by spatial BiGlobal and PSE-3D methodologies respectively, showed saturation of modal growth due to viscous spread in the downstream direction, as opposed to the uninhibited axial growth predicted by the local analysis of a parallel vortex. Results of conventional PSE in cylindrical coordinates, using spectral collocation methods, and PSE-3D in a rectangular domain, using high-order finite difference schemes [103], analyses upon the non-parallel iso-

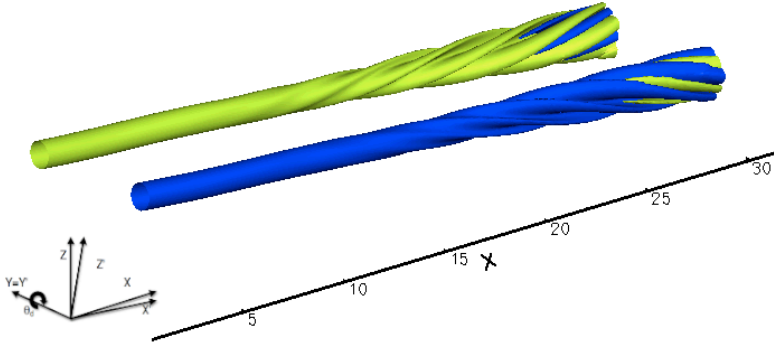


Figure 5.8: Iso-surfaces of axial vorticity flow field ($\zeta = \bar{\zeta} + \varepsilon\tilde{\zeta} = \pm 0.6$) with $\varepsilon = 10^{-5}/|\tilde{\zeta}_0|$ for the initial most unstable perturbations (plotting the symmetric eigenmode) with the selected parameters for the base flow ($\kappa_0 = 0.4$, $\gamma_0 = 0.8$, $d = 6$) at $Re = 3000$ and $\omega = 2.55$.

lated vortex base flow are compared as a cross-validation test showing excellent agreement. Furthermore, the leading spatial eigenmode is computed at each station by spatial BiGlobal analysis, showing important discrepancies between local and non-local analyses, showing the need of taking into account the non-parallel velocity term, the radial velocity, and the dependence of the base flow on the axial direction. In the case of a pair of counter-rotating vortices, the results showed similar results to those of the isolated vortex flow, but the stabilization process is suppressed as the vortices are initially located closer.

Chapter 6

Global analysis of an isothermal turbulent swirling combustor flow

6.1 Introduction

Swirling jet flows are the fundamental component of modern combustors, which in turn are an essential component of gas turbines, ramjets or scramjet engines. The swirl flow is employed for aerodynamic flame stabilization. It leads to vortex breakdown and large regions of reversed flow, acting as a flame anchor. However, swirling flows are often prone to self-excited flow oscillations that are manifested in large-scale helical flow structures, featuring a precessing vortex core (PVC) [239]. The starting point for an analytical assessment of the mechanisms that cause the PVC was its interpretation as an unstable global mode triggered by an inherent flow resonance [69, 150, 182]. This concept is further developed in this Chapter by conducting global linear stability analysis on the time- and phase-averaged flow field.

Since the seminal experiments conducted by Crow and Champagne [48], it is generally accepted that turbulent flows are organized by orderly quasi-deterministic coherent structures (CS). Follow-up work has shown that these structures comprise large portions of the overall kinetic energy, being responsible for noise [64], mixing [42], cross-stream momentum transfer [84], and many other unsteady flow phenomena. Nowadays, the analysis and modeling of CS plays an important role in modern flow data analysis strategies. The enormous data sets of flow quantities at high spatial and temporal resolutions provided by the modern experimental and numerical methods must be analyzed in order to extract the main flow features. The flow dynamic models describe the dominant flow structures within a low-dimensional subspace of the original data set and result to be the best candidate for this issue. The reconstruction of the CS may either be entirely empirical (empirical mode construction) or based on physical equations (physical mode construction). Physical modes are superior to empirical modes, since they are derived from the governing equations and provide information about

physical cause and effect of phenomena. For instance, a linear stability analysis allows differentiating between globally unstable flows that promote self-excited single-tone flow oscillations (oscillator flows; see e.g. the Karmán vortex street) and convectively unstable flows that promote a wide range of frequencies (amplifier flows; see e.g. the 2D mixing layer) [107].

The Proper Orthogonal Decomposition (POD) is the most used empirical CS reconstruction scheme, where turbulent flow data is expressed as series of orthogonal modes that are optimal in terms of energy content [83]. High energetic CS are well captured by this method [182], while frequency-ranked mode decomposition techniques are more appropriate when the energy of the structure of interest is low [212]. Empirical modes are typically used for efficient reduced order models that can be employed for closed-loop control applications [180]. On the other hand, the most representative physical mode reconstruction method is the modal linear stability analysis theory [57]. This theory is conventionally applied to low Reynolds number laminar steady flow solutions to study the flow bifurcation from a steady to an unsteady state. Such an analysis is highly valuable to describe the initial onset of instability, but it is incapable to describe the flow fluctuations at post-critical/transitional (turbulent/limit-cycle) conditions.

In order to model CS at the limit-cycle, modal instability analysis is applied to the turbulent flow, which requires additional assumptions: Firstly, the CS are seen as a superposition of instability modes with their scales to be much larger than those of the background turbulence. Secondly, the linear stability analysis is based on the time-averaged flow that represents the saturated state of the stability modes. Nonlinear interactions between the mean flow and the CS are thereby inherently accounted for, while mode-mode interactions are neglected. While the validity of the first assumptions can be readily shown, the justification of the second is difficult. Examples supporting the mean flow stability analysis are the mixing layer [70], the cylinder wake [14, 173, 192], the vortex breakdown bubble [182], the swirling jet [183], and natural and forced jets [88]. The listed examples demonstrate the high potential of the physical mode construction based on the mean turbulent flow. Particularly the most recent investigations show a good quantitative agreement between the CS and the stability eigenmodes and, most importantly, provide information about the cause and the effect. The analysis reveals the source of the flow oscillations, and how they are affected by, e.g., fluidic excitation [256], density stratification [184], or volume forces [173].

Despite of these inspiring examples, the application of linear stability analysis to turbulent flows is far from being common practice. Mean flow

stability wave models have the reputation of being inaccurate and not rigorously valid, and therefore, most investigations are still restricted to the analysis of stationary base flows, whose flow conditions are far from those corresponding to typical industrial applications.

In the present Chapter, the global mode in a strongly swirling turbulent combustor flow undergoing vortex breakdown is experimentally and analytically investigated. The experiment shows a self-excited global flow oscillation at a well-defined frequency. Based on the mean flow field, global hydrodynamic stability analysis is carried out. The dampening effect of the Reynolds stresses are accounted for by an estimated eddy viscosity. The global analysis successfully predicts the frequency of the global mode and, in addition to that, yields the global shape of the instability. The results show a precession of the vortex core and synchronized Kelvin-Helmholtz instabilities in the shear layers. In gas turbine combustors, the flow oscillations cause large-scale flame oscillation and may couple with thermoacoustic instabilities, proving the practical relevance of the investigated global mode.

6.2 Theory

6.2.1 Stability analysis of turbulent mean flows

In the present analysis, the flow of interest is unsteady and non-periodic. Therefore, the triple decomposition theory proposed by Hussain and Reynolds [110] is used to distinguish between the time-averaged base flow $\bar{\mathbf{q}}(\mathbf{x})$, the coherent or instability perturbations $\tilde{\mathbf{q}}(\mathbf{x}, \mathbf{t})$ and the stochastic or turbulent fluctuations $\mathbf{q}'(\mathbf{x}, \mathbf{t})$:

$$\mathbf{q}(\mathbf{x}, \mathbf{t}) = \bar{\mathbf{q}}(\mathbf{x}) + \tilde{\mathbf{q}}(\mathbf{x}, \mathbf{t}) + \mathbf{q}'(\mathbf{x}, \mathbf{t}) \quad (6.1)$$

Note that for a steady base flow $\mathbf{q}'(\mathbf{x}, \mathbf{t}) = \mathbf{0}$. The three components of equation (6.1) are defined as

$$\bar{\mathbf{q}}(\mathbf{x}) = \lim_{\mathcal{T} \rightarrow \infty} \frac{1}{\mathcal{T}} \int_0^{\mathcal{T}} \mathbf{q}(\mathbf{x}, \mathbf{t}) \mathbf{d}\mathbf{t}, \quad (6.2)$$

$$\tilde{\mathbf{q}}(\mathbf{x}, \mathbf{t}) = \langle \mathbf{q}(\mathbf{x}, \mathbf{t}) \rangle - \bar{\mathbf{q}}(\mathbf{x}), \quad (6.3)$$

$$\mathbf{q}'(\mathbf{x}, \mathbf{t}) = \mathbf{q}(\mathbf{x}, \mathbf{t}) - \langle \mathbf{q}(\mathbf{x}, \mathbf{t}) \rangle, \quad (6.4)$$

where the phase average is defined as

$$\langle \mathbf{q}(\mathbf{x}, \mathbf{t}) \rangle = \frac{1}{N} \sum_{n=0}^N \mathbf{q} \left(\mathbf{x}, \mathbf{t} + \frac{\mathbf{n}}{\mathbf{f}} \right), \quad (6.5)$$

with f being the frequency of the coherent perturbation and N the number of cycles used in the phase average.

The evolution equations for $\tilde{\mathbf{q}}(\mathbf{x}, \mathbf{t})$ are derived by substituting equation (6.1) into the Navier-Stokes equations (1.6-1.7). For an incompressible flow, each individual component of equation (6.1) conserves continuity. The momentum equation for $\tilde{\mathbf{q}}$ is derived phase averaging the equations and then subtracting away the time-averaged mean of the phase-averaged equations. The resulting continuity and momentum equations of the perturbations are given by

$$\begin{aligned} \nabla \cdot \tilde{\mathbf{u}} &= 0, & (6.6) \\ \left[\frac{\partial \tilde{\mathbf{u}}}{\partial t} + (\bar{\mathbf{u}} \cdot \nabla) \tilde{\mathbf{u}} + (\tilde{\mathbf{u}} \cdot \nabla) \bar{\mathbf{u}} \right] + \nabla \tilde{p} - \frac{1}{Re} \Delta \tilde{\mathbf{u}} &= -\nabla \cdot (\boldsymbol{\tau}^R + \boldsymbol{\tau}^N) \end{aligned} \quad (6.7)$$

where $\boldsymbol{\tau}^N \equiv \tilde{\mathbf{u}}\tilde{\mathbf{u}} - \overline{\tilde{\mathbf{u}}\tilde{\mathbf{u}}}$ are the non-linear terms, which are removed assuming small-amplitude perturbations, and

$$\boldsymbol{\tau}^R \equiv \langle \mathbf{u}'\mathbf{u}' \rangle - \overline{\mathbf{u}'\mathbf{u}'} = \widetilde{\mathbf{u}'\mathbf{u}'}, \quad (6.8)$$

are the remaining stresses.

These equations show that the coherent part interacts with the mean flow through the generation of coherent Reynolds stresses, the turbulent (incoherent) part interacts with the mean flow through the generation of turbulent Reynolds stresses, while the coherent part and the turbulent part interact through phase-averaged turbulent Reynolds stresses; see [205] for further details. The mean-coherent and mean-turbulent interactions are readily incorporated through the analysis of the actual mean flow, while the coherent-turbulent interactions must be accounted for by employing a turbulence model. Particularly the latter is often ignored, which leads to a wrong estimation of the CS's growth rates [70, 88].

6.2.2 Eddy-viscosity closure

In order to resolve the equations (6.6-6.7), a model relating $\boldsymbol{\tau}^R$ to $\tilde{\mathbf{q}}$ is required. In the present work, the turbulent stresses are modeled with an eddy viscosity, redefining the viscosity of the problem as the sum of the molecular plus the eddy viscosities $\nu \rightarrow \nu + \nu_t$. The well-known Boussinesq's eddy-viscosity approximation assumes that the Reynolds stresses are the product of the mean strain-rate tensor and turbulent viscosity ν_t . This is analogously to the viscous stresses in Newtonian fluids that are determined by the molecular viscosity ν and the strain-rate tensor. For a constant density flow this

hypothesis can be written as in [273]:

$$-\overline{u'_i u'_j} = \nu_t \left(\frac{\partial \bar{u}_i}{\partial x_j} + \frac{\partial \bar{u}_j}{\partial x_i} \right) - \frac{2}{3} k \delta_{ij}. \quad (6.9)$$

The turbulent kinetic energy (TKE) k is introduced to avoid an inconsistency with the continuity equation [112]. The aim is to describe the stress tensor with only one turbulent viscosity. Thus, for a three-dimensional flow, as the swirling jet, the system of equations (6.9) is overdetermined. An optimal representation of ν_t is obtained using a least-square fit over all resolved Reynolds stresses [112]

$$\nu_t = \frac{\left(-\overline{u'_i u'_j} + \frac{2}{3} k \delta_{ij} \right) \cdot \left(\frac{\partial \bar{u}_j}{\partial x_i} + \frac{\partial \bar{u}_i}{\partial x_j} \right)}{\left(\frac{\partial \bar{u}_k}{\partial x_l} + \frac{\partial \bar{u}_l}{\partial x_k} \right) \cdot \left(\frac{\partial \bar{u}_k}{\partial x_l} + \frac{\partial \bar{u}_l}{\partial x_k} \right)}, \quad (6.10)$$

with the summation over the repeating indices i, j, k , and $l = 1, 2, 3$.

6.2.3 Global analysis of axisymmetric flows

The swirling jet flow is axisymmetric, what translates that mean flow is homogeneous in the azimuthal direction, $\bar{\mathbf{q}} = \bar{\mathbf{q}}(x, r)$. Therefore, the equations (6.6-6.7) are expressed in cylindrical coordinates and the perturbations are written as

$$\tilde{\mathbf{q}}(x, r, \theta, t) = \hat{\mathbf{q}}(x, r) \exp[i(m\theta - \omega t)] + \text{c.c.}, \quad (6.11)$$

where $\hat{\mathbf{q}}$ represents the vector of two-dimensional amplitude functions, m is the azimuthal wavenumber, ω is the circular frequency and c.c. refers to complex conjugate.

Introducing the perturbation variables decomposition of equation (6.11) in equations (6.6-6.7), the temporal BiGlobal EVP (1.26) is recovered. Written using matrix notation, the operators \mathcal{A} and \mathcal{B} become

$$\mathcal{A} = \begin{pmatrix} \mathcal{L} + \bar{u}_x & \bar{u}_r & 0 & \mathcal{D}_x \\ \bar{v}_x & \mathcal{L} + \bar{v}_r + \frac{1}{Re r^2} & -\frac{2\bar{w}}{r} + \frac{2im}{Re r^2} & \frac{im}{r} \\ \bar{w}_x & \bar{w}_r + \frac{\bar{w}}{r} - \frac{2im}{Re r^2} & \mathcal{L} + \frac{\bar{v}}{r} + \frac{1}{Re r^2} & \frac{im}{r} \\ \mathcal{D}_x & \frac{1}{r} \mathcal{D}_r r & \frac{im}{r} & 0 \end{pmatrix},$$

$$\mathcal{B} = \begin{pmatrix} i & 0 & 0 & 0 \\ 0 & i & 0 & 0 \\ 0 & 0 & i & 0 \\ 0 & 0 & 0 & 0 \end{pmatrix}, \quad (6.12)$$

where $\mathcal{L} = \bar{u}\mathcal{D}_x + \bar{v}\mathcal{D}_r + \frac{\bar{w}}{r}im - \frac{1}{Re} \left(\mathcal{D}_{xx}^2 + \frac{1}{r}\mathcal{D}_r + \mathcal{D}_{rr} + \frac{m^2}{r^2} \right)$.

The elliptic EVP (1.26) is complemented with the next boundary conditions. Dealing firstly with the streamwise direction, homogeneous Neumann conditions are imposed at the inlet, homogeneous Dirichlet conditions at the walls and decay of perturbations through the imposition of a sponge region at the outlet, setting homogeneous Dirichlet boundary conditions. The main objective of this sponge region is to avoid spurious reflections. This is achieved by artificially decreasing the local Reynolds number, in the exit region, using a smooth function, say a hyperbolic tangent. The sponging strength is defined as the ratio of the decrease in the Reynolds number between the flow and the exit, to the Reynolds number of the flow. Sponging strengths of between 80% and 90% have been used. The sponged length is the fraction of the domain over which the sponging is applied, ranging from 10 to 20%. Within this range of strengths and lengths, it is seen that the results remain insensitive. For the radial coordinate, a sponge region is also used at the top boundary $r = r_m$ and homogeneous Dirichlet boundary conditions are imposed for the three velocity components. The same sponge technique was successfully used by Meliga et al. [172] for recovering the global modes of a swirling jet flow.

At the radial axis $r = 0$, the boundary conditions, originally derived by Batchelor [17], are

$$\frac{\partial \hat{u}}{\partial r} = \hat{v} = \hat{w} = 0, \quad \text{if } m = 0, \quad (6.13)$$

$$\hat{u} = \frac{\partial \hat{v}}{\partial r} = \hat{v} + m\hat{w} = 0, \quad \text{if } |m| = 1, \quad (6.14)$$

$$\hat{u} = \hat{v} = \hat{w} = 0, \quad \text{if } |m| > 1. \quad (6.15)$$

In order to avoid the use of artificial pressure boundary conditions, the pressure and continuity equation are enforced at the mid grid points. This method, so called staggered grid, was successfully used for first time in cylindrical coordinates for local stability analysis by Khorrami [122] using Chebyshev spectral collocation discretization.

Since this flow problem requires a mild clustering of points at the inflow boundary, the equation used to map the calculation domain $x \in [0, x_m]$ and $r \in [0, r_m]$ into the FD-q grid is equation (2.60). The selected mapping parameters are $x_h = 2$ and $x_m = 6$. The same equation is used for mapping the radial coordinate, setting $r_h = 1$ and $r_m = 3.2$.

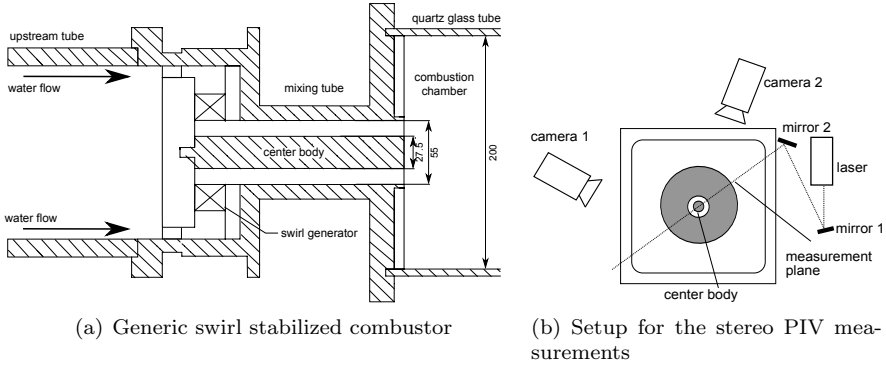


Figure 6.1: Generic burner and stereo PIV setup

6.3 Experimental setup

The swirling jet under investigation is created from a swirl-stabilized model combustor, as depicted in figure 6.1(a). It consists of an adjustable radial swirl generator, where the angular momentum is imparted on the flow. The amount of swirl was set to a theoretical swirl number of $S = 0.9$ [141] for the experiments. This swirl number is defined as

$$S = \frac{G_t}{R \cdot G_a} = \frac{2\pi\rho \int_0^R uwr^2 dr}{R \cdot 2\pi\rho \int_0^R (u^2 - 0.5w^2)r dr}, \quad (6.16)$$

where R is the hydraulic radius of the burner and G_t and G_a are the axial fluxes of tangential and axial momentum, respectively.

Downstream of the swirl generator the fluid passes an annular duct of 55 mm outer diameter and 27.5 mm inner diameter, which serves to enhance the fuel-air mixing under reacting conditions. The combustion chamber downstream of the duct has a diameter of 200 mm, a length of 300 mm and open exit boundary conditions.

The flow measurements were carried out in a vertically oriented water tunnel test facility at TU Berlin. The water is filtered at the bottom of the storage tank in order to reduce perturbations by non-seeding particles and air bubbles during testing. A flow straightener upstream of the test section homogenizes the velocity inlet profile and a rotary vane flow meter measures the water mass flow ($\pm 5\%$). The stereo PIV measurement system, shown in figure 6.1(b), consists of two PCO Sensicams and an Nd:YAG laser operating at 4 Hz with a pulse energy of 20 mJ. The flow is seeded with silver coated

hollow glass spheres of a nominal diameter of $15\ \mu\text{m}$. The laser sheet is aligned at an angle of $\approx 45^\circ$ to the windows of the rectangular test section and the cameras are aligned in an angle of $\approx 45^\circ$ to the laser sheet. Time resolved pressure data was recorded using a sensor located in burner mouth.

6.4 Results

The global mode in a strongly swirling turbulent combustor flow undergoing vortex breakdown is experimentally and analytically investigated. The experiment shows a self-excited global flow oscillation at a well-defined frequency. Based on the mean flow field, global hydrodynamic stability analysis is carried out.

6.4.1 Experimental observations

The flow studied here is the time- and azimuthally-averaged mean flow recovered by PIV experiments. The non-dimensionalisation of the equations and variables is performed using the hydraulic diameter of the combustor inlet as reference length scale, $l_r^* = D_h = 27.5\ \text{mm}$, and the inlet bulk velocity $u_r^* = 1\ \text{m/s}$ as reference velocity. The flow field inside the combustor, as depicted in figure 6.2, is composed of an emanating jet and large zones of recirculating fluid. An inner recirculation zone is located around the centerline and an outer recirculation zone near the combustor walls. In between the jet and the recirculation zones, turbulent shear layers are formed. The tangential velocities show a solid body rotation in the vortex core and a decay of the tangential velocities for higher radius. The solid body rotational speed decay quickly with the distance from the combustor inlet. The highest levels of the turbulent kinetic energy (TKE), as shown in figure 6.3(a), are encountered near the combustor inlet on the centerline and in the inner shear layers. Figure 6.3(b) shows that the calculated eddy viscosity (6.10), in contrast to the TKE, peaks in the shear layers only up to axial locations of $x^*/D_h = 3.3$.

The spectrum of the pressure signal located at the burner, depicted in figure 6.4, shows a clear peak at $9.25\ \text{Hz}$, indicating a strong periodic oscillation. The second peak is at the double frequency of $18.5\ \text{Hz}$ and corresponds to the first harmonic of the oscillation. The resulting measured Strouhal number is $St = f^* D_h/u_r^* = 0.26$ and the dimensionless circular frequency $\omega = 2\pi St = 1.61$.

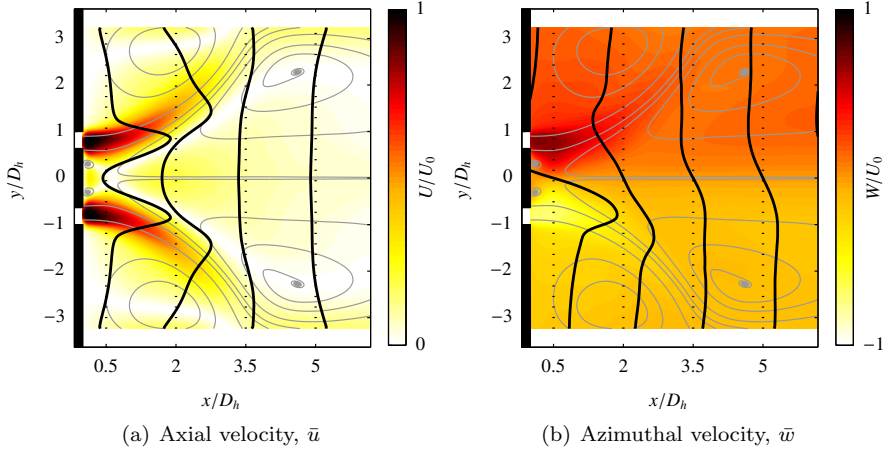


Figure 6.2: Time-averaged flow field

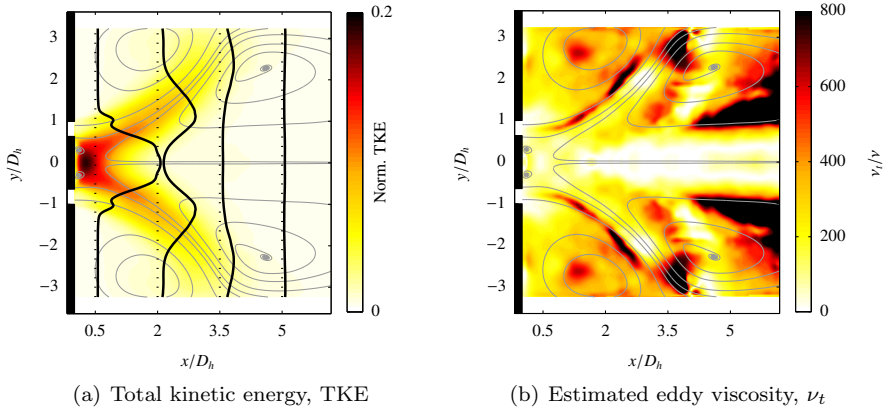


Figure 6.3: Flow field turbulence properties

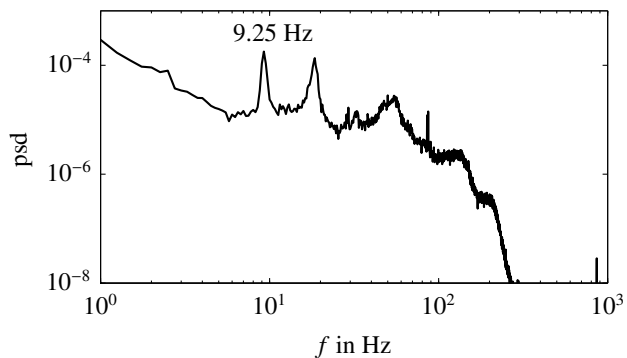


Figure 6.4: PSD of the pressure signal at the burner

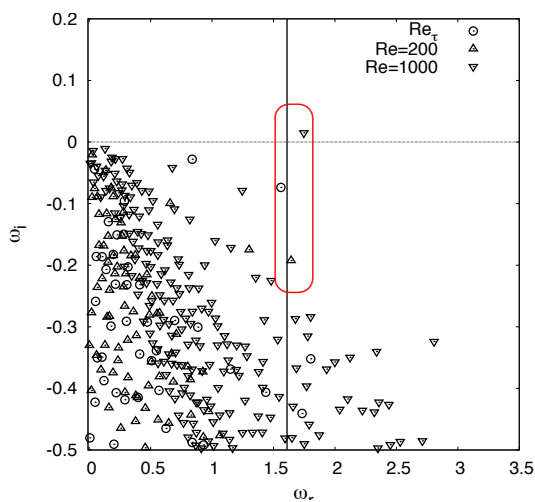


Figure 6.5: Eigenvalues of the global analysis for two fixed Reynolds numbers, $Re = 200$ and 1000 , and the eddy viscosity based Re_τ . The vertical black line denotes the instability frequency observed in the experiment. The eigenvalues described in the text are enclosed by the red line.

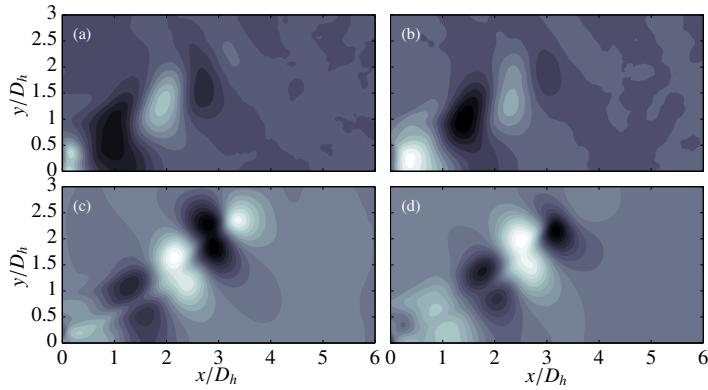


Figure 6.6: Radial velocity comparisons of the instability reconstructed from the experimental data via POD, being (a) \hat{v}_r and (b) \hat{v}_i , and the eigenfunction calculated by global analysis for the Reynolds number based on the eddy viscosity, being (c) \hat{v}_r and (d) \hat{v}_i

6.4.2 Global instability analysis

Results of the global analysis, setting $m = 1$ to capture the global helical mode (PVC), are presented in figure 6.5 for two different fixed swirl Reynolds numbers and the Reynolds number based on the calculated eddy viscosity. For the highest Reynolds number, an unstable mode is predicted at a slightly higher frequency than encountered in the experiments. For the lowest Reynolds number, a stable mode with a very similar frequency as in the experiments is calculated. With the incorporated eddy viscosity, a slightly stable mode is found at a frequency close to the measured frequency. The eigenfunctions corresponding to this eigenvalue are depicted in figure 6.6 and compared to the shape of the global mode reconstructed from the experimental data via a POD [182]. It is evident that both modes describe a similar wave pattern located in the shear layers. Some deviations exist in the distribution of the oscillation amplitude. In the experiments, it is more concentrated near the burner inlet and the axial decay is faster. However, the excellent agreement of the frequency and the reasonable agreement of the mode shape provide sufficient evidence that the global stability analysis captures the flow instability.

6.5 Summary and conclusions

The present study investigates the instability mechanisms of an isothermal turbulent swirling jet flow, simulating an annular combustor flow. The study focuses on the global stability analysis of a turbulent mean flow extracted from stereo PIV measurements at TU Berlin, by applying the triple decomposition theory proposed by Hussain and Reynolds [110]. The dampening effect of the Reynolds stresses are accounted for by an estimated eddy viscosity.

A self-excited oscillation was clearly visible from the experimental measurements. The POD decomposition of the experimental data unraveled a helical instability. The global instability results show a very good agreement to the experiments, predicting the measured frequency and helical amplitude function. The comparison of the later shows a very similar phase velocity between the most energetic POD mode and the shape function of the global mode, which peaks along the burner inlet axis and shear-layer. This provides strong evidence that the instability, including the precession of the vortex core (PVC) and the Kelvin-Helmholtz instability, is the manifestation of one global mode, what is usually explained in the literature as two unrelated instability mechanisms [151].

Although it is not shown here, local stability analysis was conducted on the same mean flow and the results also successfully predict the instability frequency. Furthermore, it provided the location of the wave maker of the instability. This wave maker is assumed to be of utmost importance for the manipulation of the instability. This can be by means of flow control or due to changes in the flow field in the presence of a flame in the swirling combustor flow.

Chapter 7

Instability study of the wake behind a discrete roughness element in high speed boundary-layers

7.1 Introduction

Experimental observations indicate that the dominant laminar-turbulent transition mechanisms in boundary-layers can be greatly modified by the presence of localized or distributed roughness, leading to a significant acceleration of the transition process both in noisy and in quiet environments [44, 67, 130, 226, 241]. Over the years, a number of possible scenarios have been postulated to explain these observations. However, despite the numerous research efforts, the underlying physical mechanisms responsible for roughness-induced transition are only partly understood. Consequently high speed vehicle design still relies on empirical transition-prediction criteria [197]. A deeper understanding of the effects of roughness on the stability of boundary-layers is thus urgently needed since it is particularly important for high speed applications, where transition to turbulence leads to a significant increase of both the skin-friction and the wall heat-transfer, with obvious implications for the design of high speed vehicles.

The early experiments of Klebanoff and Tidstrom [130] showed that discrete two-dimensional roughness elements may lead to an acceleration of the transition process due to the modified stability of the tripped boundary-layer. In particular, the growth of Tollmien-Schlichting (TS) waves was found to be enhanced by the two-dimensional roughness element. The effects of localized two-dimensional roughness elements on the stability of a compressible boundary-layer at $M = 4.5$ have recently been studied through direct numerical simulations (DNS) by Marxen et al. [169], who showed that the roughness element induces a sudden disturbance amplification (over a limited frequency band) in its vicinity but does not affect the boundary-layer stability characteristics further downstream. The sudden amplification appears to

be due to the phase-locked linear superposition of the first boundary-layer mode with a stable mode excited by the roughness element, resulting in transient energy growth. This result seems to be in line with a mechanism, originally proposed by Ruban [213] and Goldstein [75] and studied theoretically by Crouch [45] and Choudhari and Street [38], by which the interaction of free-stream disturbances with localized surface geometrical distortions can excite disturbances *tuned* (in frequency and phase speed) with the boundary-layer instability eigenmodes. An example of this mechanism for three-dimensional localized roughness elements, in the context of compressible boundary-layers, was reported in the DNS results of Balakumar [12]. However, the effect of three-dimensional roughness elements on the stability of boundary-layers seems to extend beyond the enhancement of the receptivity, that is conversion of external disturbance in boundary-layer modes, and/or amplification of boundary-layer modes. Three-dimensional roughness elements often induce subcritical disturbance amplification, leading to a “bypass”-like laminar-turbulent transition. In fact, bypass and roughness-induced transition to turbulence appear to share numerous similarities, at least in the incompressible flow regime.

Bypass transition may take place when moderate or large free-stream disturbances enter the boundary-layer and give rise to high- and low-velocity streaks through the *lift-up* mechanism of Landahl [133] [see also 4, 7, 108, 114, 199, 203]. The streaks may then interact nonlinearly with each other [29] or undergo a secondary instability before breaking down into turbulence [8]. Investigations into the secondary instability of streaks in boundary-layers have been conducted mainly for incompressible flows. The early experiments of Swearingen and Blackwelder [238] show that low velocity streaks, appearing following the formation of Görtler vortices in a concave wall boundary-layer, can sustain both sinuous (anti-symmetric) and varicose (symmetric) instabilities, the former being more prominent. More recently Asai et al. [10] experimentally investigated the linear instability of a single boundary-layer streak, showing that under certain conditions (mainly depending on the geometry of the three-dimensional high-shear layer surrounding the streak) the varicose mode can be more unstable than the sinuous mode. In the nonlinear transition stages, quasi-streamwise vortices and hairpin vortices form following a sinuous and a varicose streak instability, respectively. The growth of the varicose mode was found to be the consequence of a Kelvin-Helmholtz instability of the wall-normal detached high-shear layer, while the sinuous mode develops due to an instability of the lateral high-shear layers. Numerical simulations performed by Andersson et al. [8] indicate that the streak instability starts appearing in the form of a sinuous perturbation for streak amplitudes of about 26% of the free-stream velocity, while varicose distur-

bances become unstable only for streak amplitudes larger than 37%. Their inviscid stability simulations indicate that the sinuous mode grows faster than the varicose instability; a result which was also reported by Wu and Choudhari [276].

Roughness-induced transition may follow a similar path. In fact, the flow behind small three-dimensional localized roughness elements is characterized by the presence of counter-rotating streamwise vortices [see for example 71, 117, 206, 262], which through the “lift-up” effect can potentially lead to strong algebraic growth of boundary-layer streaks and breakdown to turbulence. A model based on the transient growth mechanism was proposed by Reshotko and Tumin [204] to predict roughness-induced transition, following a similar approach to that of Andersson et al. [8] for the bypass transition scenario. The model suggests that the transition Reynolds number (based on the momentum thickness θ) varies according to $(h/\theta)^{-1}$ for stagnation point flow with constant wall temperature, thereby agreeing with the ballistic-range data presented by Reda [197]. Reda’s review provides a detailed analysis of the available experimental data for a variety of different flows and provides strong evidence of the importance of the critical roughness Reynolds number approach ($Re_h = \bar{u}_h h / \nu_h$, where \bar{u}_h and ν_h are the streamwise velocity and kinematic viscosity taken at $y = h$ in the corresponding clean flat plate boundary-layer) for modeling laminar-turbulent transition induced by localized and distributed roughness. However, Reda also concludes that a universal critical Re_h will not be found, given the large number of different flow conditions and roughness patterns possible. Somewhat in contrast with this view, Horvath et al. [105] propose a transition criterion for isolated roughness elements based on the parameter momentum thickness Reynolds number divided by the boundary-layer edge Mach number. Critical values of this parameter appear to scale linearly (on a logarithmic scale) with the roughness height divided by the local boundary-layer thickness.

A parametric study of the effects of localized smooth roughness elements on the laminar-turbulent transition occurring in supersonic flat-plate boundary-layers was recently performed by Redford et al. [200] using DNS. Their results indicate that transition is promoted provided Re_h exceeds a critical value which increases as the parameter $M_h \bar{T}_\infty / \bar{T}_w$ increases, where M_h is the Mach number calculated at the roughness edge and \bar{T}_w is the wall temperature. They proposed a roughness-induced transition map which suggests a critical value of $Re_h = 300$ for $M_h \bar{T}_\infty / \bar{T}_w = 0$. These findings were confirmed by Bernardini et al. [20], who proposed a modified version of roughness Reynolds number $Re_h^* = \bar{u}_h h / \nu_w$, with the kinematic viscosity taken at the wall, which has a constant critical value of $Re_h^* = 460$.

The criteria mentioned above represent a useful tool for predicting transition induced by an isolated roughness element, without attempting to provide a physical explanation of the flow instability and transition to turbulence. In order to gain a better understanding of the physical mechanisms driving the roughness-induced transition process Choudhari and co-workers [40, 119] analyzed the growth of instabilities in the wake of diamond-shaped roughness elements at $M = 3.5$, both experimentally and through BiGlobal linear stability calculations. The results show that both sinuous and varicose modes can grow substantially in the linear stages of the transition process. For $Re_h = 426$ the experiments show that the transition process is driven by the varicose mode, while the sinuous mode dominates for $Re_h = 319$. This result is in agreement with the BiGlobal stability simulations, which show that the sinuous mode becomes more dominant for decreasing Re_h . The BiGlobal stability results also suggest that the varicose mode growth rate decreases more rapidly than that of the sinuous mode with increasing streamwise distance, suggesting that the latter mode may drive the final breakdown to turbulence even for high Re_h . Experimentally obtained mode shapes were found to be in good qualitative agreement with the eigenfunctions extracted from the BiGlobal stability analysis. Groskopf et al. [87] studied the instability induced by discrete three-dimensional roughness elements in a $M = 4.8$ boundary-layer, reporting good agreement between BiGlobal stability simulations and DNS. Further experimental results demonstrating the importance of the roughness wake instability as the cause of the early laminar-turbulent transition observed in the presence of isolated roughness elements were reported by Kegerise et al. [120] and Owens et al. [186]. Recently Wheaton and Schneider [269, 270] have carried out a set of experiments on roughness-induced transition at $M = 6$, reporting the first quantitative measurements of the roughness wake instability at hypersonic speeds. For the same Mach number, the numerical simulations of De Tullio and Sandham [51] and Choudhari et al. [41] show that the roughness wake can sustain the growth of a number of different instability modes, the relative importance of which seems to depend on the specific flow conditions considered.

In the wake flow behind an isolated three-dimensional roughness element, a predominant spatial direction exists along which the mean flow properties vary slowly, while the flow varies rapidly in the crossflow directions. These properties are taken into account in the derivation of the three-dimensional parabolized stability equations (PSE-3D), which represent the most efficient simplified approach for the solution of the instability problem of such flows.

In what follows we study the linear stage of the laminar-turbulent transition process induced by a sharp-edged isolated roughness element embedded in a boundary-layer at two speed regimes, firstly at a supersonic Mach num-

ber $M = 2.5$ and secondly at a hypersonic regime, $M = 6$. The first Mach number is high enough for significant compressibility effects to be expected but below the Mach number at which higher modes of instability (Mack modes) develop, what occurs in the highest Mach number case. The linear instability of the flow is investigated through full Navier-Stokes (NS) simulations, spatial BiGlobal and linear PSE-3D stability analyses. Details about the breakdown to turbulence following the linear growth of instability modes is investigated by DNS in the work of De Tullio et al. [52] for the $M = 2.5$ case.

7.2 Theory

In order to compute the convectively unstable base flows analyzed here, the compressible Navier-Stokes equations (1.1-1.3) are solved numerically using high order finite-differences. The spatial discretization is treated using a standard fourth-order central difference scheme to calculate derivatives at internal points, while close to boundaries a stable boundary treatment by Carpenter et al. [35] is applied, giving overall fourth-order accuracy. Time integration is based on a third-order compact Runge-Kutta method [274] and an entropy splitting approach developed by Sandham et al. [220] is used to split the inviscid flux derivatives into conservative and non-conservative parts, thereby improving numerical stability. The code has multi-block capabilities and is made parallel (both intra- and inter-block) using the message-passing-interface (MPI) library. Details on the implementation of the numerical schemes can be found in Li [149] and Jones [116]. The multi-block version of the code used has been extensively validated [see for example 50, 277].

The study include the effects of one roughness element with dimensionless height equal to $h = 1$. The roughness element is placed at a non-dimensional distance $x_h = x_h^*/\delta_0^* = 50$. The laminar displacement thickness (δ^*) and the boundary-layer thickness (δ_{99}) grow in the streamwise direction according to

$$\frac{\delta^*(\tilde{x}^*)}{\delta_0^*} = \Delta \frac{\sqrt{2Re_{\tilde{x}^*}}}{Re_{\delta_0^*}} \quad \text{and} \quad \frac{\delta_{99}(\tilde{x}^*)}{\delta^*(\tilde{x}^*)} = \frac{\Delta_{99}}{\Delta}, \quad (7.1)$$

where

$$Re_{\tilde{x}^*} = \frac{1}{2} \left(\frac{Re_{\delta_0^*}}{\Delta} \right)^2 + Re_{\delta_0^*} \frac{x^*}{\delta_0^*}. \quad (7.2)$$

Equations (7.1) and (7.2) were derived from the similarity solution [see the section on the Illingworth transformation in 271]. Note that \tilde{x}^* is the dimen-

sional streamwise coordinate in a reference frame positioned at the flat-plate leading-edge. The scaling factors Δ and Δ_{99} are calculated as

$$\Delta = \int_0^\infty \left(\frac{\rho_\infty^*}{\rho^*} - \frac{u^*}{u_\infty^*} \right) d\eta \quad \text{and} \quad \Delta_{99} = \int_0^{\eta_{99}} \frac{\rho_\infty^*}{\rho^*} d\eta, \quad (7.3)$$

where $\eta = [(\rho_\infty^* u_\infty^*) / (2\mu_\infty^* \tilde{x}^*)]^{1/2} \int_0^{y^*} (\rho^*) / (\rho_\infty^*) dy^*$ is the non-dimensional similarity coordinate and η_{99} is obtained at y_{99}^* , where $u^* / u_\infty^* = 0.99$. Equation (7.2) provides a straightforward method of converting from the dimensionless simulation data to a reference system based on the flat-plate that would be used in an experiment.

The reference values for velocity (u_r^*), density (ρ_r^*), temperature (T_r^*) and dynamic viscosity (μ_r^*) are taken at the free stream, while the reference length is the displacement thickness of the laminar boundary-layer at the computational domain inflow, δ_0^* .

7.3 Results

7.3.1 Supersonic regime

The laminar-turbulent transition induced by a sharp-edged isolated roughness element in an supersonic boundary-layer is analyzed. It focuses on the linear instability of the wake induced by the isolated roughness element, the full Navier-Stokes equations are simulated and compared with BiGlobal and PSE-3D simulations. Dimensionless parameters which define the problem are the Reynolds number $Re_{\delta_0^*} = 3300$, the Mach number $M = 2.5$ and the Prandtl number $Pr = 0.72$.

The roughness height expressed in terms of δ_{99}^* of the surrounding undisturbed boundary-layer at streamwise location of the roughness element is $h^* / \delta_{99}^* = 0.44$. The roughness element has length $L = 6.0$ and same width. The walls are considered no-slip and isothermal with $\bar{T}_w = \bar{T}_{ad} = 2.05$, where \bar{T}_{ad} is the laminar adiabatic-wall temperature. The roughness Reynolds numbers of $Re_h = 791$ and modified roughness Reynolds numbers [20] $Re_h^* = 788$. More details can be found in De Tullio et al. [52].

During the linear instability study using direct numerical simulations, the laminar boundary-layer base flow is subjected to a time-varying density disturbance imposed at the inflow boundary, which is placed at $x_0 = 16$, so

that the inflow condition for density reads

$$\rho(x_0, y, z, t) = \bar{\rho}(x_0, y, z) + aG_w \sum_{m=1}^M \sum_{n=1}^N \cos(\beta_m z + \phi_m) \cos(\omega_n t + \psi_n), \quad (7.4)$$

with $N = 16$ and $M = 6$ as the number of frequencies and spanwise wavenumbers respectively, $\beta_m = m2\pi/L_z$, $\omega_n = n2\pi F_0$ with $F_0 = 0.02$. Note that the non-dimensional frequency $F = f^* \delta_0^*/u_\infty^*$, f^* being the dimensional frequency (cycles per second), takes the form of a Strouhal number. The phases ϕ_m and ψ_n are set to random numbers between 0 and 2π in order to avoid local peaks in the disturbance signal which might trigger undesired non-linearities. The damping function $G_w = 1 - \exp(-y^3)$ was used to control the disturbance location with respect to the boundary-layer; it is greater than zero inside the boundary-layer and zero at the wall. An additional damping was employed to drive the forcing function to zero at the top domain boundary to avoid the onset of numerical oscillations. A small amplitude of $a = 2 \times 10^{-6}$ is used to ensure the linearity of the dominating transition mechanisms, at least for the initial stages of the instability. The boundary-layer response to the inflow disturbances is characterized by considering an integrated disturbance energy norm given by

$$\begin{aligned} \mathcal{E}_\eta(x) &= \int_0^{\delta_{99}} |\check{\rho}|_{0,(\cdot)} \left[|\check{u}|_{\eta,(\cdot)}^2 + |\check{v}|_{\eta,(\cdot)}^2 + |\check{w}|_{\eta,(\cdot)}^2 \right] \\ &+ \frac{|\check{\rho}|_{\eta,(\cdot)}^2 |\check{T}|_{0,(\cdot)}}{\gamma |\check{\rho}|_{0,(\cdot)} M_\infty^2} + \frac{|\check{T}|_{\eta,(\cdot)}^2 |\check{\rho}|_{0,(\cdot)}}{\gamma(\gamma-1) |\check{T}|_{0,(\cdot)} M_\infty^2} dy. \end{aligned} \quad (7.5)$$

The wake of the roughness element is characterized by the presence of regions of high streamwise vorticity. A pair of strong counter-rotating streamwise vortices form as the flow reattaches downstream of the roughness. Figure 7.1 shows shaded contours of $\bar{u}_s = [(\partial\bar{u}/\partial y)^2 + (\partial\bar{u}/\partial z)^2]^{1/2}$ at three different streamwise positions. The strong streamwise vortices induced downstream of the roughness element lift-up low momentum fluid from the near wall region and give rise to a low velocity streak away from the wall as shown in figures 7.1(a), 7.1(b) and 7.1(c). As the low velocity streak forms, it induces a three-dimensional detached high shear-layer in its surroundings, leading to a highly unstable roughness wake. Note that the shape of the low velocity streak changes notably along the streamwise extent of the computational domain, suggesting that non-parallel flow effects might play an important role in the determination of the stability characteristics of the wake.

Figure 7.2 compares the growth rates of the dominant modes extracted

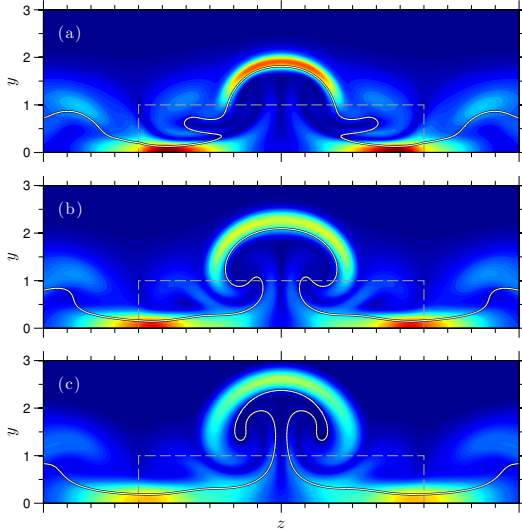


Figure 7.1: Contours of \bar{u}_s in crossflow planes at $x = 76.025$, 93.665 and 114.665 for (a), (b) and (c) respectively, showing the localized shear generated by the roughness-induced counter-rotating vortices. The solid lines show contours of $\bar{u} = 0.38$ and the dashed ones correspond to the roughness element position.

from the PSE-3D results at different streamwise locations with the NS results for a selection of frequencies. The NS growth rates are measured as

$$\sigma_{\mathcal{E}} = \frac{1}{2} \frac{d \ln[\mathcal{E}_{\eta}(x)]}{dx}, \quad \text{for } \eta = 1, 2, \dots, J/2 - 1, \quad (7.6)$$

while for the PSE-3D results the effective growth rate calculated using equation (1.44) is used to account for the residual slow variation of disturbance kinetic energy (K) with x . Note that the PSE-3D growth rates can also be computed from the streamwise variation of the mode amplitudes, similarly to what was done for the NS results. The growth rates obtained using the two methodologies were found to be practically indistinguishable from each other. This aspect was also reported by Bertolotti and Herbert [21], who showed the use of normalization condition (1.43) and consequent definition of the effective growth rate (σ_K) does not change the results. Therefore the definition in equation (1.44) was used here for the comparison with the NS results. Both NS and PSE-3D results show that disturbances with $F = 0.14$ are the most unstable, with an averaged growth rate of $\sigma_K \approx 0.21$ for $80 \leq x \leq 116$. This is roughly thirty times higher than the smooth flat plate primary instability for the same Mach and Reynolds numbers, which has $F \approx 0.013$

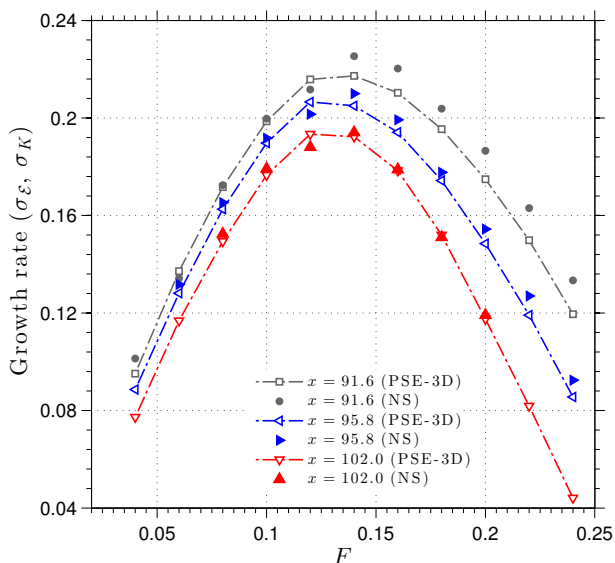


Figure 7.2: Disturbance growth rate at different streamwise positions for a selection of the most unstable frequencies ($\sigma_{\mathcal{E}}$ for NS and σ_K for PSE-3D).

and $-\alpha_i \approx 0.0075$ according to parallel linear stability theory. While the NS and PSE-3D growth rates agree closely for $x \geq 95.8$, a slight disagreement is evident at $x = 91.6$ for $F \geq 0.14$. This is believed to be due to the fact that, as will be shown in the following, multiple modes with different growth rates contribute to the growth of \mathcal{E}_η in the NS simulations. In the linear limit the disturbed flow field is given by the sum of these modes and $\sqrt{\mathcal{E}_\eta}$ can potentially grow faster than the most unstable mode, as is the case for $F \geq 0.14$ in figure 7.2(b). The mechanism is similar to that responsible for the transient growth of disturbances in the presence of non-orthogonal stable modes, only here two (or potentially more) unstable modes combine linearly and lead to a total disturbance energy growing faster than the most unstable mode during a certain transient.

A more complete picture of the modes taking part in the instability of the wake can be obtained by analysing the linear stability of y - z slices of the roughness wake. Figure 7.3(a) gives the spatial BiGlobal eigenspectrum obtained for $F = 0.08$ at $x = 93.66$. It can be seen that, in addition to the dominant varicose and sinuous modes, figures 7.3(b) and 7.3(c) respectively, the wake of the roughness element sustains the growth of four additional modes for the frequency and streamwise position considered. The modes

7. Roughness-induced transition in high speed boundary-layers

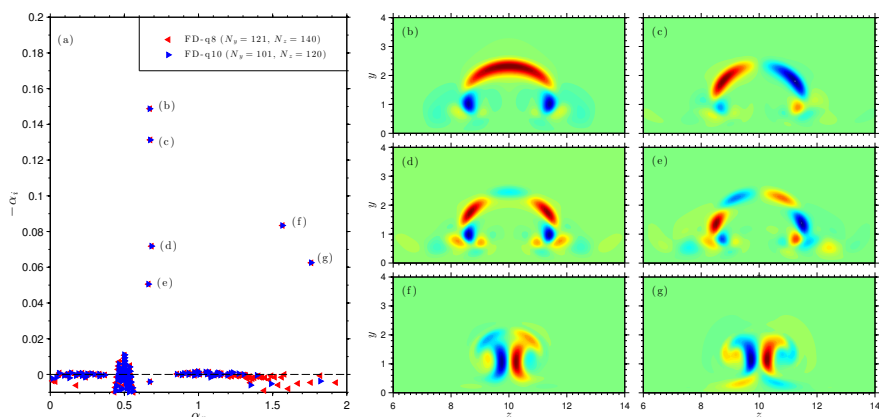


Figure 7.3: Spatial BiGlobal spectrum (a), with letters in brackets referring to subsequent figures, and contours of the real part of the temperature eigenfunctions (blue for negative and red for positive). Spectrum and eigenfunctions were obtained for $F = 0.08$ at $x = 93.66$.

shown in figures 7.3(d) and 7.3(e) belong to the family of modes growing in the three-dimensional high-shear layer surrounding the low-velocity streak, while the modes shown in figures 7.3(d) and 7.3(e) reflect disturbances growing in the streak itself. The growth rate obtained from the BiGlobal eigenvalue problem for the dominant varicose mode is $-\alpha_i = 0.149$, while the NS and PSE-3D results give respectively $\sigma_{\mathcal{E}} = 0.169$ and $\sigma_K = 0.167$ for the same mode. A disagreement between NS and BiGlobal results was expected given the degree of non-parallelism of the base flow. On the other hand, the agreement between NS and PSE-3D is remarkable.

Difficulties in recovering accurate amplification rates from BiGlobal stability results were also reported by Bonfigli and Kloker [27] while studying the secondary instability of crossflow vortices in an incompressible flow. On the other hand, they show that a BiGlobal stability analysis can give reliable results in terms of mode eigenfunctions and dispersion relation.

Here, the u -, v -, and w -velocity amplitude functions of the dominant modes obtained from the BiGlobal eigenvalue analysis are compared with those obtained from the NS simulations in figure 7.4 for $F = 0.08$ and $F = 0.26$. It can be seen that the two results are in excellent qualitative agreement. The varicose mode dominates the wake instability for $F = 0.08$, but there is a non-negligible contribution of the sinuous mode to the NS amplitude functions, which leads a slight asymmetry. On the other hand, for $F = 0.26$ both the BiGlobal stability and the NS results indicate that

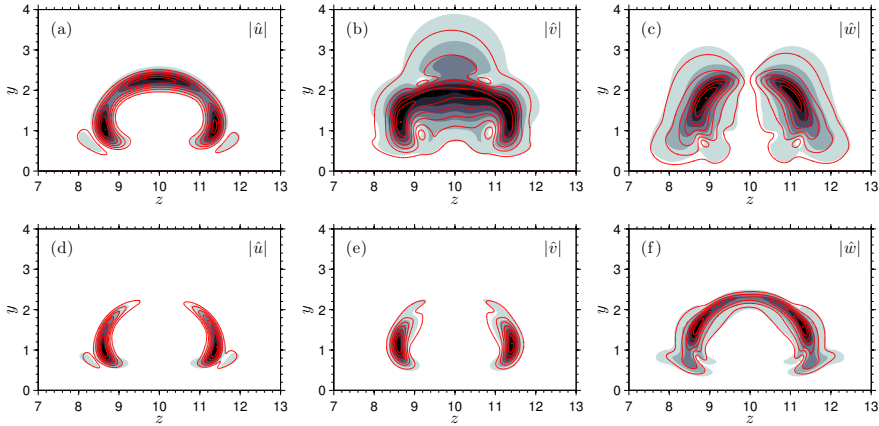


Figure 7.4: Mode shape comparison between Navier-Stokes (red contour-lines) and BiGlobal stability (shaded contours) results for $x = 93.66$. The Navier-Stokes and BiGlobal mode amplitudes were normalised with the maximum attained over y and z and plotted at the same contour levels, eight equally spaced contours from 0 to 1. (a), (b) and (c) for $F = 0.08$ (varicose mode) and (d), (e) and (f) for $F = 0.26$ (sinuous mode).

the only unstable mode is sinuous and grows in the lateral high-shear layers induced at the sides of the low-velocity streak.

The structure of the dominant modes taking part in the wake instability can be used to estimate the growth rates of the varicose and sinuous modes separately from the NS results, which can then be compared with those obtained from the PSE-3D simulations. For this purpose it is worth noting that growth of v' disturbances at the roughness mid-plane reflects solely the growth of the varicose mode, while w' disturbances at the same location are only influenced by the sinuous mode development (note that $|\hat{w}| = 0$ for the varicose mode and $|\hat{v}| = 0$ for the sinuous mode at the roughness mid-plane). Figure 7.5 gives a comparison of the streamwise variation of the sinuous and varicose mode amplitudes obtained from the NS and PSE-3D simulations for some of the most unstable frequencies. Varicose and sinuous mode amplitudes are obtained respectively as $\int_0^{\delta_{99}} |\hat{v}| dy$ and $\int_0^{\delta_{99}} |\hat{w}| dy$ at $z = 10$ (roughness mid-plane) from the NS results, while the PSE-3D mode amplitudes are calculated as $\int_x \sigma_K(x) dx$. Again NS and PSE-3D results agree closely and indicate that varicose and sinuous modes are unstable for overlapping frequency ranges. The varicose mode dominates throughout the streamwise extent of the computational domain for the most unstable frequencies. In fact, at $x = 90$ the growth rate of the varicose mode is higher

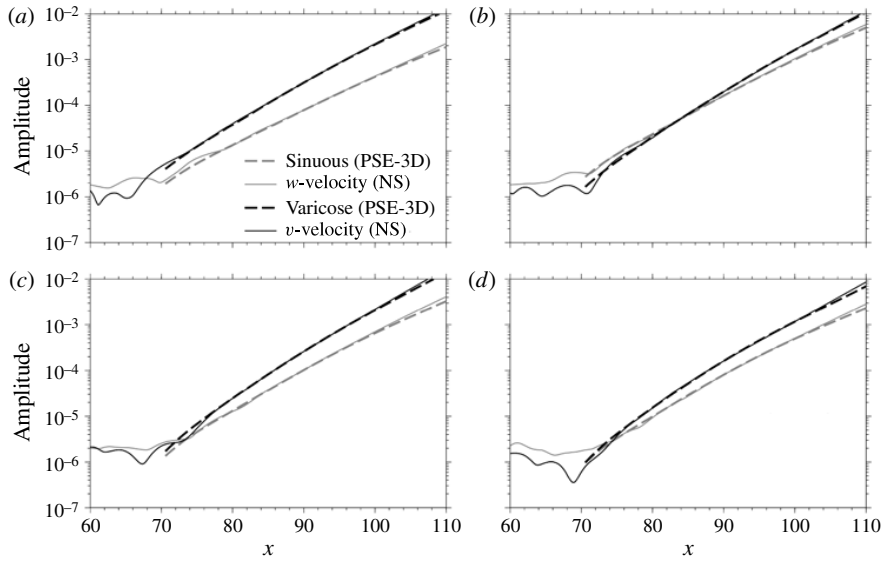


Figure 7.5: Growth of the dominant varicose and sinuous modes; comparison between NS and PSE-3D results. The NS mode amplitudes are calculated as $\int_0^{\delta_{99}} |\hat{s}| dy$ at the roughness mid-plane, where $s = v$ for the varicose mode and $s = w$ for the sinuous mode. The varicose and sinuous PSE-3D mode amplitudes were calculated as $\int_x \sigma_K(x) dx$ and normalised to match, respectively, the v -velocity and w -velocity NS amplitudes at $x = 90$.

than that of the sinuous mode by about 15% for $F = 0.10$ and $F = 0.12$, 11% for $F = 0.14$ and 8% for $F = 0.16$, while at $x = 112$ the growth rate differences are about 16%, 19%, 21% and 22%, respectively. On average (for $80 \leq x \leq 116$) the most unstable varicose mode grows about 17% faster than the most unstable sinuous mode ($\sigma_K = 0.18$ for $F = 0.14$).

These results are in agreement with the BiGlobal stability and experimental results of Choudhari et al. [40] and Kegerise et al. [119], which suggest that the varicose mode dominates over the sinuous mode for high Re_h (arguably $Re_h \geq 426$). However, contrary to what was found by Choudhari et al. [40], here the difference in growth rates between varicose and sinuous modes increases for increasing x -position, at least within the streamwise extent of the computational domain used, which could be due to a number of reasons including the higher Re_h considered here, increased compressibility effects at the higher Mach number or a dependence on the shape of the roughness element. Additional parametric studies would be needed to clarify these findings. Using the N-factor concept [230, 263] and assuming $N = 9$ as the transition criterion, both the NS and PSE-3D results indicate that transition to turbulence occurs within about 40 roughness heights from the point of excitation of the varicose mode, which can be considered to be positioned immediately downstream of the separation bubble at the back of the roughness element ($x = 66$). Therefore, transition to turbulence occurs about 50 roughness heights downstream of the roughness trailing edge. This prediction is in agreement with the non-linear simulation of De Tullio et al. [52].

7.3.2 Hypersonic regime

Here, the laminar-turbulent transition induced by a sharp-edged isolated roughness element in an hypersonic boundary-layer is analyzed. It focuses on the linear instability of the wake induced by the isolated roughness element with dimensionless height $h = 1$. The roughness height expressed in terms of δ_{99}^* of the surrounding undisturbed boundary-layer at streamwise location of the roughness element is $h^*/\delta_{99}^* = 0.44$. The roughness element has length $L = 6.0$ and same width. The Reynolds number is $Re_{\delta_0^*} = 8200$ and the Mach number is $M = 6$. The walls are considered no-slip and isothermal with $\bar{T}_w = \bar{T}_{ad} = 7.022$, where \bar{T}_{ad} is the laminar adiabatic-wall temperature. The roughness Reynolds number is $Re_h = 331$ [200].

The laminar base flow is calculated through full Navier-Stokes simulations. The roughness element induces two regions of three-dimensional separated flow, located immediately upstream and downstream of it. The wake of

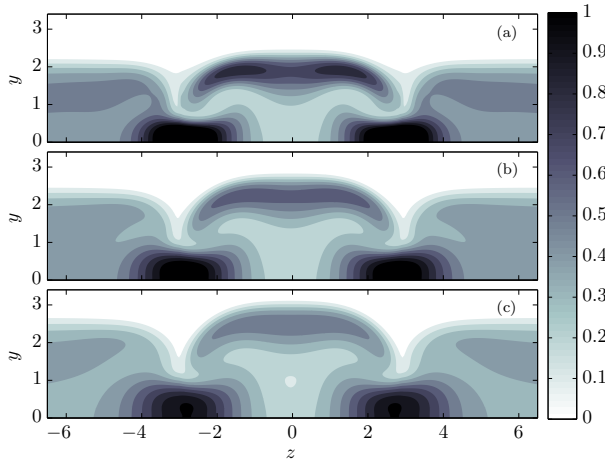


Figure 7.6: Contours of \bar{u}_s in crossflow planes at $x = 79.6, 113.2$ and 142.6 for (a), (b) and (c) respectively, showing the localized shear generated by the roughness-induced counter-rotating vortices.

the roughness element is convectively unstable for the condition studied here. The bubble lengths are $5.9\delta_0^*$ upstream and $9.9\delta_0^*$ downstream. The wake of the roughness element is characterised by the presence of regions of high streamwise vorticity. A pair of counter-rotating streamwise vortices form at the edges of the roughness element, inducing lift-up of low momentum fluid from the near wall region and give rise to a low velocity streak. Figure 7.6 shows shaded contours of $\bar{u}_s = [(\partial\bar{u}/\partial y)^2 + (\partial\bar{u}/\partial z)^2]^{1/2}$ at three different streamwise positions. A further description of the base flow is found in De Tullio and Sandham [51], where also the flow is subjected to disturbances, recovering the main stability aspects of it.

Here, the u -velocity amplitude functions of the dominant wake modes obtained from the BiGlobal eigenvalue analysis at $x = 142.6$ are shown in figure 7.7 for $F = 0.02, 0.06, 0.12$ and 0.14 . For $F = 0.02$ (figure 7.7(a)), the shape function peaks near the lateral shear layer and the instability mode manifests itself as a sinuous deformation of the low velocity streak generated in the region near the roughness centreline. At higher frequencies the instability of the wall normal detached shear induced at the roughness centreline starts appearing in the disturbance amplitude function, as shown in figure 7.7(c) for $F = 0.12$, which also induces a varicose deformation of the streak. This becomes dominant for $F = 0.14$, as shown in figure 7.7(d), which is the frequency with the highest disturbance growth rate. These shape functions compare very well with those recovered by full NS simulations [51]

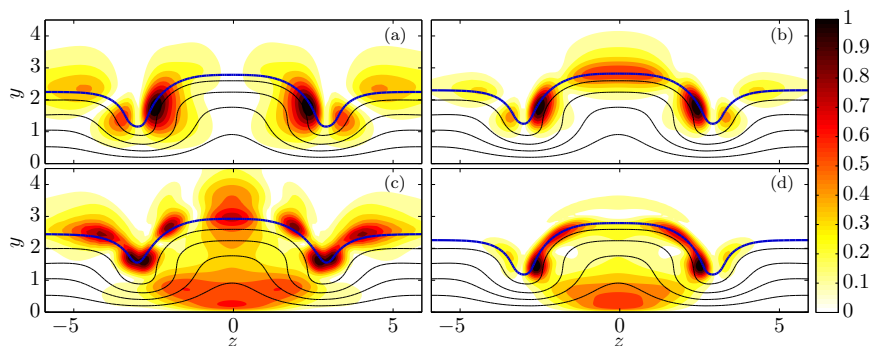


Figure 7.7: Contours of streamwise velocity eigenfunctions of leading roughness-induced modes at different frequencies for $x = 142.6$ recovered by spatial BiGlobal analysis. (a) for $F = 0.02$ (sinuous mode) and (b), (c) and (d) for $F = 0.06$, $F = 0.12$ and $F = 0.14$ respectively (varicose modes). The black isolines correspond to $\bar{u} = (0 : 0.2 : 0.8)$ and the thicker blue lines indicate the critical layers ($\bar{u} = c_{ph}$, where c_{ph} is the phase speed of the instability modes).

for the same set of frequencies and streamwise position.

A more complete picture of the modes taking part in the instability of the wake is observed in figure 7.8, which shows the spatial BiGlobal eigenspectrum obtained for $F = 0.14$ at $x = 142.6$ and the discrete unstable eigenfunctions. In agreement with the full NS predictions [51] is the amplification of the Mack mode in the lateral boundary-layer, observing the growth of a two-dimensional instability 7.8(a) in a clean flat plate at the same frequency, $F = 0.14$, for $x > 100$. Furthermore, a second unstable mode peaks in the lateral boundary-layer with lower amplification rate, showing a antisymmetric shape function about the roughness mid-plane 7.8(b). Finally, the streamwise velocity eigenfunction of the unstable varicose wake mode is shown in figure 7.8(c).

Having identified the structure of the modes dominating the wake instability, PSE-3D simulations are carried out to determine their growth rates. The frequency is set to $F = 0.14$ since it corresponds to the maximum linear growth rate [51]. To this end, the PSE-3D marching integration is performed for $F = 0.14$, starting from the dominant BiGlobal eigenfunctions obtained at $x = 67$ for the wake instability mode and from $x = 105$ for the boundary-layer or Mack mode. Figure 7.9 compares the growth rates of the dominant modes extracted from the PSE-3D and BiGlobal results at different streamwise locations. The PSE-3D effective growth rates are defined in equation 1.44 in order to account for the residual slow variation of

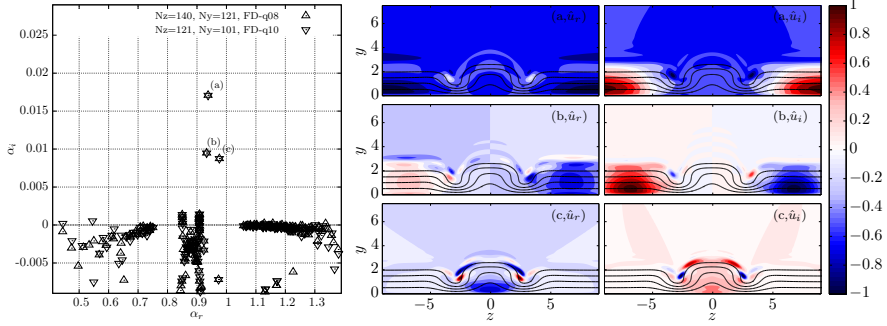


Figure 7.8: Spatial BiGlobal spectrum, with letters in parentheses referring to subsequent figures, and contours of streamwise velocity eigenfunctions. The isolines correspond to $\bar{u} = (0 : 0.2 : 0.8)$. The spectrum and eigenfunctions were obtained for $F = 0.14$ at $x = 142.6$

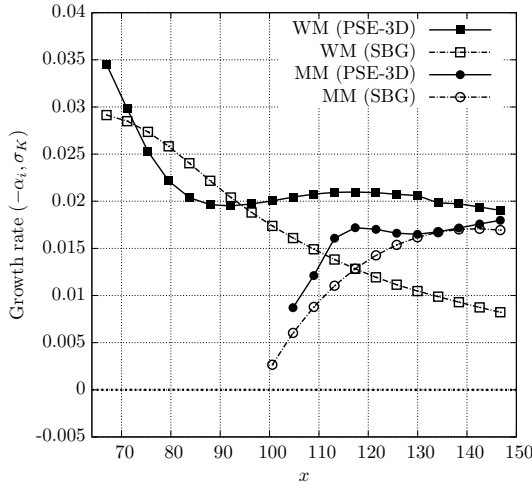


Figure 7.9: Disturbance growth rates at different streamwise positions for $F = 0.14$, being $-\alpha_i$ for spatial BiGlobal (SBG) and σ_K for PSE-3D, differentiating for the leading roughness-induced wake mode (WM) and the leading Mack mode (MM).

disturbance kinetic energy ($K = \int_y \int_z \bar{\rho}(\hat{u}^2 + \hat{v}^2 + \hat{w}^2) dy dz$) with x . In fact, regarding the changes of the roughness-induced wake along x , strong discrepancies are found between PSE-3D and BiGlobal predictions for the varicose wake mode. In the other hand, the growth rate results for the second Mack mode differ less. It is important to notice the very good prediction of the PSE-3D effective growth rate comparing with the DNS results of [51], where the amplification slope of the most amplified mode, namely the growth rate, is nearly constant ≈ 0.021 for $80 \leq x \leq 147$ and the averaged $\sigma_K = 0.0203$.

7.4 Summary and conclusions

The laminar-turbulent transition induced by a sharp-edged quadrilateral isolated roughness element at Mach numbers $M = 2.5$ and $M = 6$ was thoroughly investigated. The study focused on the linear instability of the roughness-modified steady but convectively unstable base flow. The main contributions of the present work are an in-depth analysis of the linear instability of the wake generated behind the roughness element and a cross validation of full NS, spatial BiGlobal stability and PSE-3D simulations. The latter two analyses were found to agree very well with the NS results. The application of these different methods to the same problem allows the effect of multiple modes and flow non-parallelism to be separated out. PSE-3D simulations were performed here for the first time in the context of compressible flows. The results show that the base flow changes introduced by the roughness elements can lead to a drastic modification of the stability characteristics of the flow depending on the roughness height considered. Of particular importance is the generation of pairs of counter-rotating stream-wise vortices, which, through the lift-up of low momentum fluid from the near wall region, give rise to a low velocity streak surrounded by regions of high wall-normal and lateral shear, forming the roughness wake. Focusing on the supersonic case, $M = 2.5$ and $Re_{\delta_0^*} = 3300$, a roughness element with height over boundary-layer thickness ratio of $h^*/\delta_{99} = 0.44$ ($Re_h = 791$) gives rise to a highly unstable wake, where instability modes grow for all frequencies of the forcing. Note that δ_{99} is taken at streamwise location of the roughness element in the surrounding undisturbed boundary-layer. The spatial BiGlobal stability results show that at least six different modes may grow in the wake of the roughness element. Four of these modes are manifestations of the instability of the three-dimensional shear-layer bounding the low-velocity streak, while the remaining two modes reflect disturbances growing in different parts of the streak itself. The two most unstable modes belong to the family of modes developing in the three-dimensional shear-

layer and are associated with characteristic varicose (symmetric u' about the roughness mid-plane) and sinuous (anti-symmetric u' about the roughness mid-plane) deformations of the low-velocity streak. The dominant varicose mode differs from that reported in the experiments of Asai et al. [10] in that it is a consequence of an instability of the 3D shear-layer as a whole rather than a Kelvin-Helmholtz instability of its $\partial\bar{u}/\partial y$ part. Both varicose and sinuous modes are most unstable for a non-dimensional frequency $F = 0.14$. The varicose mode grows on average about 17% faster than the sinuous mode, in qualitative agreement with the findings of Choudhari et al. [40] and Kegerise et al. [119], and reaches $N = 9$ within about 50 roughness heights from the roughness element trailing edge. The NS results also indicate that when varicose and sinuous modes present similar amplitudes, the total disturbance energy may grow faster than the most unstable mode, as a consequence of the linear superposition of the two modes. This effect was found to be limited for the cases analysed here but it may have wider significance under different conditions. The results obtained from the NS simulations are found to be in excellent agreement with those obtained from the stability analyses. The shape functions and growth rates of the most unstable modes extracted from the NS data are in close agreement with the two-dimensional eigenfunctions obtained from the BiGlobal stability analysis and the growth rates obtained from the PSE-3D simulations, respectively.

The second case analyzed through spatial BiGlobal and PSE-3D analyses, commenting some qualitative comparisons with NS simulations [51], corresponds to the same flow configuration at hypersonic speed, $M = 6$ and $Re_{\delta_0^*} = 8200$. At this high speed, Mack modes develop in the surrounding undisturbed boundary-layer, as it would do in a clean flat-boundary-layer at these conditions. Mack modes are found to grow slower and in a smaller region of instability than roughness-induced wake modes. The results are found in a qualitatively good agreement with the same NS simulations. Varicose instability modes were found to be the most unstable, which is also observed in NS simulations [51].

Chapter 8

Global instability analysis of an elliptic cone flow at hypersonic flight conditions

8.1 Introduction

The elliptic cone is a frequently used model to understand transition over components of next-generation high speed vehicles. Evidence has been accumulated regarding laminar-turbulent transition scenarios on elliptic cones at aspect ratios 2:1 and 4:1, exposed at zero angle of attack to oncoming flows for Mach numbers (M) between 4 and 8 in different experimental facilities [109, 195, 224, 225], while recently large-scale computations of the same phenomenon have appeared in the literature [16]. All these studies reported the formation of large structures near the minor-axis centerline of the cone; these structures were first experimentally found by Schmisser et al. [224, 225] to be most receptive to amplification of perturbations in a 4:1 elliptic cone at $M = 4$. Simultaneously, Poggie and Kimmel [195] reported evidence of the classical crossflow and second Mack mode [161] instabilities in a 2:1 elliptic cone at $M = 8$; the transition front was asymmetric, with early transition near the top centerline and delayed transition near the leading edge. Images taken by Huntley and Smits [109] of the early stages of transition, on a sharp-nosed 4:1 elliptic cone at same $M = 8$, confirm that transition begins with the emergence of small-scale structures near the centerline axis of the cone, rather than in the outboard crossflow region.

In the last two decades, stability analyses of boundary-layers on sharp-nosed cones with elliptical cross sections have been performed, using linear stability theory and cross flow correlations. These calculations relied on base flow solutions recovered using the Parabolized Navier-Stokes equations. In 90's of last century, research into three-dimensional boundary-layers over elliptic cross-section cones was undertaken by Lyttle and Reed [158], who presented solutions of the PNS equations for adiabatic wall elliptic cones of eccentricities of 2:1, 3:1 and 4:1 at $M = 4$, applying Reynolds number correlations based on the parameter $Re_{cf(R\&H)} = HLR_{cf}$, where Re_{cf} is

the traditional crossflow Reynolds number and the factors H and L are introduced to account for compressibility and cooling effects of the wall [201], for stability analysis. The parameter $Re_{cf(R\&H)}$ for these configurations peaked near the top centerline, outside the region of validity of the above correlation. Boundary-layer velocity profiles near the top centerline were inflectional and unstable. Kimmel et al. [125] used an extended version of the the UPS PNS code [134, 232], enabling the study of cool-wall cases, for computing the base flow around cones with eccentricities of 1.5:1, 2:1 and 4:1 at $M = 7.95$. The e^{Malik} code [163] was used to calculate boundary-layer stability, demonstrating that all the three cases showed crossflow instability, with the 4:1 configuration attaining the highest N -factors. Later experimental studies by the same authors delivered results in reasonable agreement with linear stability calculations and were suggestive of a traveling crossflow instability mode [196]. The flow in the vicinity of the top centerline was found to be highly unstable and for this region both the experiments and the computations showed an unstable frequency band that coincided with the characteristic second Mack mode frequency [161].

Recently, Gosse and Kimmel [80] compared the base flow and transition correlating parameters of a 2:1 elliptic cone at a free-stream Mach number of 7.95 calculated using both a full Navier-Stokes CFD solver and a PNS code, resulting in good agreement. From then on, efforts have concentrated on the HIFiRE-5 geometry, also studied in this work. Details of the HIFiRE-5 configuration are discussed in Kimmel et al. [124]. The works of Choudhari et al. [39] and Li et al. [148] present a thorough instability analysis of this configuration using local and non-local theories, respectively based on the solution of the one-dimensional EVP or the Parabolized Stability Equations. These approaches base the transition prediction on the N -factor over streamlines or grid lines of the cone, mainly the top centerline or the attachment-line. Furthermore, in the work of Choudhari et al. [39], also a two-dimensional stability theory is used, focusing this analysis on the vicinity of the mayor- and minor-axis meridians, without accounting for surface curvature effects. In the last work, between the flow condition studied, two were selected for flight condition at altitudes 18 *km* and 33 *km*. The latter corresponds with the conditions studied here, but they used a lower free-stream velocity, having a slightly smaller Reynolds number, $Re' = 1.65 \times 10^6 / m$. The two-dimensional global linear EVP (called here BiGlobal analysis [250]) results showed unstable modes in both conditions, but the onset for transition was not reached for the larger altitude flow conditions case. Furthermore, leading-edge instabilities were not found for this case, since the attachment-line Reynolds number with compressibility correction [166] did not exceed the critical threshold.

Large-scale computations by Bartkowicz et al. [16] confirm the co-existence of all these scenarios and attempt a first classification of their significance at different Reynolds number (Re) range: while the centerline structures lead flow to transition at lower Re values, crossflow instability near the elliptic cone leading-edge becomes competitive at higher Reynolds numbers. The origin and role of the large centerline structures in the laminar-turbulent transition process on the elliptic cone is presently unclear. Mapping of the parameter space with respect to critical conditions and study of nonlinear interactions of different modal scenarios potentially leading flow to transition are issues hardly to be addressed by large-scale computations; spatial BiGlobal linear analysis and PSE-3D are called for in order to accomplish these tasks.

In this Chapter, the linear instability of the three-dimensional boundary-layer over the HIFiRE-5 flight test vehicle modeling a rounded-tip 2:1 elliptic cone at Mach number $M = 7$ was investigated. The main contribution of the present work is an analysis of the liner instability of the overall geometry through spatial BiGlobal stability simulations including surface curvature effects.

8.2 Spatial BiGlobal analysis for general coordinate transformation

Regarding Chapter 1, spatial BiGlobal analysis is the analog of classic spatial linear theory in a local framework [202], in case two inhomogeneous spatial directions are resolved simultaneously on a plane, while the third direction is considered locally homogeneous. In the elliptic cone geometry both the plane of amplitude functions and the homogeneous spatial direction are defined on a transformed coordinate system as follows. A three-dimensional coordinate transformation of the form

$$\xi = \xi(x), \quad \eta = \eta(x, y, z), \quad \zeta = \zeta(x, y, z), \quad (8.1)$$

is used to transform the governing equations into the (ξ, η, ζ) system. Regarding this transformation, it restricts the (η, ζ) solution surfaces to be in a plane normal to the x axis, resulting $\xi_y = \xi_z = 0$. Using the chain rule, the derivatives with respect to physical coordinates system are related to those with respect to the computational coordinates system through the metrics $(\xi_x, \eta_x, \eta_y, \eta_z, \zeta_x, \zeta_y, \zeta_z)$. More details are found in Subsection 2.3.

8. *Instability analysis of the hypersonic flow over an elliptic cone*

Here, the transformed coordinate system (ξ, η, ζ) is taken such that

$$L_\xi \gg L_\eta, L_\zeta, \quad \partial(\cdot)/\partial\xi \ll \partial(\cdot)/\partial\eta, \partial(\cdot)/\partial\zeta, \quad (8.2)$$

where L_ξ , L_η and L_ζ are the characteristic lengths on the streamwise and normal to it spatial directions respectively. In order to proceed, the base flow is assumed to be locally independent of one spatial coordinate ξ (but depending on the other two spatial directions, η and ζ , in a coupled inhomogeneous manner). Flow quantities are then decomposed according to

$$\mathbf{q}(\xi, \eta, \zeta, t) = \bar{\mathbf{q}}(\eta, \zeta) + \varepsilon \tilde{\mathbf{q}}(\xi, \eta, \zeta, t), \quad \varepsilon \ll 1, \quad (8.3)$$

where $\varepsilon \tilde{\mathbf{q}}$ represents the unsteady three-dimensional infinitesimal perturbations, being inhomogeneous in η and ζ and periodic in ξ . Thus, one may write

$$\tilde{\mathbf{q}}(\xi, \eta, \zeta, t) = \hat{\mathbf{q}}(\eta, \zeta) \exp[i(\alpha\xi - \omega t)] + \text{c.c.}, \quad (8.4)$$

with $\hat{\mathbf{q}}$ representing the vector of two-dimensional complex amplitude functions.

The resulting two-dimensional partial derivative generalized EVP follows equation (1.28) and its entries are derived from the TriGlobal operators of Appendix E substituting the derivatives with respect to physical coordinates by expressions (2.39) and (2.40), setting $\frac{\partial \bar{\mathbf{q}}}{\partial \xi} = 0$. Furthermore, next terms arise from the decomposition of streamwise derivatives of amplitude functions

$$\mathcal{D}_x = i\alpha + \mathcal{D}'_x, \quad (8.5)$$

$$\mathcal{D}_{xx}^2 = -\alpha^2 + \mathcal{D}'_{xx}{}^2 + \mathcal{D}''_{xx} i\alpha, \quad (8.6)$$

$$\mathcal{D}_{xy}^2 = \mathcal{D}'_{xy}{}^2 + \mathcal{D}''_{xy} i\alpha, \quad (8.7)$$

$$\mathcal{D}_{xz}^2 = \mathcal{D}'_{xz}{}^2 + \mathcal{D}''_{xz} i\alpha, \quad (8.8)$$

which are defined as

$$\mathcal{D}'_x = \eta_x \mathcal{D}_\eta + \zeta_x \mathcal{D}_\zeta, \quad (8.9)$$

$$\begin{aligned} \mathcal{D}'_{xx}{}^2 &= \eta_x^2 \mathcal{D}_{\eta\eta}^2 + \zeta_x^2 \mathcal{D}_{\zeta\zeta}^2 + 2\zeta_x \eta_x \mathcal{D}_{\eta\zeta}^2 \\ &+ J \left[\left(\frac{\eta_x^2}{J} \right)_\eta + \left(\frac{\zeta_x \eta_x}{J} \right)_\zeta \right] \mathcal{D}_\eta \\ &+ J \left[\left(\frac{\eta_x \zeta_x}{J} \right)_\eta + \left(\frac{\zeta_x^2}{J} \right)_\zeta \right] \mathcal{D}_\zeta, \end{aligned} \quad (8.10)$$

$$\mathcal{D}''_{xx} = 2\eta_x \mathcal{D}_\eta + 2\zeta_x \mathcal{D}_\zeta + J \left[\left(\frac{\eta_x}{J} \right)_\eta + \left(\frac{\zeta_x}{J} \right)_\zeta \right], \quad (8.11)$$

$$\begin{aligned}
 \mathcal{D}_{xy}^{\prime 2} &= \eta_x \eta_y \mathcal{D}_{\eta\eta}^2 + \zeta_x \zeta_y \mathcal{D}_{\zeta\zeta}^2 + (\eta_x \zeta_y + \eta_y \zeta_x) \mathcal{D}_{\eta\zeta}^2 \\
 &+ J \left[\left(\frac{\eta_x \eta_y}{J} \right)_\eta + \left(\frac{\zeta_x \zeta_y}{J} \right)_\zeta \right] \mathcal{D}_\eta \\
 &+ J \left[\left(\frac{\eta_x \zeta_y}{J} \right)_\eta + \left(\frac{\zeta_x \zeta_y}{J} \right)_\zeta \right] \mathcal{D}_\zeta, \tag{8.12}
 \end{aligned}$$

$$\mathcal{D}_{xy}'' = \mathcal{D}_y, \tag{8.13}$$

$$\begin{aligned}
 \mathcal{D}_{xz}^{\prime 2} &= \eta_x \eta_z \mathcal{D}_{\eta\eta}^2 + \zeta_x \zeta_z \mathcal{D}_{\zeta\zeta}^2 + (\eta_x \zeta_z + \eta_z \zeta_x) \mathcal{D}_{\eta\zeta}^2 \\
 &+ J \left[\left(\frac{\eta_x \eta_z}{J} \right)_\eta + \left(\frac{\zeta_x \eta_z}{J} \right)_\zeta \right] \mathcal{D}_\eta \\
 &+ J \left[\left(\frac{\eta_x \zeta_z}{J} \right)_\eta + \left(\frac{\zeta_x \zeta_z}{J} \right)_\zeta \right] \mathcal{D}_\zeta, \tag{8.14}
 \end{aligned}$$

$$\mathcal{D}_{xz}'' = \mathcal{D}_z. \tag{8.15}$$

8.3 Numerical considerations

8.3.1 Elliptic cone transformation

The computational domain coordinate system (ξ, η, ζ) is transformed into the desired physical coordinate system (x, y, z) using a modified confocal elliptic transformation, written as follows

$$x = \xi, \quad y = c\xi \sinh(\eta_0 + sp(\zeta)\eta) \sin \zeta, \quad z = c\xi \cosh(\eta_0 + sp(\zeta)\eta) \cos \zeta, \tag{8.16}$$

where c sets the half angle of the cone minor-axis, $c = \tan \alpha / \sinh \eta_0$, $sp(\zeta)$ truncates the wall-normal domain and η_0 is a parameter controlling the Aspect Ratio (AR) of the cone, $\eta_0 = \operatorname{atanh}(1/AR)$.

8.3.2 Boundary conditions

The elliptic EVP (1.28) must be complemented with adequate boundary conditions for the disturbance variables. Dealing firstly with the azimuthal direction, ζ , the symmetries of the problem are exploited in order to reduce the computational requirements. Depending on the case, either symmetric or antisymmetric boundary for each flow component, the corresponding homogeneous Dirichlet or Neumann boundary conditions are imposed at $\zeta = 0$

and $\zeta = \pi/2$. The combination of these conditions gives rise to four cases, but it is reduced to two due to the linearity of the modes and the clear independence of the structure of the shape functions either if it is located near $\zeta = 0$ or $\zeta = \pi/2$. For the wall-normal direction, the perturbations are forced to decay through the imposition of a sponge region outside the shock layer in the free-stream region, setting homogeneous Dirichlet boundary conditions at $\eta = 1$. The main objective of this sponge region is to avoid spurious reflections. This is achieved by artificially decreasing the local Reynolds number using a smoothing function. At the wall, $\eta = 0$, no-slip conditions are imposed by setting homogeneous Dirichlet boundary conditions and the same condition is set for temperature amplitude function. No boundary condition needs to be imposed for density amplitude function at the wall, since the linearized continuity equation is satisfied at $\eta = 0$.

Appropriate mappings between the finite-difference grids ($\xi \in [-1, 1]$) and the computational domain are needed. Since the boundary-layer problem requires clustering of points at the wall, the equation (2.60) is used to map the calculation domain grid $\eta \in [0, 1]$ into the FD-q grid, setting $\eta_h = 0.2$. For the spanwise direction, the same transformation is used in order to cluster point near the top center-line with $\zeta_h = 3\pi/4$.

8.4 Base flow

The geometry studied here corresponds to the HIFiRE-5 configuration. The HIFiRE program is a hypersonic flight test program executed by the Air Force Research Laboratory (AFRL) and the Australian Defense Science and Technology Organization (DSRO) [56]. The HIFiRE-5 test payload consists of a blunt-nosed elliptic cone of 2:1 ellipticity, 0.86 *m* in length. The nose tip cross-section in the minor-axis describes a 2.5 *mm* radius circular arc, tangent to the cone ray describing the minor-axis, and retains a 2:1 elliptical cross-section to the tip. Flight conditions were calculated for a Mach 7 flow at altitude of 33.0 *km*[81]. The free-stream velocity is 2452.17 *m/s* and the unit Reynolds number is $Re' = 1.89 \times 10^6 /m$. The surface temperature was defined using a prescribed temperature based on heat conduction analysis of an estimated trajectory for the vehicle. The surface temperature near the nose is approximately 650 *K* and varies between 300 *K* and 400 *K* over much of the surface of the cone. This results in a cold surface temperature accomplishing $T_w/T_{a,w} < 0.3$ over most of the cone surface downstream of the nose. The steady laminar flow solution has been calculated using the US3D non-equilibrium solver with shock fitting algorithm [181] by Gosse et al. [81] and has been used to extract the base flow analyzed here at

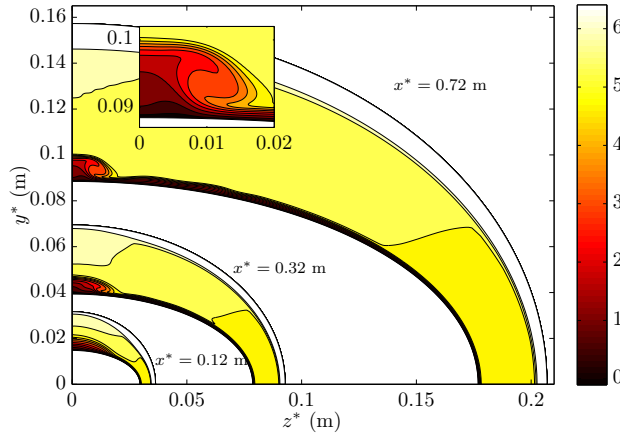


Figure 8.1: Streamwise Mach number at axial positions $x^* = 0.12, 0.32$ and 0.72 m . The vicinity of the minor-axis meridian is zoomed at $x^* = 0.72$ m .

different distances from the cone vertex.

The three-dimensional shape of the elliptic cone inevitably produces spanwise pressure gradients, which induce crossflow and the flow direction of the interior of the boundary-layer is no longer co-planar with the edge velocity vector, as in circular cones at zero angle of attack. The low-momentum boundary-layer fluid near the surface is deflected from the leading-edge or major-axis meridian towards the minor-axis meridian or centerline. This fact produces a lift-up of low-momentum boundary-layer fluid at the centerline, generating a low velocity streak away from the wall, as it is observed in figure 8.1. This figure shows contours of streamwise Mach number, M_ξ , at different intermediate axial sections of the cone. In the same figure, the mushroom-like structure formed in the vicinity of the minor-axis meridian is zoomed to show its complex shape. As the low velocity streak forms, it induces a three-dimensional detached high shear-layer in its surroundings. Note that the shape of the low velocity streak changes notably along the streamwise extent of the computational domain, suggesting that non-parallel flow effects might play an important role in the determination of the stability characteristics of it. A further description of the base flow is found in Gosse et al. [81]. The analysis of such flow structure is only accessible to the present multidimensional global stability analysis.

8.5 Results

The steady laminar base flow introduced in previous section is interpolated onto the grid constructed by equation (8.16) for spatial BiGlobal analysis at different distances from the tip. The instability analysis of Choudhari et al. [39], Paredes and Theofilis [187] on the same elliptic cone geometry for different flight conditions show that the onset for transition may be due to either one or more instability mechanisms, cataloged as centerline, crossflow and attachment-line modes. The structure of the attachment-line modes is located near the major-axis meridian and are well-understood in the incompressible [253] and compressible [159] regimes, as well as the well-known crossflow modes [143]. On the other hand, the centerline modes are accessible only to the present type of global EVP solution and their role in the transition process is still unclear.

As discussed in Section 8.3, the symmetries of the elliptic cone geometry allow the reduction of the discretized domain to one quarter of the cone, using either symmetric or antisymmetric boundary conditions on the minor-axis meridian, recovering the centerline varicose (\tilde{u} symmetric about the minor-axis meridian) and sinuous (antisymmetric \tilde{u} about the same meridian) modes respectively. Same strategy is followed at the major-axis meridian for computation of symmetric and antisymmetric attachment-line modes. On the other hand, the crossflow modes are not dependent on the boundary conditions used.

Computations are carried out for a wide a wide range of frequencies, from 50 to 300 kHz , at several distances from the cone tip. The number of discretization points per direction was checked for convergence and the following results were calculated using $N_\zeta = 181$ and $N_\eta = 141$ points.

The solution of the spatial BiGlobal analysis is composed by the complex eigenvalue α and the related complex eigenvectors, i.e. the two dimensional amplitude functions $\hat{\mathbf{q}}(y, z)$. Firstly, the real and imaginary parts of α , i.e. the wavenumber α_r and growth rate $-\alpha_i$ respectively, are shown in figure 8.2 for the dominant unstable centerline and crossflow modes. It is relevant to notice that no unstable attachment-line modes were found, what is in agreement with theory. Although the frequency of attachment-line stabilities is much higher [39], for the flight conditions studied here, height of 33 km and using a slightly lower $Re' = 1.65 \times 10^6 / m$, Choudhari et al. [39] showed that the attachment-line Reynolds number with compressibility correction [166] was far to exceed the critical threshold.

Focusing firstly on the centerline modes, figure 8.2(a) shows a constant

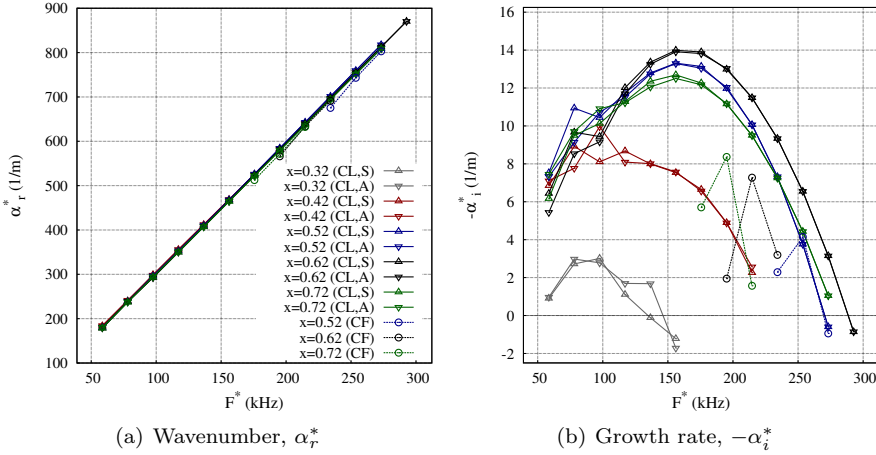


Figure 8.2: Wavenumber (a) and growth rate (b) of most amplified centerline and crossflow modes for a range of frequencies $F^* \in (50, 300)$ kHz. Note that **A** refers to antisymmetric and **S** to symmetric boundary conditions at $\zeta = 0$ and $\zeta = \pi/2$ and **CL** and **CF** refer respectively to centerline and crossflow modes.

slope of the wavenumber α_r versus frequency curves with an approximately constant phase velocity of these modes for all the axial stations; for example, $c_{ph} = 0.856$ for $F^* = 156$ kHz at $x^* = 0.52$ m. For the same frequencies and axial positions, figure 8.2(b) shows the growth rate curves. It is observed that the growth rates for varicose and sinuous modes exhibit some differences and oscillations for lower frequencies but approximate each other as the distance from the cone vertex and frequency increase. The amplification peak is found at $x^* = 0.52$ m for a frequency around $F^* \approx 156$ kHz. The amplification rate of the most unstable mode decays for larger x^* , while the most amplified frequency is unchanged. The maximum N-factor [221] reached by this mode along the cone is lower than 6, what does not exceed the typical threshold of transition, $N = 9$. Furthermore, unstable crossflow modes are found for $x^* > 0.52$ m and $F^* > 150$ kHz. Their phase velocity is slightly larger and the frequency bandwidth becomes more narrow, ≈ 100 kHz, varying its most amplified frequency at each axial position and thus leading to a localized amplification and decay of perturbations.

The eigenspectrum and eigenfunctions resulting from the spatial BiGlobal analysis are shown in figures 8.3 and 8.4 for $x^* = 0.62$ and frequencies $F^* = 156$ kHz and $F^* = 215$ kHz, respectively. In figure 8.3 only unstable centerline modes are found. The symmetric and antisymmetric centerline modes are associated with varicose or sinuous deformations of the

8. Instability analysis of the hypersonic flow over an elliptic cone

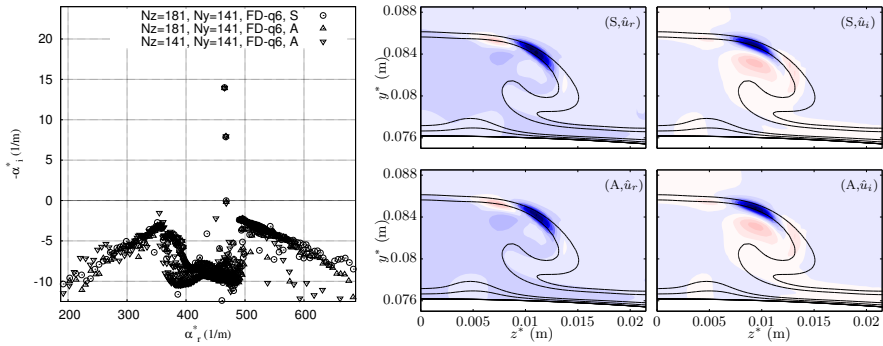


Figure 8.3: Spatial BiGlobal spectrum and contours of the real and imaginary parts of the streamwise velocity leading mode eigenfunctions for symmetric and antisymmetric boundary conditions (red for positive and blue for negative). The iso-lines correspond to base flow nondimensional streamwise velocity $u_b = (0 : 0.2 : 0.8)$. The spectrum and eigenfunctions were obtained for $F^* = 156 \text{ kHz}$ and $x^* = 0.62 \text{ m}$.

low-velocity streak formed in the centerline; they are a consequence of the instability developing in the three-dimensional shear layer. As can be observed in figure 8.3, both the leading varicose and sinuous modes have almost equal amplitude function, what refers to the fact that they are localized in the lateral shear. This explains why their associated wavenumbers and growth rates are almost equal. The main difference is that the sinuous mode would break the symmetries exhibited by the base flow.

At a higher frequency, $F^* = 215 \text{ kHz}$, figure 8.4 shows a higher number of unstable modes. The leading mode at this condition is a centerline mode, but several boundary-layer modes appear in the unstable region of the spectrum. These modes peaking far from the minor-axis meridian and localized in the regions of high near-wall spanwise velocity are called crossflow modes. The axial velocity amplitude function of the leading crossflow mode at the previously mentioned conditions is shown in figure 8.4. The structure of this mode is localized at an azimuthal position of $\zeta \approx 80$ and is composed by one negative and one positive peaks in the spanwise/azimuthal direction.

8.6 Summary and conclusions

The linear instability of the three-dimensional boundary-layer over a rounded-tip 2:1 elliptic cone at Mach number $M = 7$ was investigated. The main

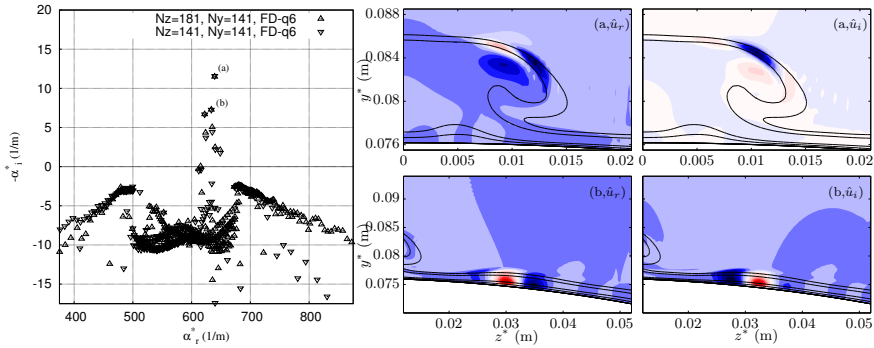


Figure 8.4: Spatial BiGlobal spectrum, with letters in parentheses referring to subsequent figures, and contours of the real and imaginary parts of the streamwise velocity eigenfunctions (red for positive and blue for negative). The iso-lines correspond to base flow nondimensional streamwise velocity $u_b = (0 : 0.2 : 0.8)$. The spectrum and eigenfunctions were obtained for $F^* = 215 \text{ kHz}$ and $x^* = 0.62 \text{ m}$, setting symmetric boundary conditions.

contribution of the present work is an analysis of the liner instability of the overall geometry through spatial BiGlobal stability simulations.

The leading instability modes were found to peak in the vicinity of the minor-axis meridian of the cone, denominated centerline in the text, where a mushroom-like structured is formed as consequence of the three-dimensional shape of the elliptic cone geometry. Crossflow is induced from the leading-edges to the centerline, producing a lift-up of low-momentum boundary-layer fluid at the centerline, generating a low velocity streak away from the wall. This streak induces a three-dimensional detached shear-layer in its surroundings capable to sustain the growth of different modes. The two most unstable modes in the range of frequencies studied ($50 - 300 \text{ kHz}$) belong to the family of modes developing in the three-dimensional shear-layer and are associated with characteristic varicose and sinuous deformations of the low-velocity streak. Both modes are found to have similar wavenumbers and growth rates as a consequence of their amplitude function shape, which is localized in the lateral shear of the centerline flow structure. Furthermore, unstable crossflow modes are found for $x^* > 0.52 \text{ m}$ and $F^* > 150 \text{ kHz}$. Their associated most amplified frequency differs at each axial position, resulting in a localized amplification and decay of perturbations. On the other hand, no unstable attachment-line modes were found at studied frequencies, what agrees with the theory [39].

The assumption of parallelism made in the spatial BiGlobal analysis may

lead to approximate wave number and growth rates predictions as shown in previous Chapter 7 and literature [52, 77, 188]. Regarding this issue, a relative error of approximately 10% is found between spatial BiGlobal and PSE-3D or full Navier-Stokes growth rate predictions. In order to account for the non-parallelism of the flow, the present analysis must be extended by performing PSE-3D analysis.

Chapter 9

Non-linear PSE-3D

9.1 Introduction

In this Chapter, in an analogous manner to the addition of non-linear effects into the conventional PSE [22], the linear PSE-3D are extended to predict the non-linear development of perturbations on this kind of complex three-dimensional flows.

The typical modal instability theory based on linear ordinary differential equations of Orr-Sommerfeld or the linear partial differential equations of BiGlobal analyses neglect the interaction between modes. Hence, its application is restricted to regions of small disturbance amplitude, i.e. regions where modes develop practically independent from each. Non-local non-linear methods based on PSE, as the DLR/FOI transition analysis code NOLOT/PSE [90, 94, 96], used here for comparisons, do not require linearization. Therefore, they also model the non-linear early stages of laminar-turbulent breakdown. The same methodology used for the addition of non-linear effects in the PSE is extended here for the PSE-3D, enabling the study of complex three-dimensional flows that so far were only accessible to the much more computationally expensive full Navier-Stokes spatial evolving simulations.

The linear version of the in-house developed stability codes have been validated against DNS results analyzing instability of the wake behind an isolated roughness element in supersonic flow in previous Chapter 7 and De Tullio et al. [52]. In the latter work, the first linear PSE-3D analysis for high-speed flows is performed, showing excellent agreement when compared with DNS results in the linear regime. The theoretical formulation and numerical treatment of the non-linear PSE-3D are explained in Subsection 1.3.4 and Section 2.5, respectively. The full listing of the operators of the parabolic PDE system of equations (1.57) is found in Appendix D. In this Chapter, the new in-house developed non-linear PSE-3D code is used firstly on the flat plate boundary-layer, showing excellent agreement with the NOLOT/PSE

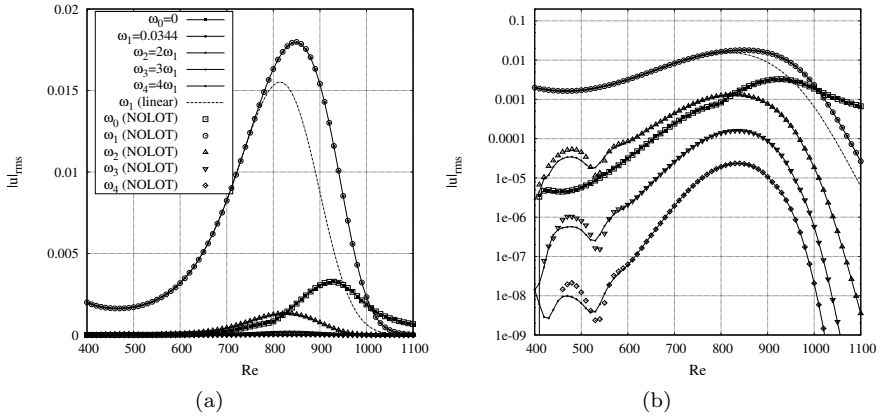


Figure 9.1: Comparison of $|\tilde{u}|_{rms}$ evolution in local $Re = \sqrt{x Re_0}$, for the incompressible flat-plate boundary-layer using the non-linear PSE-3D and the NOLOT/PSE codes, showing (a) linear and (b) logarithmic scalings. Also, the linear evolution of fundamental mode for same initial amplitude is shown.

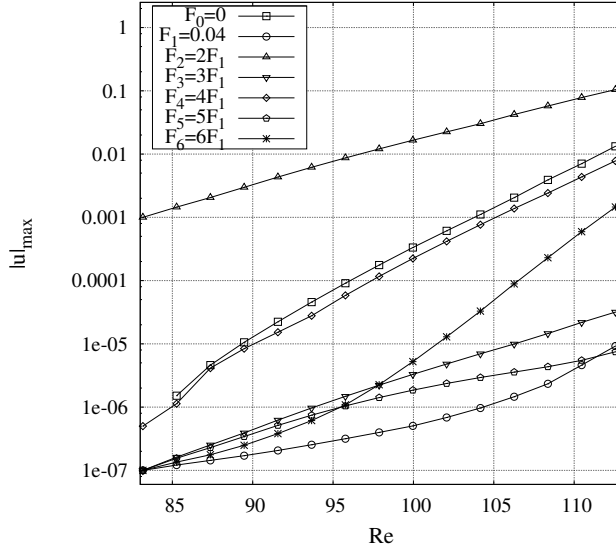
results, and secondly on the wake of an isolated roughness-element imbedded in a supersonic boundary-layer.

9.2 Results

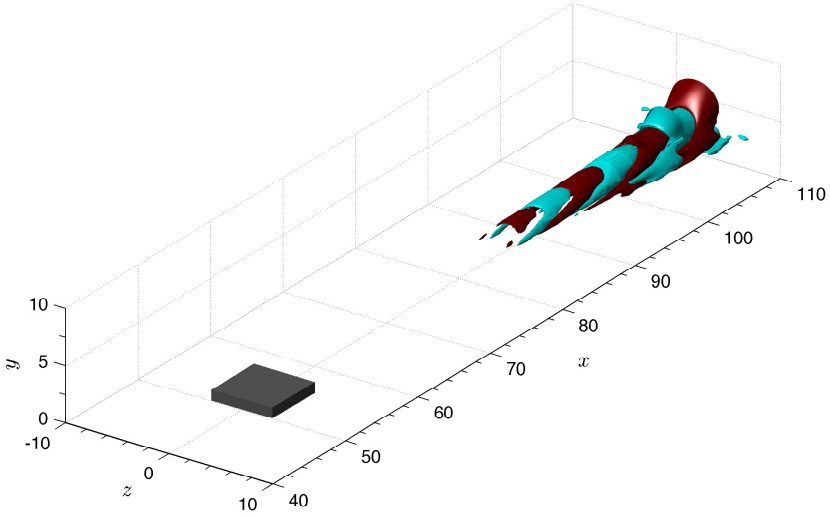
The non-linear PSE-3D are firstly used here to compute the non-linear evolution of two-dimensional perturbations in the incompressible flat-plate boundary-layer flow. Reference values are taken at the initial station, setting $Re_0 = 400$. Figure 9.1 shows the evolution of the root-mean-square (RMS) streamwise velocity perturbation for each time Fourier component, including the mean flow distortion (MFD), which correspond to the zero frequency mode. The fundamental frequency is set to $\omega = 0.0344$. The spanwise direction is discretized with $N_z = 4$ Fourier collocation points and the wall-normal direction with $N_y = 101$ eight order finite differences scheme (FD-q8) [189]. Results show excellent agreement against those computed with the NOLOT/PSE code [90, 94, 96]. The non-linear effects are clearly visible, exhibiting a strong difference of the fundamental mode from $Re > 800$ with the linear simulation, together with an important growth of the MFD.

Secondly, the convectively unstable wake of an isolated roughness element

in a boundary-layer at Mach 2.5 and $Re_{\delta^*} = 3300$, presented in Chapter 7, is analyzed through non-linear PSE-3D. The same base flow has been analyzed by means of direct numerical simulations, aided by spatial BiGlobal and linear PSE-3D analyses, showing excellent agreement with each other and validating the use of simplified theories for this flow configuration. Results are performed using $N_z = 140$ and $N_y = 121$ FD-q8 discretization points. Figure 9.2 shows the evolution of maximum amplitude of \check{u} on the streamwise direction for the MFD and six traveling modes, setting initial amplitude $|\check{u}|_{2,max} = 10^{-3}$ to the mode with frequency $F_2 = \omega_2/(2\pi) = 0.08$. The non-linear effects are clearly visible since the modes with multiple frequencies to the amplified one, i.e. $|\check{u}|_{4,max}$ and $|\check{u}|_{6,max}$, grow more than the rest, what would not happen in a linear simulation. Also, the three-dimensional view of the iso-surfaces of the perturbation quantity \check{u} is shown in the same figure, together with the roughness element in gray color.



(a)



(b)

Figure 9.2: Evolution of $|\tilde{u}|_{max}$ with streamwise direction of the different modes setting as fundamental frequency $F_1 = \omega_1/(2\pi) = 0.04$, but given the initial highest amplitude of $|\tilde{u}_0|_{max} = 10^{-3}$ to the first harmonic. Also, three-dimensional view of iso-surfaces of $\tilde{u} = \pm 10^{-2}$.

Appendix A

Linearized Navier-Stokes equations

In order to recover the linearized stability equations, the decomposition of variables (1.8) is introduced into the governing equations of fluid motion (1.1-1.3), resulting

$$\begin{aligned}
 & \frac{\partial \tilde{\rho}}{\partial t} + \bar{\rho}_x \tilde{u} + \bar{\rho} \tilde{u}_x + \bar{\rho}_y \tilde{v} + \bar{\rho} \tilde{v}_y + \bar{\rho}_z \tilde{w} + \bar{\rho} \tilde{w}_z \\
 & \quad + \tilde{\rho}_x \bar{u} + \bar{\rho} \tilde{u}_x + \tilde{\rho}_y \bar{v} + \bar{\rho} \tilde{v}_y + \tilde{\rho}_z \bar{w} + \bar{\rho} \tilde{w}_z \\
 & \quad = -\tilde{\rho}_x \bar{u} - \bar{\rho} \tilde{u}_x - \tilde{\rho}_y \bar{v} - \bar{\rho} \tilde{v}_y - \tilde{\rho}_z \bar{w} - \bar{\rho} \tilde{w}_z, \tag{A.1} \\
 & \bar{\rho} \left(\frac{\partial \tilde{u}}{\partial t} + \tilde{u} \bar{u}_x + \bar{u} \tilde{u}_x + \tilde{v} \bar{u}_y + \bar{v} \tilde{u}_y + \tilde{w} \bar{u}_z + \bar{w} \tilde{u}_z \right) \\
 & \quad + \tilde{\rho} (\bar{u} \bar{u}_x + \bar{v} \bar{u}_y + \bar{w} \bar{u}_z) + \frac{1}{\gamma M^2} \left(\tilde{T} \tilde{\rho}_x + \bar{\rho} \tilde{T}_x + \bar{T} \tilde{\rho}_x + \tilde{\rho} \bar{T}_x \right) \\
 & \quad - \frac{1}{Re} \left[\bar{\mu} (\tilde{u}_{xx} + \tilde{u}_{yy} + \tilde{u}_{zz}) + \frac{\bar{\mu}}{3} (\tilde{u}_{xx} + \tilde{v}_{xy} + \tilde{w}_{xz}) \right. \\
 & \quad \left. + \frac{2\bar{\mu}_x}{3} (2\tilde{u}_x - \tilde{v}_y - \tilde{w}_z) + \bar{\mu}_y (\tilde{u}_y + \tilde{v}_x) + \bar{\mu}_z (\tilde{u}_z + \tilde{w}_x) \right] \\
 & \quad - \frac{\bar{\mu}'}{Re} \left[\tilde{T} (\bar{u}_{xx} + \bar{u}_{yy} + \bar{u}_{zz}) + \frac{\tilde{T}}{3} (\bar{u}_{xx} + \bar{v}_{xy} + \bar{w}_{xz}) \right. \\
 & \quad \left. + \frac{2\tilde{T}_x}{3} (2\bar{u}_x - \bar{v}_y - \bar{w}_z) + \tilde{T}_y (\bar{u}_y + \bar{v}_x) + \tilde{T}_z (\bar{u}_z + \bar{w}_x) \right] \\
 & \quad - \frac{\bar{\mu}''}{Re} \tilde{T} \left[\frac{2\tilde{T}_x}{3} (2\bar{u}_x - \bar{v}_y - \bar{w}_z) + \tilde{T}_y (\bar{u}_y + \bar{v}_x) + \tilde{T}_z (\bar{u}_z + \bar{w}_x) \right] \\
 & \quad = -\tilde{\rho} \frac{\partial \tilde{u}}{\partial t} - (\tilde{\rho} + \bar{\rho}) (\tilde{u} \bar{u}_x + \tilde{v} \bar{u}_y + \tilde{w} \bar{u}_z) \\
 & \quad - \tilde{\rho} (\bar{u} \tilde{u}_x + \bar{v} \tilde{u}_y + \bar{w} \tilde{u}_z + \tilde{u} \bar{u}_x + \tilde{v} \bar{u}_y + \tilde{w} \bar{u}_z) - \frac{1}{\gamma M^2} \left(\tilde{T} \tilde{\rho}_x + \tilde{\rho} \tilde{T}_x \right) \\
 & \quad + \frac{\bar{\mu}'}{Re} \left[\tilde{T} (\tilde{u}_{xx} + \tilde{u}_{yy} + \tilde{u}_{zz}) + \frac{\tilde{T}}{3} (\tilde{u}_{xx} + \tilde{v}_{xy} + \tilde{w}_{xz}) \right]
 \end{aligned}$$

A. Linearized Navier-Stokes equations

$$\begin{aligned}
& + \frac{2\tilde{T}_x}{3} (2\tilde{u}_x - \tilde{v}_y - \tilde{w}_z) + \tilde{T}_y (\tilde{u}_y + \tilde{v}_x) + \tilde{T}_z (\tilde{u}_z + \tilde{w}_x) \Big] \\
& + \frac{\bar{\mu}''\tilde{T}}{Re} \left[\frac{2\bar{T}_x}{3} (2\tilde{u}_x - \tilde{v}_y - \tilde{w}_z) + \bar{T}_y (\tilde{u}_y + \tilde{v}_x) + \bar{T}_z (\tilde{u}_z + \tilde{w}_x) \right], \quad (\text{A.2}) \\
\bar{\rho} \left(\frac{\partial \tilde{v}}{\partial t} + \tilde{u}\bar{v}_x + \bar{u}\tilde{v}_x + \tilde{v}\bar{v}_y + \bar{v}\tilde{v}_y + \tilde{w}\bar{v}_z + \bar{w}\tilde{v}_z \right) \\
& + \tilde{\rho} (\bar{u}\bar{v}_x + \bar{v}\bar{v}_y + \bar{w}\bar{v}_z) + \frac{1}{\gamma M^2} \left(\tilde{T}\tilde{\rho}_y + \bar{\rho}\tilde{T}_y + \bar{T}\tilde{\rho}_y + \tilde{\rho}\bar{T}_y \right) \\
& - \frac{1}{Re} \left[\bar{\mu} (\tilde{v}_{xx} + \tilde{v}_{yy} + \tilde{v}_{zz}) + \frac{\bar{\mu}}{3} (\tilde{u}_{xy} + \tilde{v}_{yy} + \tilde{w}_{yz}) \right] \\
& + \bar{\mu}_x (\tilde{v}_x + \tilde{u}_y) + \frac{2\bar{\mu}_y}{3} (2\tilde{v}_y - \tilde{u}_x - \tilde{w}_z) + \bar{\mu}_z (\tilde{v}_z + \tilde{w}_y) \Big] \\
& - \frac{\bar{\mu}'}{Re} \left[\tilde{T} (\bar{v}_{xx} + \bar{v}_{yy} + \bar{v}_{zz}) + \frac{\tilde{T}}{3} (\bar{u}_{xy} + \bar{v}_{yy} + \bar{w}_{yz}) \right] \\
& + \tilde{T}_x (\bar{v}_x + \bar{u}_y) + \frac{2\tilde{T}_y}{3} (2\bar{v}_y - \bar{u}_x - \bar{w}_z) + \tilde{T}_z (\bar{v}_z + \bar{w}_y) \Big] \\
& - \frac{\bar{\mu}''}{Re} \tilde{T} \left[\bar{T}_x (\bar{v}_x + \bar{u}_y) + \frac{2\bar{T}_y}{3} (2\bar{v}_y - \bar{u}_x - \bar{w}_z) + \bar{T}_z (\bar{v}_z + \bar{w}_y) \right] \\
& = -\tilde{\rho} \frac{\partial \tilde{v}}{\partial t} - (\tilde{\rho} + \bar{\rho}) (\tilde{u}\tilde{v}_x + \tilde{v}\tilde{v}_y + \tilde{w}\tilde{v}_z) \\
& - \tilde{\rho} (\bar{u}\bar{v}_x + \bar{v}\bar{v}_y + \bar{w}\bar{v}_z + \tilde{u}\bar{v}_x + \tilde{v}\bar{v}_y + \tilde{w}\bar{v}_z) - \frac{1}{\gamma M^2} \left(\tilde{T}\tilde{\rho}_y + \bar{\rho}\tilde{T}_y \right) \\
& + \frac{\bar{\mu}'}{Re} \left[\tilde{T} (\tilde{v}_{xx} + \tilde{v}_{yy} + \tilde{v}_{zz}) + \frac{\tilde{T}}{3} (\tilde{u}_{xy} + \tilde{v}_{yy} + \tilde{w}_{yz}) \right] \\
& + \tilde{T}_x (\tilde{v}_x + \tilde{u}_y) + \frac{2\tilde{T}_y}{3} (2\tilde{v}_y - \tilde{u}_x - \tilde{w}_z) + \tilde{T}_z (\tilde{v}_z + \tilde{w}_y) \Big] \\
& + \frac{\bar{\mu}''\tilde{T}}{Re} \left[\bar{T}_x (\tilde{v}_x + \tilde{u}_y) + \frac{2\bar{T}_y}{3} (2\tilde{v}_y - \tilde{u}_x - \tilde{w}_z) + \bar{T}_z (\tilde{v}_z + \tilde{w}_y) \right], \quad (\text{A.3}) \\
\bar{\rho} \left(\frac{\partial \tilde{w}}{\partial t} + \tilde{u}\bar{w}_x + \bar{u}\tilde{w}_x + \tilde{v}\bar{w}_y + \bar{v}\tilde{w}_y + \tilde{w}\bar{w}_z + \bar{w}\tilde{w}_z \right) \\
& + \tilde{\rho} (\bar{u}\bar{w}_x + \bar{v}\bar{w}_y + \bar{w}\bar{w}_z) + \frac{1}{\gamma M^2} \left(\tilde{T}\tilde{\rho}_z + \bar{\rho}\tilde{T}_z + \bar{T}\tilde{\rho}_z + \tilde{\rho}\bar{T}_z \right) \\
& - \frac{1}{Re} \left[\bar{\mu} (\tilde{w}_{xx} + \tilde{w}_{yy} + \tilde{w}_{zz}) + \frac{\bar{\mu}}{3} (\tilde{u}_{xz} + \tilde{v}_{yz} + \tilde{w}_{zz}) \right] \\
& + \bar{\mu}_x (\tilde{w}_x + \tilde{u}_z) + \bar{\mu}_y (\tilde{v}_z + \tilde{w}_y) + \frac{2\bar{\mu}_z}{3} (2\tilde{w}_z - \tilde{u}_x - \tilde{v}_y) \Big]
\end{aligned}$$

$$\begin{aligned}
& - \frac{\bar{\mu}'}{Re} \left[\tilde{T} (\bar{w}_{xx} + \bar{w}_{yy} + \bar{w}_{zz}) + \frac{\tilde{T}}{3} (\bar{u}_{xz} + \bar{v}_{yz} + \bar{w}_{zz}) \right. \\
& + \tilde{T}_x (\bar{w}_x + \bar{u}_z) + \tilde{T}_y (\bar{v}_z + \bar{w}_y) + \left. \frac{2\tilde{T}_z}{3} (2\bar{w}_z - \bar{u}_x - \bar{v}_y) \right] \\
& - \frac{\bar{\mu}''}{Re} \tilde{T} \left[\bar{T}_x (\bar{w}_x + \bar{u}_z) + \bar{T}_y (\bar{v}_z + \bar{w}_y) + \frac{2\bar{T}_z}{3} (2\bar{w}_z - \bar{u}_x - \bar{v}_y) \right] \\
& = -\tilde{\rho} \frac{\partial \tilde{w}}{\partial t} - (\tilde{\rho} + \bar{\rho}) (\tilde{u}\tilde{w}_x + \tilde{v}\tilde{w}_y + \tilde{w}\tilde{w}_z) \\
& - \tilde{\rho} (\bar{u}\tilde{w}_x + \bar{v}\tilde{w}_y + \bar{w}\tilde{w}_z + \tilde{u}\bar{w}_x + \tilde{v}\bar{w}_y + \tilde{w}\bar{w}_z) - \frac{1}{\gamma M^2} (\tilde{T}\tilde{\rho}_z + \tilde{\rho}\tilde{T}_z) \\
& + \frac{\bar{\mu}'}{Re} \left[\tilde{T} (\tilde{w}_{xx} + \tilde{w}_{yy} + \tilde{w}_{zz}) + \frac{\tilde{T}}{3} (\tilde{u}_{xz} + \tilde{v}_{yz} + \tilde{w}_{zz}) \right. \\
& + \tilde{T}_x (\tilde{w}_x + \tilde{u}_z) + \tilde{T}_y (\tilde{v}_z + \tilde{w}_y) + \left. \frac{2\tilde{T}_z}{3} (2\tilde{w}_z - \tilde{u}_x - \tilde{v}_y) \right] \\
& + \frac{\bar{\mu}''\tilde{T}}{Re} \left[\bar{T}_x (\tilde{w}_x + \tilde{u}_z) + \bar{T}_y (\tilde{v}_z + \tilde{w}_y) + \frac{2\bar{T}_z}{3} (2\tilde{w}_z - \tilde{u}_x - \tilde{v}_y) \right], \quad (A.4) \\
& \bar{\rho} \left(\frac{\partial \tilde{T}}{\partial t} + \bar{u}\tilde{T}_x + \bar{v}\tilde{T}_y + \bar{w}\tilde{T}_z + \tilde{u}\bar{T}_x + \tilde{v}\bar{T}_y + \tilde{w}\bar{T}_z \right) + \bar{\rho} (\bar{T}_x\bar{u} + \bar{T}_y\bar{v} + \bar{T}_z\bar{w}) \\
& - (\gamma - 1)\bar{T} \left(\frac{\partial \tilde{\rho}}{\partial t} + \bar{u}\tilde{\rho}_x + \bar{v}\tilde{\rho}_y + \bar{w}\tilde{\rho}_z \right) - (\gamma - 1) (\tilde{u}\bar{\rho}_x\bar{T} + \tilde{v}\bar{\rho}_y\bar{T} + \tilde{w}\bar{\rho}_z\bar{T}) \\
& - (\gamma - 1)\tilde{T} (\bar{u}\bar{\rho}_x + \bar{v}\bar{\rho}_y + \bar{w}\bar{\rho}_z) \\
& - \frac{\gamma}{Re Pr} \left[\bar{\kappa} (\bar{T}_{xx} + \bar{T}_{yy} + \bar{T}_{zz}) + 2\bar{\kappa}' (\bar{T}_x\bar{T}_x + \bar{T}_y\bar{T}_y + \bar{T}_z\bar{T}_z) \right. \\
& + \bar{\kappa}\tilde{T} (\bar{T}_{xx} + \bar{T}_{yy} + \bar{T}_{zz}) + \bar{\kappa}''\tilde{T} (\bar{T}_x^2 + \bar{T}_y^2 + \bar{T}_z^2) \left. \right] \\
& - \frac{2\gamma(\gamma - 1)M^2\bar{\mu}}{Re} \left[\frac{2}{3} (2\bar{u}_x - \bar{v}_y - \bar{w}_z) \tilde{u}_x + (\bar{u}_y + \bar{v}_x) \tilde{u}_y + (\bar{u}_z + \bar{w}_x) \tilde{u}_z \right. \\
& + (\bar{u}_y + \bar{v}_x) \tilde{v}_x + \frac{2}{3} (2\bar{v}_y - \bar{u}_x - \bar{w}_z) \tilde{v}_y + (\bar{w}_y + \bar{v}_z) \tilde{v}_z \\
& + (\bar{w}_x + \bar{u}_z) \tilde{w}_x + (\bar{w}_y + \bar{v}_z) \tilde{w}_y + \left. \frac{2}{3} (2\bar{w}_z - \bar{u}_x - \bar{v}_y) \tilde{w}_z \right] \\
& - \frac{\gamma(\gamma - 1)M^2\bar{\mu}'}{Re} \tilde{T} \left[\frac{4}{3} (\bar{u}_x^2 + \bar{v}_y^2 + \bar{w}_z^2 - \bar{u}_x\bar{v}_y - \bar{u}_x\bar{w}_z - \bar{v}_y\bar{w}_z) \right. \\
& + \left. \bar{u}_y^2 + \bar{v}_x^2 + \bar{u}_z^2 + \bar{v}_z^2 + \bar{w}_x^2 + \bar{w}_y^2 + 2\bar{u}_y\bar{v}_x + 2\bar{u}_z\bar{w}_y + 2\bar{v}_z\bar{w}_y \right]
\end{aligned}$$

A. Linearized Navier-Stokes equations

$$\begin{aligned}
&= -\tilde{\rho} \frac{\partial \tilde{T}}{\partial t} - (\bar{\rho} + \tilde{\rho}) \left(\tilde{u} \tilde{T}_x + \tilde{v} \tilde{T}_y + \tilde{w} \tilde{T}_z \right) \\
&- \tilde{\rho} \left(\bar{u} \tilde{T}_x + \bar{v} \tilde{T}_y + \bar{w} \tilde{T}_z + \tilde{u} \bar{T}_x + \tilde{v} \bar{T}_y + \tilde{w} \bar{T}_z \right) \\
&+ (\gamma - 1) \tilde{T} \frac{\partial \tilde{\rho}}{\partial t} + (\gamma - 1) (\tilde{T} + \bar{T}) (\tilde{u} \tilde{\rho}_x + \tilde{v} \tilde{\rho}_y + \tilde{w} \tilde{\rho}_z) \\
&+ (\gamma - 1) \tilde{T} (\bar{u} \tilde{\rho}_x + \bar{v} \tilde{\rho}_y + \bar{w} \tilde{\rho}_z + \tilde{u} \bar{\rho}_x + \tilde{v} \bar{\rho}_y + \tilde{w} \bar{\rho}_z) \\
&+ \frac{\gamma}{Re Pr} \left[\tilde{\kappa}' \tilde{T} (\tilde{T}_{xx} + \tilde{T}_{yy} + \tilde{T}_{zz}) + \tilde{\kappa}' (\tilde{T}_x^2 + \tilde{T}_y^2 + \tilde{T}_z^2) \right. \\
&+ \left. \tilde{\kappa}'' \tilde{T} (\bar{T}_x \tilde{T}_x + \bar{T}_y \tilde{T}_y + \bar{T}_z \tilde{T}_z) \right] \\
&+ \frac{\gamma(\gamma - 1) M^2 \tilde{\mu}' \tilde{T}}{Re} \left[\frac{2}{3} (2\bar{u}_x - \bar{v}_y - \bar{w}_z) \tilde{u}_x + (\bar{u}_y + \bar{v}_x) \tilde{u}_y + (\bar{u}_z + \bar{w}_x) \tilde{u}_z \right. \\
&+ (\bar{u}_y + \bar{v}_x) \tilde{v}_x + \frac{2}{3} (2\bar{v}_y - \bar{u}_x - \bar{w}_z) \tilde{v}_y + (\bar{w}_y + \bar{v}_z) \tilde{v}_z \\
&+ (\bar{w}_x + \bar{u}_z) \tilde{w}_x + (\bar{w}_y + \bar{v}_z) \tilde{w}_y + \frac{2}{3} (2\bar{w}_z - \bar{u}_x - \bar{v}_y) \tilde{w}_z \\
&+ \frac{2}{3} (2\tilde{u}_x - \tilde{v}_y - \tilde{w}_z) \bar{u}_x + (\tilde{u}_y + \tilde{v}_x) \bar{u}_y + (\tilde{u}_z + \tilde{w}_x) \bar{u}_z \\
&+ (\tilde{u}_y + \tilde{v}_x) \bar{v}_x + \frac{2}{3} (2\tilde{v}_y - \tilde{u}_x - \tilde{w}_z) \bar{v}_y + (\tilde{w}_y + \tilde{v}_z) \bar{v}_z \\
&+ (\tilde{w}_x + \tilde{u}_z) \bar{w}_x + (\tilde{w}_y + \tilde{v}_z) \bar{w}_y + \frac{2}{3} (2\tilde{w}_z - \tilde{u}_x - \tilde{v}_y) \bar{w}_z \left. \right] \\
&+ \frac{\gamma(\gamma - 1) M^2 (\tilde{\mu}' \tilde{T} + \bar{\mu})}{Re} \left[\frac{4}{3} (\tilde{u}_x^2 + \tilde{v}_y^2 + \tilde{w}_z^2 - \tilde{u}_x \tilde{v}_y - \tilde{u}_x \tilde{w}_z - \tilde{v}_y \tilde{w}_z) \right. \\
&+ \left. \tilde{u}_y^2 + \tilde{v}_x^2 + \tilde{u}_z^2 + \tilde{v}_z^2 + \tilde{w}_x^2 + \tilde{w}_y^2 + 2\tilde{u}_y \tilde{v}_x + 2\tilde{u}_z \tilde{w}_y + 2\tilde{v}_z \tilde{w}_y \right]. \quad (\text{A.5})
\end{aligned}$$

Here, $(\cdot)' = \frac{\partial(\cdot)}{\partial T}$ and $(\cdot)'' = \frac{\partial^2(\cdot)}{\partial T^2}$. Note that the right-hand-side (RHS) terms are the non-linear terms of $\mathcal{O}(\epsilon^2)$ and $\mathcal{O}(\epsilon^3)$, which are neglected to recover the linearized Navier-Stokes equations.

Appendix B

Temporal BiGlobal EVP operators

The operators of the temporal BiGlobal EVP (1.26) for compressible flows are structured as follows

$$\omega \begin{pmatrix} \mathcal{A}_{11} & \mathcal{A}_{12} & \mathcal{A}_{13} & \mathcal{A}_{14} & 0 \\ \mathcal{A}_{21} & \mathcal{A}_{22} & \mathcal{A}_{23} & \mathcal{A}_{24} & \mathcal{A}_{25} \\ \mathcal{A}_{31} & \mathcal{A}_{32} & \mathcal{A}_{33} & \mathcal{A}_{34} & \mathcal{A}_{35} \\ \mathcal{A}_{41} & \mathcal{A}_{42} & \mathcal{A}_{43} & \mathcal{A}_{44} & \mathcal{A}_{45} \\ \mathcal{A}_{51} & \mathcal{A}_{52} & \mathcal{A}_{53} & \mathcal{A}_{54} & \mathcal{A}_{55} \end{pmatrix} \begin{pmatrix} \hat{\rho} \\ \hat{u} \\ \hat{v} \\ \hat{w} \\ \hat{T} \end{pmatrix} = \begin{pmatrix} \mathcal{B}_{11} & 0 & 0 & 0 & 0 \\ 0 & \mathcal{B}_{22} & 0 & 0 & 0 \\ 0 & 0 & \mathcal{B}_{33} & 0 & 0 \\ 0 & 0 & 0 & \mathcal{B}_{44} & 0 \\ \mathcal{B}_{51} & 0 & 0 & 0 & \mathcal{B}_{55} \end{pmatrix} \begin{pmatrix} \hat{\rho} \\ \hat{u} \\ \hat{v} \\ \hat{w} \\ \hat{T} \end{pmatrix} \quad (\text{B.1})$$

The full listing of the operators in equation (B.1) follows

$$\begin{aligned} \mathcal{A}_{11} &= \bar{v}\mathcal{D}_y + \bar{w}\mathcal{D}_z + \bar{v}_y + \bar{w}_z + \bar{u}\alpha \\ \mathcal{A}_{12} &= \bar{\rho}\alpha \\ \mathcal{A}_{13} &= \bar{\rho}\mathcal{D}_y + \bar{\rho}_y \\ \mathcal{A}_{14} &= \bar{\rho}\mathcal{D}_z + \bar{\rho}_z \\ \mathcal{A}_{21} &= \bar{v}\bar{u}_y + \bar{w}\bar{u}_z + \frac{1}{\gamma M^2}(\bar{T}\bar{i}\alpha) \\ \mathcal{A}_{22} &= -\frac{\bar{\mu}}{Re}(\mathcal{D}_{yy}^2 + \mathcal{D}_{zz}^2) + \left(\bar{\rho}\bar{v} - \frac{\bar{\mu}_y}{Re}\right)\mathcal{D}_y \\ &\quad + \left(\bar{\rho}\bar{w} - \frac{\bar{\mu}_z}{Re}\right)\mathcal{D}_z + \bar{\rho}\bar{u}\alpha + \frac{4}{3}\frac{\bar{\mu}}{Re}\alpha^2 \\ \mathcal{A}_{23} &= -\frac{\bar{\mu}}{3Re}\alpha\mathcal{D}_y + \bar{\rho}\bar{u}_y - \frac{\bar{\mu}_y}{Re}\alpha \\ \mathcal{A}_{24} &= -\frac{\bar{\mu}}{3Re}\alpha\mathcal{D}_z + \bar{\rho}\bar{u}_z - \frac{\bar{\mu}_z}{Re}\alpha \\ \mathcal{A}_{25} &= -\frac{\bar{\mu}'}{Re}(\bar{u}_y\mathcal{D}_y + \bar{u}_z\mathcal{D}_z) + \frac{1}{\gamma M^2}\bar{\rho}\bar{i}\alpha \end{aligned}$$

B. Temporal BiGlobal EVP operators

$$\begin{aligned}
& - \frac{\bar{\mu}'}{Re} \left[\bar{u}_{yy} + \bar{u}_{zz} - \frac{2}{3}(\bar{v}_y + \bar{w}_z)\text{i}\alpha \right] - \frac{\bar{\mu}''}{Re} [\bar{u}_y \bar{T}_y + \bar{u}_z \bar{T}_z] \\
\mathcal{A}_{31} &= \frac{\bar{T}}{\gamma M^2} \mathcal{D}_y + \bar{v} \bar{v}_y + \bar{w} \bar{w}_z + \frac{1}{\gamma M^2} \bar{T}_y \\
\mathcal{A}_{32} &= -\frac{\bar{\mu}}{3 Re} \text{i}\alpha \mathcal{D}_y + \frac{2\bar{\mu}_y}{3 Re} \text{i}\alpha \\
\mathcal{A}_{33} &= -\frac{\bar{\mu}}{Re} \left(\frac{4}{3} \mathcal{D}_{yy}^2 + \mathcal{D}_{zz}^2 \right) + \left(\bar{\rho} \bar{v} - \frac{4\bar{\mu}_y}{3 Re} \right) \mathcal{D}_y + \left(\bar{\rho} \bar{w} - \frac{\bar{\mu}_z}{Re} \right) \mathcal{D}_z \\
&+ \bar{\rho}(\bar{u} \text{i}\alpha + \bar{v}_y) + \frac{\bar{\mu}}{Re} \alpha^2 \\
\mathcal{A}_{34} &= -\frac{\bar{\mu}}{3 Re} \mathcal{D}_{yz}^2 - \frac{\bar{\mu}_z}{Re} \mathcal{D}_y + \frac{2\bar{\mu}_y}{3 Re} \mathcal{D}_z + \bar{\rho} \bar{v}_z \\
\mathcal{A}_{35} &= \left[\frac{\bar{\rho}}{\gamma M^2} - \frac{\bar{\mu}'}{Re} \frac{2}{3} (2\bar{v}_y - \bar{w}_z) \right] \mathcal{D}_y - \frac{\bar{\mu}'}{Re} (\bar{v}_z + \bar{w}_y) \mathcal{D}_z \\
&+ \frac{\bar{\rho}_y}{\gamma M^2} - \frac{\bar{\mu}''}{Re} \left[\frac{2}{3} (2\bar{v}_y - \bar{w}_z) \bar{T}_y + (\bar{v}_z + \bar{w}_y) \bar{T}_z \right] \\
&- \frac{\bar{\mu}'}{Re} \left(\frac{4}{3} \bar{v}_{yy} + \bar{v}_{zz} + \frac{1}{3} \bar{w}_{yz} + \bar{u}_y \text{i}\alpha \right) \\
\mathcal{A}_{41} &= \frac{\bar{T}}{\gamma M^2} \mathcal{D}_z + \bar{v} \bar{w}_y + \bar{w} \bar{w}_z + \frac{1}{\gamma M^2} \bar{T}_z \\
\mathcal{A}_{42} &= -\frac{\bar{\mu}}{3 Re} \text{i}\alpha \mathcal{D}_z + \frac{2\bar{\mu}_z}{3 Re} \text{i}\alpha \\
\mathcal{A}_{43} &= -\frac{\bar{\mu}}{3 Re} \mathcal{D}_{yz}^2 + \frac{2\bar{\mu}_z}{3 Re} \mathcal{D}_y - \frac{\bar{\mu}_y}{Re} \mathcal{D}_z + \bar{\rho} \bar{w}_y \\
\mathcal{A}_{44} &= -\frac{\bar{\mu}}{Re} \left(\mathcal{D}_{yy}^2 + \frac{4}{3} \mathcal{D}_{zz}^2 \right) + \left(\bar{\rho} \bar{v} - \frac{\bar{\mu}_y}{Re} \right) \mathcal{D}_y + \left(\bar{\rho} \bar{w} - \frac{4\bar{\mu}_z}{3 Re} \right) \mathcal{D}_z \\
&+ \bar{\rho}(\bar{u} \text{i}\alpha + \bar{w}_z) + \frac{\bar{\mu}}{Re} \alpha^2 \\
\mathcal{A}_{45} &= -\frac{\bar{\mu}'}{Re} (\bar{w}_y + \bar{v}_z) \mathcal{D}_y + \left[\frac{\bar{\rho}}{\gamma M^2} - \frac{\bar{\mu}'}{Re} \frac{2}{3} (2\bar{w}_z - \bar{v}_y) \right] \mathcal{D}_z \\
&+ \frac{1}{\gamma M^2} \bar{\rho}_z - \frac{\bar{\mu}''}{Re} \left[(\bar{w}_y + \bar{v}_z) \bar{T}_y + \frac{2}{3} (2\bar{w}_z - \bar{v}_y) \bar{T}_z \right] \\
&- \frac{\bar{\mu}'}{Re} \left[\frac{4}{3} \bar{w}_{zz} + \bar{w}_{yy} + \frac{1}{3} \bar{v}_{yz} + \bar{u}_z \text{i}\alpha \right] \\
\mathcal{A}_{51} &= -(\gamma - 1) \bar{T} (\bar{v} \mathcal{D}_y + \bar{w} \mathcal{D}_z) + \gamma (\bar{T}_y \bar{v} + \bar{T}_z \bar{w}) - (\gamma - 1) \bar{T} \bar{u} \text{i}\alpha \\
\mathcal{A}_{52} &= -\frac{2\gamma(\gamma - 1)M^2 \bar{\mu}}{Re} \left[\bar{u}_y \mathcal{D}_y + \bar{u}_z \mathcal{D}_z - \frac{2}{3} (\bar{v}_y + \bar{w}_z) \text{i}\alpha \right]
\end{aligned}$$

$$\begin{aligned}
\mathcal{A}_{53} &= -\frac{2\gamma(\gamma-1)M^2\bar{\mu}}{Re} \left[\frac{2}{3}(2\bar{v}_y - \bar{w}_z)\mathcal{D}_y + (\bar{v}_z + \bar{w}_y)\mathcal{D}_z + \bar{u}_y i\alpha \right] \\
&\quad - (\gamma-1)(\bar{T}_y\bar{\rho} + \bar{T}\bar{\rho}_y) + \gamma\bar{\rho}\bar{T}_y \\
\mathcal{A}_{54} &= -\frac{2\gamma(\gamma-1)M^2\bar{\mu}}{Re} \left[(\bar{v}_z + \bar{w}_y)\mathcal{D}_y + \frac{2}{3}(2\bar{w}_z - \bar{v}_y)\mathcal{D}_z + \bar{u}_z i\alpha \right] \\
&\quad - (\gamma-1)(\bar{T}_z\bar{\rho} + \bar{T}\bar{\rho}_z) + \gamma\bar{\rho}\bar{T}_z \\
\mathcal{A}_{55} &= -\frac{\gamma}{Re Pr} \bar{\kappa} (\mathcal{D}_{yy}^2 + \mathcal{D}_{zz}^2) + \left(\bar{\rho}\bar{v} - \frac{\gamma}{Re Pr} 2\bar{\kappa}'\bar{T}_y \right) \mathcal{D}_y \\
&\quad + \left(\bar{\rho}\bar{w} - \frac{\gamma}{Re Pr} 2\bar{\kappa}'\bar{T}_z \right) \mathcal{D}_z - (\gamma-1)(\bar{\rho}_y\bar{v} + \bar{\rho}_z\bar{w}) + \bar{\rho}\bar{u}i\alpha \\
&\quad - \frac{\gamma}{Re Pr} \left[-\bar{\kappa}\alpha^2 + \bar{\kappa}'(\bar{T}_{yy} + \bar{T}_{zz}) + \bar{\kappa}''(\bar{T}_y^2 + \bar{T}_z^2) \right] \\
&\quad - \frac{\gamma(\gamma-1)M^2\bar{\mu}'}{Re} \left[\frac{4}{3}(\bar{v}_y^2 + \bar{w}_z^2 - \bar{v}_y\bar{w}_z) + \bar{u}_y^2 + \bar{u}_z^2 + \bar{v}_z^2 + \bar{w}_y^2 + 2\bar{v}_z\bar{w}_y \right] \\
\mathcal{B}_{11} &= i \\
\mathcal{B}_{22} &= \bar{\rho}i \\
\mathcal{B}_{33} &= \bar{\rho}i \\
\mathcal{B}_{44} &= \bar{\rho}i \\
\mathcal{B}_{51} &= (1-\gamma)\bar{T}i \\
\mathcal{B}_{55} &= \bar{\rho}i
\end{aligned}$$

Appendix C

Spatial BiGlobal EVP operators

The operators of the spatial BiGlobal EVP (1.28) for compressible flows are structured as follows

$$\alpha \begin{pmatrix} \mathcal{A}_{11} & 0 & \mathcal{A}_{13} & \mathcal{A}_{14} & 0 & 0 & 0 & 0 & 0 \\ \mathcal{A}_{21} & \mathcal{A}_{22} & \mathcal{A}_{23} & \mathcal{A}_{24} & \mathcal{A}_{25} & 0 & 0 & 0 & 0 \\ \mathcal{A}_{31} & 0 & \mathcal{A}_{33} & \mathcal{A}_{34} & \mathcal{A}_{35} & 0 & 0 & 0 & 0 \\ \mathcal{A}_{41} & 0 & \mathcal{A}_{43} & \mathcal{A}_{44} & \mathcal{A}_{45} & 0 & 0 & 0 & 0 \\ \mathcal{A}_{51} & \mathcal{A}_{52} & \mathcal{A}_{53} & \mathcal{A}_{54} & \mathcal{A}_{55} & 0 & 0 & 0 & 0 \\ 0 & 0 & 0 & 0 & 0 & \mathcal{I} & 0 & 0 & 0 \\ 0 & 0 & 0 & 0 & 0 & 0 & \mathcal{I} & 0 & 0 \\ 0 & 0 & 0 & 0 & 0 & 0 & 0 & \mathcal{I} & 0 \\ 0 & 0 & 0 & 0 & 0 & 0 & 0 & 0 & \mathcal{I} \end{pmatrix} \begin{pmatrix} \hat{\rho} \\ \hat{u} \\ \hat{v} \\ \hat{w} \\ \hat{T} \\ \alpha \hat{u} \\ \alpha \hat{v} \\ \alpha \hat{w} \\ \alpha \hat{T} \end{pmatrix} =$$

$$\alpha \begin{pmatrix} \mathcal{B}_{11} & \mathcal{B}_{12} & 0 & 0 & 0 & 0 & 0 & 0 & 0 \\ \mathcal{B}_{21} & \mathcal{B}_{22} & \mathcal{B}_{23} & \mathcal{B}_{24} & \mathcal{B}_{25} & \mathcal{B}_{26} & 0 & 0 & 0 \\ 0 & \mathcal{B}_{32} & \mathcal{B}_{33} & 0 & \mathcal{B}_{35} & 0 & \mathcal{B}_{37} & 0 & 0 \\ 0 & \mathcal{B}_{42} & 0 & \mathcal{B}_{44} & \mathcal{B}_{45} & 0 & 0 & \mathcal{B}_{48} & 0 \\ \mathcal{B}_{51} & \mathcal{B}_{52} & \mathcal{B}_{53} & \mathcal{B}_{54} & \mathcal{B}_{55} & 0 & 0 & 0 & \mathcal{B}_{59} \\ 0 & \mathcal{I} & 0 & 0 & 0 & 0 & 0 & 0 & 0 \\ 0 & 0 & \mathcal{I} & 0 & 0 & 0 & 0 & 0 & 0 \\ 0 & 0 & 0 & \mathcal{I} & 0 & 0 & 0 & 0 & 0 \\ 0 & 0 & 0 & 0 & \mathcal{I} & 0 & 0 & 0 & 0 \end{pmatrix} \begin{pmatrix} \hat{\rho} \\ \hat{u} \\ \hat{v} \\ \hat{w} \\ \hat{T} \\ \alpha \hat{u} \\ \alpha \hat{v} \\ \alpha \hat{w} \\ \alpha \hat{T} \end{pmatrix} \quad (\text{C.1})$$

The full listing of the operators in equation (C.1) follows

$$\begin{aligned} \mathcal{A}_{11} &= \bar{v} \mathcal{D}_y + \bar{w} \mathcal{D}_z + \bar{v}_y + \bar{w}_z - i\omega \\ \mathcal{A}_{13} &= \bar{\rho} \mathcal{D}_y + \bar{\rho}_y \\ \mathcal{A}_{14} &= \bar{\rho} \mathcal{D}_z + \bar{\rho}_z \\ \mathcal{A}_{21} &= \bar{v} \bar{u}_y + \bar{w} \bar{u}_z \\ \mathcal{A}_{22} &= -\frac{\bar{\mu}}{Re} (\mathcal{D}_{yy}^2 + \mathcal{D}_{zz}^2) + \left(\bar{\rho} \bar{v} - \frac{\bar{\mu}_y}{Re} \right) \mathcal{D}_y + \left(\bar{\rho} \bar{w} - \frac{\bar{\mu}_z}{Re} \right) \mathcal{D}_z - i \bar{\rho} \omega \\ \mathcal{A}_{23} &= \bar{\rho} \bar{u}_y \\ \mathcal{A}_{24} &= \bar{\rho} \bar{u}_z \end{aligned}$$

$$\begin{aligned}
\mathcal{A}_{25} &= -\frac{\bar{\mu}'}{Re}(\bar{u}_y \mathcal{D}_y + \bar{u}_z \mathcal{D}_z) \\
&\quad - \frac{\bar{\mu}'}{Re}[\bar{u}_{yy} + \bar{u}_{zz}] - \frac{\bar{\mu}''}{Re}[\bar{u}_y \bar{T}_y + \bar{u}_z \bar{T}_z] \\
\mathcal{A}_{31} &= \frac{\bar{T}}{\gamma M^2} \mathcal{D}_y + \bar{v} \bar{v}_y + \bar{w} \bar{v}_z + \frac{1}{\gamma M^2} \bar{T}_y \\
\mathcal{A}_{33} &= -\frac{\bar{\mu}}{Re} \left(\frac{4}{3} \mathcal{D}_{yy}^2 + \mathcal{D}_{zz}^2 \right) + \left(\bar{\rho} \bar{v} - \frac{4 \bar{\mu}_y}{3 Re} \right) \mathcal{D}_y \\
&\quad + \left(\bar{\rho} \bar{w} - \frac{\bar{\mu}_z}{Re} \right) \mathcal{D}_z + \bar{\rho} \bar{v}_y - i \bar{\rho} \omega \\
\mathcal{A}_{34} &= -\frac{\bar{\mu}}{3 Re} \mathcal{D}_{yz}^2 - \frac{\bar{\mu}_z}{Re} \mathcal{D}_y + \frac{2 \bar{\mu}_y}{3 Re} \mathcal{D}_z + \bar{\rho} \bar{v}_z \\
\mathcal{A}_{35} &= \left[\frac{\bar{\rho}}{\gamma M^2} - \frac{\bar{\mu}'}{Re} \frac{2}{3} (2 \bar{v}_y - \bar{w}_z) \right] \mathcal{D}_y - \frac{\bar{\mu}'}{Re} (\bar{v}_z + \bar{w}_y) \mathcal{D}_z \\
&\quad + \frac{\bar{\rho}_y}{\gamma M^2} - \frac{\bar{\mu}''}{Re} \left[\frac{2}{3} (2 \bar{v}_y - \bar{w}_z) \bar{T}_y + (\bar{v}_z + \bar{w}_y) \bar{T}_z \right] \\
&\quad - \frac{\bar{\mu}'}{Re} \left(\frac{4}{3} \bar{v}_{yy} + \bar{v}_{zz} + \frac{1}{3} \bar{w}_{yz} \right) \\
\mathcal{A}_{41} &= \frac{\bar{T}}{\gamma M^2} \mathcal{D}_z + \bar{v} \bar{w}_y + \bar{w} \bar{w}_z + \frac{1}{\gamma M^2} \bar{T}_z \\
\mathcal{A}_{43} &= -\frac{\bar{\mu}}{3 Re} \mathcal{D}_{yz}^2 + \frac{2 \bar{\mu}_z}{3 Re} \mathcal{D}_y - \frac{\bar{\mu}_y}{Re} \mathcal{D}_z + \bar{\rho} \bar{w}_y \\
\mathcal{A}_{44} &= -\frac{\bar{\mu}}{Re} \left(\mathcal{D}_{yy}^2 + \frac{4}{3} \mathcal{D}_{zz}^2 \right) + \left(\bar{\rho} \bar{v} - \frac{\bar{\mu}_y}{Re} \right) \mathcal{D}_y \\
&\quad + \left(\bar{\rho} \bar{w} - \frac{4 \bar{\mu}_z}{3 Re} \right) \mathcal{D}_z + \bar{\rho} \bar{w}_z - i \bar{\rho} \omega \\
\mathcal{A}_{45} &= -\frac{\bar{\mu}'}{Re} (\bar{w}_y + \bar{v}_z) \mathcal{D}_y + \left[\frac{\bar{\rho}}{\gamma M^2} - \frac{\bar{\mu}'}{Re} \frac{2}{3} (2 \bar{w}_z - \bar{v}_y) \right] \mathcal{D}_z \\
&\quad + \frac{1}{\gamma M^2} \bar{\rho}_z - \frac{\bar{\mu}''}{Re} \left[(\bar{w}_y + \bar{v}_z) \bar{T}_y + \frac{2}{3} (2 \bar{w}_z - \bar{v}_y) \bar{T}_z \right] \\
&\quad - \frac{\bar{\mu}'}{Re} \left[\frac{4}{3} \bar{w}_{zz} + \bar{w}_{yy} + \frac{1}{3} \bar{v}_{yz} \right] \\
\mathcal{A}_{51} &= -(\gamma - 1) \bar{T} (\bar{v} \mathcal{D}_y + \bar{w} \mathcal{D}_z) + (\bar{T}_y \bar{v} + \bar{T}_z \bar{w}) + (\gamma - 1) \bar{T} i \omega \\
\mathcal{A}_{52} &= -\frac{2\gamma(\gamma - 1)M^2 \bar{\mu}}{Re} [\bar{u}_y \mathcal{D}_y + \bar{u}_z \mathcal{D}_z] \\
\mathcal{A}_{53} &= -\frac{2\gamma(\gamma - 1)M^2 \bar{\mu}}{Re} \left[\frac{2}{3} (2 \bar{v}_y - \bar{w}_z) \mathcal{D}_y + (\bar{v}_z + \bar{w}_y) \mathcal{D}_z \right] \\
&\quad - (\gamma - 1) \bar{T} \bar{\rho}_y + \bar{\rho} \bar{T}_y
\end{aligned}$$

$$\begin{aligned}
\mathcal{A}_{54} &= -\frac{2\gamma(\gamma-1)M^2\bar{\mu}}{Re} \left[(\bar{v}_z + \bar{w}_y)\mathcal{D}_y + \frac{2}{3}(2\bar{w}_z - \bar{v}_y)\mathcal{D}_z \right] \\
&\quad - (\gamma-1)\bar{T}\bar{\rho}_z + \bar{\rho}\bar{T}_z \\
\mathcal{A}_{55} &= -\frac{\gamma}{Re Pr} \bar{\kappa} (\mathcal{D}_{yy}^2 + \mathcal{D}_{zz}^2) + \left(\bar{\rho}\bar{v} - \frac{\gamma}{Re Pr} 2\bar{\kappa}'\bar{T}_y \right) \mathcal{D}_y \\
&\quad + \left(\bar{\rho}\bar{w} - \frac{\gamma}{Re Pr} 2\bar{\kappa}'\bar{T}_z \right) \mathcal{D}_z - (\gamma-1)(\bar{\rho}_y\bar{v} + \bar{\rho}_z\bar{w}) - \bar{\rho}i\omega \\
&\quad - \frac{\gamma}{Re Pr} [\bar{\kappa}'(\bar{T}_{yy} + \bar{T}_{zz}) + \bar{\kappa}''(\bar{T}_y^2 + \bar{T}_z^2)] \\
&\quad - \frac{\gamma(\gamma-1)M^2\bar{\mu}'}{Re} \left[\frac{4}{3}(\bar{v}_y^2 + \bar{w}_z^2 - \bar{v}_y\bar{w}_z) + \bar{u}_y^2 + \bar{u}_z^2 + \bar{v}_z^2 + \bar{w}_y^2 + 2\bar{v}_z\bar{w}_y \right] \\
\mathcal{B}_{11} &= -i\bar{u} \\
\mathcal{B}_{12} &= -i\bar{\rho} \\
\mathcal{B}_{21} &= \frac{-i\bar{T}}{\gamma M^2} \\
\mathcal{B}_{22} &= -i\bar{\rho}\bar{u} \\
\mathcal{B}_{23} &= \frac{\bar{\mu}i}{3 Re} \mathcal{D}_y + \frac{\bar{\mu}_y i}{Re} \\
\mathcal{B}_{24} &= \frac{\bar{\mu}i}{3 Re} \mathcal{D}_z + \frac{\bar{\mu}_z i}{Re} \\
\mathcal{B}_{25} &= -\frac{\bar{\rho}i}{\gamma M^2} - \frac{2i\bar{\mu}'}{3 Re} (\bar{v}_y + \bar{w}_z) \\
\mathcal{B}_{26} &= -\frac{4\bar{\mu}}{3 Re} \\
\mathcal{B}_{32} &= \frac{\bar{\mu}}{3 Re} i\mathcal{D}_y - \frac{2\bar{\mu}_y i}{3 Re} \\
\mathcal{B}_{33} &= -i\bar{\rho}\bar{u} \\
\mathcal{B}_{35} &= \frac{\bar{\mu}'i}{Re} \bar{u}_y \\
\mathcal{B}_{37} &= -\frac{\bar{\mu}}{Re} \\
\mathcal{B}_{42} &= \frac{\bar{\mu}i}{3 Re} \mathcal{D}_z - \frac{2i\bar{\mu}_z}{3 Re} \\
\mathcal{B}_{44} &= -i\bar{\rho}\bar{u} \\
\mathcal{B}_{45} &= \frac{\bar{\mu}'}{Re} \bar{u}_z i \\
\mathcal{B}_{48} &= -\frac{\bar{\mu}}{Re} \\
\mathcal{B}_{51} &= (\gamma-1)\bar{T}\bar{u}i
\end{aligned}$$

C. Spatial BiGlobal EVP operators

$$\mathcal{B}_{52} = -\frac{4\gamma(\gamma-1)M^2\bar{\mu}}{3Re}(\bar{v}_y + \bar{w}_z)\mathbf{i}$$

$$\mathcal{B}_{54} = \frac{2\gamma(\gamma-1)M^2\bar{\mu}}{Re}\bar{u}_y\mathbf{i}$$

$$\mathcal{B}_{54} = \frac{2\gamma(\gamma-1)M^2\bar{\mu}}{Re}\bar{u}_z\mathbf{i}$$

$$\mathcal{B}_{55} = -i\bar{\rho}\bar{u}$$

$$\mathcal{B}_{59} = -\frac{\gamma\bar{\kappa}}{RePr}$$

Appendix D

Non-linear PSE-3D operators

Equation (1.57) for compressible flows expressed in matrix form results (index n is suppressed for simplification)

$$\begin{aligned}
 & \begin{pmatrix} \mathcal{L}_{11} & \mathcal{L}_{12} & \mathcal{L}_{13} & \mathcal{L}_{14} & 0 \\ \mathcal{L}_{21} & \mathcal{L}_{22} & \mathcal{L}_{23} & \mathcal{L}_{24} & \mathcal{L}_{25} \\ \mathcal{L}_{31} & \mathcal{L}_{32} & \mathcal{L}_{33} & \mathcal{L}_{34} & \mathcal{L}_{35} \\ \mathcal{L}_{41} & \mathcal{L}_{42} & \mathcal{L}_{43} & \mathcal{L}_{44} & \mathcal{L}_{45} \\ \mathcal{L}_{51} & \mathcal{L}_{52} & \mathcal{L}_{53} & \mathcal{L}_{54} & \mathcal{L}_{55} \end{pmatrix} \begin{pmatrix} \hat{\rho} \\ \hat{u} \\ \hat{v} \\ \hat{w} \\ \hat{T} \end{pmatrix} \\
 + & \begin{pmatrix} \mathcal{M}_{11} & \mathcal{M}_{12} & 0 & 0 & 0 \\ \mathcal{M}_{21} & \mathcal{M}_{22} & 0 & 0 & \mathcal{M}_{25} \\ 0 & 0 & \mathcal{M}_{33} & 0 & 0 \\ 0 & 0 & 0 & \mathcal{M}_{44} & 0 \\ \mathcal{M}_{51} & 0 & 0 & 0 & \mathcal{M}_{55} \end{pmatrix} \begin{pmatrix} \hat{\rho}_x \\ \hat{u}_x \\ \hat{v}_x \\ \hat{w}_x \\ \hat{T}_x \end{pmatrix} = \begin{pmatrix} \mathcal{F}_1 \\ \mathcal{F}_2 \\ \mathcal{F}_3 \\ \mathcal{F}_4 \\ \mathcal{F}_5 \end{pmatrix} \quad (\text{D.1})
 \end{aligned}$$

The full listing of the operators in equation (D.1) follows

$$\begin{aligned}
 \mathcal{L}_{11} &= \bar{v}\mathcal{D}_y + \bar{w}\mathcal{D}_z + \bar{u}_x + \bar{v}_y + \bar{w}_z + \bar{u}i\alpha - i\omega \\
 \mathcal{L}_{12} &= \bar{\rho}i\alpha + \bar{\rho}_x \\
 \mathcal{L}_{13} &= \bar{\rho}\mathcal{D}_y + \bar{\rho}_y \\
 \mathcal{L}_{14} &= \bar{\rho}\mathcal{D}_z + \bar{\rho}_z \\
 \mathcal{L}_{21} &= \bar{u}\bar{u}_x + \bar{v}\bar{u}_y + \bar{w}\bar{u}_z + \frac{1}{\gamma M^2}(\bar{T}i\alpha + \bar{T}_x) \\
 \mathcal{L}_{22} &= -\frac{\bar{\mu}}{Re}(\mathcal{D}_{yy}^2 + \mathcal{D}_{zz}^2) + \left(\bar{\rho}\bar{v} - \frac{\bar{\mu}_y}{Re}\right)\mathcal{D}_y + \left(\bar{\rho}\bar{w} - \frac{\bar{\mu}_z}{Re}\right)\mathcal{D}_z \\
 &+ \bar{\rho}(\bar{u}i\alpha + \bar{u}_x - i\omega) + \frac{4}{3}\frac{\bar{\mu}}{Re}\alpha^2 \\
 \mathcal{L}_{23} &= -\frac{\bar{\mu}}{3Re}i\alpha\mathcal{D}_y + \bar{\rho}\bar{u}_y - \frac{\bar{\mu}_y}{Re}i\alpha \\
 \mathcal{L}_{24} &= -\frac{\bar{\mu}}{3Re}i\alpha\mathcal{D}_z + \bar{\rho}\bar{u}_z - \frac{\bar{\mu}_z}{Re}i\alpha \\
 \mathcal{L}_{25} &= -\frac{\bar{\mu}'}{Re}(\bar{u}_y\mathcal{D}_y + \bar{u}_z\mathcal{D}_z) + \frac{1}{\gamma M^2}(\bar{\rho}i\alpha + \bar{\rho}_x)
 \end{aligned}$$

$$\begin{aligned}
 & - \frac{\bar{\mu}'}{Re} \left[\bar{u}_{yy} + \bar{u}_{zz} - \frac{2}{3}(\bar{v}_y + \bar{w}_z)\text{i}\alpha \right] - \frac{\bar{\mu}''}{Re} (\bar{u}_y \bar{T}_y + \bar{u}_z \bar{T}_z) \\
 \mathcal{L}_{31} & = \frac{\bar{T}}{\gamma M^2} \mathcal{D}_y + \bar{u} \bar{v}_x + \bar{v} \bar{v}_y + \bar{w} \bar{v}_z + \frac{1}{\gamma M^2} \bar{T}_y \\
 \mathcal{L}_{32} & = -\frac{\bar{\mu}}{3 Re} \text{i}\alpha \mathcal{D}_y + \bar{\rho} \bar{v}_x + \frac{2 \bar{\mu}_y}{3 Re} \text{i}\alpha \\
 \mathcal{L}_{33} & = -\frac{\bar{\mu}}{Re} \left(\frac{4}{3} \mathcal{D}_{yy}^2 + \mathcal{D}_{zz}^2 \right) + \left(\bar{\rho} \bar{v} - \frac{4 \bar{\mu}_y}{3 Re} \right) \mathcal{D}_y + \left(\bar{\rho} \bar{w} - \frac{\bar{\mu}_z}{Re} \right) \mathcal{D}_z \\
 & + \bar{\rho} (\bar{u} \text{i}\alpha + \bar{v}_y - \text{i}\omega) + \frac{\bar{\mu}}{Re} \alpha^2 \\
 \mathcal{L}_{34} & = -\frac{\bar{\mu}}{3 Re} \mathcal{D}_{yz}^2 - \frac{\bar{\mu}_z}{Re} \mathcal{D}_y + \frac{2 \bar{\mu}_y}{3 Re} \mathcal{D}_z + \bar{\rho} \bar{v}_z \\
 \mathcal{L}_{35} & = \left[\frac{\bar{\rho}}{\gamma M^2} - \frac{\bar{\mu}'}{Re} \frac{2}{3} (2\bar{v}_y - \bar{w}_z) \right] \mathcal{D}_y - \frac{\bar{\mu}'}{Re} (\bar{v}_z + \bar{w}_y) \mathcal{D}_z + \frac{\bar{\rho}_y}{\gamma M^2} \\
 & - \frac{\bar{\mu}''}{Re} \left[\frac{2}{3} (2\bar{v}_y - \bar{w}_z) \bar{T}_y + (\bar{v}_z + \bar{w}_y) \bar{T}_z \right] \\
 & - \frac{\bar{\mu}'}{Re} \left(\frac{4}{3} \bar{v}_{yy} + \bar{v}_{zz} + \frac{1}{3} \bar{w}_{yz} + \bar{u}_y \text{i}\alpha \right) \\
 \mathcal{L}_{41} & = \frac{\bar{T}}{\gamma M^2} \mathcal{D}_z + \bar{u} \bar{w}_x + \bar{v} \bar{w}_y + \bar{w} \bar{w}_z + \frac{1}{\gamma M^2} \bar{T}_z \\
 \mathcal{L}_{42} & = -\frac{\bar{\mu}}{3 Re} \text{i}\alpha \mathcal{D}_z + \bar{\rho} \bar{w}_x + \frac{2 \bar{\mu}_z}{3 Re} \text{i}\alpha \\
 \mathcal{L}_{43} & = -\frac{\bar{\mu}}{3 Re} \mathcal{D}_{yz}^2 + \frac{2 \bar{\mu}_z}{3 Re} \mathcal{D}_y - \frac{\bar{\mu}_y}{Re} \mathcal{D}_z + \bar{\rho} \bar{w}_y \\
 \mathcal{L}_{44} & = -\frac{\bar{\mu}}{Re} \left(\mathcal{D}_{yy}^2 + \frac{4}{3} \mathcal{D}_{zz}^2 \right) + \left(\bar{\rho} \bar{v} - \frac{\bar{\mu}_y}{Re} \right) \mathcal{D}_y + \left(\bar{\rho} \bar{w} - \frac{4 \bar{\mu}_z}{3 Re} \right) \mathcal{D}_z \\
 & + \bar{\rho} (\bar{u} \text{i}\alpha + \bar{w}_z - \text{i}\omega) + \frac{\bar{\mu}}{Re} \alpha^2 \\
 \mathcal{L}_{45} & = -\frac{\bar{\mu}'}{Re} (\bar{w}_y + \bar{v}_z) \mathcal{D}_y + \left[\frac{\bar{\rho}}{\gamma M^2} - \frac{\bar{\mu}'}{Re} \frac{2}{3} (2\bar{w}_z - \bar{v}_y) \right] \mathcal{D}_z + \frac{\bar{\rho}_z}{\gamma M^2} \\
 & - \frac{\bar{\mu}''}{Re} \left[(\bar{w}_y + \bar{v}_z) \bar{T}_y + \frac{2}{3} (2\bar{w}_z - \bar{v}_y) \bar{T}_z \right] \\
 & - \frac{\bar{\mu}'}{Re} \left(\frac{4}{3} \bar{w}_{zz} + \bar{w}_{yy} + \frac{1}{3} \bar{v}_{yz} + \bar{u}_z \text{i}\alpha \right) \\
 \mathcal{L}_{51} & = -(\gamma - 1) \bar{T} (\bar{v} \mathcal{D}_y + \bar{w} \mathcal{D}_z + \bar{u} \text{i}\alpha - \text{i}\omega) + (\bar{T}_x \bar{u} + \bar{T}_y \bar{v} + \bar{T}_z \bar{w}) \\
 \mathcal{L}_{52} & = -\frac{2\gamma(\gamma - 1)M^2 \bar{\mu}}{Re} \left[\bar{u}_y \mathcal{D}_y + \bar{u}_z \mathcal{D}_z - \frac{2}{3} (\bar{v}_y + \bar{w}_z) \text{i}\alpha \right] \\
 & - (\gamma - 1) \bar{T} \bar{\rho}_x + \bar{\rho} \bar{T}_x
 \end{aligned}$$

$$\begin{aligned}
\mathcal{L}_{53} &= -\frac{2\gamma(\gamma-1)M^2\bar{\mu}}{Re} \left[\frac{2}{3}(2\bar{v}_y - \bar{w}_z)\mathcal{D}_y + (\bar{v}_z + \bar{w}_y)\mathcal{D}_z + \bar{u}_y i\alpha \right] \\
&\quad - (\gamma-1)\bar{T}\bar{\rho}_y + \bar{\rho}\bar{T}_y \\
\mathcal{L}_{54} &= -\frac{2\gamma(\gamma-1)M^2\bar{\mu}}{Re} \left[(\bar{v}_z + \bar{w}_y)\mathcal{D}_y + \frac{2}{3}(2\bar{w}_z - \bar{v}_y)\mathcal{D}_z + \bar{u}_z i\alpha \right] \\
&\quad - (\gamma-1)\bar{T}\bar{\rho}_z + \bar{\rho}\bar{T}_z \\
\mathcal{L}_{55} &= -\frac{\gamma}{Re Pr} \bar{\kappa} (\mathcal{D}_{yy}^2 + \mathcal{D}_{zz}^2) + \left(\bar{\rho}\bar{v} - \frac{\gamma}{Re Pr} 2\bar{\kappa}'\bar{T}_y \right) \mathcal{D}_y \\
&\quad + \left(\bar{\rho}\bar{w} - \frac{\gamma}{Re Pr} 2\bar{\kappa}'\bar{T}_z \right) \mathcal{D}_z - (\gamma-1)(\bar{\rho}_x\bar{u} + \bar{\rho}_y\bar{v} + \bar{\rho}_z\bar{w}) \\
&\quad + \bar{\rho}(\bar{u}\alpha - i\omega) - \frac{\gamma}{Re Pr} [-\bar{\kappa}\alpha^2 + \bar{\kappa}'(\bar{T}_{yy} + \bar{T}_{zz}) + \bar{\kappa}''(\bar{T}_y^2 + \bar{T}_z^2)] \\
&\quad - \frac{\gamma(\gamma-1)M^2\bar{\mu}'}{Re} \left[\frac{4}{3}(\bar{v}_y^2 + \bar{w}_z^2 - \bar{v}_y\bar{w}_z) + \bar{u}_y^2 + \bar{u}_z^2 + \bar{v}_z^2 + \bar{w}_y^2 + 2\bar{v}_z\bar{w}_y \right] \\
\mathcal{M}_{11} &= \bar{u} \\
\mathcal{M}_{12} &= \bar{\rho} \\
\mathcal{M}_{21} &= \frac{1}{\gamma M^2} \bar{T} \\
\mathcal{M}_{22} &= \bar{\rho}\bar{u} \\
\mathcal{M}_{25} &= \frac{\bar{\rho}}{\gamma M^2} \\
\mathcal{M}_{33} &= \bar{\rho}\bar{u} \\
\mathcal{M}_{44} &= \bar{\rho}\bar{u} \\
\mathcal{M}_{51} &= -(\gamma-1)\bar{T}\bar{u} \\
\mathcal{M}_{55} &= \bar{\rho}\bar{u} \\
\mathcal{F}_1 &= -\bar{\rho}_x\bar{u} - \bar{\rho}\bar{u}_x - \bar{\rho}_y\bar{v} - \bar{\rho}\bar{v}_y - \bar{\rho}_z\bar{w} - \bar{\rho}\bar{w}_z \\
\mathcal{F}_2 &= -\bar{\rho}\frac{\partial\bar{u}}{\partial t} - \bar{\rho}(\bar{u}\bar{u}_x + \bar{v}\bar{u}_y + \bar{w}\bar{u}_z) \\
&\quad - \bar{\rho}(\bar{u}\bar{u}_x + \bar{v}\bar{u}_y + \bar{w}\bar{u}_z + \bar{u}\bar{u}_x + \bar{v}\bar{u}_y + \bar{w}\bar{u}_z) - \frac{1}{\gamma M^2} (\bar{T}\bar{\rho}_x + \bar{\rho}\bar{T}_x) \\
&\quad + \frac{\bar{\mu}'}{Re} \left[\bar{T}(\bar{u}_{xx} + \bar{u}_{yy} + \bar{u}_{zz}) + \frac{\bar{T}}{3}(\bar{u}_{xx} + \bar{v}_{xy} + \bar{w}_{xz}) \right] \\
&\quad + \frac{2\bar{T}_x}{3}(2\bar{u}_x - \bar{v}_y - \bar{w}_z) + \bar{T}_y(\bar{u}_y + \bar{v}_x) + \bar{T}_z(\bar{u}_z + \bar{w}_x) \\
&\quad + \frac{\bar{\mu}''\bar{T}}{Re} \left[\frac{2\bar{T}_x}{3}(2\bar{u}_x - \bar{v}_y - \bar{w}_z) + \bar{T}_y(\bar{u}_y + \bar{v}_x) + \bar{T}_z(\bar{u}_z + \bar{w}_x) \right] \\
\mathcal{F}_3 &= -\bar{\rho}\frac{\partial\bar{v}}{\partial t} - \bar{\rho}(\bar{u}\bar{v}_x + \bar{v}\bar{v}_y + \bar{w}\bar{v}_z)
\end{aligned}$$

$$\begin{aligned}
& - \bar{\rho} (\bar{u}\bar{v}_x + \bar{v}\bar{v}_y + \bar{w}\bar{v}_z + \bar{u}\bar{v}_x + \bar{v}\bar{v}_y + \bar{w}\bar{v}_z) - \frac{1}{\gamma M^2} \left(\tilde{T}\tilde{\rho}_y + \tilde{\rho}\tilde{T}_y \right) \\
& + \frac{\bar{\mu}'}{Re} \left[\tilde{T} (\tilde{v}_{xx} + \tilde{v}_{yy} + \tilde{v}_{zz}) + \frac{\tilde{T}}{3} (\tilde{u}_{xy} + \tilde{v}_{yy} + \tilde{w}_{yz}) \right. \\
& + \left. \tilde{T}_x (\tilde{v}_x + \tilde{u}_y) + \frac{2\tilde{T}_y}{3} (2\tilde{v}_y - \tilde{u}_x - \tilde{w}_z) + \tilde{T}_z (\tilde{v}_z + \tilde{w}_y) \right] \\
& + \frac{\bar{\mu}''\tilde{T}}{Re} \left[\bar{T}_x (\bar{v}_x + \bar{u}_y) + \frac{2\bar{T}_y}{3} (2\bar{v}_y - \bar{u}_x - \bar{w}_z) + \bar{T}_z (\bar{v}_z + \bar{w}_y) \right] \\
\mathcal{F}_4 = & - \tilde{\rho} \frac{\partial \tilde{w}}{\partial t} - \bar{\rho} (\tilde{u}\tilde{w}_x + \tilde{v}\tilde{w}_y + \tilde{w}\tilde{w}_z) \\
& - \bar{\rho} (\bar{u}\bar{w}_x + \bar{v}\bar{w}_y + \bar{w}\bar{w}_z + \tilde{u}\bar{w}_x + \tilde{v}\bar{w}_y + \tilde{w}\bar{w}_z) - \frac{1}{\gamma M^2} \left(\tilde{T}\tilde{\rho}_z + \tilde{\rho}\tilde{T}_z \right) \\
& + \frac{\bar{\mu}'}{Re} \left[\tilde{T} (\tilde{w}_{xx} + \tilde{w}_{yy} + \tilde{w}_{zz}) + \frac{\tilde{T}}{3} (\tilde{u}_{xz} + \tilde{v}_{yz} + \tilde{w}_{zz}) \right. \\
& + \left. \tilde{T}_x (\tilde{w}_x + \tilde{u}_z) + \tilde{T}_y (\tilde{v}_z + \tilde{w}_y) + \frac{2\tilde{T}_z}{3} (2\tilde{w}_z - \tilde{u}_x - \tilde{v}_y) \right] \\
& + \frac{\bar{\mu}''\tilde{T}}{Re} \left[\bar{T}_x (\bar{w}_x + \bar{u}_z) + \bar{T}_y (\bar{v}_z + \bar{w}_y) + \frac{2\bar{T}_z}{3} (2\bar{w}_z - \bar{u}_x - \bar{v}_y) \right] \\
\mathcal{F}_5 = & - \tilde{\rho} \frac{\partial \tilde{T}}{\partial t} - \bar{\rho} (\tilde{u}\tilde{T}_x + \tilde{v}\tilde{T}_y + \tilde{w}\tilde{T}_z) \\
& - \bar{\rho} (\bar{u}\bar{T}_x + \bar{v}\bar{T}_y + \bar{w}\bar{T}_z + \tilde{u}\bar{T}_x + \tilde{v}\bar{T}_y + \tilde{w}\bar{T}_z) \\
& + (\gamma - 1)\tilde{T} \frac{\partial \tilde{\rho}}{\partial t} + (\gamma - 1)\bar{T} (\tilde{u}\tilde{\rho}_x + \tilde{v}\tilde{\rho}_y + \tilde{w}\tilde{\rho}_z) \\
& + (\gamma - 1)\tilde{T} (\bar{u}\bar{\rho}_x + \bar{v}\bar{\rho}_y + \bar{w}\bar{\rho}_z + \tilde{u}\bar{\rho}_x + \tilde{v}\bar{\rho}_y + \tilde{w}\bar{\rho}_z) \\
& + \frac{\gamma}{Re Pr} \left[\bar{\kappa}'\tilde{T} (\tilde{T}_{xx} + \tilde{T}_{yy} + \tilde{T}_{zz}) + \bar{\kappa}' (\tilde{T}_x^2 + \tilde{T}_y^2 + \tilde{T}_z^2) \right. \\
& + \left. \bar{\kappa}''\tilde{T} (\bar{T}_x\bar{T}_x + \bar{T}_y\bar{T}_y + \bar{T}_z\bar{T}_z) \right] \\
& + \frac{\gamma(\gamma - 1)M^2\bar{\mu}'\tilde{T}}{Re} \left[\frac{2}{3} (2\bar{u}_x - \bar{v}_y - \bar{w}_z) \tilde{u}_x + (\bar{u}_y + \bar{v}_x) \tilde{u}_y \right. \\
& + (\bar{u}_z + \bar{w}_x) \tilde{u}_z + (\bar{u}_y + \bar{v}_x) \tilde{v}_x + \frac{2}{3} (2\bar{v}_y - \bar{u}_x - \bar{w}_z) \tilde{v}_y + (\bar{w}_y + \bar{v}_z) \tilde{v}_z \\
& + (\bar{w}_x + \bar{u}_z) \tilde{w}_x + (\bar{w}_y + \bar{v}_z) \tilde{w}_y + \frac{2}{3} (2\bar{w}_z - \bar{u}_x - \bar{v}_y) \tilde{w}_z \\
& + \left. \frac{2}{3} (2\tilde{u}_x - \tilde{v}_y - \tilde{w}_z) \bar{u}_x + (\tilde{u}_y + \tilde{v}_x) \bar{u}_y + (\tilde{u}_z + \tilde{w}_x) \bar{u}_z \right]
\end{aligned}$$

$$\begin{aligned}
& + (\tilde{u}_y + \tilde{v}_x) \bar{v}_x + \frac{2}{3} (2\tilde{v}_y - \tilde{u}_x - \tilde{w}_z) \bar{v}_y + (\tilde{w}_y + \tilde{v}_z) \bar{v}_z \\
& + (\tilde{w}_x + \tilde{u}_z) \bar{w}_x + (\tilde{w}_y + \tilde{v}_z) \bar{w}_y + \frac{2}{3} (2\tilde{w}_z - \tilde{u}_x - \tilde{v}_y) \bar{w}_z \Big] \\
& + \frac{\gamma(\gamma-1)M^2\bar{\mu}}{Re} \Big[\frac{4}{3} (\tilde{u}_x^2 + \tilde{v}_y^2 + \tilde{w}_z^2 - \tilde{u}_x\tilde{v}_y - \tilde{u}_x\tilde{w}_z - \tilde{v}_y\tilde{w}_z) \\
& + \tilde{u}_y^2 + \tilde{v}_x^2 + \tilde{u}_z^2 + \tilde{v}_z^2 + \tilde{w}_x^2 + \tilde{w}_y^2 + 2\tilde{u}_y\tilde{v}_x + 2\tilde{u}_z\tilde{w}_y + 2\tilde{v}_z\tilde{w}_y \Big]
\end{aligned}$$

Appendix E

TriGlobal EVP operators

The operators of the three-dimensional partial derivative EVP (1.26) for TriGlobal analysis upon compressible flows are structured as follows

$$\omega \begin{pmatrix} \mathcal{A}_{11} & \mathcal{A}_{12} & \mathcal{A}_{13} & \mathcal{A}_{14} & 0 \\ \mathcal{A}_{21} & \mathcal{A}_{22} & \mathcal{A}_{23} & \mathcal{A}_{24} & \mathcal{A}_{25} \\ \mathcal{A}_{31} & \mathcal{A}_{32} & \mathcal{A}_{33} & \mathcal{A}_{34} & \mathcal{A}_{35} \\ \mathcal{A}_{41} & \mathcal{A}_{42} & \mathcal{A}_{43} & \mathcal{A}_{44} & \mathcal{A}_{45} \\ \mathcal{A}_{51} & \mathcal{A}_{52} & \mathcal{A}_{53} & \mathcal{A}_{54} & \mathcal{A}_{55} \end{pmatrix} \begin{pmatrix} \hat{\rho} \\ \hat{u} \\ \hat{v} \\ \hat{w} \\ \hat{T} \end{pmatrix} = \begin{pmatrix} \mathcal{B}_{11} & 0 & 0 & 0 & 0 \\ 0 & \mathcal{B}_{22} & 0 & 0 & 0 \\ 0 & 0 & \mathcal{B}_{33} & 0 & 0 \\ 0 & 0 & 0 & \mathcal{B}_{44} & 0 \\ \mathcal{B}_{51} & 0 & 0 & 0 & \mathcal{B}_{55} \end{pmatrix} \begin{pmatrix} \hat{\rho} \\ \hat{u} \\ \hat{v} \\ \hat{w} \\ \hat{T} \end{pmatrix} \quad (\text{E.1})$$

The full listing of the operators in equation (E.1) follows

$$\begin{aligned} \mathcal{A}_{11} &= \bar{u}\mathcal{D}_x + \bar{v}\mathcal{D}_y + \bar{w}\mathcal{D}_z + \bar{u}_x + \bar{v}_y + \bar{w}_z \\ \mathcal{A}_{12} &= \bar{\rho}\mathcal{D}_x + \bar{\rho}_x \\ \mathcal{A}_{13} &= \bar{\rho}\mathcal{D}_y + \bar{\rho}_y \\ \mathcal{A}_{14} &= \bar{\rho}\mathcal{D}_z + \bar{\rho}_z \\ \mathcal{A}_{21} &= \frac{\bar{T}}{\gamma M^2}\mathcal{D}_x + \bar{u}\bar{u}_x + \bar{v}\bar{u}_y + \bar{w}\bar{u}_z + \frac{1}{\gamma M^2}(\bar{T}_x) \\ \mathcal{A}_{22} &= -\frac{\bar{\mu}}{Re}\left(\frac{4}{3}\mathcal{D}_{xx}^2 + \mathcal{D}_{yy}^2 + \mathcal{D}_{zz}^2\right) + \left(\bar{\rho}\bar{u} - \frac{4\bar{\mu}_x}{3Re}\right)\mathcal{D}_x \\ &\quad + \left(\bar{\rho}\bar{v} - \frac{\bar{\mu}_y}{Re}\right)\mathcal{D}_y + \left(\bar{\rho}\bar{w} - \frac{\bar{\mu}_z}{Re}\right)\mathcal{D}_z + \bar{\rho}\bar{u}_x \\ \mathcal{A}_{23} &= -\frac{\bar{\mu}}{3Re}\mathcal{D}_{xy}^2 - \frac{\bar{\mu}_y}{Re}\mathcal{D}_x - \frac{2\bar{\mu}_x}{3Re}\mathcal{D}_y + \bar{\rho}\bar{u}_y \\ \mathcal{A}_{24} &= -\frac{\bar{\mu}}{3Re}\mathcal{D}_{xz}^2 - \frac{\bar{\mu}_z}{Re}\mathcal{D}_x - \frac{2\bar{\mu}_x}{3Re}\mathcal{D}_z + \bar{\rho}\bar{u}_z \\ \mathcal{A}_{25} &= \left[\frac{\bar{\rho}}{\gamma M^2} - \frac{2\bar{\mu}'}{3Re}(2\bar{u}_x - \bar{v}_y - \bar{w}_x)\right]\mathcal{D}_x + \frac{1}{\gamma M^2}\bar{\rho}_x \end{aligned}$$

$$\begin{aligned}
& - \frac{\bar{\mu}'}{Re} [(\bar{u}_y + \bar{v}_x)\mathcal{D}_y + (\bar{u}_z + \bar{w}_x)\mathcal{D}_z] \\
& - \frac{\bar{\mu}'}{Re} \left[\frac{4}{3}\bar{u}_{xx} + \bar{u}_{yy} + \bar{u}_{zz} + \frac{1}{3}(\bar{v}_{xy} + \bar{w}_{xz}) \right] \\
& - \frac{\bar{\mu}''}{Re} \left[\frac{2}{3}(2\bar{u}_x - \bar{v}_y - \bar{w}_x)\bar{T}_x + (\bar{u}_y + \bar{v}_x)\bar{T}_y + (\bar{u}_z + \bar{w}_x)\bar{T}_z \right] \\
\mathcal{A}_{31} &= \frac{\bar{T}}{\gamma M^2} \mathcal{D}_y + \bar{u}\bar{v}_x + \bar{v}\bar{v}_y + \bar{w}\bar{v}_z + \frac{1}{\gamma M^2}(\bar{T}_y) \\
\mathcal{A}_{33} &= -\frac{\bar{\mu}}{Re} \left(\frac{4}{3}\mathcal{D}_{yy}^2 + \mathcal{D}_{zz}^2 + \mathcal{D}_{zz}^2 \right) + \left(\bar{\rho}\bar{v} - \frac{4\bar{\mu}_y}{3Re} \right) \mathcal{D}_y \\
& + \left(\bar{\rho}\bar{u} - \frac{\bar{\mu}_x}{Re} \right) \mathcal{D}_x + \left(\bar{\rho}\bar{w} - \frac{\bar{\mu}_z}{Re} \right) \mathcal{D}_z + \bar{\rho}\bar{v}_y \\
\mathcal{A}_{32} &= -\frac{\bar{\mu}}{3Re} \mathcal{D}_{xy}^2 - \frac{\bar{\mu}_x}{Re} \mathcal{D}_y - \frac{2\bar{\mu}_y}{3Re} \mathcal{D}_x + \bar{\rho}\bar{v}_x \\
\mathcal{A}_{34} &= -\frac{\bar{\mu}}{3Re} \mathcal{D}_{xz}^2 - \frac{\bar{\mu}_z}{Re} \mathcal{D}_x - \frac{2\bar{\mu}_x}{3Re} \mathcal{D}_z + \bar{\rho}\bar{v}_z \\
\mathcal{A}_{35} &= \left[\frac{\bar{\rho}}{\gamma M^2} - \frac{2\bar{\mu}'}{3Re}(2\bar{v}_y - \bar{u}_x - \bar{w}_x) \right] \mathcal{D}_y + \frac{1}{\gamma M^2} \bar{\rho}_y \\
& - \frac{\bar{\mu}'}{Re} [(\bar{v}_x + \bar{u}_y)\mathcal{D}_x + (\bar{v}_z + \bar{w}_y)\mathcal{D}_z] \\
& - \frac{\bar{\mu}'}{Re} \left[\frac{4}{3}\bar{v}_{yy} + \bar{v}_{xx} + \bar{v}_{zz} + \frac{1}{3}(\bar{u}_{xy} + \bar{w}_{yz}) \right] \\
& - \frac{\bar{\mu}''}{Re} \left[\frac{2}{3}(2\bar{v}_y - \bar{u}_x - \bar{w}_y)\bar{T}_y + (\bar{u}_y + \bar{v}_x)\bar{T}_x + (\bar{v}_z + \bar{w}_y)\bar{T}_z \right] \\
\mathcal{A}_{41} &= \frac{\bar{T}}{\gamma M^2} \mathcal{D}_z + \bar{u}\bar{w}_x + \bar{v}\bar{w}_y + \bar{w}\bar{w}_z + \frac{1}{\gamma M^2}(\bar{T}_z) \\
\mathcal{A}_{44} &= -\frac{\bar{\mu}}{Re} \left(\frac{4}{3}\mathcal{D}_{zz}^2 + \mathcal{D}_{yy}^2 + \mathcal{D}_{xx}^2 \right) + \left(\bar{\rho}\bar{w} - \frac{4\bar{\mu}_z}{3Re} \right) \mathcal{D}_z \\
& + \left(\bar{\rho}\bar{v} - \frac{\bar{\mu}_y}{Re} \right) \mathcal{D}_y + \left(\bar{\rho}\bar{u} - \frac{\bar{\mu}_x}{Re} \right) \mathcal{D}_x + \bar{\rho}\bar{w}_z \\
\mathcal{A}_{43} &= -\frac{\bar{\mu}}{3Re} \mathcal{D}_{yz}^2 - \frac{\bar{\mu}_y}{Re} \mathcal{D}_z - \frac{2\bar{\mu}_z}{3Re} \mathcal{D}_y + \bar{\rho}\bar{w}_y \\
\mathcal{A}_{42} &= -\frac{\bar{\mu}}{3Re} \mathcal{D}_{xz}^2 - \frac{\bar{\mu}_x}{Re} \mathcal{D}_z - \frac{2\bar{\mu}_z}{3Re} \mathcal{D}_x + \bar{\rho}\bar{w}_x \\
\mathcal{A}_{45} &= \left[\frac{\bar{\rho}}{\gamma M^2} - \frac{2\bar{\mu}'}{3Re}(2\bar{w}_z - \bar{v}_y - \bar{u}_x) \right] \mathcal{D}_z + \frac{1}{\gamma M^2} \bar{\rho}_z \\
& - \frac{\bar{\mu}'}{Re} [(\bar{w}_y + \bar{v}_z)\mathcal{D}_y + (\bar{w}_x + \bar{u}_z)\mathcal{D}_x]
\end{aligned}$$

$$\begin{aligned}
& - \frac{\bar{\mu}'}{Re} \left[\frac{4}{3} \bar{w}_{zz} + \bar{w}_{yy} + \bar{w}_{xx} + \frac{1}{3} (\bar{v}_{zy} + \bar{u}_{xz}) \right] \\
& - \frac{\bar{\mu}''}{Re} \left[\frac{2}{3} (2\bar{w}_z - \bar{v}_y - \bar{u}_z) \bar{T}_z + (\bar{u}_y + \bar{v}_z) \bar{T}_y + (\bar{w}_x + \bar{u}_z) \bar{T}_x \right] \\
\mathcal{A}_{51} &= -(\gamma - 1) \bar{T} (\bar{u} \mathcal{D}_x + \bar{v} \mathcal{D}_y + \bar{w} \mathcal{D}_z) + \gamma (\bar{T}_x \bar{u} + \bar{T}_y \bar{v} + \bar{T}_z \bar{w}) \\
\mathcal{A}_{52} &= -\frac{2\gamma(\gamma - 1) M^2 \bar{\mu}}{Re} \left[\frac{2}{3} (2\bar{u}_x - \bar{v}_y - \bar{w}_z) \mathcal{D}_x + (\bar{u}_y + \bar{v}_x) \mathcal{D}_y \right. \\
& \quad \left. + (\bar{u}_z + \bar{w}_x) \mathcal{D}_z \right] - (\gamma - 1) (\bar{T}_x \bar{\rho} + \bar{T} \bar{\rho}_x) + \gamma \bar{\rho} \bar{T}_x \\
\mathcal{A}_{53} &= -\frac{2\gamma(\gamma - 1) M^2 \bar{\mu}}{Re} \left[\frac{2}{3} (2\bar{v}_y - \bar{u}_x - \bar{w}_z) \mathcal{D}_y + (\bar{v}_x + \bar{u}_y) \mathcal{D}_x \right. \\
& \quad \left. + (\bar{v}_z + \bar{w}_y) \mathcal{D}_z \right] - (\gamma - 1) (\bar{T}_y \bar{\rho} + \bar{T} \bar{\rho}_y) + \gamma \bar{\rho} \bar{T}_y \\
\mathcal{A}_{54} &= -\frac{2\gamma(\gamma - 1) M^2 \bar{\mu}}{Re} \left[\frac{2}{3} (2\bar{w}_z - \bar{v}_y - \bar{u}_x) \mathcal{D}_z + (\bar{w}_y + \bar{v}_z) \mathcal{D}_y \right. \\
& \quad \left. + (\bar{w}_x + \bar{u}_z) \mathcal{D}_x \right] - (\gamma - 1) (\bar{T}_z \bar{\rho} + \bar{T} \bar{\rho}_z) + \gamma \bar{\rho} \bar{T}_z \\
\mathcal{A}_{55} &= -\frac{\gamma}{Re Pr} \bar{\kappa} (\mathcal{D}_{xx}^2 + \mathcal{D}_{yy}^2 + \mathcal{D}_{zz}^2) + \left(\bar{\rho} \bar{u} - \frac{\gamma}{Re Pr} 2\bar{\kappa}' \bar{T}_x \right) \mathcal{D}_x \\
& \quad + \left(\bar{\rho} \bar{v} - \frac{\gamma}{Re Pr} 2\bar{\kappa}' \bar{T}_y \right) \mathcal{D}_y + \left(\bar{\rho} \bar{w} - \frac{\gamma}{Re Pr} 2\bar{\kappa}' \bar{T}_z \right) \mathcal{D}_z \\
& \quad - (\gamma - 1) (\bar{\rho}_y \bar{v} + \bar{\rho}_z \bar{w}) - \frac{\gamma}{Re Pr} [\bar{\kappa}' (\bar{T}_{yy} + \bar{T}_{zz}) + \bar{\kappa}'' (\bar{T}_x^2 + \bar{T}_y^2 + \bar{T}_z^2)] \\
& \quad - \frac{\gamma(\gamma - 1) M^2 \bar{\mu}'}{Re} \left[\frac{4}{3} (\bar{u}_x^2 + \bar{v}_y^2 + \bar{w}_z^2 - \bar{u}_x \bar{v}_y - \bar{u}_x \bar{w}_z - \bar{v}_y \bar{w}_z) \right. \\
& \quad \left. + \bar{u}_y^2 + \bar{v}_x^2 + \bar{u}_z^2 + \bar{v}_z^2 + \bar{w}_x^2 + \bar{w}_y^2 + 2\bar{u}_y \bar{v}_x + 2\bar{u}_z \bar{w}_y + 2\bar{v}_z \bar{w}_y \right] \\
\mathcal{B}_{11} &= 1 \\
\mathcal{B}_{22} &= \bar{\rho} \\
\mathcal{B}_{33} &= \bar{\rho} \\
\mathcal{B}_{44} &= \bar{\rho} \\
\mathcal{B}_{51} &= -(\gamma - 1) \bar{T} \\
\mathcal{B}_{55} &= \bar{\rho}
\end{aligned}$$

Appendix F

Compressible PNS operators

Equation (4.3) for compressible flows expressed in matrix form results

$$\begin{pmatrix} \mathcal{J}_{11} & \mathcal{J}_{12} & \mathcal{J}_{13} & \mathcal{J}_{14} & 0 \\ \mathcal{J}_{21} & \mathcal{J}_{22} & \mathcal{J}_{23} & \mathcal{J}_{24} & \mathcal{J}_{25} \\ \mathcal{J}_{31} & \mathcal{J}_{32} & \mathcal{J}_{33} & \mathcal{J}_{34} & \mathcal{J}_{35} \\ \mathcal{J}_{41} & \mathcal{J}_{42} & \mathcal{J}_{43} & \mathcal{J}_{44} & \mathcal{J}_{45} \\ \mathcal{J}_{51} & \mathcal{J}_{52} & \mathcal{J}_{53} & \mathcal{J}_{54} & \mathcal{J}_{55} \end{pmatrix} \begin{pmatrix} \Delta\rho \\ \Delta u \\ \Delta v \\ \Delta\bar{w} \\ \Delta T \end{pmatrix} = - \begin{pmatrix} \mathcal{F}_1 \\ \mathcal{F}_2 \\ \mathcal{F}_3 \\ \mathcal{F}_4 \\ \mathcal{F}_5 \end{pmatrix} \quad (\text{F.1})$$

The full listing of the operators in equation (F.1) without dropping streamwise derivative terms in the viscous part follows

$$\begin{aligned} \mathcal{J}_{11} &= \bar{u}\mathcal{D}_x + \bar{v}\mathcal{D}_y + \bar{w}\mathcal{D}_z + \bar{u}_x + \bar{v}_y + \bar{w}_z \\ \mathcal{J}_{12} &= \bar{\rho}\mathcal{D}_x + \bar{\rho}_x \\ \mathcal{J}_{13} &= \bar{\rho}\mathcal{D}_y + \bar{\rho}_y \\ \mathcal{J}_{14} &= \bar{\rho}\mathcal{D}_z + \bar{\rho}_z \\ \mathcal{J}_{21} &= \bar{u}\bar{u}_x + \bar{v}\bar{u}_y + \bar{w}\bar{u}_z + \frac{\Omega}{\gamma M^2}(\bar{T}\mathcal{D}_x + \bar{T}_x) \\ \mathcal{J}_{22} &= -\frac{\bar{\mu}}{Re} \left(\frac{4}{3}\mathcal{D}_{xx}^2 + \mathcal{D}_{yy}^2 + \mathcal{D}_{zz}^2 \right) + \left(\bar{\rho}\bar{u} - \frac{4\bar{\mu}_x}{3Re} \right) \mathcal{D}_x \\ &\quad + \left(\bar{\rho}\bar{v} - \frac{\bar{\mu}_y}{Re} \right) \mathcal{D}_y + \left(\bar{\rho}\bar{w} - \frac{\bar{\mu}_z}{Re} \right) \mathcal{D}_z + \bar{\rho}\bar{u}_x \\ \mathcal{J}_{23} &= -\frac{\bar{\mu}}{3Re} \mathcal{D}_{xy}^2 - \frac{\bar{\mu}_y}{Re} \mathcal{D}_x - \frac{2\bar{\mu}_x}{3Re} \mathcal{D}_y + \bar{\rho}\bar{u}_y \\ \mathcal{J}_{24} &= -\frac{\bar{\mu}}{3Re} \mathcal{D}_{xz}^2 - \frac{\bar{\mu}_z}{Re} \mathcal{D}_x - \frac{2\bar{\mu}_x}{3Re} \mathcal{D}_z + \bar{\rho}\bar{u}_z \\ \mathcal{J}_{25} &= \left[\frac{\bar{\rho}}{\gamma M^2} - \frac{2\bar{\mu}'}{3Re} (2\bar{u}_x - \bar{v}_y - \bar{w}_x) \right] \mathcal{D}_x \\ &\quad - \frac{\bar{\mu}'}{Re} [(\bar{v}_x + \bar{u}_y)\mathcal{D}_y + (\bar{w}_x + \bar{u}_z)\mathcal{D}_z] \\ &\quad + \frac{\Omega}{\gamma M^2} \bar{\rho}_x - \frac{\bar{\mu}'}{Re} \left[\frac{4}{3}\bar{u}_{xx} + \bar{u}_{yy} + \bar{u}_{zz} + \frac{1}{3}(\bar{v}_{xy} + \bar{w}_{xz}) \right] \end{aligned}$$

$$\begin{aligned}
& - \frac{\bar{\mu}''}{Re} \left[\frac{2}{3} (2\bar{u}_x - \bar{v}_y - \bar{w}_x) \bar{T}_x + (\bar{u}_y + \bar{v}_x) \bar{T}_y + (\bar{u}_z + \bar{w}_x) \bar{T}_z \right] \\
\mathcal{J}_{31} &= \frac{\bar{T}}{\gamma M^2} \mathcal{D}_y + \bar{u} \bar{v}_x + \bar{v} \bar{v}_y + \bar{w} \bar{v}_z + \frac{1}{\gamma M^2} \bar{T}_y \\
\mathcal{J}_{32} &= -\frac{\bar{\mu}}{3 Re} \mathcal{D}_{xy}^2 - \frac{\bar{\mu}_x}{Re} \mathcal{D}_y + \frac{2\bar{\mu}_y}{3 Re} \mathcal{D}_x + \bar{\rho} \bar{v}_x \\
\mathcal{J}_{33} &= -\frac{\bar{\mu}}{Re} \left(\frac{4}{3} \mathcal{D}_{yy}^2 + \mathcal{D}_{xx}^2 + \mathcal{D}_{zz}^2 \right) + \left(\bar{\rho} \bar{v} - \frac{4\bar{\mu}_y}{3 Re} \right) \mathcal{D}_y \\
&+ \left(\bar{\rho} \bar{u} - \frac{\bar{\mu}_x}{Re} \right) \mathcal{D}_x + \left(\bar{\rho} \bar{w} - \frac{\bar{\mu}_z}{Re} \right) \mathcal{D}_z + \bar{\rho} \bar{v}_y \\
\mathcal{J}_{34} &= -\frac{\bar{\mu}}{3 Re} \mathcal{D}_{yz}^2 - \frac{\bar{\mu}_z}{Re} \mathcal{D}_y + \frac{2\bar{\mu}_y}{3 Re} \mathcal{D}_z + \bar{\rho} \bar{v}_z \\
\mathcal{J}_{35} &= \left[\frac{\bar{\rho}}{\gamma M^2} - \frac{\bar{\mu}'}{Re} \frac{2}{3} (2\bar{v}_y - \bar{u}_x - \bar{w}_z) \right] \mathcal{D}_y \\
&- \frac{\bar{\mu}'}{Re} [(\bar{v}_x + \bar{u}_y) \mathcal{D}_x + (\bar{v}_z + \bar{w}_y) \mathcal{D}_z] \\
&+ \frac{\bar{\rho}_y}{\gamma M^2} - \frac{\bar{\mu}'}{Re} \left[\frac{4}{3} \bar{v}_{yy} + \bar{v}_{xx} + \bar{v}_{zz} + \frac{1}{3} (\bar{u}_{xy} + \bar{w}_{yz}) \right] \\
&- \frac{\bar{\mu}''}{Re} \left[\frac{2}{3} (2\bar{v}_y - \bar{u}_x - \bar{w}_z) \bar{T}_y + (\bar{u}_y + \bar{v}_x) \bar{T}_x + (\bar{v}_z + \bar{w}_y) \bar{T}_z \right] \\
\mathcal{J}_{41} &= \frac{\bar{T}}{\gamma M^2} \mathcal{D}_z + \bar{u} \bar{w}_x + \bar{v} \bar{w}_y + \bar{w} \bar{w}_z + \frac{1}{\gamma M^2} \bar{T}_z \\
\mathcal{J}_{42} &= -\frac{\bar{\mu}}{3 Re} \mathcal{D}_{xz}^2 - \frac{\bar{\mu}_x}{Re} \mathcal{D}_z + \frac{2\bar{\mu}_z}{3 Re} \mathcal{D}_x + \bar{\rho} \bar{w}_x \\
\mathcal{J}_{43} &= -\frac{\bar{\mu}}{3 Re} \mathcal{D}_{yz}^2 + \frac{2\bar{\mu}_z}{3 Re} \mathcal{D}_y - \frac{\bar{\mu}_y}{Re} \mathcal{D}_z + \bar{\rho} \bar{w}_y \\
\mathcal{J}_{44} &= -\frac{\bar{\mu}}{Re} \left(\frac{4}{3} \mathcal{D}_{zz}^2 + \mathcal{D}_{yy}^2 + \mathcal{D}_{xx}^2 \right) + \left(\bar{\rho} \bar{w} - \frac{4\bar{\mu}_z}{3 Re} \right) \mathcal{D}_z \\
&+ \left(\bar{\rho} \bar{v} - \frac{\bar{\mu}_y}{Re} \right) \mathcal{D}_y + \left(\bar{\rho} \bar{u} - \frac{\bar{\mu}_x}{Re} \right) \mathcal{D}_x + \bar{\rho} \bar{w}_z \\
\mathcal{J}_{45} &= \left[\frac{\bar{\rho}}{\gamma M^2} - \frac{2\bar{\mu}'}{3 Re} (2\bar{w}_z - \bar{v}_y - \bar{u}_x) \right] \mathcal{D}_z \\
&- \frac{\bar{\mu}'}{Re} [(\bar{w}_y + \bar{v}_z) \mathcal{D}_y + (\bar{w}_x + \bar{u}_z) \mathcal{D}_x] \\
&+ \frac{1}{\gamma M^2} \bar{\rho}_z - \frac{\bar{\mu}'}{Re} \left[\frac{4}{3} \bar{w}_{zz} + \bar{w}_{yy} + \bar{w}_{xx} + \frac{1}{3} (\bar{v}_{zy} + \bar{u}_{xz}) \right] \\
&- \frac{\bar{\mu}''}{Re} \left[\frac{2}{3} (2\bar{w}_z - \bar{v}_y - \bar{u}_x) \bar{T}_z + (\bar{u}_y + \bar{v}_z) \bar{T}_y + (\bar{w}_x + \bar{u}_z) \bar{T}_x \right]
\end{aligned}$$

$$\begin{aligned}
\mathcal{J}_{51} &= \bar{u}\bar{T}_x + \bar{v}\bar{T}_y + \bar{w}\bar{T}_z + (\gamma - 1)\bar{T}(\bar{u}_x + \bar{v}_y + \bar{w}_z) \\
\mathcal{J}_{52} &= -\frac{2\gamma(\gamma - 1)M^2}{Re}\bar{\mu}\left[\frac{2}{3}(2\bar{u}_x - \bar{v}_y - \bar{w}_z)\mathcal{D}_x + (\bar{u}_y + \bar{v}_x)\mathcal{D}_y \right. \\
&\quad \left. + (\bar{u}_z + \bar{w}_x)\mathcal{D}_z\right] + (\gamma - 1)\bar{T}\bar{\rho}\mathcal{D}_x + \bar{\rho}\bar{T}_x \\
\mathcal{J}_{53} &= -\frac{2\gamma(\gamma - 1)M^2\bar{\mu}}{Re}\left[\frac{2}{3}(2\bar{v}_y - \bar{u}_x - \bar{w}_z)\mathcal{D}_y + (\bar{v}_x + \bar{u}_y)\mathcal{D}_x \right. \\
&\quad \left. + (\bar{v}_z + \bar{w}_y)\mathcal{D}_z\right] + (\gamma - 1)\bar{T}\bar{\rho}\mathcal{D}_y + \bar{\rho}\bar{T}_y \\
\mathcal{J}_{54} &= -\frac{2\gamma(\gamma - 1)M^2\bar{\mu}}{Re}\left[\frac{2}{3}(2\bar{w}_z - \bar{v}_y - \bar{u}_x)\mathcal{D}_z + (\bar{w}_y + \bar{v}_z)\mathcal{D}_y \right. \\
&\quad \left. + (\bar{w}_x + \bar{u}_z)\mathcal{D}_x\right] + (\gamma - 1)\bar{T}\bar{\rho}\mathcal{D}_z + \bar{\rho}\bar{T}_z \\
\mathcal{J}_{55} &= -\frac{\gamma}{Re Pr}\bar{\kappa}(\mathcal{D}_{xx}^2 + \mathcal{D}_{yy}^2 + \mathcal{D}_{zz}^2) + \left(\bar{\rho}\bar{u} - \frac{\gamma}{Re Pr}2\bar{\kappa}'\bar{T}_x\right)\mathcal{D}_x \\
&\quad + \left(\bar{\rho}\bar{v} - \frac{\gamma}{Re Pr}2\bar{\kappa}'\bar{T}_y\right)\mathcal{D}_y + \left(\bar{\rho}\bar{w} - \frac{\gamma}{Re Pr}2\bar{\kappa}'\bar{T}_z\right)\mathcal{D}_z \\
&\quad + (\gamma - 1)\bar{\rho}(\bar{u}_x + \bar{v}_y + \bar{w}_z) \\
&\quad - \frac{\gamma}{Re Pr}\left[\bar{\kappa}'(\bar{T}_{xx} + \bar{T}_{yy} + \bar{T}_{zz}) + \bar{\kappa}''(\bar{T}_x^2 + \bar{T}_y^2 + \bar{T}_z^2)\right] \\
&\quad - \frac{\gamma(\gamma - 1)M^2\bar{\mu}'}{Re}\left[\frac{4}{3}(\bar{u}_x^2 + \bar{v}_y^2 + \bar{w}_z^2 - \bar{u}_x\bar{v}_y - \bar{u}_x\bar{w}_z - \bar{v}_y\bar{w}_z) \right. \\
&\quad \left. + \bar{u}_y^2 + \bar{v}_x^2 + \bar{u}_z^2 + \bar{v}_z^2 + \bar{w}_x^2 + \bar{w}_y^2 + 2\bar{u}_y\bar{v}_x + 2\bar{u}_z\bar{w}_x + 2\bar{v}_z\bar{w}_y\right] \\
\mathcal{F}_1 &= \bar{\rho}_x\bar{u} + \bar{\rho}\bar{u}_x + \bar{\rho}_y\bar{v} + \bar{\rho}\bar{v}_y + \bar{\rho}_z\bar{w} + \bar{\rho}\bar{w}_z \\
\mathcal{F}_2 &= \bar{\rho}(\bar{u}\bar{u}_x + \bar{v}\bar{u}_y + \bar{w}\bar{u}_z) + \frac{\Omega}{\gamma M^2}(\bar{\rho}_x\bar{T} + \bar{\rho}\bar{T}_x) \\
&\quad - \frac{1}{Re}\left[\bar{\mu}\left(\frac{4}{3}\bar{u}_{xx} + \bar{u}_{yy} + \bar{u}_{zz} + \frac{1}{3}(\bar{v}_{xy} + \bar{w}_{xz})\right) \right. \\
&\quad \left. + \frac{2}{3}\bar{\mu}_x(2\bar{u}_x - \bar{v}_y - \bar{w}_z) + \bar{\mu}_y(\bar{u}_y + \bar{v}_x) + \bar{\mu}_z(\bar{u}_z + \bar{w}_x)\right] \\
\mathcal{F}_3 &= \bar{\rho}(\bar{u}\bar{v}_x + \bar{v}\bar{v}_y + \bar{w}\bar{v}_z) + \frac{1}{\gamma M^2}(\bar{\rho}_y\bar{T} + \bar{\rho}\bar{T}_y) \\
&\quad - \frac{1}{Re}\left[\bar{\mu}\left(\frac{4}{3}\bar{v}_{yy} + \bar{v}_{xx} + \bar{v}_{zz} + \frac{1}{3}(\bar{u}_{xy} + \bar{w}_{yz})\right) \right.
\end{aligned}$$

$$\begin{aligned}
 & + \bar{\mu}_x(\bar{v}_x + \bar{u}_y) + \frac{2}{3}\bar{\mu}_y(2\bar{v}_y - u_x - \bar{w}_z) + \bar{\mu}_z(\bar{v}_z + \bar{w}_y) \Big] \\
 \mathcal{F}_4 & = \bar{\rho}(\bar{u}\bar{w}_x + \bar{v}\bar{w}_y + \bar{w}\bar{w}_z) + \frac{1}{\gamma M^2}(\bar{\rho}_z\bar{T} + \bar{\rho}\bar{T}_z) \\
 & - \frac{1}{Re} \left[\bar{\mu} \left(\frac{4}{3}\bar{w}_{zz} + \bar{w}_{xx} + \bar{w}_{yy} + \frac{1}{3}(u_{xz} + \bar{v}_{yz}) \right) \right. \\
 & \left. + \bar{\mu}_x(\bar{w}_x + \bar{u}_z) + \bar{\mu}_y(\bar{v}_z + \bar{w}_y) + \frac{2}{3}\bar{\mu}_z(2\bar{w}_z - \bar{u}_x - \bar{v}_y) \right] \\
 \mathcal{F}_5 & = \bar{\rho}(\bar{u}\bar{T}_x + \bar{v}\bar{T}_y + \bar{w}\bar{T}_z) + (\gamma - 1)\bar{\rho}\bar{T}(\bar{u}_x + \bar{v}_y + \bar{w}_z) \\
 & - \frac{\gamma}{Re Pr} [\bar{\kappa}(\bar{T}_{xx} + \bar{T}_{yy} + \bar{T}_{zz}) + \bar{\kappa}_x\bar{T}_x + \bar{\kappa}_y\bar{T}_y + \bar{\kappa}_z\bar{T}_z] \\
 & - \frac{\gamma(\gamma - 1)M^2}{Re} \bar{\mu} \left[\frac{4}{3}(\bar{u}_x^2 + \bar{v}_y^2 + \bar{w}_z^2 - \bar{u}_x\bar{v}_y - \bar{u}_x\bar{w}_z - \bar{v}_y\bar{w}_z) \right. \\
 & \left. + \bar{u}_y^2 + \bar{u}_z^2 + \bar{v}_x^2 + \bar{v}_z^2 + \bar{w}_x^2 + \bar{w}_y^2 + 2\bar{u}_y\bar{v}_x + 2\bar{u}_z\bar{w}_x + 2\bar{v}_z\bar{w}_y \right]
 \end{aligned}$$

Bibliography

- [1] N. Abdessemed, S.J. Sherwin, and V. Theofilis. Linear instability analysis of low pressure turbine flows. *J. Fluid Mech.*, 628:57–83, 2009.
- [2] M. Abid and M.E. Brachet. Direct numerical simulations of the batchelor training vortex by a spectral element method. *Physics of Fluids*, 10(2), 1998.
- [3] S. Albensoeder, H.C. Kuhlmann, and H.J. Rath. Three-dimensional centrifugal-flow instabilities in the lid-driven-cavity problem. *Phys. Fluids*, 13(1):121–136, 2001.
- [4] P.H. Alfredson and M. Matsubara. *Streaky structures in transition.*, pages 374–386. Elsevier, 1996.
- [5] P.R. Amestoy, I.S. Duff, J. Koster, and J.-Y. L’Excellent. A fully asynchronous multifrontal solver using distributed dynamic scheduling. *SIAM Journal of Matrix Analysis and Applications.*, 1:15–41, 2001.
- [6] P.R. Amestoy, A. Guermouche, J.-Y. L’Excellent, and S. Pralet. Hybrid scheduling for the parallel solution of linear systems. *Parallel Computing*, 2:136–156, 2006.
- [7] P. Andersson, M. Berggren, and D.S. Henningson. Optimal disturbances and bypass transition in boundary layers. *Phys. Fluids*, 11(1): 134–150, 1999.
- [8] P. Andersson, L. Brandt, A. Bottaro, and D.S. Henningson. On the breakdown of boundary layer streaks. *J. Fluid Mech.*, 428:29–60, 2001.
- [9] E. Arkevik, J. Hoepffner, and D.S. Henningson. Optimal growth, model reduction and control in a separated boundary-layer flow using global eigenmodes. *J. Fluid Mech.*, 579:223–241, 2007.
- [10] M. Asai, M. Minagawa, and M. Nishioka. The instability and breakdown of a near-wall low-speed streak. *J. Fluid Mech.*, 455:289–314, 2002.

- [11] S. Bagheri, P. Schlatter, P.J. Schmid, and D.S. Henningson. Global stability of a jet in crossflow. *J. Fluid Mech.*, 624:33 – 44, 2009.
- [12] P. Balakumar. Boundary layer receptivity due to roughness and freestream sound for supersonic flows over axisymmetric cones. *AIAA 2008-4399*, 2008.
- [13] P. Balakumar and L.R. Owens. Stability of hypersonic three-dimensional boundary layer transition on a cone at angle of attack. *AIAA 2010-4718*, 2010.
- [14] D. Barkley. Linear analysis of the cylinder wake mean flow. *Europhys. Lett.*, 75:750–756, 2006.
- [15] D. Barkley and R.D. Henderson. Three-dimensional Floquet stability analysis of the wake of a circular cylinder. *J. Fluid Mech.*, 322:215–241, 1996.
- [16] M.D. Bartkowicz, P.K. Subbareddy, and G.V. Candler. Simulation of boundary layer transition of elliptic cones in hypersonic flow. *AIAA 2010-1064*, 2010.
- [17] G.K. Batchelor. Axial flow in trailing line vortices. *J. Fluid Mech.*, 4: 645–658, 1964.
- [18] B.J. Bayly, S.A. Orszag, and T. Herbert. Instability mechanisms in shear-flow transition. *Annu. Rev. Fluid Mech.*, 20:359–391, 1988.
- [19] P.S. Beran and F.E.C. Culick. The role of nonuniqueness in the development of vortex breakdown in tubes. *J. Fluid Mech.*, 242:491, 1992.
- [20] M. Bernardini, S. Pirozzoli, and P. Orlandi. Compressibility effects on roughness-induced boundary layer transition. *Int. J. Heat Fluid Fl.*, 35:45–51, 2012.
- [21] F.P. Bertolotti and T. Herbert. Analysis of the linear stability of compressible boundary layers using the pse. *Theoretical and Computational Fluid Dynamics*, 3(2):117–124, 1991.
- [22] F.P. Bertolotti, T. Herbert, and P. Spalart. Linear and nonlinear stability of the Blasius boundary layer. *J. Fluid Mech.*, 242:441–474, 1992.
- [23] H.M. Blackburn, D. Barkley, and S.J. Sherwin. Convective instability and transient growth in flow over a backward facing step. *J. Fluid Mech.*, 603:271–304, 2008.

-
- [24] H.M. Blackburn, D. Barkley, and S.J. Sherwin. Convective instability and transient growth in flow over a backward-facing step. *J. Fluid Mech.*, 603:271–304, 2008.
- [25] H.M. Blackburn, S.J. Sherwin, and D. Barkley. Convective instability and transient growth in steady and pulsatile stenotic flows. *J. Fluid Mech.*, 607:267–277, 2008.
- [26] L.S. Blackford, J. Choi, A. Cleary, A. Petitet, R. C. Whaley, J. Demmel, I. Dhillon, K. Stanley, J. Dongarra, S. Hammarling, G. Henry, and D. Walker. ScaLAPACK: A portable linear algebra library for distributed memory computers — design issues and performance, <http://www.netlib.org/scalapack/>, 1996, 1996. URL citeseer.ist.psu.edu/article/choi95scalapack.html.
- [27] G. Bonfigli and M. Kloker. Secondary instability of crossflow vortices: validation of the stability theory by direct numerical simulation. *J. Fluid Mech.*, 583:229–272, 2007.
- [28] J.P. Boyd. *Chebyshev & Fourier Spectral Methods*. Springer-Verlag, 1989.
- [29] L. Brandt and H.C. de Lange. Streak interactions and breakdown in boundary layer flows. *Phys. Fluids*, 20(024107), 2008.
- [30] T.J. Bridges and P.J. Morris. Differential eigenvalue problems in which the parameter appears nonlinearly. *J. Comp. Phys.*, 55:437–460, 1984.
- [31] M. Broadhurst and S. Sherwin. The parabolised stability equations for 3d-flows: implementation and numerical stability. *Applied Numerical Mathematics*, 58(7):1017–1029, 2008.
- [32] M. Broadhurst, V. Theofilis, and S. Sherwin. Spectral element stability analysis of vortical flows. In R. Govindarajan, editor, *IUTAM Symposium on Laminar-Turbulent Transition*, pages 153–158. 13-17 December 2004, Bangalore, India, Springer, 2006.
- [33] K. Butler and B.F. Farrell. Three-dimensional optimal perturbations in viscous shear flow. *Phys. Fluids*, 4(8), 1992.
- [34] C. Canuto, M.Y. Hussaini, A. Quarteroni, and T.A. Zang. *Spectral Methods*. Springer, 1988.
- [35] M.H. Carpenter, J. Nordstrom, and D. Gottlieb. A stable and conservative interface treatment of arbitrary spatial accuracy. *J. Comp. Phys.*, 148:341–365, 1999.
-

- [36] M.H. Carpenter, J. Nordström, and D. Gottlieb. Revisting and extending interface penalties for multi-domain summation-by-parts operators. *J. Sci. Comput*, 45:118–150, 2011.
- [37] C.L. Chang, M.R. Malik, G. Erlebacher, and M.Y. Hussaini. Compressible stability of growing boundary layers using parabolized stability equations. *AIAA*, 91:1636, 1991.
- [38] M. Choudhari and C.L. Street. A finite Reynolds-number approach for the prediction of boundary-layer receptivity in localized regions. *Phys. Fluids A*, 4(11):2495–2514, 1992.
- [39] M. Choudhari, C. Chang, T. Jentink, F. Li, K. Berger, G. Candler, and R. Kimmel. Transition analysis for the HIFiRE-5 vehicle. *AIAA* 2009-4056, 2009.
- [40] M. Choudhari, F. Li, W. Minwei, C.L. Chang, and J. Edwards. Laminar-turbulent transition behind discrete roughness elements in a high-speed boundary layer. *AIAA 2010-1575*, 2010.
- [41] M. Choudhari, F. Li, C.L. Chang, A. Norris, and J. Edwards. Wake instabilities behind discrete roughness elements in high speed boundary layers. *AIAA 2013-0081*, 2013.
- [42] C.M. Coats. Coherent structures in combustion. *Prog. Energ. Combust.*, 22(5):427–509, 1996.
- [43] T. Colonius. *Direct computation of aerodynamic sound generation*. PhD thesis, Stanford University, 1994.
- [44] T.C. Corke, A. Bar-Server, and M.V. Morkovin. Experiments on transition enhancement by distributed roughness. *Phys. Fluids*, 29(10): 3199–3213, 1986.
- [45] J.D. Crouch. Localized receptivity of boundary layers. *Phys. Fluids A*, 4(7):1408–1414, 1992.
- [46] J.D. Crouch. Instability and transient growth of two trailing-vortex pairs. *J. Fluid Mech.*, 350:311–330, 1997.
- [47] J.D. Crouch, A. Garbaruk, and D. Magidov. Predicting the onset of flow unsteadiness based on global instability. *J. Comp. Phys.*, 224: 924–940, 2007.
- [48] C. Crow and F.H. Champagne. Orderly structure in jet turbulence. *J. Fluid Mech.*, 48:547–591, 1971.

-
- [49] S.C. Crow. Stability theory for a pair of trailing vortices. *AIAA J.*, 8: 2172–2179, 1970.
- [50] N. De Tullio and N.D. Sandham. Direct numerical simulation of breakdown to turbulence in a Mach 6 boundary layer over a porous surface. *Phys. Fluids*, 22(094105), 2010.
- [51] N. De Tullio and N.D. Sandham. Direct numerical simulations of roughness receptivity and transitional shock-wave/boundary-layer interactions. RTO-MP-AVT-200. Art. 22, NATO, 2012.
- [52] N. De Tullio, P. Paredes, N.D. Sandham, and V. Theofilis. Roughness-induced instability and breakdown to turbulence in a supersonic boundary-layer. *J. Fluid Mech.*, 735:613–646, 2013.
- [53] C. Del Pino, L. Parras, M. Felli, and R. Fernandez-Feria. Structure of trailing vortices: Comparison between particle image velocimetry measurements and theoretical models. *Phys. Fluids*, 23:013602, 2011.
- [54] I. Delbende, J.M. Chomaz, and P. Huerre. Absolute/convective instabilities in the Batchelor vortex: a numerical study of the linear impulse response. *J. Fluid Mech.*, 355:229–254, 1998.
- [55] H.A. Dijkstra. On the structure of cellular solutions in rayleigh-benard-marangoni flows in small-aspect-ratio containers. *J. Fluid Mech.*, 243: 73–102, 1992.
- [56] D. Dolvin. Hypersonic International Flight Research and Experimentation (HIFiRE) fundamental science and technology development strategy. AIAA 2008-2581, 2008.
- [57] P.G. Drazin and W.H. Reid. *Hydrodynamic Stability*. Cambridge University Press, 1981.
- [58] P.W. Duck. On the downstream development and breakup of systems of trailing-line vortices. *Theor. Comp. Fluid Dyn.*, 25:43–52, 2011.
- [59] W.S. Edwards, L.S. Tuckerman, R.A. Friesner, and D.C. Sorensen. Krylov methods for the incompressible Navier-Stokes equations. *J. Comp. Phys.*, 110:82–102, 1994.
- [60] U. Ehrenstein and R. Peyret. A chebyshev-collocation method for the navier-stokes equations with application to double-diffusive convection. *Int. J. Numer. Meth. Fluids*, 9:427–452, 1989.
-

- [61] L.E. Eriksson and A. Rizzi. Computer-aided analysis of the convergence to steady state of discrete approximations to the euler equations. *J. Comp. Phys.*, 57:90–128, 1985.
- [62] D. Fabre and L. Jacquin. Stability of a four-vortex aircraft wake model. *Phys. Fluids*, 12:1–6, 2000.
- [63] Y. Feldman and A. Gelfgat. Oscillatory instability in a 3d lid-driven flow in a cube. *Phys. Fluids*, 22:093602, 2010.
- [64] J.E. Ffowcs Williams and A.J. Kempton. The noise from the large-scale structure of a jet. *J. Fluid Mech.*, 84:673–694, 1978.
- [65] B. Fornberg. *A Practical Guide to Pseudospectral Methods*. Cambridge University Press, 1998.
- [66] B. Fornberg. Calculation of weights in finite difference formulas. *SIAM Review*, 40:685–691, 1998.
- [67] K. Fujii. Experiment of the two-dimensional roughness effect on hyper-sonic boundary-layer transition. *J. Spacecraft Rockets*, 43(4):731–738, 2006.
- [68] I. Galionis and P. Hall. Spatial stability of the incompressible corner flow. *Theor. Comp. Fluid Dyn.*, 19:77–113, 2005.
- [69] F. Gallaire, M.R. Ruith, E. Meiburg, J.M. Chomaz, and P. Huerre. Spiral vortex breakdown as a global mode. *J. Fluid Mech.*, 549:71–90, 2006.
- [70] M. Gaster, E. Kit, and I. Wygnanski. Large-scale structures in a forced turbulent mixing layer. *J. Fluid Mech.*, 150:23–39, 1985.
- [71] M. Gaster, C.E. Grosch, and T.L. Jackson. The velocity field created by a shallow bump in a boundary layer. *Phys. Fluids*, 6(9):3079–3085, 1994.
- [72] E.M. Gennaro, D. Rodríguez, M.A.F. Medeiros, and V. Theofilis. Sparse techniques in global flow instability with application to compressible leading-edge flow. *AIAA J.*, 51:2295–2303, 2013.
- [73] U. Ghia, K.N. Ghia, and C.T. Shin. High-Re solutions for incompressible flow using the Navier-Stokes equations and a multigrid method. *J. Comput. Phys.*, 48:387–411, 1982.

-
- [74] F. Giannetti, P. Luchini, and L. Marino. Linear stability analysis of three-dimensional lid-driven cavity flow. In *Atti del XIX Congresso AIMETA di Meccanica Teorica e Applicata*, pages 738.1–10, Ancona 14-17 Sep. 2009, 2009. Aras Edizioni, Ancona, Italy.
- [75] M.E. Goldstein. Scattering of acoustic waves into Tollmien-Schlichting waves by small streamwise variations in surface geometry. *J. Fluid Mech.*, 154:509–529, 1985.
- [76] G.H. Golub and C.F. van Loan. *Matrix Computations*. The Johns Hopkins University Press, 3 edition, 1996.
- [77] F. Gómez, S. Le Clainche, P. Paredes, M. Hermanns, and V. Theofilis. Decades of studying global linear instability: progress and challenges. *AIAA J.*, 50(12):2731–2743, 2012.
- [78] F. Gómez, P. Paredes, R. Gómez, and V. Theofilis. Global stability of cubic and large aspect ratio three-dimensional lid-driven cavities. *AIAA 2012-3274*, 2012.
- [79] L.M. González, V. Theofilis, and R. Gomez-Blanco. Finite element methods for viscous incompressible BiGlobal instability analysis on unstructured meshes. *AIAA J.*, 45(4):840–854, 2007.
- [80] R. Gosse and R. Kimmel. CFD study of three-dimensional hypersonic laminar boundary layer transition on a Mach 8 elliptic cone. *AIAA 2009-4053*, 2009.
- [81] R. Gosse, R. L. Kimmel, and H. Johnson. Cfd study of the HIFiRE-5 flight experiment. *AIAA 2010-4854*, 2010.
- [82] D. Gottlieb, M.Y. Hussaini, and S.A. Orszag. Theory and applications of spectral methods. In *Spectral Methods for Partial Differential Equations*, pages 1–54. SIAM, Philadelphia, 1984.
- [83] D. Greenblatt and I.J. Wygnanski. The proper orthogonal decomposition in the analysis of turbulent flows. *Ann. Rev. Fluid Mech.*, 25: 539–575, 1993.
- [84] D. Greenblatt and I.J. Wygnanski. The control of flow separation by periodic excitation. *Prog. Aero. Sciences*, 36(7):487–454, 2000.
- [85] J.E. Gronvall, H.B. Johnson, and G.V. Candler. Hypersonic three-dimensional boundary layer transition on a cone at angle of attack. *AIAA 2011-3561*, 2011.
-

- [86] J.E. Gronvall, H.B. Johnson, and G.V. Candler. Hypersonic three-dimensional boundary layer transition on a cone at angle of attack. AIAA 2012-2822, 2012.
- [87] G. Groskopf, M.J. Kloker, and O. Marxen. Bi-global crossplane stability analysis of high-speed boundary-layer flows with discrete roughness. In D. Henningson P. Schlatter, editor, *IUTAM Symposium on Laminar-Turbulent Transition*, pages 171–176. Springer, 2009.
- [88] K. Gudmundsson and T. Colonius. Instability wave models for the near-field fluctuations of turbulent jets. *J. Fluid Mech.*, 689:97–128, 2011.
- [89] M.G. Hall. Vortex breakdown. *Annu. Rev. Fluid Mech.*, 4:195–218, 1972.
- [90] A. Hanifi, D. Henningson, S. Hein, F.P. Bertolotti, and M. Simen. Linear nonlocal instability analysis - the linear NOLOT code. Technical Report TN 1994-54, FFA, 1994.
- [91] A. Hanifi, P.J. Schmid, and D.S. Henningson. Transient growth in compressible boundary layer flow. *Phys. Fluids*, 8(3):826–837, 1996.
- [92] C.J. Heaton, J.W. Nichols, and P.J. Schmid. Global linear stability of the non-parallel Batchelor vortex. *J. Fluid Mech.*, 17:139–160, 2009.
- [93] R.S. Heeg and J. Geurts. Spatial instabilities of the incompressible attachment-line flow using sparse matrix jacobi-davidson techniques. *Applied Scientific Research*, 59:315–329, 1998.
- [94] S. Hein. *Nonlinear nonlocal transition analysis*. PhD thesis, University of Stuttgart, September 2005. DLR-FD 2005-10.
- [95] S. Hein and V. Theofilis. On instability characteristics of isolated vortices and models of trailing-vortex systems. *Computers & Fluids*, 33:741–753, 2004.
- [96] S. Hein, F.P. Bertolotti, M. Simen, A. Hanifi, and D. Henningson. Linear nonlocal instability analysis - the linear NOLOT code. Technical Report IB 223-94 A56, DLR, 1994.
- [97] W.S. Helliwell and S.C. Lubard. An implicit method for three dimensional viscous flow with application to cones at angle of attack. *Compt. Fluids*, 3:83–101, 1973.
- [98] R.D. Henderson and D. Barkley. Secondary instability of the wake of a circular cylinder. *Phys. Fluids*, 8(6):65–112, 1996.

-
- [99] T. Herbert. Secondary instability of shear flows. In *AGARD-R-709 Special Course on Stability and Transition of Laminar Flow*, pages 7.1–7.13, 1984.
- [100] T. Herbert. Boundary-layer transition – analysis and prediction revisited. *AIAA*, 91:0737, 1991.
- [101] T. Herbert. Parabolized stability equations. *AGARD Report No. 793. Special Course on Progress in Transition Modelling*, pages 4(1)–4(34), 1994.
- [102] T. Herbert. Parabolized stability equations. *Ann. Rev. Fluid Mech.*, 29:245–283, 1997.
- [103] M. Hermanns and J.A. Hernández. Stable high-order finite-difference methods based on non-uniform grid point distributions. *International Journal for Numerical Methods in Fluids*, 56:233–255, 2008.
- [104] F. Hildebrand. *Introduction to Numerical Analysis*. Dover, 1987.
- [105] T.J. Horvath, S.A. Berri, and N.R. Merski. Hypersonic Boundary/Shear Layer Transition for Blunt to Slender Configurations: A NASA Langley Experimental Perspective. Technical Report RTO-MP-AVT-111 (22), NATO, 2004.
- [106] P. Huerre and P.A. Monkewitz. Absolute and convective instabilities in free shear layers. *J. Fluid Mech.*, 159:151–168, 1985.
- [107] P. Huerre and P.A. Monkewitz. Local and global instabilities in spatially developing flows. *Ann. Rev. Fluid Mech.*, 22:473–537, 1990.
- [108] L.S. Hultgren and H. Gustavsson. Algebraic growth of disturbances in a laminar boundary layer. *Phys. Fluids*, 24(1000), 1981.
- [109] M. Huntley and A.J. Smits. Transition studies on an elliptic cone in Mach 8 flow using filtered Rayleigh scattering. *European Journal of Mechanics B - Fluids*, 19(5):695–706, 2000.
- [110] A.K.M.F. Hussain and W.C. Reynolds. The mechanisms of an organized wave in turbulent shear flow. *J. Fluid Mech.*, 41:241–258, 1970.
- [111] E. Isaacson and H. Keller. *Analysis of Numerical Methods*. Dover, 1994.
- [112] E. Ivanova. *Numerical Simulations of Turbulent Mixing in Complex Flows*. Phd thesis, University of Stuttgart, 2012.
-

- [113] C.P. Jackson. A finite-element study of the onset of vortex shedding in flow past variously shaped bodies. *J. Fluid Mech.*, 182:23–45, 1987.
- [114] R.G. Jacobs and P.A. Durbin. Simulations of bypass transition. *J. Fluid Mech.*, 428:185–212, 2001.
- [115] J. Jiménez. Stability of a pair of co-rotating vortices. *Phys. Fluids*, 18:1580–1581, 1975.
- [116] L.E. Jones. *Numerical study of the flow around an airfoil at low Reynolds number*. PhD thesis, School of Engineering Sciences, University of Southampton, 2008.
- [117] R.D. Joslin and C.E. Grosch. Growth characteristics downstream of a shallow bump: Computation and experiment. *Phys. Fluids*, 7(12): 3042–3047, 1995.
- [118] G.E. Karniadakis and S.J. Sherwin. *Spectral/hp element methods for Computational Fluid Dynamics (2nd ed.)*. Oxford University Press, 2005.
- [119] M. Kegerise, R. King, L. Owens, M. Choudhari, F. Li, C.L. Chang, and A. Norris. An experimental and numerical study of roughness-induced instabilities in a Mach 3.5 boundary layer. RTO-MP-AVT-200. Art. 29., NATO, 2012.
- [120] M.A. Kegerise, L.R. Owens, and A.K. Rudolf. High-Speed Boundary-Layer Transition Induced by an Isolated Roughness Element. *AIAA 2010-4999*, 2010.
- [121] R.R. Kerswell. Elliptical instability. *Annu. Rev. Fluid Mech.*, 34:83–113, 2002.
- [122] M.R. Khorrami. A chebyshev spectral collocation method using a staggered grid for the stability of cylindrical flows. *Int. J. Numer. Meth. Fluids*, 12:825–833, 1991.
- [123] M.R. Khorrami, M.R. Malik, and R.L. Ash. Application of spectral collocation techniques to the stability of swirling flows. *Journal of Computational Physics*, 81:206–229, 1989.
- [124] R. Kimmel, D. Adamczak, K. Berger, and M. Choudhari. HIFiRE-5 flight vehicle design. *AIAA 2010-4985*, 2010.
- [125] R.L. Kimmel, M.A. Klein, and S.N. Schwoerke. Three-dimensional hypersonic laminar boundary-layer computations for transition experiment design. *J. Spacecraft Rockets*, 34(4):409–415, 1997.

-
- [126] R.A. King. Three-dimensional boundary-layer transition on a cone at Mach 3.5. *Exp. Fluids*, 13:305–314, 1992.
- [127] N.P. Kirchner. Computational aspects of the spectral galerkin fem for the orr-sommerfeld equation. *Int. J. Numer. Meth. Fluids*, 32:119–137, 2000.
- [128] E. Kit, I. Wygnanski, D. Friedman, O. Krivonosova, and D. Zhilenko. On the periodically excited plane turbulent mixing layer, emanating from a jagged partition. *J. Fluid Mech.*, 589:479–507, 2007.
- [129] V. Kitsios, D. Rodríguez, V. Theofilis, A. Ooi, and J. Soria. BiGlobal stability analysis in curvilinear coordinates of massively separated lifting bodies. *J. Comp. Phys.*, 228:7181–7196, 2009.
- [130] P.S. Klebanoff and K.D. Tidstrom. Mechanism by which a two-dimensional roughness element induces boundary layer transition. *Phys. Fluids*, 15(7):1173–1188, 1972.
- [131] J.J. Kuehl, E. Perez, and H.L. Reed. JoKHeR: NPSE simulations of hypersonic cross flow instability. AIAA 2012-0921, 2012.
- [132] L. Lacaze, K. Ryan, and S. Le Dizès. Elliptic instability in a strained Batchelor vortex. *J. Fluid Mech.*, 577:341–361, 2007.
- [133] M.T. Landahl. Wave breakdown and turbulence. *SIAM J. Appl. Math.*, 28(4):735–756, 1975.
- [134] S.L. Lawrence, J.C. Tannehill, and D.S. Chaussee. An upwind algorithm for the parabolized Navier-Stokes equations. *AIAA*, 86:1117, 1986.
- [135] S.L. Lawrence, D.S. Chaussee, and J.C. Tannehill. Application of an upwind algorithm to the three-dimensional parabolized Navier-Stokes equations. *AIAA J.*, 87:1112, 1987.
- [136] S. Leibovich. The structure of vortex breakdown. *Ann. Rev. Fluid Mech.*, 10:221–246, 1978.
- [137] S. Leibovich. Vortex stability and breakdown: Survey and extension. *AIAA J.*, 22:1192–1206, 1984.
- [138] S. Lele. Compact finite difference schemes with spectral- like resolution. *J. Comp. Phys.*, 103:16–42, 1992.
- [139] M. Lessen and F. Paillet. The stability of a trailing line vortex. part 2. viscous theory. *J. Fluid Mech.*, 65:769–779, 1974.
-

- [140] M. Lessen, P.J. Singh, and F. Paillet. The stability of a trailing line vortex. part 1. inviscid theory. *J. Fluid Mech.*, 63:753–763, 1974.
- [141] W. Leuckel. Swirl intensities, swirl types and energy losses of different swirl generating devices. *IFRF Doc. Nr. G*, 2:1–53, 1967.
- [142] T. Leweke and C.H.K. Williamson. Cooperative elliptic instability of a vortex pair. *J. Fluid Mech.*, 360:85–119, 1998.
- [143] F. Li and M. Choudhari. Spatially developing secondary instabilities in compressible swept airfoil boundary layers. *Theor. Comp. Fluid Dyn.*, 25:65–84, 2011.
- [144] F. Li and M.R. Malik. Mathematical nature of parabolized stability equations. *R. Kobayashi (Ed.), Laminar-Turbulent Transition, Springer*, pages 205–212, 1994.
- [145] F. Li and M.R. Malik. On the nature of the pse approximation. *Theoretical and Computational Fluid Dynamics*, 8:253–273, 1996.
- [146] F. Li and M.R. Malik. Spectral analysis of parabolized stability equations. *Computers and Fluids*, 26 (3):279–297, 1997.
- [147] F. Li, M. Choudhari, C. Chang, and J. White. Analysis of instabilities in non-axisymmetric hypersonic boundary layers over cones. AIAA 2010-4643, 2010.
- [148] F. Li, M. Choudhari, C. Chang, J. White, R. Kimmel, D. Adamczak, M. Borg, S. Stanfield, and M. Smith. Stability analysis for HIFiRE experiments. AIAA 2012-2961, 2012.
- [149] Q. Li. *Numerical study of the Mach number effect in compressible wall-bounded turbulence*. PhD thesis, School of Engineering Sciences, University of Southampton, 2003.
- [150] H. Liang and T. Maxworthy. An experimental investigation of swirling jets. *J. Fluid Mech.*, 525:115–159, 2005.
- [151] T.C. Lieuwen. *Unsteady combustor physics*. Cambridge, 1st edition, 2012.
- [152] C.C. Lin. *The theory of hydrodynamic stability*. Cambridge University Press, 1955.
- [153] R.-S. Lin and M.R. Malik. On the stability of attachment-line boundary layers. Part 1. the incompressible swept Hiemenz flow. *J. Fluid Mech.*, 311:239–255, 1996.

-
- [154] T.C. Lin and S.G. Rubin. Viscous flow over a cone at moderate incidence-I: Hypersonic tip region. *Compt. Fluids*, 1:37–57, 1973.
- [155] T.C. Lin and S.G. Rubin. Viscous flow over a cone at moderate incidence-I: Supersonic boundary layer. *J. Fluid Mech.*, 59:593–620, 1973.
- [156] T.C. Lin and S.G. Rubin. Viscous flow over spinning cones at angle of attack. *AIAA J.*, 12(7):975–985, 1974.
- [157] S.C. Lubard and W.S. Helliwell. Calculation of the flow on a cone at high angle of attack. *AIAA J.*, 11:965–974, 1974.
- [158] I.J. Lyttle and H.L. Reed. Use of transition correlations for three-dimensional boundary layers within hypersonic flows. AIAA 95-2293, 1995.
- [159] C.J. Mack and P.J. Schmid. Global stability of swept flow around a parabolic body: features of the global spectrum. *J. Fluid Mech.*, 669:375–396, 2011.
- [160] L.M. Mack. A numerical study of the temporal eigenvalue spectrum of the blasius boundary layer. *J. Fluid Mech.*, 73:497–520, 1976.
- [161] L.M. Mack. Boundary-layer stability theory. *AGARD Report No. 709. Special Course on Stability and Transition of Laminar Flow*, pages 3–1–3–81, 1984.
- [162] M.R. Malik. Prediction and control of transition in hypersonic boundary layers. AIAA 87-1414, 1987.
- [163] M.R. Malik. e^{Malik} : a new spatial stability analysis program for transition prediction using the e^N method. Rept. HTC-8902, High Technology Corp., Hampton, VA, 1989.
- [164] M.R. Malik. Numerical methods for hypersonic boundary layer stability. *J. Comp. Phys.*, 86:376–413, 1990.
- [165] M.R. Malik and E.C. Anderson. Real gas effects on hypersonic boundary-layer stability. *Phys. Fluids A*, 3(5):803–821, 1991.
- [166] M.R. Malik, F. Li, and M. Choudhari. Analysis of crossflow transition flight experiment aboard Pegasus Launch Vehicle. AIAA 2007-4487, 2007.
- [167] W. Mangler. Boundary layers on bodies of revolution in symmetrical flows. Report 45/A/17, Ber. Aerodyn. Versuchsanst. Goett., 1945.
-

- [168] J.A. Martín and C. Martel. Nonlinear streak computation using boundary region equations. *Fluid Dyn. Res.*, 44:045503 (23pp), 2012.
- [169] O. Marxen, G. Iaccarino, and S.G. Shaqfeh. Disturbance evolution in a Mach 4.8 boundary layer with two-dimensional roughness-induced separation and shock. *J. Fluid Mech.*, 648:435–469, 2010.
- [170] K. Mattson and J. Nordström. Summation by parts operators for finite difference approximations of second derivatives. *J. Comp. Phys.*, 199(2):503–540, 2004.
- [171] E.W. Mayer and K.G. Powell. Viscous and inviscid instabilities of a trailing vortex. *J. Fluid Mech.*, 245:94–114, 1992.
- [172] P. Meliga, F. Gallaire, and J.-M. Chomaz. A weakly nonlinear mechanism for mode selection in swirling jets. *J. Fluid Mech.*, 699:216–262, 2012.
- [173] P. Meliga, G. Pujals, and É. Serre. Sensitivity of 2-d turbulent flow past a d-shaped cylinder using global stability. *Phys. Fluids*, 24(6):061701, 2012.
- [174] X. Merle, F. Alizard, and J.-Ch. Robinet. Finite difference methods for viscous incompressible global instability analysis. *Comput. Fluids*, 39:911–925, 2010.
- [175] X. Merle, F. Alizard, and J.-Ch. Robinet. Finite difference methods for viscous incompressible global stability analysis. *Comput. Fluids*, 39(6):911–925, 2010.
- [176] D.W. Moore and P.G. Saffman. Axial flow in laminar trailing vortices. *Proc. R. Soc. London Ser. A*, 333:491, 1973.
- [177] P.M. Morse and H. Feshbach. *Methods of Theoretical Physics, Parts I, II*. McGraw-Hill, 1953.
- [178] M. Morzyński and F. Thiele. Finite element method for global stability analysis of 3D flows. AIAA 2008-3865, 2008.
- [179] M.S. Mughal. Stability analysis of complex wing geometries: Parabolised stability equations in generalised non-orthogonal coordinates. AIAA 2006-3222, 2006.
- [180] B.R. Noack, K. Afanasiev, M. Morzyński, G. Tadmor, and F. Thiele. A hierarchy of low-dimensional models for the transient and post-transient cylinder wake. *J. Fluid Mech.*, 497:335–363, 2003.

-
- [181] I. Nompelis, T. Drayna, and G. Candler. A parallel unstructured implicit solver for hypersonic reacting flow simulation. *AIAA 2005-4867*, 2005.
- [182] K. Oberleithner, M. Sieber, C.N. Nayeri, C.O. Paschereit, C. Petz, H.C. Hege, B.R. Noack, and I. Wygnanski. Three-dimensional coherent structures in a swirling jet undergoing vortex breakdown: stability analysis and empirical mode construction. *J. Fluid Mech.*, 679:383–414, 2011.
- [183] K. Oberleithner, C.O. Paschereit, and I. Wygnanski. On the impact of swirl on the growth of coherent structures. *J. Fluid Mech.*, 741:156–199, 2013.
- [184] K. Oberleithner, S. Terhaar, L. Rukes, and C.O. Paschereit. Why non-uniform density suppresses the precessing vortex core. *J. Eng. Gas Turb. Power*, 135(2):121506 (9 pages), 2013.
- [185] S.A. Orszag. Accurate solution of the Orr-Sommerfeld stability equation. *J. Fluid Mech.*, 50:689–703, 1971.
- [186] L.R. Owens, M.A. Kegerise, and S.P. Wilkinson. Off-Body Boundary-Layer Measurement Techniques Development for Supersonic Low-Disturbance Flows. *AIAA 2011-0284*, 2011.
- [187] P. Paredes and V. Theofilis. Spatial linear global instability analysis of the HIFiRE-5 elliptic cone model flow. *AIAA 2013-2880*, 2013.
- [188] P. Paredes, V. Theofilis, D. Rodríguez, and J. A. Tendero. The PSE-3D instability analysis methodology for flows depending strongly on two and weakly on the third spatial dimension. *AIAA 2011-3752*, 2011.
- [189] P. Paredes, M. Hermanns, S. Le Clainche, and V. Theofilis. Order 10^4 speedup in global linear instability analysis using matrix formation. *Comput. Meth. Appl. Mech. Eng.*, 253:287–304, 2013.
- [190] E. Perez, H.L. Reed, and J.J. Kuehl. Instabilities on a hypersonic yawed straight cone. *AIAA 2013-2879*, 2012.
- [191] J.M. Pérez, D. Rodríguez, and V. Theofilis. Linear global instability of non-orthogonal incompressible swept attachment-line boundary-layer flow. *J. Fluid Mech.*, 710:131–153, 2012.
- [192] B. Pier. On the frequency selection of finite-amplitude vortex shedding in the cylinder wake. *J. Fluid Mech.*, 458:407–417, 2002.
-

- [193] R.T. Pierrehumbert. Universal shortwave instability of two-dimensional eddies in an inviscid fluid. *Phys. Rev. Lett.*, 57:2157–2159, 1986.
- [194] R.T. Pierrehumbert and S.E. Widnall. The two- and three-dimensional instabilities of a spatially periodic shear layer. *J. Fluid Mech.*, 114:59–82, 1982.
- [195] J. Poggie and R.L. Kimmel. Traveling instabilities in elliptic cone boundary-layer transition at $Ma=8$. AIAA 98-0435, 1998.
- [196] J. Poggie, R.L. Kimmel, and S.N. Schwoerke. Traveling instability waves in a Mach 8 flow over an elliptic cone. *AIAA J.*, 38(2):251–258, 2000.
- [197] D.C. Reda. Review and synthesis of roughness-dominated transition correlations for reentry vehicles. *J. Spacecraft Rockets*, 39(2):161–167, 2002.
- [198] S.C. Reddy, P.J. Schmid, and D.S. Henningson. Pseudospectra of the Orr-Sommerfeld equation. *SIAM J. Appl. Math.*, 53(1):15 – 47, 1993.
- [199] S.C. Reddy, P.J. Schmid, J.S. Baggett, and D. S. Henningson. Simulations of bypass transition. *J. Fluid Mech.*, 428:185–212, 2001.
- [200] J.A. Redford, N.D. Sandham, and G.T. Roberts. Compressibility effects on boundary-layer transition induced by an isolated roughness element. *AIAA J.*, 48(12):2818–1830, 2010.
- [201] H.L. Reed and T.S. Haynes. Transition correlations in three-dimensional boundary layers. *AIAA J.*, 32:923–929, 1994.
- [202] H.L. Reed, W.S. Saric, and D. Arnal. Linear stability theory applied to boundary layers. *Ann. Rev. Fluid Mech.*, 28:389–428, 1996.
- [203] E. Reshotko. Transient growth: A factor in bypass transition. *Phys. Fluids*, 13(5):1067–1075, 2001.
- [204] E. Reshotko and A. Tumin. Role of transient growth on roughness-induced transition. *AIAA J.*, 42(4):766–770, 2004.
- [205] W.C. Reynolds and A.K.M.F. Hussain. The mechanisms of an organized wave in turbulent shear flow. part 3. theoretical models and comparison with experiments. *J. Fluid Mech.*, 54:263–288, 1972.
- [206] D.P. Rizzetta and M.R. Visbal. Direct numerical simulations of flow past an array of distributed roughness elements. *AIAA J.*, 45(8):1967–1976, 2007.

-
- [207] J.-Ch. Robinet. Bifurcations in shock-wave/laminar-boundary-layer interaction: global instability approach. *J. Fluid Mech.*, 579:85–112, 2007.
- [208] D. Rodríguez and V. Theofilis. Massively parallel numerical solution of the BiGlobal linear instability eigenvalue problem using dense linear algebra. *AIAA J.*, 47(10):2449–2459, 2009.
- [209] D. Rodríguez and V. Theofilis. Structural changes of laminar separation bubbles induced by global linear instability. *J. Fluid Mech.*, 655:280–305, 2010.
- [210] D. Rodríguez and V. Theofilis. On the birth of stall cells on airfoils. *Theor. Comp. Fluid Dyn.*, 25(1-4):105–118, 2011.
- [211] L. Rosenhead. *Laminar Boundary Layers*. Oxford University Press, 1963.
- [212] C.W. Rowley, I. Mezić, S. Bagheri, P. Schlatter, and D.S. Henningson. Spectral analysis of nonlinear flows. *J. Fluid Mech.*, 641:115–127, 2009.
- [213] A.I. Ruban. On Tollmien-Schlichting wave generation by sound. *Izv. Akad. Nauk SSSR Mekh. Zhidk. Gaza*, 5:44–52, 1984.
- [214] S.G. Rubin and T.C. Lin. Marching with the PNS equations. *Ist J. Technol.*, 18:21–31, 1981.
- [215] S.G. Rubin and J.C. Tannehill. Parabolized/reduced navier-stokes computational techniques. *Ann. Rev. Fluid Mech.*, 24:117–144, 2004.
- [216] S. Rudman and S.G. Rubin. Hypersonic viscous flow over slender bodies with sharp leading edges. *AIAA J.*, 6:1883–1889, 1968.
- [217] Z. Rusak and K.P. Judd. The stability of noncolumnar swirling flows in diverging streamtubes. *Phys. Fluids*, 13:2835–2844, 2001.
- [218] Y. Saad. Variations of Arnoldi’s method for computing eigenelements of large unsymmetric matrices. *Linear Algebra Appl.*, 34:269–295, 1980.
- [219] Y. Saad. Sparskit: a basic tool kit for sparse matrix computations. Technical report, NAS Systems Division, 1994.
- [220] N.D. Sandham, Q. Li, and H.C. Yee. Entropy splitting for high-order numerical simulation of compressible turbulence. *J. Comp. Phys.*, 178:307–322, 2002.
-

- [221] P. Schmid and D. Henningson. *Stability and transition in shear flows*. Springer, 2001.
- [222] O.T. Schmidt and U. Rist. Linear stability of compressible flow in a streamwise corner. *J. Fluid Mech.*, 688:569–590, 2011.
- [223] O.T. Schmidt and U. Rist. Viscid-inviscid pseudo-resonance in streamwise corner flow. *J. Fluid Mech.*, 743:327–357, 2014.
- [224] J.D. Schmisser, S.P. Schneider, and S.H. Collicott. Receptivity of the Mach-4 boundary-layer on an elliptic cone to laser-generated localized free stream perturbations. AIAA 98-0532, 1998.
- [225] J.D. Schmisser, S.P. Schneider, and S.H. Collicott. Response of the Mach-4 boundary layer on an elliptic cone to laser-generated free stream perturbations. AIAA 99-0410, 1999.
- [226] S.P. Schneider. Effects of roughness on hypersonic boundary-layer transition. *J. Spacecraft Rockets*, 45(2):193–209, 2008.
- [227] R. Schreiber and H.B. Keller. Driven cavity flows by efficient numerical techniques. *J. Comput. Phys.*, 49:310–433, 1983.
- [228] A.H. Shapiro. *The dynamics and thermodynamics of compressible fluid flow. Vol. 2*. Ronald Press, New York, 1954.
- [229] D. Sipp, L. Jacquin, and C. Cosssu. Self-adaptation and viscous selection in concentrated two-dimensional vortex dipoles. *Physics of Fluids*, 12:245–248, 2000.
- [230] A.M.O. Smith and N. Gamberoni. Transition, pressure gradient and stability theory. Rept. ES-26388., Douglas Aircraft Co., El Segundo, California, 1956.
- [231] P.C. Stainback. Effect of unit Reynolds number, nose bluntness, angle of attack and roughness on transition on a 5 deg half-angle cone at Mach 8. Technical Report TN D-4961, NASA, 1969.
- [232] J.F. Stalnaker, L.A. Nicholson, D.S. Hanline, and E.H. McGraw. Improvements to the AFWAL parabolized Navier-Stokes code formulation. U.S. AirForce Wright Aeronautical Labs., TR AFWAL-TR-86-3076, Wright-Patterson AFB, OH, 1986.
- [233] K.F. Stetson. Mach 6 experiments of transition on a cone at angle of attack. *J. Spacecraft Rockets*, 19(5):397–403, 1982.

-
- [234] B. Strand. Summation by parts for finite difference approximations for d/dx . *J. Comp. Phys.*, 110:47–67, 1994.
- [235] G. Stuckert and H. Reed. Linear disturbances in hypersonic, chemically reacting shock layers. *AIAA Journal*, 32:1384–1393, 1994.
- [236] G. Stuckert and H.L. Reed. Linear disturbances in hypersonic, chemically reacting shock layers. *AIAA J.*, 32(7):1384–1393, 1994.
- [237] E.O. Swanson and S.P. Schneider. Boundary-layer transition on cones at angle of attack in a Mach-6 quiet tunnel. AIAA 2010-1062, 2010.
- [238] J.D. Swearingen and R.F. Blackwelder. The growth and breakdown of streamwise vortices in the presence of a wall. *J. Fluid Mech.*, 182:255–290, 1987.
- [239] N. Syred. A review of oscillation mechanisms and the role of the precessing vortex core (pvc) in swirl combustion systems. *Prog. Energy Combust.*, 32(2):93–161, 2006.
- [240] C. Tam and J. Webb. Dispersion-relation-preserving finite difference schemes for computational acoustics. *J. Comp. Phys.*, 107:262–281, 1993.
- [241] I. Tani and H. Sato. Boundary-layer transition by roughness element. *J. Phys. Soc. Jpn.*, 11(12):1284–1291, 1956.
- [242] J.C. Tannehill, E. Venkatapathy, and J.V. Rakich. Numerical solution of supersonic viscous flow over blunt delta wings. *AIAA J.*, 20:203–210, 1982.
- [243] J.C. Tannehill, D. Anderson, and R. Pletcher. *Computational Fluid Mechanics and Heat Transfer*. Taylor & Francis, second edition, 1997.
- [244] T. Tatsumi and T. Yoshimura. Stability of the laminar flow in a rectangular duct. *J. Fluid Mech.*, 212:437–449, 1990.
- [245] G.I. Taylor and J.W. Maccoll. The air pressure on a cone moving at high speed. *Proc. R. Soc. London Ser. A*, 139:278–311, 1933.
- [246] A. Tezuka and K. Suzuki. Three-dimensional global linear stability analysis of flow around a spheroid. *AIAA J.*, 44(8):1697–1708, 2006.
- [247] V. Theofilis. Spatial stability of incompressible attachment-line flow. *Theor. Comp. Fluid Dyn.*, 7(3):159–171, 1995.
- [248] V. Theofilis. Globally-unstable flows in open cavities. AIAA 2000-1965, 2000.
-

- [249] V. Theofilis. Advances in global linear instability of nonparallel and three-dimensional flows. *Prog. Aero. Sciences*, 39 (4):249–315, 2003.
- [250] V. Theofilis. Global linear instability. *Annu. Rev. Fluid Mech.*, 43: 319–352, 2011.
- [251] V. Theofilis and T. Colonius. Three-dimensional instabilities of compressible flow over open cavities: Direct solution of the BiGlobal eigenvalue problem. AIAA 2004-2544, 2004.
- [252] V. Theofilis, D. Barkley, and S. J. Sherwin. Spectral/hp element technology for flow instability and control. *Aero. J.*, 106:619–625, 2002.
- [253] V. Theofilis, A. Fedorov, D. Obrist, and U. Ch. Dallmann. The extended Görtler-Hämmerlin model for linear instability of three-dimensional incompressible swept attachment-line boundary layer flow. *J. Fluid Mech.*, 487:271–313, 2003.
- [254] V. Theofilis, P.W. Duck, and J. Owen. Viscous linear stability analysis of rectangular duct and cavity flows. *J. Fluid Mech.*, 505:249–286, 2004.
- [255] V. Theofilis, A.V. Fedorov, and S.S. Collis. Leading-edge boundary layer flow - Prandtl’s vision, current developments and future perspectives. *IUTAM Symposium on One Hundred Years of Boundary Layer Research*, 129, 2004.
- [256] B. Thiria and J.E. Wesfreid. Stability properties of forced wakes. *J. Fluid Mech.*, 579:137–161, 2007.
- [257] W. Tollmien. *Über die Entstehung der Turbulenz. 1. Mitteilung.* Nachr. Ges. Wiss. Göttingen, Math. Phys. Klasse, 1929.
- [258] L.N. Trefethen. *Spectral Methods in Matlab*. SIAM, 2000.
- [259] L.N. Trefethen, A.E. Trefethen, S.C. Reddy, and T. Driscoll. Hydrodynamic stability without eigenvalues. *Science*, 261:578–584, 1993.
- [260] V.N. Trigub. The problem of breakdown of a vortex line. *J. Appl. Math. Mech.*, 49:166–171, 1985.
- [261] L.S. Tuckerman and D. Barkley. Bifurcation analysis for timesteppers. In *Numerical methods for bifurcation problems and large-scale dynamical systems*, pages 453–566. Springer, 2000.
- [262] A. Tumin and E. Reshotko. Receptivity of a boundary-layer flow to a three-dimensional hump at finite Reynolds numbers. *Phys. Fluids*, 17 (094101), 2005.

-
- [263] J.L. Van Ingen. A suggested semi-empirical method for the calculation of boundary layer transition region. Rept. UTH-74., Univ. of Techn., Dept. of Aero. Eng., Delft, 1956.
- [264] Y.C. Vigneron, J.V. Rakich, and J.C. Tannehill. Calculation of supersonic viscous flow over delta wings with sharp subsonic leading edges. AIAA 78-1337, 1978.
- [265] S. Wang and Z. Rusak. The time-asymptotic behavior of vortex breakdown in tubes. *Compt. Fluids*, 23:913, 1994.
- [266] S. Wang and Z. Rusak. The dynamics of a swirling flow in a pipe and transition to axisymmetric vortex breakdown. *J. Fluid Mech.*, 340:177, 1997.
- [267] S. Wang and Z. Rusak. The effect of slight viscosity on a near-critical swirling flow in a pipe. *Phys. Fluids*, 9:1914–1927, 1997.
- [268] P. Wassermann and M. Kloker. Transition mechanisms induced by travelling crossflow vortices in a three-dimensional boundary layer. *J. Fluid Mech.*, 483:67 – 89, 2003.
- [269] B.M. Wheaton and S.P. Schneider. Roughness-induced instability in a hypersonic laminar boundary layer. *AIAA J.*, 5(6):1245–1256, 2012.
- [270] B.M. Wheaton and S.P. Schneider. Instability and transition due to near-critical roughness in a hypersonic laminar boundary layer. *AIAA 2013-0084*, 2013.
- [271] F.M. White. *Viscous fluid flow*. McGraw-Hill, 3rd edition, 2005.
- [272] S.E. Widnall. The structure and dynamics of vortex filaments. *Ann. Rev. Fluid Mech.*, 7:141–165, 1975.
- [273] D.C. Wilcox. *Turbulence Modeling for CFD*. DCW Industries, 3rd edition, 2006.
- [274] A.A. Wray. Minimal storage time advancement schemes for spectral methods. Rept. M.S. 202 A-1., NASA Ames Research Centre, 1990.
- [275] T.G. Wright. Eigtool. Technical report, Oxford University Computing Laboratory, 2002. Available at <http://www.comlab.ox.ac.uk/pseudospectra/eigtool/>.
- [276] X. Wu and M. Choudhari. Linear and nonlinear instabilities of a Blasius boundary layer perturbed by streamwise vortices. Part 2: Intermittent instability induced by long-wavelength Klebanoff modes. *J. Fluid Mech.*, 483:249–286, 2003.

Bibliography

- [277] Y. Yao, Z. Shang, J. Castagna, R. Johnstone, R.E. Jones, J.A. Redford, R.D. Sandberg, N.D. Sandham, V. Suponitsky, and N. De Tullio. Re-engineering a DNS code for high-performance computation of turbulent flows. AIAA 2009-566, 2009.
- [278] A. Zebib. Stability of viscous flow past a circular cylinder. *J. Eng. Math.*, 21:155–165, 1987.